VYTAUTAS KAVALIŪNAS

THE FORMATION AND INVESTIGATION OF TITANIUM DIOXIDE STRUCTURES FOR PHOTOCATALYTIC APPLICATIONS

DOCTORAL DISSERTATION

Kaunas
2023

KAUNAS UNIVERSITY OF TECHNOLOGY

VYTAUTAS KAVALIŪNAS

THE FORMATION AND INVESTIGATION OF TITANIUM DIOXIDE STRUCTURES FOR PHOTOCATALYTIC APPLICATIONS

Doctoral dissertation
Technological Sciences, Materials Engineering (T 008)

2023, Kaunas

This doctoral dissertation was prepared at Kaunas University of Technology, Faculty of Mathematics and Natural Sciences, Department of Physics during the period of 2017–2022. The studies were supported by Kaunas University of Technology with a one-time scholarship granted for the achieved results (RD3030100) and by the scholarship provided by the Ministry of Education, Culture, Sports, Science, and Technology of Japan (MEXT-Japan).

Scientific Supervisors:
Prof. Dr. Giedrius LAUKAITIS (Kaunas University of Technology, Physical Sciences, Physics, N 002)

Edited by: English language editor Dr. Armandas Rumšas (Publishing House *Technologija*), Lithuanian language editor Rozita Znamenskaitė (Publishing House *Technologija*)

The public defense of the dissertation will be held at 13:00 on the 14 February, 2023 at the public meeting of Dissertation Defense Board of Materials Engineering Science Field in M7 Hall at the Campus Library of Kaunas University of Technology.

Address: Studentų 48, Kaunas, LT-51367, Lithuania
Phone: (+370) 608 28 527; e-mail doktorantura@ktu.lt

Doctoral dissertation was sent out on 13 January, 2023.
The doctoral dissertation is available on the internet http://ktu.edu and at the library of Kaunas University of Technology (Donelaičio 20, Kaunas, LT-44239, Lithuania).

KAUNO TECHNOLOGIJOS UNIVERSITETAS

VYTAUTAS KAVALIŪNAS

TITANO DIOKSIDO STRUKTŪRŲ FORMAVIMAS IR TYRIMAS FOTOKATALIZINIŲ PROCESŲ PRITAIKYMUI

Daktaro disertacija
Technologijos mokslai, medžiagų inžinerija (T 008)

2023, Kaunas

Disertacija rengta 2017–2022 metais Kauno technologijos universiteto Matematikos ir gamtos mokslų fakultete Fizikos katedroje. Moksliniai tyrimai buvo dalinai paremti gavus vienkartinę skatinamąją stipendiją iš Kauno Technologijos Universiteto (RD3030100 lėšomis) ir švietimo, kultūros, sporto, mokslo bei technologijų ministerijos (MEXT – Japonija) skirta stipendija.

Moksliniai vadovai

prof. dr. Giedrius LAUKAITIS (Kauno technologijos universitetas, fiziniai mokslai, fizika, N 002)

Redagavo: anglų kalbos redaktorius dr. Armandas Rumšas (leidykla „Technologija“), lietuvių kalbos redaktorė Rozita Znamenskaitė (leidykla „Technologija“)

Medžiagų inžinerijos mokslo krypties disertacijos gynimo taryba:
habil. dr. Sigitas TAMULEVIČIUS (Kauno technologijos universitetas, technologijos mokslai, medžiagų inžinerija, T 008) – **pirmininkas**;
prof. dr. Liutauras MARCINAUSKAS (Kauno technologijos universitetas, technologijos mokslai, medžiagų inžinerija, T 008);
dr. Šarūnas MEŠKINIS (Kauno technologijos universitetas, technologijos mokslai, medžiagų inžinerija, T 008);
dr. Pavels ONUFRIJEVS (Rygos technikos universitetas, Latvija, technologijos mokslai, medžiagų inžinerija, T 008);
dr. Gediminas RAČIUKAITIS (Fizinių ir technologijų mokslo centras, technologijos mokslai, medžiagų inžinerija, T 008).

Disertacija bus ginama viešame Medžiagų inžinerijos mokslo krypties disertacijos gynimo tarybos posėdyje 2023 m. vasario 14 d., 13 val. Kauno technologijos universiteto Studentų miestelio bibliotekoje, M7 salėje.

Adresas: Studentų g. 48, Kaunas, LT-51367, Lietuva
Tel: (+370) 608 28 527; el. paštas doktorantura@ktu.lt

Disertacija išsiųsta 2023 m. sausio 13 d.
Su disertacija galima susipažinti internetinėje svetainėje http://ktu.edu ir Kauno technologijos universiteto bibliotekoje (K. Donelaičio g. 20, Kaunas, LT-44239, Lietuva).

Table of Contents

ABBREVIATIONS

AC – air conditioning system;
AFM – atomic force microscopy;
AM 1.5G – a filter for recreating sunlight irradiation in laboratory conditions;
ALD – atomic layer deposition;
AOP – advanced oxidation process;
ASTM – American Society for Testing and Materials;
BE – binding energy;
BHF – buffered hydrofluoric acid;
CBM – conduction band minimum;
CBO – conduction band offset;
CDs – carbon dots;
CE – counter electrode;
CS – cooling system;
CVD – chemical vapor deposition;
DC – direct current;
EBE – electron beam evaporation;
FE-SEM – field emission scanning electron microscopy;
FTO – Fluorine-doped Tin Oxide;
FWHM – full width half maximum;
HMDS – hexamethyldisilane;
HOMO – highest occupied molecular orbit;
HPE – hybrid photoelectrode;
IR – infrared;
ISO – International Organization for Standardization;
LA – lactic acid;
LSPR – localized surface plasmon resonance;
LUMO – lowest unoccupied molecular orbit;
MB – methylene blue;
MOCVD – metal-organic chemical vapor deposition;
MOF – metal-organic framework;
NC – nanoclusters;
NMD – aqueous solution for the development of photoresist;
NMNPs – noble metal nanoparticles;
NP – nanoparticles;
NS – nano spherical;
NTa – nanotube arrays;
OCD – aqueous solution for phosphorous diffusion;
OFPR – photoresists;
P25 – TiO_2 (anatase/rutile mix);
PACVD – plasma-assisted chemical vapor deposition;
PEC – photo electrochemistry;
PECVD – plasma-enhanced chemical vapor deposition;
PBF – poly-Boron film;
PGc – palygorskite clay;
PC – computer;
PIN – p-type/insulator/n-type diode;
PPh – polyphenylene;
Pt-free – platinum-free counter electrode;
PVD – physical vapor deposition;
QD – quantum dots;
QFL – quasi-Fermi level;
RF – radio frequency;
rGO – reduced graphene oxide;
RhB – Rhodamine B;
RMS – reactive magnetron sputtering;
RPM – rotations per minute;
SEI – secondary electron imaging;
SIMS – secondary ion mass spectrometry;
SS – sodium sulphide;
SSD – solid state dewetting;
STH – solar-to-hydrogen;
STS-21 – photocatalytic TiO_2 hydrosol;
TC – temperature controller;
TNT – TiO_2 nanotubes;
TOC – total organic carbon;
TRPL – time-resolved photoluminescence;
UV – ultraviolet light;
VBM – valence band maximum;
VBO – valence band offset;
VOC – volatile organic compound;
VTE – vacuum thermal evaporation;
XPS – X-ray photoelectron spectroscopy;
XRD – X-ray diffraction;
XY – initial elements.

Introduction

Photocatalysis covers a wide range of applications, but, in terms of what is most important these days, it contributes to environmental remediation. The application for water and/or air purification and solar-to-energy conversion brings the most attention as the pollutants in air and water have been increasing as a result of human activities over the years [1–4]. The main processes occurring in parallel during photocatalysis are photogeneration, recombination, trapping of the charge carrier, and redox reactions. While the first three of them occur in bulk and depend on the energy bandgap and the defect states [5–7], the efficiency of the last one depends on the charge carrier recombination/separation, the surface area of a/the semiconductor, and its redox potentials [8].

Such semiconductors as TiO_2, ZrO_2, WO_3, Nb_2O_5, SnO_2, Ga_2O_3, GeO_2 (wide energy bandgap semiconductors) and NbO_2, In_2O_3, Fe_2O_3, etc. (narrow energy bandgap semiconductors) or their combinations are being widely studied for photocatalysis application [9, 10]. When considering a combination of two (or more) semiconductors (monolithic structures), it is crucial to design and engineer the energy band alignment throughout the layers of semiconductors. If any misalignment occurs between the semiconductors, a metal or another semiconductor interlayer can be implemented to solve the issue. A carefully engineered energy band alignment creates an internal electric field which might enhance the photogenerated charge carrier separation [11, 12]. As T. Munawar *et al*. reported, the combined structure of TiO_2/WO_3/CeO_2 nanoclusters (*NC*) achieved a higher photocatalytic efficiency compared to TiO_2 and WO_3 alone in the course of photodegradation of dyes [13]. The explanation behind the enhanced photocatalytic efficiency was that synergy between the different semiconductors and the energy band alignment resulting in enhanced charge carrier separation and transition rates. Moreover, D. Chen *et al*. provided a detailed comparison between the photocatalytic efficiency of TiO_2 vs. Pt, TiO_2/rGO vs. Pt, and TiO_2/*NS*-rGO (nano spherical – *NS*,) vs. Pt [14]. The first modification, when TiO_2 was mixed with rGO, resulted in charge carrier separation at the TiO_2 and rGO interface. However, it was suggested that recombination might still appear on the rGO sheets. Therefore, while further changing the structure of the photocatalyst (and the structure of rGO to *NS*-rGO in particular), the charge carriers transitioned from TiO_2 to rGO might freely drift not only on the surface but even be trapped in the inner layers as well, thus eliminating the recombination in rGO. Even though it is difficult to measure the recombination of charge carriers, a design of the energy band alignment might give a good assumption of how charge carriers would move in the semiconductor or in their multi-layered structures. Thus, so far, very few studies have been carried out and provided the actual measurements on the charge carrier recombination. Additionally, at which process the photocatalysts are being used is also important. To be more specific, the photocatalyst (if the combination consists of at least two semiconductors with photocatalytic properties) can be used for either reduction (on the surface of the photocathode) or oxidation (on the surface of the photoanode) reactions. Therefore, as T. Marino *et al*. study shows, in a comparison between TiO_2/Au and CeO_2/Au as the photoanode and the photocathode, respectively

(and vice versa), a higher efficiency is reached when TiO_2/Au is used as the photoanode and CeO_2/Au as the photocathode, which results in almost 7-fold difference [15]. In many cases, the Pt electrode is being used as the cathode on which the reduction reaction occurs because of its superior reduction capabilities [16, 17]. However, with reference to the price of Pt, this raises another issue – cost-efficiency. Therefore, the search for a Pt-free (photo)cathode is as important as looking for an efficient photocatalyst (photoanode). Nevertheless, it was noticed that, in many cases, TiO_2 is used as the main photocatalyst or as a protection layer for other photocatalysts [18, 19]. This is because TiO_2 shows unique oxidation properties and offers high thermodynamic stability against photo-corrosion. The latter is based on the position of the valence band maximum (*VBM*) and the conduction band minimum (*CBM*), as well as the redox potentials [20]. Additionally, in order to accurately compare the different photocatalyst systems and their efficiency, it is crucial to maintain the same conditions (the light source and its power, the concentration of the electrolyte or organic dyes) during the measurements. On the grounds of the review of different studies for the photogeneration of hydrogen, a sacrificial agent is used to increase the hydrogen concentration in the aqueous solution, which results in higher hydrogen generation rates. Even though this is mainly done with the objective to better analyze the overall efficiency of the photocatalyst, the result might not be comparable to a real-life situation – i.e., hydrogen generation from pure water.

Setting aside the scientific approaches to a higher photocatalytic efficiency of TiO_2, it is crucial to mention the reason behind all the researches – the climate change. According to the agreements which were initiated in many conferences of parties (COP) and once more in COP26 (Glasgow, 2021) [21, 22], it is as important to decrease the usage of fossil fuels as it is to increase the support for renewable energy sources. To be more specific, 'green hydrogen economy' is being pushed to all the countries. Meanwhile, 'green hydrogen' stands for the production of hydrogen, during which, none of greenhouse gases is being produced. In this case, hydrogen generation through photocatalysis is probably the closest solution for such a problem. Even though, there are many studies which cover the photogeneration of hydrogen through photocatalysis, there are still no commercially available and energy efficient solutions currently available.

Therefore, this study is focused on TiO_2 as a photocatalyst and its modifications to increase the photocatalytic efficiency. The study was carried out by trying to keep as similar conditions as possible when applying the different measurement techniques. Deep analysis was done on the TiO_2 crystallization and morphology dependence on the deposition parameters and techniques. Additionally, several different approaches to enhance the photocatalytic efficiency were done by manufacturing a doped TiO_2 (in bulk and on the surface) and TiO_2 hybrid photoelectrode. Nevertheless, a design for an alternative platinum-free counter was proposed and analyzed. The photocatalytic efficiency (photodegradation, photoconductivity) was measured for pure the TiO_2 crystal phases, doped TiO_2, and TiO_2 hybrid photoelectrode. The analysis was carried out by X-ray diffraction, field-emission scanning electron microscopy, X-ray photoelectron spectroscopy, atomic force microscopy, current-

voltage characteristics and photoconductivity, and photodegradation in the dark and under *UV* irradiation.

The Aim of the Dissertation

The aim of this work is to investigate different approaches of enhancing the photocatalytic efficiency for TiO_2 thin films.

When pursuing the aim, the following tasks were solved:

1. The investigation of the dependence of TiO_2 thin film properties on the deposition methods and parameters.
2. The formation of metal-doped TiO_2 thin films and their photocatalytic efficiency evaluation in comparison with plain TiO_2.
3. The formation of metal nanoparticles on the surface of TiO_2 thin films and their photocatalytic efficiency evaluation in comparison with plain TiO_2.
4. The formation of TiO_2 and Si heterojunction followed by the manufacturing of TiO_2/Si hybrid photoelectrode and the evaluation of optical and electrical properties for the photocatalytic application.

The Novelty of the Presented Study

The formation of Mg, Cu, and Ni-doped TiO_2 thin films by the *PVD RMS* (further on abbreviated as *RMS*) technique, and the optimization of the dopant concentration in TiO_2 thin films to enhance the photocatalytic efficiency. The evaluation of photocatalytic efficiency under the same conditions to investigate the influence of the dopant and its concentration on TiO_2 photocatalytic properties. Moreover, the formation of gold nanoparticles on TiO_2 thin films by the *RMS* technique, and the investigation of how the formation parameters together with TiO_2 morphology affect the Au*NP* parameters and the photocatalytic activity of the prepared TiO_2/Au*NP*. Additionally, the TiO_2/Si hybrid photoelectrode, as a photocatalyst, and a platinum-free photoelectrode, as a counter electrode and an alternative for the Pt electrode, were manufactured, and the photocatalytic efficiency was evaluated for the proposed system.

Author's Contribution

The formation of TiO_2 thin films by *RMS* and the sol-gel spin-coating technique and the investigation of the formed structures by *XRD*, *FE-SEM*, *XPS*, *UV-Vis*, followed by I–V measurements for the energy band structure evaluation. The validation and curation of the data and the research of the dependence of the morphology and properties on the deposition parameters. Additionally, the formation of TiO_2 thin films on patterned structures by the *RMS* technique, and the formal data analysis of the photocatalytic efficiency for the prepared structures. Moreover, the formation of Mg, Cu, and Ni-doped TiO_2 thin films by the *RMS* technique and the investigation of the formed structures by *XRD*, *XPS*, *EDS*, *UV-Vis*, for the analysis of morphology, electronic, chemical, and optical properties and I–V measurements for the evaluation of the energy band structure. The methodology and investigation of the

photocatalytic efficiency of the formed structures followed by the data curation and analysis. The formal data analysis of TiO_2/Au*NP* photocatalytic efficiency. Also, the conceptualization and formation of the TiO_2/Si hybrid photoelectrode and the platinum-free photoelectrode structure. The engineering of the energy band alignment throughout the TiO_2/Si hybrid photoelectrode structure by *XPS* and I–V measurements. The investigation of the photocatalytic efficiency for the prepared TiO_2/Si hybrid photoelectrode and the platinum-free photoelectrode system followed by the validation and analysis of the gathered data.

Acknowledgments

First and foremost, the gratitude for the contribution to this doctoral dissertation goes to my supervisors: Prof. G. Laukaitis and Prof. H. Mimura, for the provision of the research resources, the management and coordination of the research, and the critical revision of my articles and dissertation. An important mention is for Prof. Y. Hatanaka, for the conceptualization, consistent validation, and curation of the research and data. Furthermore, my gratitude goes to Prof. M. Shimomura for the lead on X-ray photoelectron spectroscopy measurements and data analysis; Prof. Y. Neo, for the supervision of experimental techniques; Mr. S. Takeuchi for the operation of the computer lithography process during the sample preparation; Dr. M. Sriubas for the investigation and formal analysis of TiO_2 deposited by *RMS*; Dr. P. Palevičius and Prof. M. K. Ragulskis for the software, formal analysis, and data curation; Dr. R. Sidaravičiūtė for the methodology and investigation, and for anyone else involved in this research for their contribution to this doctoral dissertation.

Structure and Scope of the Dissertation

The dissertation contains an introduction (in English and Lithuanian languages), literature review, experimental technique and methodology, results and discussion, conclusions, and reference list. The volume of the dissertation is 156 pages. The thesis features 65 graphical illustrations, 11 tables, and 358 references.

Dissertation Approbation

The results reviewed in the dissertation were presented in the below listed international conferences and published in journals having a citation index.

List of scientific publications which were published in peer-reviewed scientific journals indexed in the *Web of Science* with Impact Factor:

1. **Kavaliūnas, V.**, Hatanaka, Y., Neo, Y., Laukaitis, G., Mimura, H. *Structural design of TiO_2/Si hybrid photoelectrode and Pt-free counter photoelectrodes for charge carrier separation in water-splitting reactions*. ECS Journal of solid state science and technology, 2021, vol. 10, iss. 10, art. No. 103015, p. 1-6.
2. Sriubas, M., **Kavaliūnas, V.**, Bočkutė, K., Palevičius, P., Kaminskas, M., Rinkevičius, Ž., Ragulskis, M., Laukaitis, G. *Formation of Au nanostructures on the surfaces of annealed TiO_2 thin films*. Surfaces and interfaces, 2021, vol. 25, art. No. 101239, p. 1-10.
3. **Kavaliunas, V.**, Krugly, E., Sriubas, M., Mimura, H., Laukaitis, G., Hatanaka, Y. *Influence of Mg, Cu, and Ni dopants on amorphous TiO_2 thin films photocatalytic activity*. Materials, 2020, vol. 13, iss. 4, art. No. 886, p. 1-14.
4. **Kavaliūnas, V.**, Čeplikas, P., Sriubas, M., Laukaitis, G. *The Sensitization of TiO_2 Thin Film by Ag Nanoparticles for the Improvement of Photocatalytic Efficiency*. Applied Sciences, 2022, vol. 12, iss. 11, art No. 5725, p. 1-11.

Other scientific publications published in peer-reviewed scientific journals indexed in the *Web of Science* with Impact Factor:

1. **Kavaliunas, V**., Hatanaka, Y., Neo, Y., Laukaitis, G., Mimura, H. *Conduction band discontinuity in n-type Si/TiO_2 heterojunction interfaces*. ECS Journal of solid state science and technology, 2021, vol. 10, iss. 1, art. No. 015005, p. 1-7.
2. Sidaraviciute, R., **Kavaliunas, V**., Puodziukynas, L., Guobiene, A., Martuzevicius, D., Andrulevicius, M. *Enhancement of photocatalytic pollutant decomposition efficiency of surface mounted TiO_2 via lithographic surface patterning*. Environmental technology and innovation, 2020, vol. 19, art. No. 100983, p. 1-9.

Articles in conference proceedings:

1. **Kavaliunas, V.**, Sestakauskaite, A., Sriubas, M., Laukaitis, G. *Influence of deposition parameters on the structure of TiO_2 thin films prepared by reactive magnetron sputtering technique*. Recent advances in technology research and education: proceedings of the 17th international conference on global research and education Inter-Academia – 2018, 2019, p. 49-57.

Other conference abstracts and non-peer-reviewed conference papers:

1. Sriubas, M., **Kavaliūnas, V.**, Bočkutė, K., Palevičius, P., Kaminskas, M., Rinkevičius, Ž., Ragulskis, M., Mimura, H., Laukaitis, G. *Surface modification of thin TiO_2 films by Au and Ag nanoparticles*. 44th LNFK *Lithuanian National Physics Conference*, 2021, October 6-8, Vilnius, Lithuania. p. 245.
2. Sriubas, M., **Kavaliūnas, V.**, Bočkutė, K., Palevičius, P., Kaminskas, M., Rinkevičius, Ž., Ragulskis, M., Mimura, H., Laukaitis, G. *Surface modification of thin TiO_2 films by Au nanoparticles*. 43rd LNFK *Lithuanian National Physics Conference*, 2019, October 3-5, Kaunas, Lithuania. p. 230.
3. **Kavaliūnas, V.**, Šeštakauskaitė, A., Sriubas, M., Laukaitis, G. *Influence of deposition parameters on the structure of TiO_2 thin films prepared by reactive magnetron sputtering technique*. Inter-Academia 2018: *17th international conference on global research and education*, September 24-27, 2018 Kaunas, Lithuania. p. 61.
4. Galdikas, A., Kairaitis, G., Moskaliovienė, T., Bočkutė, K., Virbukas, D., Sriubas, M., **Kavaliūnas, V.**, Kaminskas, M., Laukaitis, G., Petruškevičius, K. *Modeling of properties of single chamber fuel cell components*. Inter-Academia 2018: *17th international conference on global research and education*, September 24-27, 2018 Kaunas, Lithuania. p. 49.
5. **Kavaliūnas, V.**, Krugly, E., Laukaitis, G. *Photocatalytic performance of doped TiO_2 films under UV light*. *14th Kudowa summer school: towards fusion energy*, 4 – 8 June 2018. p. 62.
6. **Kavaliūnas, V.**, Krugly, E., Laukaitis, G. *Photocatalytic performance of Mg-, Cu-, Ni-doped TiO_2 films under UV light*. 42nd LNFK *Lithuanian National Physics Conference*, 2017, October 4-6, Vilnius, Lithuania. p. 154.
7. **Kavaliunas, V.**, Hatanaka, Y., Laukaitis, G., Mimura, H. *A design study of TiO_2/n-Si energy band structure for charge carrier transportation in water splitting electrode*. 68th JSAP *Japan Society of Applied Physics*, Spring meeting, 2021, March 16-19, Japan.
8. **Kavaliūnas, V.,** Hatanaka, Y., Neo, Y., Laukaitis, G., Mimura, H. *Synthesis of Si/TiO_2 hybrid solar cell as water splitting electrode*. E-MRS *European Materials Research Society*, Spring meeting, 2021, May 31 – June 3.
9. **Kavaliūnas, V.**, Čeplikas, P., Sriubas, M., Laukaitis, G. *The sensitization of TiO_2 thin films by Ag nanoparticles for the improvement of photocatalytic efficiency. Cyseni 2022, 18th international conference of young scientists on energy and natural sciences issues*, 2022, May 24 – 27.

1. Review on Photocatalysis and Photocatalysts

1.1. Fundamentals of Photocatalysis

Photocatalysis is one of the catalysis types, during which, the rates of chemical reactions are being modified by light and additive substances (an organic or inorganic semiconductor with photocatalytic properties – further referred to as a photocatalyst) where the latter is not consumed in the reaction. In short, it is a type of chemical reaction that is driven by the light energy, and thus it is called a photoreaction. In parallel to this, four different processes occur in bulk or on the surface of a photocatalyst (**Fig. 1.1**): photogeneration of charge carriers (electrons and holes); recombination of charge carriers; charge carrier trapping inside the energy bandgap, and redox reactions [23]. All the presently mentioned processes shall be explained in detail below.

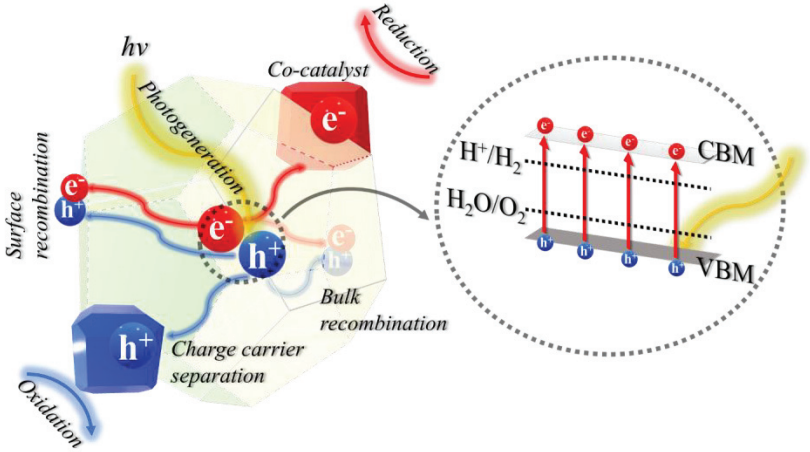

Fig. 1.1. Visual representation of processes occurring during photogeneration of charge carriers in a photocatalyst under incident light. *CBM* – conduction band minimum; *VBM* – valence band maximum; H^+/H_2 – energy level for hydrogen reduction potential; H_2O/O_2 – energy level for water oxidation potential; *hv* – photon energy; e^- – electrons; h^+ – holes

Photogeneration of charge carriers

The first process which occurs during photocatalysis is the photogeneration of charge carriers. This requires the photon energy to be equal to or higher than the width of the energy bandgap of the photocatalyst: $h\nu \geq E_g$. In general, the energy transfer between the photon and the electron occurs when photons interact with electrons in the valence band (E_V) (for an inorganic semiconductor) or *HOMO* (the highest occupied molecular orbital) (for an organic semiconductor). If the photon energy is higher than the energy bandgap, the electron is excited to the conduction band (E_C) or the *LUMO* (the lowest unoccupied molecular orbit) by leaving a hole behind itself in the E_V/*HOMO* (**Fig. 1.2**) [5]. The ability of materials which serves to describe the

photogeneration efficiency is photoconductivity. Such optical/electrical phenomena describe the change in the electrical conductivity of materials under the influence of either visible light, ultraviolet light (UV), infrared light (IR), or other types of radiation [24].

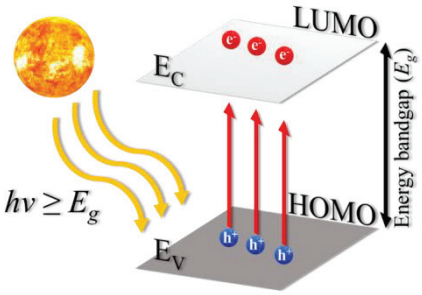

Fig. 1.2. Photogeneration of charge carriers (electrons and holes). E_V – valence band; E_C – conduction band; *HOMO* – highest occupied molecular orbits; *LUMO* – lowest unoccupied molecular orbits; E_g – energy bandgap; hv – photon energy; e^- – electrons; h^+ – holes

Furthermore, the probability of an electron 'escaping' the energy bandgap depends on the direction in which the electron moves: towards another atom (the highest chance of 'escaping'), or it channels through the same atom (the lowest chance of 'escaping'). In addition, the chance of transition from E_V to E_C for an electron is higher for a semiconductor with a direct energy bandgap, compared to an indirect energy bandgap. However, when considering atom vibrations, the chance of transition could increase in the indirect energy bandgap as well [25–27]. For this reason, the energy bandgap can be considered as a function of momentum. Considering the fact that an electron reaches E_C, it can either recombine with a hole (E_C-to-E_V transition), or be trapped inside the energy bandgap.

Charge carrier recombination

The charge carrier recombination is a process, during which, a semiconductor reaches the equilibrium state by annihilating the excess charge carriers.

Equilibrium state	$n_0 p_0 = {n_i}^2$ or $\mu_n^0 + \mu_p^0 = -\varepsilon_g,$	1.1
Non-equilibrium state	$np \neq {n_i}^2$ or $\mu_n + \mu_p \neq -\varepsilon_g,$	1.2

Here, n_0 and p_0 is the initial concentration of electrons and holes, accordingly, n_i is the intrinsic carrier concentration, μ_n^0 and μ_p^0 is the equilibrium chemical potential of electrons and holes, accordingly, n and p is the non-equilibrium concentration of electrons and holes, μ_n and μ_p is the non-equilibrium chemical potentials of electrons and holes, and ε_g is the energy bandgap [6, 28]. The recombination rates are directly dependent on the charge carrier concentration. Thus, a higher concentration of charge

carriers (higher photogeneration rates) leads to higher recombination rates and vice versa.

Even though the theory of this process is well-understood and has already been known for a while, it is still complicated and requires additional study. However, the main key points shall be addressed in this paragraph. In short, when an electron is excited from an atom and drifts through the material, there is a chance of a hole appearing in its path. In this case, recombination of two charge carriers occurs [29, 30]. This can take place either on the surface or in a bulk. Furthermore, in the photocatalysis process, recombination can be either radiative or non-radiative. The difference here is the emitted particle: a particle of light – a photon (radiative recombination), or a particle of heat – a phonon (non-radiative recombination) is being emitted during the electron-hole recombination. During direct recombination (**Fig. 1.3 (a)**), a photon is emitted as a result of the energy loss for electrons. On the other hand, when indirect recombination (trap assisted recombination) takes place (**Fig. 1.3 (b)**), either a photon or a phonon can be emitted [31–33].

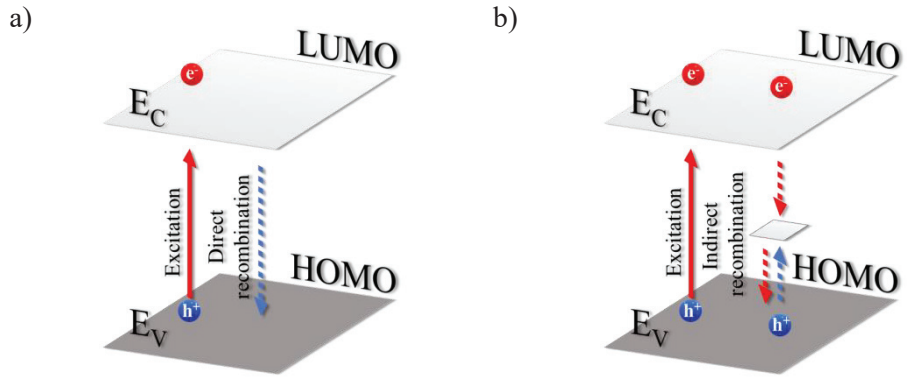

Fig. 1.3. Recombination of charger carriers: a) direct (radiative) recombination; b) indirect (radiative/non radiative) recombination. E_V – valence band; E_C – conduction band; *HOMO* – highest occupied molecular orbits; *LUMO* – lowest unoccupied molecular orbits; *hv* – photon energy; e^- – electrons; h^+ – holes

The rate of the recombination process is merely a fraction of a second (~10 ns) [34]. Therefore, it is difficult to accurately measure the recombination of charge carriers. In addition to the fast recombination rates, such processes as recombination-assisted photogeneration or exothermic chemical reactions make it difficult to distinguish the latter from the recombination process [35]. Further on, any fluctuation in light can cause a different result in the recombination rates. Thus, measuring it in a laboratory (which requires high-frequency laser beams) might result in a different outcome from that obtained when measuring the case of sunlight irradiation [36]. Given these points, many researchers only assume that the recombination process is a/the reason behind the low photocatalytic efficiency, without providing any experimental data to prove it. The charge carrier recombination can be evaluated by using time-resolved photoluminescence (*TRPL*) [37, 38], which enables the analysis of fast recombination processes resulting in photon emission. Other measurement

techniques involve transient terahertz spectroscopy (*TTHzS)* [39], quasi-steady-state photoconductance [40], microwave photoconductivity [41], or temperature and illumination dependent current-voltage measurements [42].

Trapping of charge carriers

During photocatalysis, a system is trying to reach the equilibrium state at all times by annihilating the excess non-equilibrium charge carriers (the recombination process described above). However, during recombination, a charge carrier can be captured by the localized state (the trapping site). In general, a trapping site is a location with an energy E_t, where any movement of the charge carrier is restricted. If an opposite charge carrier is captured by the same trapping site, a process called trap-assisted recombination takes place. On the other hand, if a charge carrier is released to the conduction band or the valence band, these sites are called traps. The trapping site can be either band tails, defects, or impurities (dopants) [7]. These sites are divided into shallow and deep traps according to their position in the energy bandgap [43]. Shallow traps appear near the conduction band minimum (*CBM*) and are called acceptor traps, whereas the ones located near the valence band maximum (*VBM*) are called donor traps (**Fig. 1.4**). The latter traps immobilize holes, while the former traps immobilize electrons. On the other hand, deep traps can work as electron or hole trapping sites as their position in the energy bandgap is close to $\frac{E_g}{2}$. Nevertheless, these traps can also exist inside the conduction or valence bands.

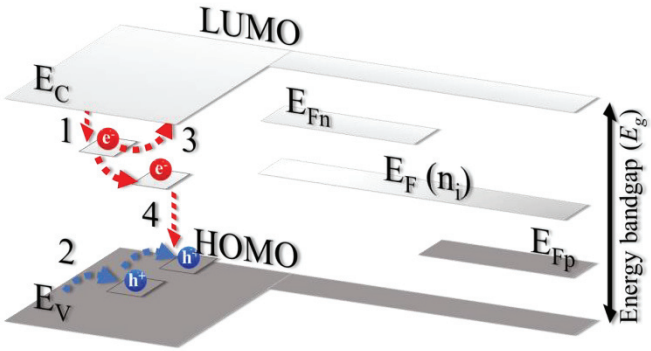

Fig. 1.4. Charge carrier trapping inside the energy bandgap. 1) electron capture in shallow traps; 2) hole capture in shallow traps; 3) electron release from a shallow trap to conduction band; 4) trap-assisted recombination. E_V – valence band; E_C – conduction band; *HOMO* – highest occupied molecular orbits; *LUMO* – lowest unoccupied molecular orbits; E_{Fn} – Fermi energy level for *n*-type semiconductor; E_{Fp} – Fermi energy level for *p*-type semiconductor; E_F (n_i) – Fermi energy level for intrinsic semiconductor

The Fermi energy level plays an important role in the semiconductor energy bandgap as it describes the type of the semiconductor. An intrinsic semiconductor (a pure semiconductor) has the Fermi energy level at $E_F \sim \frac{E_g}{2}$, while, for the *n*-type, $E_F >$

$\frac{E_g}{2}$, and for the *p*-type $E_F < \frac{E_g}{2}$ [44, 45]. A perfect example for the latter two is *n*-type and *p*-type Si. The Fermi energy level represents a location in the energy bandgap (E_V to E_F) which is filled with electrons at 0 K temperature (T_0). At this point, electrons do not have enough energy to be excited to the conduction band. When the temperature is increased ($T > T_0$), a probability for the electron to occupy a state in the Fermi energy level is at 50% [46]. Moreover, if the temperature is even higher ($T >> T_0$), the Fermi energy level can occupy a position inside the conduction band [46, 47]. The Fermi energy level is best described by the Fermi-Dirac distribution [48, 49]:

$$f(E) = \frac{1}{e^{(E_g - E_F)/kT} + 1} \quad 1.3$$

Here, *f(E)* results in a probability for a particle to have an energy equal to *E*, *k* is Boltzmann's constant ($1.38064852 \cdot 10^{-23} \frac{m^2 kg}{s^2 K}$), and *T* is the absolute temperature in Kelvin. According to the equation, at low temperatures, the energy states which are below E_F result in the probability of ~1, and, for the cases above E_F, the probability is close to 0. At high temperatures, when particles are given excess energy, the probability to fill the states above the E_F increases.

What concerns the trapping sites created by impurities, they can shift the Fermi energy level closer to *CBM* or closer to *VBM*, thus creating a quasi-Fermi level (*QFL*). The traps inside the Fermi energy level can be defined as [50, 51]:

for electrons: $$E_{Fn} = E_F + kT \ln \frac{1+\Delta n}{n_0}, \quad 1.4$$

for holes: $$E_{Fp} = E_F + kT \ln \frac{1+\Delta p}{p_0}, \quad 1.5$$

Here, E_{Fn} is the quasi-Fermi energy level for electrons, E_{Fp} is the quasi-Fermi energy levels for holes, Δn and Δp define the excess concentration of electrons and holes, whereas n_0 is the initial concentration of electrons, and p_0 is the initial concentration of holes.

Redox reactions

Granted that a charge carrier successfully reaches the surface (liquid (electrolyte) – solid (semiconductor) interface) by overcoming the recombination process, redox (reduction-oxidation) reactions take place (**Fig. 1.5**).

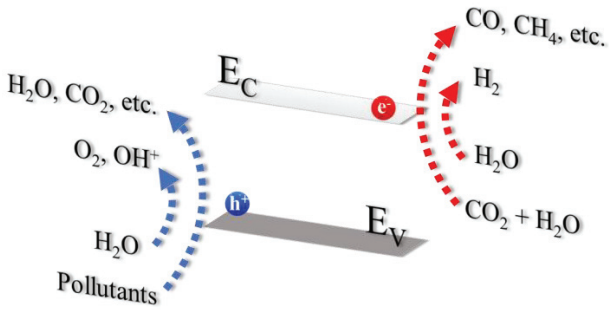

Fig. 1.5. Visual representation of redox reactions in the electrolyte–semiconductor interface. E_C – conduction band; E_V – valence band; e^- – electrons; h^+ – holes

There are several types of redox reactions: combination, decomposition, displacement, and disproportionate reactions. Let us see the schematic representations for the above mentioned reactions below, in Eqs. 1.6 to 1.9 [52]:

combination: $$X^0 + Y^0 \rightarrow X^+Y^- \; or \; X^0 + Y^0 \rightarrow Z^{\pm}, \quad (1.6)$$

decomposition: $$X^+Y^- \rightarrow X^0 + Y^0, \quad (1.7)$$

displacement: $$X^+Y^- + Z^0 \rightarrow X^0 + Y^+Z^-, \quad (1.8)$$

disproportionate: $$X^+Y^- \rightarrow X^+Y^- + Y^0, \quad (1.9)$$

where $X^0$and Y^0 is the initial element produced in the chemical reaction, X^+Y^- and $Z^{\pm}$ is the chemical product after X^0 and Y^0 reaction, or the new product, respectively.

During a combination reaction, the elemental form of *X* or *Y* is required to form a combination of *XY* or a new element *Z*. The simple example of this is $C^0 + O_2^0 \rightarrow C^{4+}O_2^{2-}$. This is the opposite reaction compared to the decomposition reaction for which a simple example is the decomposition of a water molecule: $2H_2^{1+}O^{2-} \rightarrow 2H_2^0 + O_2^0$. However, in contrast to the combination reaction, a decomposition reaction requires external heat, light, etc. to drive the reaction. The latter is the main reaction describing the photocatalytic degradation of an electrolyte. When considering the displacement reaction, a simple example would be by adding *Na* to water: $2Na^0 + 2H_2^{1+}O^{2-} \rightarrow 2Na^{1+}O^{2+}H^{1+} + H_2^0$. A displacement reaction can also occur between two solids where a metal with a higher reduction potential replaces another metal in a compound, i.e.: $Ti^{4+}Cl_4^{1+} + 2Mg^0 \rightarrow Ti^0 + 2Mg^{2+}Cl_2^{1-}$. A disproportionate reaction takes place when the same chemical substance undergoes an oxidation and reduction reaction. For example, the redox reaction of hydrogen peroxide is as follows: $2H_2^{1+}O_2^{1-} \rightarrow 2H_2^{1+}O^{2-} + O_2^0$ [53–55].

What concerns photocatalysis, the decomposition reaction takes place on the surface (at the electrolyte–semiconductor interface) of a photocatalyst (**Fig. 1.1**). The electrons from the conduction band take a role (they act as a donor) in reduction reactions, while holes from the valence band (acting as an acceptor) take a role in

oxidation reactions. A simplified decomposition reaction of a water molecule during photocatalysis is shown below [8]:

oxidation reaction	$2H_2O + 4h^+ \rightarrow O_2 + 4H^+,$	1.10
reduction reaction	$4H^+ + 4e^- \rightarrow 2H_2,$	1.11
final reaction	$2H_2O \xrightarrow{photocatalyst+h\nu} 2H_2 + O_2.$	1.12

Theoretically, during water decomposition, an oxidation reaction requires a potential of E^O = 1.23 eV in order to split the water molecule. However, this applies only in ideal conditions. Thus, in reality, a slightly higher potential might be required based on the conditions, and it can reach from 1.3 up to 1.8 eV [56]. However, this is not the only condition to drive the water-splitting reaction. When considering the properties of a photocatalyst (organic or inorganic), the hydrogen evolution reaction requires a position of *CBM* or *LUMO* at a more negative potential than the hydrogen reduction potential (H^+/H_2). On the contrary, the oxygen evolution reaction requires a position of *VBM* or *HOMO* at more positive potential than water oxidation potential (O_2/H_2O). Consequently, a photocatalyst must be thermodynamically stable against photo-corrosion [20]. Thus, the above mentioned properties of a photocatalyst also describe its stability during redox reactions. In general, a photocatalyst is stable against oxidation by photogenerated holes if the position of its oxidation potential is lower than the oxidation potential of water (H_2O/O_2) or *VBM* [20]. Likewise, a photocatalyst is stable against the reduction by photogenerated electrons if its reduction potential is higher than the reduction potential of hydrogen (H^+/H_2) or *CBM* [20].

Given these points, not many semiconductors pass the above mentioned requirements for redox reactions, and even though it meets the requirements, the thermodynamical stability has to be taken into account [57, 58].

1.2. Photocatalysis Applications

The continuous increase in the average CO_2 emission from human activities (deforestation, burning fossil fuels, etc.) over the years [1] has had a significant impact on environmental pollution. Such an increase in human-caused CO_2 emission resulted in an increased annual average temperature [2] followed by the decrease of the ice coverage in the Arctic Sea and Iceland [3] as well as in the Antarctic [4]. Thus, renewable energy sources have become considerably appealing for environmental remediation as an eco-friendly technology. This can be seen from the increase in the number of publications based on photocatalysis, which increased by up to 60 times from 2000 to 2020 [23].

Photocatalysis covers a wide range of applications: water and air purification, energy production, anti-bacterial (self-sterilizing) coatings, self-cleaning and anti-fogging surfaces, chemical synthesis, and even photocatalytic paints or tiles [59]. However, only the ones which play the most important role in environmental

remediation shall be reviewed below, and an extra focus shall be given to TiO_2 as a unique photocatalyst with superior oxidation properties.

Water purification

The increase in the global average temperature brings a huge challenge for the accessible pure water (mainly in the third-world countries). Thus, a study on a cost-effective and accessible technology for water purification is considered to be crucial. To this matter, advanced oxidation processes (*AOP*) are being investigated. *AOP* is chemical water treatment, during which, organic and/or inorganic compounds are removed from water or wastewater by oxidation processes [60]. Even though many *AOP*s are comparably cheap to create, the operational costs (chemicals required energy, etc.) are too high for more extensive application [61, 62]. Therefore, *AOP*s based on photocatalysis have been gathering most attention so far [63].

In short, water purification by photocatalysis application is somewhat similar to water-splitting reactions presented above (Eqs. 1.10–1.12). Pollutants in wastewater are surrounded by strong oxidising agents (OH^*) and disintegrated over time. A simplified reaction is shown in Eq. 1.13 [64]:

$$Polluted\ water \xrightarrow{Photocatalyst+h\nu} CO_2 + H_2O \qquad 1.13$$

The most popular photocatalysts, including Fe_2O_3, ZnO, WO_3, TiO_2, SnO_2, are characterized as eco-friendly, low-cost, and chemically stable semiconductors [65–68]. However, considering the latter, it is debatable if the presently mentioned semiconductors (except for TiO_2) exhibit chemical stability which can withstand photo-corrosion [69, 70]. Additionally, many other semiconductor structures contain TiO_2 as a substrate, an interlayer, etc. Apart from the already exaggerated chemical stability, the unique oxidation properties bring TiO_2 on top of other photocatalysts. A recent analysis by T.H. Huy *et al*. [71] reveals that as-prepared SnO_2 has a lower photocatalytic efficiency compared to TiO_2 nanotubes (*TNT*), and an even higher efficiency is reached by preparing a SnO_2/*TNT* heterojunction. Based on their findings, recombination rates were dramatically decreased. According to the energy band alignment and the internal electric field, photogenerated electrons and holes were directed in the opposite ways: electrons from the TiO_2 to SnO_2 conduction band, and holes from the SnO_2 to TiO_2 valence band. Similarly, T. Munawar *et al*. [13] observed a significant increase in the photocatalytic efficiency when $TiO_2/WO_3/CeO_2$ (*NC*) was used for the photodegradation of various dyes, compared to stand-alone TiO_2 and WO_3. The synergy between the layers significantly lowered the recombination rates by increasing the charger carriers' transition/separation rates. A study by O. F. S. Khasawneh *et al*. [72] suggests a combination of Fe_2O_3 and TiO_2 for water treatment application by presenting a high (from ~90 up to 100%) photodegradation efficiency. Their findings are mainly attributed to a drastic decrease in the energy bandgap: from 3.18 eV (TiO_2) to 1.6 eV ((5 wt.%) Fe_2O_3/TiO_2).

To conclude, many combined photocatalysts achieve higher photocatalytic efficiencies when combined with TiO_2. Thus, the uniqueness of TiO_2 has been proven once more.

Air purification

In parallel with the industrial revolution, the concentration of volatile organic compounds (*VOC*s) increased in the outdoor and indoor air [73]. As a consequence, long exposure to polluted air leads to diseases. Therefore, air purification through a cost-effective and eco-friendly technology started gaining interest. Especially, air purification through photocatalysis as photocatalysts has proven its sustainability and versatility. One of the many ways to improve air purification outdoors is a pavement with a photocatalytic coating. Results reported by E. Boonen *et al*. [74] and Z. Hu *et al*. [75] suggest that the use of a combination of a photocatalyst and cement-based products offers a potentially high efficiency reduction of air pollution in traffic. Z. Hu *et al.* studied the efficiency of Fe-doped TiO_2 (this team had formerly worked only with TiO_2) on photocatalytic purification of HC and NO_x. To this matter, the obtained by-products were CO_2 and H_2O HC, and nitrate with H_2O for NO_x decomposition. However, low efficiency in CO_2 reduction was observed, and thus the problem of CO_2 pollution was not resolved. Likewise, M. Hassan *et al*. [76, 77] studied the benefits of TiO_2 addition to pavements. The author came to similar findings of the increased photodegradation of *VOC*s, especially with the increased UV irradiation. However, it was observed that the relative humidity might negatively affect the efficiency, thus limiting the potential of the application. In terms of considering photocatalytic pavements, many authors agree on the same outcome – high photoreduction of many *VOC*s, except for CO_2 (trees can do this particular job). Besides cement-based products, asphalt, ceramics or other external construction material can be coated with a photocatalyst. Although the presented results are far from perfect, it is a small step towards having a 'green' pavement technology. A simplified representation of photodegradation of *VOC*s on the pavement with a photocatalytic coating is shown in **Fig. 1.6**. Again, the chemical process does not differ much from the above mentioned ones, only the decomposed particles and the by-products may differ.

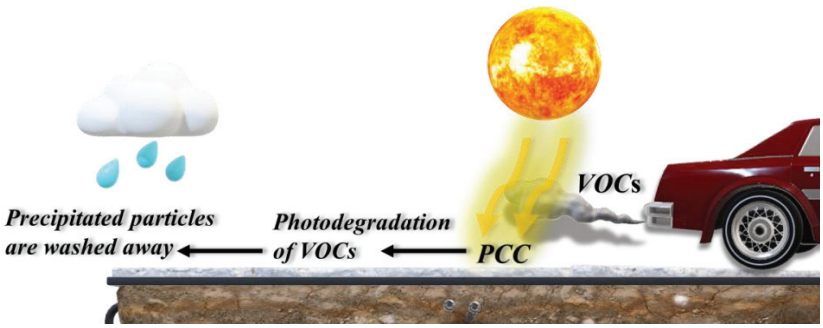

Fig. 1.6. Visual representation of photocatalytic pavement catalysis. *VOC*s – volatile organic compounds; *PCC* – photocatalytic coating

On the other hand, indoor air pollution is more important as humans spend most of the time (70% up to 90%) inside. The advantages (at some point) in indoor air purification are a controllable light source, air flow rate, moisture level, and temperature (within the scope of the available technology). Moreover, the variety of objects which can be coated with a photocatalyst is much higher indoors, compared to outdoors. In his dissertation, B. Stefanov proposed the idea of TiO_2 being coated with UV transparent glass [78]. In such a way, coating UV transparent window glass with a TiO_2 thin film would result in high-efficiency photodegradation of *VOC*s. The easiest and already commercially available air purification methods are air conditioning systems (ACs); humidifiers; ventilators, etc.). By simply adding a stand-alone or an array of UV lamps together with photocatalytic layers/filters (nanofibers) (**Fig. 1.7**), the photodegradation of *VOC*s takes place [79]. In short, when polluted air enters the system, then *VOC*s are being oxidized on the filters of the UV-activated photocatalyst and precipitates in the system (yet, additional cleaning of the system is required to maintain the purification efficiency), and, as a result, purified air exits the system. In addition, systems that could be applicable for both indoors and outdoors, have also been presented. A recent analysis by A. Mavrikos *et al*. [80] suggested a versatile photocatalyst for indoor and outdoor air purification applications. They synthesized a modified palygorskite clay (*PGc*) structure by adding TiO_2 nanocomposites together with Zn/Cu metal ions. However, as the results suggest, modifying the *PGc* structure with Zn increased the efficiency under UV and visible light irradiation, which was the opposite for Cu. The explanation behind this is the deactivation of TiO_2 nanocomposites by additive Cu ions [80]. Likewise to the water purification method, air purification reaches high efficiency when a photocatalyst containing TiO_2 is used.

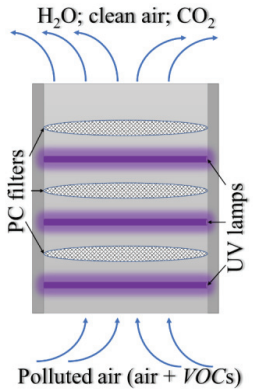

Fig. 1.7. Visual representation of the system used for indoor air purification. *PC* filters – filters with photocatalytic coating

Anti-bacterial (self-sterilizing) coatings

Alongside the previously mentioned methods, anti-bacterial coatings could be applied in the same way as the photocatalytic reactions are similar. However, the

improvement of the photocatalytic efficiency might differ. To this matter, mainly noble metal nanoparticles (*NMNP*s) are used with TiO_2 as the main photocatalyst [81]. *NMNP*s show unique localized surface plasmon resonance (*LSPR*) properties which are based on the nanometric structure of *NMNP*s [82]. In general, *LSPR* is an optical phenomenon when light interacts with *NP*s at a size smaller than that of the wavelength. Thus, the optical properties of *NP*s differ from bulk material. The process behind this is that the plane-wave excitation of *NP*s with a size of $\frac{R}{\lambda} < 0.1$ (where R is the radius of the *NP*s, and λ is the wavelength) causes coherent oscillation of the electrons by the oscillating electric field [83]. This results in an increase of polarization charges on the surface of *NP*s [84]. Noble metals, such as silver (Ag) and gold (Au), show unique *LSPR* properties under visible light irradiation, which makes them a viable choice in the photocatalytic application for anti-bacterial coatings. S. Karagoz *et al*. discussed Ag/TiO_2 application for anti-bacterial coatings [85]. Beside the positive results in bacterial removal, their findings in photocatalytic degradation of methylene blue (*MB*) yielded other interesting results. They observed that the photocatalytic efficiency of Ag/TiO_2 was enhanced compared to plain TiO_2. This suggests that *LSPR* caused by the *NMNP*s might increase the photocatalytic efficiency in other applications as well. M. A. Subhan *et al*.'s [86] findings are in line with those of T. H. Huy *et al*. [71], as both groups of authors suggested an effective combination of TiO_2 and SnO_2. Thus, the former suggested an improvement of the TiO_2/SnO_2 structure by adding Ag_2O for enhanced anti-bacterial application. As a result, they suggested a versatile and efficient method for water purification and bacteria removal.

Energy generation

Probably the first thought that comes to mind when people are thinking about photocatalysis and energy production is hydrogen (more specifically – green hydrogen). Even though hydrogen generation through water splitting reactions has been known for several decades, it started gathering most interest after the latest Conference of the Parties (COP26, 2021). Government leaders decided to 'push' the green hydrogen economy agenda even further as a renewable energy source for environmental remediation [21, 22]. On top of that, lots of research has already been done on energy generation through photocatalytic applications, and requirements for sustainable and cost-efficient photocatalyst have already been presented.

Controversially, photocatalysis can be used not only for solar-to-energy conversion but for CO_2-to-energy conversion as well. Thus, two birds get killed with one stone [1] [87]. However, the term 'CO_2-to-energy conversion' is an oversimplification as the process is actually more complex. In short, the CO_2-to-energy conversion works as storage of sunlight energy in the form of chemical bonds by hydrogenation of CO_2. This way, solar fuels, such as methane (CH_4) and methanol (CH_3OH), are generated [88, 89]. However, the reduction of CO_2 by the photo/electrochemical process requires more energy compared to the reduction of

[1] To succeed on solving two problems in a single action [87].

hydrogen (in hydrogen generation). Therefore, it is mainly done by an electrochemical process than by photocatalysis [90]. However, a debate has arisen whether CO_2-to-energy conversion is more favorable than solar-to-energy conversion, especially when considering the energy losses and environmental issues. Alternative ways of CO_2 utilization by reduction/conversion have been widely reviewed in other studies [91].

Considering the solar-to-hydrogen (*STH*) conversion, several requirements must be met: the energy must be higher than 1.23 eV (which in equivalent is the energy of a photon with a wavelength of ~1000 nm); a thermodynamically stable photocatalyst is required [20, 92] (the requirements for *CBM* and *VBM* are described above in *Redox reactions*) for the efficient decomposition of a water molecule. In this context, visible light (approximately 400 to 700 nm) photocatalysis is more than sufficient, with a photon energy of ~3.1 to 1.8 eV, respectively [93, 94]. Moreover, a system that separates and captures photogenerated H_2 is required.

On the contrary to the previously discussed photocatalysis applications, energy production through photocatalysis is much more difficult. Despite the fact that TiO_2 shows superior efficiency in water or air purification, a high energy bandgap limits its application for *STH* conversion [95]. By using plain TiO_2, only a fraction (~5%) of sunlight energy (mostly UV) can be converted to the energy required for water splitting reactions [96]. Considering the other above mentioned photocatalysts, either thermodynamical stability or photosensitivity issues arise. Therefore, the process of energy generation through photocatalysis requires careful manufacturing of modified semiconductor, a structure containing several semiconductors (monolithic structures), or dual-semiconductor (anode and cathode) systems to achieve efficient solar-to-hydrogen conversion levels.

1.3. Photocatalysts

Semiconductors having photocatalytic properties and the ability to split water molecules can be divided into two groups: metal oxides with a metal electronic structure of d^0 and d^{10}. The former metal oxides are TiO_2, ZrO_2, WO_3, NbO_2 or Nb_2O_5, etc., while the latter are SnO_2, In_2O_3, Ga_2O_3, GeO_2, etc. [9, 10]. In general, a semiconductor having a *CBM* higher than (or close to) the hydrogen reduction potential and a *VBM* value lower than the oxidation potential is suitable. However, most semiconductors have either a large energy bandgap, utilizing only UV light (<400 nm), or have a low redox potential, which results in high recombination rates [97, 98]. Thus, a combination of two or more semiconductors (monolithic structures) is being implemented for hydrogen production.

Taking in mind a combination of several semiconductors, heterojunction interface must be carefully designed for the efficient transfer of charge carriers. In general, the heterojunction interface can be divided into three categories (types): a straddling gap, a staggered gap, and a broken gap [99]. In short, the straddling gap at the heterojunction forms when the *VBM* and *CBM* of one semiconductor are lower and higher, respectively, than those of the second semiconductor (**Fig. 1.8 (a)**). This way, based on the internal electric field, charge carriers (either electrons or holes) accumulate at the semiconductor having a lower energy bandgap [100]. The staggered gap forms between two semiconductors when *VBM* and *CBM* are at higher energy

levels than those of the second semiconductor, accordingly (**Fig. 1.8 (b)**) [11, 12]. This results in a high probability of the charge carrier separation. On the other hand, a broken gap forms at the heterojunction where no overlapping of energy bands occurs (**Fig. 1.8 (c)**). The *VBM* of one semiconductor is at a higher energy level than the *CBM* of the second semiconductor [101, 102]. Considering a photocatalytic application, mainly a staggered or a straddling gap is formed between the two semiconductors photocatalysts, and a broken gap never forms.

Additionally, a depletion layer (a space charge region), which forms at the heterojunction between the two semiconductors or between the solution and the photocatalyst, has to be taken into the equation [103–105]. Under equilibrium, a depletion layer forms at the junction of *n*-type and *p*-type semiconductors. However, this layer can form at the junction of two same-type semiconductors as well. At the *pn* junction, the depletion layer forms due to the diffusion of electrons into the *p*-type semiconductor and holes on the opposite side. At the heterojunction of the same type of semiconductors, the depletion layer mainly spreads into the one with a lower conductivity (a lower concentration of free charge carriers) [106]. The width of such a depletion layer can be calculated by the following equation (simplified) [107–109]:

$$W = \sqrt{\frac{2\varepsilon_s V_{bi}}{qN_D}}, \tag{1.14}$$

where W is the width of the depletion layer, ε_s is the dielectric permittivity of a semiconductor, V_{bi} is the built-in potential, q is the electron charge ($1.6 \cdot 10^{-19}$ C) and N_D is the dopant concentration in the particular semiconductor. Whereas, V_{bi} can be evaluated by:

$$V_{bi} = \phi_B - E_A\,, \tag{1.15}$$

$$\phi_B = \phi_m - \chi, \tag{1.16}$$

where ϕ_B is the barrier height formed at the semiconductor, E_A is the activation energy (the distance between *CBM* and E_F, ϕ_m is the work function of a metal, and χ is the electron affinity. For the semiconductor, i.e., TiO_2, the depletion layer depends on the crystallinity and morphology, and it ranges from several to tens of nanometres [110]. Band bending is another criterion that has to be considered before designing a combined photocatalyst [111]. This phenomenon appears under thermal equilibrium when the Fermi energy level of both semiconductors equalizes, thus a band bending appears. The band bends either upwards or downwards, and this mainly depends on the electron affinity of the semiconductor: upwards due to a higher electron affinity; downwards due to a lower electron affinity [111].

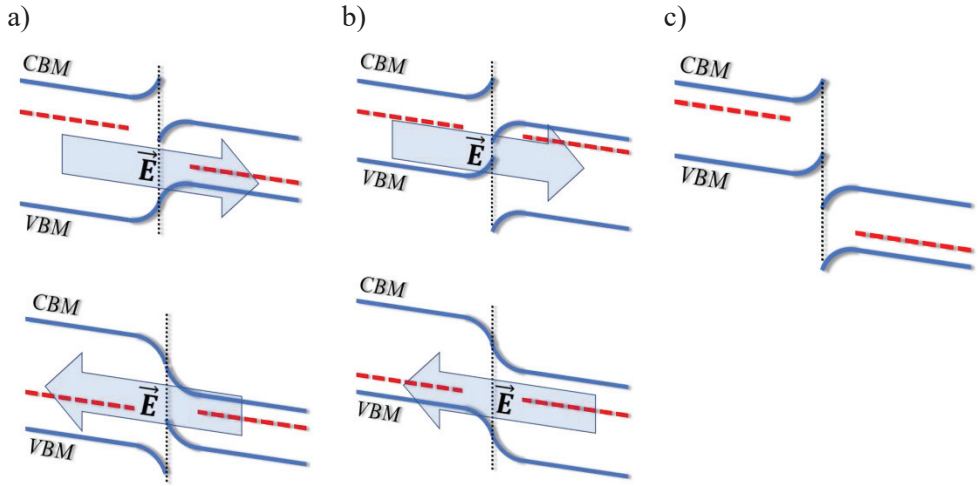

Fig. 1.8. Visual representation of types of heterojunction between two semiconductors: a) a straddling gap; b) a staggered gap; c) a broken gap. $\vec{E}$ represents the internal electric field; *CBM* is the conduction band minimum; *VBM* is the valence band maximum

Considering the photocatalytic water splitting in particular, the depletion layer spreads into the photocatalyst as the conductivity of the electrolyte (in all cases) is higher (similar to the metal-semiconductor heterojunction) [109]. Therefore, according to the theory of the depletion layer formation, electrons would drift from the electrolyte to the photocatalyst, whereas holes would drift in the opposite direction, thus trying to reach equilibrium between the electrolyte and the photocatalyst [103]. However, a problem arises at this point, as the charge carrier recombination occurs at the depletion layer. Thus, again, it is required to suggest a careful design of combined photocatalysts in order to overcome the recombination at the electrolyte–photocatalyst heterojunction. In addition, the depletion layer may also appear in the semiconductor – between different crystal phases or between different facets [101]. Different crystal structures have slightly different energy bands, thus creating a depletion layer at the interface [112, 113]. Taking in mind the crystalline structure of TiO_2, different facets have different electronic structures [16]. This gives a slightly wider perspective on manufacturing efficient TiO_2 as a photocatalyst. Additionally, the redox potential has to be taken into account when designing a structure containing two semiconductors. According to the redox reactions described above, the oxidation reaction has a higher chance to occur on the surface of the semiconductor with a higher oxidation potential. Likewise, the reduction reaction will take place on the surface of a semiconductor with a higher reduction potential [114]. To this matter, it is difficult to analyze the redox potentials of the material, thus many articles use some already measured and calculated values from the Pourbaix diagram [115–117]. Given these points, the mechanisms behind photocatalysis, or, in other words, behind the generation of charge carriers, are more complicated than it seems at the first glance.

During the last few decades, a wide variety of studies has been made to manufacture and optimize a combined or modified photocatalyst with the objective to achieve cost-effective and efficient hydrogen generation. Therefore, a list of several photocatalysts and their combinations is presented in **Table 1.1**. As D. Chen *et al*.'s study shows, TiO_2 with a considerably low energy bandgap of 3.16 eV and Pt (as co-catalyst) results in 4053 *µmol/h* hydrogen production under UV-vis light irradiation (300 W, Xenon arc lamp). In addition, a slightly higher efficiency was observed with TiO_2 doped by reduced graphene oxide (rGO) (as a photocatalyst) vs. Pt (as a counter electrode) as hydrogen production rates increased to 4588 *µmol/h*. Moreover, when nano-spherical rGO was used, the hydrogen production rates increased 3 times (up to 13996 *µmol/h*) [14]. In the first case, 2D rGO (sheets) was mixed with TiO_2 and Pt *NP*. Therefore, an excited electron transferred from TiO_2 to rGO could freely drift down the rGO sheets, which was enough for recombination to occur between holes in TiO_2 and between electrons on rGO. However, when the rGO structure was changed to 3D (nano-spherical), an electron could drift not only on the surface but to the inner layers of *NS*-rGO as well. Thus, it acts as a trapping center for charge carriers. Another analysis was made with similar TiO_2 having an energy bandgap of 3.19 eV, but without Pt as a co-catalyst, and only under *UV* irradiation (18 W). Thus, only ~9 *µmol/h* of hydrogen was generated [118]. The same study observed photogeneration of hydrogen when CuS (E_g = 1.35 eV) was used as a photocatalyst, with a result of ~20 *µmol/h*. Further study shows that mixing two photocatalysts with a much higher efficiency was reached with a result of up to 190 *µmol/h* of hydrogen when CuS was mixed with TiO_2 at a ratio of 1:4, respectively. However, no data was presented if and how the energy bandgap changes for CuS/TiO_2.

Nonetheless, the explanation behind the increased hydrogen generation is similar to the one stated by D. Chen *et al*. – the slower recombination process between the charge carriers. Thus, so far, no experimental proof has been presented on this matter. A different analysis by co-doping TiO_2 with Ag was done by comparing the photocatalytic efficiency under UV and simulated sunlight irradiation [119]. The study on photocatalytic efficiency between as-deposited TiO_2 and Ag co-doped TiO_2 under *UV* irradiation shows an increase of photogenerated hydrogen at almost 3 times (from ~500 up to 1500 *µmol/h*). Even more significant difference was observed under simulated solar light irradiation with a difference of photogenerated hydrogen from ~10–20 *µmol/h* (with as-deposited TiO_2) to 450 *µmol/h* (with TiO_2/Ag). Thus, as the results show, a higher efficiency was reached under *UV* irradiation for both cases: TiO_2 and TiO_2/Ag, compared to the same samples set under the simulated solar light. This suggests that a decrease in the energy bandgap, which was 3.2 eV (for as-deposited TiO_2) and 2.77 eV (for TiO_2/Ag), was not enough to increase the photosensitivity under visible light irradiation.

Table 1.1. List of semiconductors and their combinations as photocatalysts with equivalent H_2 production rates observed in other studies. Co-catalyst – a co-doped or a separate catalyst; sacrificial agent – the electron donor or hole acceptor which reduces the recombination process between the two and increases H_2 generation rates; *Xe* – xenon lamp; *Hg* – mercury lamp. Some authors do not present or do not measure the required data, thus it is referred to as 'no data'

Photocatalyst	E_g, *eV*	Co-catalyst	Sacrificial agent	Light source	H_2, *μmol/h*	Ref.
TiO_2	3.16	Pt	Methanol	UV-vis (300 W, Xe)	4053	[14]
TiO_2/Au	No data	Pt	Propanol	Vis (300 W, Xe)	0.5	[120]
TiO_2/Ag	2.77	None	No data	UV (8 W, Hg)	~1500	[119]
NTa[1] TiO_2/Ag	3.20	None	No data	Vis (35 mW/cm^2)	1.56	[121]
TiO_2/Ag	2.77	None	No data	Sunlight[2]	~450	[119]
TiO_2/rGO	3.12	Pt	Methanol	UV-vis (300 W, Xe)	4588	[14]
TiO_2/NS-rGO[3]	2.88	Pt	Methanol	UV-vis (300 W, Xe)	13996	[14]
P25[4] TiO_2/Au	No data	CeO_2/Au	No data	UV-vis (125 W, *Hg*)	~70	[15]
CeO_2/Au	No data	P25 TiO_2/Au	No data	UV-vis (125 W, *Hg*)	~10	[15]
CuS	1.35	None	Methanol	UV (18 W)	20	[118]
TiO_2	3.19	None	Methanol	UV (18 W)	9	[118]
CuS/TiO_2 (1:1)	No data	None	Methanol	UV (18 W)	75	[118]
CuS/TiO_2 (1:4)	No data	None	Methanol	UV (18 W)	190	[118]
CuS/TiO_2 (1:5)	No data	None	Methanol	UV (18 W)	150	[118]
CdS	2.30	CDs[5]	LA[9]	Vis (300 W, Xe)	4640	[122]
WO_2/Na_xWO_3	No data	None	Sea water	Solar[6] (1000 W, Xe)	5.76	[123]
CdS/ZnS	No data	None	SS[7]	Vis (300 W, Xe)	239	[124]
H:ZnO NRa[8]	3.27	None	SS	Vis (300 W, Xe)	122500	[125]
Fe_2O_3/TiO_2	3.20	None	SS	Vis (300 W, Xe)	7253	[126]
ZnO/CdS	No data	None	SS	Vis (500 W, Xe)	851	[127]
ZnO/CdS	No data	Pt	SS	Vis (300 W, Xe)	2960	[128]
ZnO/CdS	~2.34	None	SS	Vis (500 W, Xe)	354	[129]
P25 TiO_2/CdS	No data	Pt	SS	Vis (450 W, Xe arc)	6720	[130]
P25 TiO_2/CdS	No data	Pt	SS	Vis (450 W, Xe arc)	4848	[131]
TiO_2/CdS	No data	Au	SS	Vis (300 W, Xe)	1970	[132]
WO_3/Au	No data	Pt	Glycerol	Vis (300 W, Xe)	132	[133]
Ga_2O_3	~4.80	Pt	LA	Vis (300 W, Xe)	0.12	[134]
Ga_2O_3/CdSQD[10]	~2.25	Pt	LA	Vis (300 W, Xe)	901.6	[134]
In_2O_3	~2.76	Pt	LA	Vis (300 W, Xe)	0.05	[134]
In_2O_3/CdSQD	~2.25	Pt	LA	Vis (300 W, Xe)	506.9	[134]
In_2O_3/ZnO	2.47	None	Methanol	Vis (300 W, Xe)	1784	[135]

[1]NTa – nanotube arrays
[2]Simulated sunlight (Science-Tech, SF300B with AM 1.5G filter)
[3]NS-rGO – nano-spherical reduced graphene oxide
[4]P25 TiO_2 – Anatase/Rutile mixture
[5]CDs – carbon dots
[6]Simulated solar light
[7]SS – Sodium sulphide + sodium sulphite (Na_2S + Na_2SO_3)
[8]H:ZnO NRa – hydrogenated ZnO nanorod arrays
[9]LA – Lactic acid ($C_3H_6O_3$)
[10]QD – quantum dots

Further on, in their 2008 paper, H. Park *et al*. reported a high photocatalytic efficiency of CdS/TiO_2 as a photocatalyst with a Pt as co-catalyst for hydrogen production with a result of 6720 *μmol/h* [130]. Later on, the same authors modified

the CdS/TiO_2 structure, which resulted in a lower photocatalytic efficiency with a hydrogen production rate reaching 4848 *μmol/h* [131]. Both studies analyzed the photocatalytic efficiency dependence on the preparation technique and the final structure of the photocatalyst. The findings show that an efficient charge carrier separation is achieved when the Pt co-catalyst is deposited on TiO_2 instead of CdS. Moreover, the changes in the CdS stoichiometry may also negatively affect the overall photocatalytic efficiency. According to this study, it is clear that a careful design of a system of semiconductors and the deep analysis of the photocatalytic efficiency dependence on the structure is crucial in order to determine the optimal parameters. Similar to H. Park *et al*., J. Fang *et al*. reported a photocatalytic efficiency of CdS/TiO_2 under similar conditions, but with Au as a co-catalyst (instead of Pt) [132]. The hydrogen generation measurements resulted in 1970 *μmol/h*, which, in comparison, is lower than the values presented by H. Park *et al*. Since the only difference between the two studies was the a co-catalyst, the outcome can be attributed to the nature of Au and Pt, as the latter is known for its superior reduction capabilities, compared to Au [16, 17]. Despite that, the high price of Pt makes it commercially inconvenient, and cheaper alternatives are being analyzed.

On the contrary, X. Zou *et al*. [127] and X. Wang *et al*. [128] suggested a combination of ZnO and CdS as a photocatalyst. Both studies used similar conditions for hydrogen generation analysis to what had been previously described in H. Park *et al*. Therefore, differences in the photocatalytic efficiency between TiO_2 and ZnO as photocatalysts can be observed. As X. Zou *et al*. presented, ZnO/CdS without a co-catalyst achieved an 851 *μmol/h* of hydrogen generation. Higher efficiency with a result of 2960 *μmol/h* hydrogen generation was observed in X. Wang *et al*.'s study, where Pt was used as a co-catalyst. The importance of the co-catalyst and its effect on the total photocatalytic efficiency is indisputable. Moreover, the lower efficiency of ZnO, compared to TiO_2, may be attributed to a higher oxidation potential of TiO_2. The importance of this factor was reviewed in the previous chapters.

C. Zhu *et al*. suggested a system of CdS as a photocatalyst and carbon dots (*CD*s) as a co-catalyst, resulting in 4640 *μmol/h* of hydrogen generation under similar light irradiation as in the studies discussed above, but it employed a different sacrificial agent (Lactic acid) [122]. Beside the low energy bandgap of CdS (~2.3 eV), the *CD*s co-catalyst improved the photogenerated charge carrier separation and stabilization. It is worth mentioning that the photocatalytic efficiency in this particular case was higher when the analysis was being done in seawater than in pure water. Thus, a different approach was suggested to hydrogen generation by decomposing seawater.

A more complex structure of Ga_2O_3 and In_2O_3 containing CdS quantum dots (*QD*) and Pt as a co-catalyst was presented by Y. Pan *et al*. [134]. The measured energy bandgaps for stand-alone Ga_2O_3 and In_2O_3 were around 4.8 eV and 2.76 eV, respectively. Even though the energy bandgap of Ga_2O_3 is much higher than that of In_2O_3, the former achieved a better photocatalytic efficiency under visible light irradiation with a result of 0.12 *μmol/h* (compared to 0.05 *μmol/h* for In_2O_3). The authors explain that a small amount of UV light might still pass through the filter, thus activating Ga_2O_3, and the low activity of In_2O_3 is attributed to the limited light absorbance after 420 nm wavelength and a higher chance of recombination due to

defects in bulk or grain boundaries. For comparison, in this study, CdS vs. Pt achieved hydrogen generation of 108.1 *μmol/h*. Further implementing CdS*QD* into the Ga_2O_3 and In_2O_3 resulted in 901.6 and 506.9 *μmol/h* of hydrogen generation, respectively (603 *μmol/h* for CdS/TiO_2 vs. Pt). The study results are consistent with those obtained by H. Park *et al*. as both studies suggested that the highest efficiency is achieved when the co-catalyst is deposited on the metal oxide instead of CdS. In short, the increased photocatalytic efficiency is explained by the efficient charge carrier transfer from the photocatalyst to the co-catalyst and reduced recombination.

In their ground-breaking paper, X. Lu *et al*. presented a superior ZnO photocatalyst for hydrogen generation from water. The hydrogenated ZnO nanorods array (*NRa*) achieved a hydrogen production of 122500 *μmol/h* [125]. Such impressive results might be attributed to the concentration of defects which was increased during the hydrogenation process. Moreover, the color of the ZnO nanorods array changed from transparent to black, which resulted in higher optical absorption. Furthermore, hydrogenated ZnO *NRa* resulted in lower light reflectance compared to ZnO *NRa*. The higher probability of charge carrier separation is affected by the morphology of ZnO *NRa*. Even though the results stand out from the others presented in **Table 1.1** and might look debatable, other studies also showed a similar approach with the results being comparable to this one [136–138].

The study by L. Li *et al*. shed more light on designing a photocatalyst having a more complex structure [139]. To be more specific, they manufactured an $H_3PW_{12}O_{40}$/TiO_2-g-C_3N_4 photocatalyst by the ultrasonic method. According to the energy band alignment throughout the structure, the path of the photogenerated electron would be g-C_3N_4 → TiO_2 → $H_3PW_{12}O_{40}$. Therefore, it increased the probability of charge carrier separation. In the end, the photogenerated holes at g-C_3N_4 would be utilized in oxidation reactions, whereas electrons at $H_3PW_{12}O_{40}$ would be consumed in reduction reactions. However, the authors suggested such a structure for water purification application by analysing the decomposition of organic compounds under visible light irradiation. Additionally, based on the results, such a structure can be utilized up to 4 times with an excellent result, thus raising a problem of reusability. Since the decomposition of organic compounds is, at some point, similar to the decomposition of a water molecule, such a structure, or a slightly modified version of it, might reach superior capabilities in hydrogen generation application.

C. Lu *et al*. drew attention to a staggered gap (type II) heterojunction by manufacturing $ZnIn_2S_4$/$BiPO_4$ photocatalyst for enhanced photocatalytic efficiency under solar light irradiation [140]. The works of both L. Li *et al*. and C. Lu *et al*. focused on designing type II heterojunction in order to increase the separation efficiency of photogenerated charge carriers. Moreover, such a design and energy bandgap engineering throughout the layers may lead to higher photosensitivity under visible light irradiation, compared to stand-alone photocatalysts.

In short, an efficient charge carrier separation can be achieved by carefully engineering a monolithic structure to create an internal electric field. This electric field would act as an additional force driving the separation of charge carriers: electrons and holes would drift into separate directions [109]. A simple example of such engineering would be the *n*-type Si and *p*-type Si junction.

It is difficult to compare the photocatalytic efficiencies reported by different studies as different conditions were maintained during the process, yet, a general view of the data presented in **Table 1.1** shows some key points:

- The presence of a co-catalyst is crucial for efficient hydrogen production;
- A low energy bandgap is not the only factor that is important in photocatalysis;
- A careful design and deep analysis of combined semiconductors as a photocatalyst must be done in order to find an/the optimal structure;
- In order to accurately compare the photocatalytic efficiency, the same conditions must be maintained as any fluctuation might end up in totally different results.

On the other hand, not every study analyzes hydrogen generation due to lack of equipment. Therefore, photodegradation of methylene blue (*MB*), Rhodamine B (*RhB*), or other electrolytes requiring similar activation energy for the decomposition of molecules as that for water are used [141].

Even though, in its pure phase, TiO_2 has a wide energy bandgap (~3.0 to 3.7 eV) [142], it 'checks' all other requirements for photocatalysts: thermodynamical stability against photo-corrosion by photogenerated electrons and holes; redox potentials are suitable for water splitting applications; it is eco-friendly and non-toxic [143]. Moreover, on the grounds of the previously reviewed studies, TiO_2 is used as a protective layer for other photocatalysts to eliminate the photodegradation of the latter [19]. Therefore, further review and study shall be focused on TiO_2 as a photocatalyst, its application, and how to solve the issue of the wide energy bandgap, which is probably the only parameter affecting the photocatalytic efficiency.

1.4. TiO_2 as Photocatalyst

Probably the first to observe the strange phenomenon that occurs on the surface of TiO_2 when it is immersed in water and is irradiated with light was Prof. Fujishima [144]. He noticed that small bubbles of oxygen appear on the surface of TiO_2 when it is set in water under sunlight irradiation. Later on, an experiment was set with TiO_2 vs. Pt resulting in hydrogen generation on the surface of Pt. During that time, the strange phenomenon was called the Honda-Fujishima effect, and it was later described as photocatalysis. The interest in TiO_2 application as a photocatalyst started to develop with the number of articles increasing exponentially over the decades [145]. The application of TiO_2 for water and air purification [146–150], decomposition of CO_2 [151, 152], and water splitting reactions [153–155] gathered the most interest. Despite the interest, TiO_2 as a stand-alone semiconductor is not able to achieve high photocatalytic efficiency because of its relatively wide energy bandgap which varies in the range of ~3.0 to 3.7 eV, based on the crystal structure and other morphological properties [156–160]. The wider the energy bandgap is, the narrower wavelength of the solar spectrum reaching the Earth's surface can be utilized. Therefore, photosensitivity under visible light irradiation is one of the main goals to achieve high photocatalytic efficiency.

Properties of TiO_2 crystal phases

Naturally, TiO_2 has three different crystal phases: anatase, brookite, and rutile. The rutile phase TiO_2 is denoted by the highest thermodynamic stability, thus exceeding the value of anatase, and brookite is mainly a transition phase between anatase and rutile. In general, crystallization from anatase to rutile occurs at an average temperature of 600 to 800 °C [161–163]. As for the properties of different crystal structures, the main differences are presented in **Table 1.2**. Here, 2 Ti-O and 4 Ti-O represent long (covalent) and short (dative) Ti-O bonds, together with the angle α and β, respectively. Even though these TiO_2 phases consist of the same TiO_6 octahedrons, the difference in bond lengths and the angle between them results in a slightly different crystal structure.

Table 1.2. Characteristics of different TiO_2 crystal phases [156, 164–171]. 2 Ti-O is attributed to the long (covalent) bond; 4 Ti-O is attributed to the short (dative) bond; α is the angle between the covalent bonds; β is the angle between the dative bonds

Crystal structure of TiO_2	Crystal system	Density, g/cm^3	2 Ti-O (α)	α, °	4 Ti-O (β)	β, °	Energy bandgap, eV	Refractive index, n
Anatase	Tetragonal (*ditetragonal dipyramidal*)	3.83	~1.964	102.3	~1.937	92.6	~3.2–3.7	2.568
Brookite	Orthorhombic (*dipyramidal*)	4.17	~1.978		~1.941		~3.1–3.5	2.809
Rutile	Tetragonal (*ditetragonal dipyramidal*)	4.24	~1.984	90.0	~1.946	98.9	~3.0–3.3	2.947

When considering the photocatalytic application, further analysis of the given data will be done for anatase and rutile, as brookite has already been proven to be inefficient in comparison with the two other varieties [172, 173]. The two TiO_2 phases, anatase and rutile, share the same tetragonal crystal system and the same ditetragonal dipyramidal crystal type. However, in terms of their crystal habit, the TiO_2 rutile phase is equivalent to the 'squished' TiO_2 anatase phase. Therefore, the density of the TiO_2 rutile phase (4.24 g/cm^3) is higher than that of the TiO_2 anatase phase (3.83 g/cm^3). On the other hand, the short and long Ti-O bonds are longer in the TiO_2 rutile phase than in the TiO_2 anatase phase. It is worth mentioning that longer Ti-O bonds result in a lower activation energy which is required for the excitation of the charge carrier. Thus, the TiO_2 rutile phase has a lower energy bandgap (~3.0 up to 3.3 eV) than the TiO_2 anatase phase (~3.2 up to 3.7 eV).

Given these points, the TiO_2 rutile phase might achieve a higher photocatalytic efficiency compared to the TiO_2 anatase phase. However, when considering the density of crystal phases, the TiO_2 anatase phase has a higher surface area, which has been proven to increase the photocatalytic efficiency, as more surface area is in contact with the electrolyte. Nevertheless, the reduction potential of the TiO_2 anatase phase is at a higher energy level than that of the TiO_2 rutile phase [174, 175]. Moreover, the concentration of defects is higher in the TiO_2 anatase phase than in the

TiO_2 rutile phase, which results in a lower activation energy of ~0.4 and ~1 eV, accordingly [176–178]. Thus, there are more variables in the equation than only the energy bandgap.

Alongside the TiO_2 crystal phases, amorphous TiO_2 (further referred to as a-TiO_2) is worth mentioning as it is known as a reliable and low-cost alternative for the TiO_2 anatase and rutile phases [179]. The high photocatalytic efficiency of a-TiO_2 is attributed to the concentration of defects, which results in a higher probability of charge carrier separation. However, the defects are positioned mainly in the bulk rather than on the surface [18]. Thus, it can be considered as a cheaper alternative to the TiO_2 anatase or rutile phase.

Manufacturing of TiO_2 thin films

There is a variety of deposition techniques to perform TiO_2 thin films deposition. These techniques can be divided into two categories: *PVD* vs. *CVD*. The latter consists of atomic layer deposition (*ALD*) [180], sol-gel [181], or a range of chemical vapor deposition (*CVD*) techniques: metal-organic chemical vapor deposition (*MOCVD*), plasma-enhanced chemical vapor deposition (*PECVD*), or plasma-assisted chemical vapor deposition (*PACVD*) [182–184]. However, chemical deposition techniques are not eco-friendly, as toxic precursors of the TiO_2 monomer are used during the deposition. This is not the case for the physical deposition techniques. These can be divided into two categories based on the nature of deposition: evaporation or sputtering. Evaporation techniques consist of vacuum thermal evaporation (*VTE*), electron beam evaporation (*EBE*), molecular beam epitaxy (*MBE*), etc. Meanwhile, sputtering can be either direct current (*DC* sputtering) or radiofrequency (*RF* sputtering) [185], and both of them are known as magnetron sputtering. It is difficult to put the mentioned techniques in comparison when it comes to photocatalytic efficiency; however, taking in mind deposition on patterned structures, the *PVD* and *CVD* techniques are more suitable than sol-gel spin-coating [186]. In general, it all comes to what type of equipment is available, and neither one nor the other has any advantages or disadvantages over the alternative option.

Granted that, the *RMS* technique and the sol-gel spin-coating technique shall be described in more detail as these two are the main deposition techniques used in this dissertation.

The common properties, such as the morphology and crystal structure of TiO_2 deposited via the sol-gel spin-coating technique, mainly depend on the initial chemical structure of the pre-prepared[2] TiO_2 precursor, and, secondly, on the spin-coating deposition parameters, such as the spinning rate (*RPM* as rotations-per-minute) and the spinning time [156, 181, 187, 188]. Therefore, when having one precursor, only the thickness (followed by the energy bandgap), morphology, and crystallinity (based on the annealing temperature) can be modified. Whereas, during *PVD* deposition by sputtering the Ti or TiO_2 cathode, such parameters as the type of sputtering (*DC* or *RF*), the magnetron power, argon and oxygen pressure, and the ratio of the

[2] By using a commercially available TiO_2 precursor

oxygen/total pressure, the distance between the substrate and the cathode, the deposition temperature, etc. [189]. Moreover, photocatalytic efficiency highly depends on the surface area of the photocatalyst, thus the sol-gel spin-coating technique is probably the only one that enables the deposition of highly porous thin films. Provided that, the versatility of TiO_2 deposition techniques is indisputable. After all, there is one parameter that highly affects the morphology and the crystal structure of the deposited TiO_2, despite the deposition technique is the material of a substrate on which TiO_2 is being deposited. As the study by P. Singh *et al*. presented, using $LaAlO_3$ and α-Al_2O_3 as substrates for TiO_2 deposition affects the crystal orientation and the phase transition of TiO_2 due to the lattice mismatch [190]. The deposition of TiO_2 at 650 °C temperature resulted in the rutile phase formation when α-Al_2O_3 was used as a substrate, and, in the case of $LaAlO_3$, anatase phase formation was observed according to the *XRD* data. Moreover, different morphology in terms of the roughness and grain size was observed when TiO_2 was deposited on different substrates under the same conditions. The reason behind this, as the authors explain, is the lattice mismatch between TiO_2 and $LaAlO_3$ or α-Al_2O_3. Another study by S. Miszczak and B. Pietrzyk suggested that TiO_2 anatase-to-rutile transition strongly depends on the substrate material [191]. Their study shows that the average annealing temperature at which the TiO_2 anatase phase (powder) forms is ~400 °C, whereas the TiO_2 anatase-to-rutile phase transition ends at 800 °C. On the contrary, the temperature which is required for the TiO_2 anatase-to-rutile phase transition increases to 800, 850, and even 1000 °C when TiO_2 is deposited on stainless steel (304L), Co-Cr-Mo alloy, and Si substrates, respectively. Nevertheless, it was observed that a TiO_2 thin film deposited on the Si substrate and annealed at 1000 °C contains a mixture of anatase/rutile, with anatase being the dominant phase. They suggest that the TiO_2 anatase-to-rutile phase transition might be affected by the diffusion of additives from the substrate material. E. Blanco *et al*.'s data confirms S. Miszczak's and B. Pietrzyk's point that the diffusion process occurs between the substrate and TiO_2 [192]. They deposited TiO_2 thin films (of a thickness of around 40 to 70 nm) on Si substrates and annealed them at different temperatures. *XPS* analysis showed a considerably high amount of Si detected in TiO_2. A significant increase in the Si concentration was observed when the annealing temperature increased from 150 °C (with 4.3% of Si detected) to 800 °C (with 31% of Si detected). Taking into account that the detection depth of *XPS* analysis is around 10 nm, and TiO_2 thickness is of 40 to 70 nm, it is clear that Si diffusion into the TiO_2 lattice occurred. E. Blanco *et al*.'s results are comparable to those previously obtained by J. Yu *et al*. [170] as it shows an increase of Si concentration in TiO_2 with an increased annealing temperature. According to E. Blanco *et al*. and C. Anderson *et al*. [193], the reason behind the slower TiO_2 anatase-to-rutile phase transition is that Si locks the Ti-O species at the interface. The Si diffusion into the TiO_2 lattice prevents the nucleation process which is necessary for the phase transition. Therefore, a higher annealing temperature is required to activate the nucleation process. Such a phenomenon of Si diffusion into the TiO_2 lattice could also affect the photocatalytic efficiency as presented by L. Lopez *et al*. [194]. According to their study, TiO_2 deposited on the glass substrate achieved higher photocatalytic efficiency compared to the ones deposited on 6061Al alloy or a glazed

ceramic tile. However, the only explanation behind this was the higher surface area of TiO_2 deposited on the glass substrate, compared to 6061Al alloy and a glazed ceramic tile. Nonetheless, the diffusion of Si into TiO_2 may increase the defect concentration, which can act as trap centers for photogenerated charge carriers. This results in reduced recombination rates. Thus, it ultimately increases the photocatalytic efficiency.

When considering doping TiO_2 with metal or non-metal ions, *PVD* and *CVD* techniques are probably the best solution for that. During TiO_2 deposition by the *PVD* technique, simply another magnetron (with the dopant cathode) can be set in parallel to the one with a Ti or TiO_x cathode [195]. The dopant concentration can be controlled by controlling the magnetron shutter or power. Whereas, during *CVD* deposition, a dopant material can be injected from another precursor, and the concentration is controlled by the amount of the precursor injected into the system [157, 196]. Thus, for the sol-gel spin-coating technique, TiO_2 and dopant precursors have to be mixed, which requires chemical stability between the precursors [157]. On the other hand, by depositing TiO_2 by the sol-gel spin-coating technique, dopants can be deposited on the surface by *PVD* later on.

Influence of doping on photocatalytic properties of TiO_2

To enhance the photocatalytic efficiency of TiO_2, the latter can be doped with other metals, such as Mg, Cu or Ni [195] in bulk or by depositing precious metals, such as Ag, Au or Pt on the surface [197, 198] so that to increase the spectral selectivity and the rates of the charge carrier separation. This has been widely studied over the last decades, and some examples are already presented in the previous chapter. In general, with an increased dopant concentration, the defects and the trap state concentration increase as well. Thus, the recombination process is cancelled or enhanced as a result [199]. The latter is also a common issue in other photocatalysts.

Considering TiO_2 as a photocatalyst, its photocatalytic efficiency can be enhanced by doping it with other metal or non-metal ions. Doping can be done by depositing a metal (Au or Ag) *NP* on the surface of thin films [200], or by doping TiO_2 in bulk with other metal ions [195] by employing a deposition-precipitation method [15] when depositing is done from an aqueous solution on TiO_2 samples, or with various chemical methods of doping an aqueous TiO_2 solution (which contains TiO_2 *NP* or powders) by mixing with a dopant solution, *NP* or other nano-structures [14, 121, 193, 201–203]. There are two main reasons behind the modification of TiO_2: sensitization under visible light irradiation and enhancing the charge carrier separation. The former describes the ability of TiO_2 to become photoactive under a wider range of the solar spectrum. In other words, the utilization of TiO_2 as a photocatalyst would be possible under sunlight. Whereas, the latter increases the chance to efficiently utilize the photogenerated charge carriers before the recombination occurs. The recombination of photogenerated charge carriers could occur either in bulk or on the surface of TiO_2, thus reducing the rates of redox reactions [204]. Therefore, when doping TiO_2 with other materials, the latter works as a trapping

center for either photogenerated holes or electrons [199]. In this case, there are two paths for the electron to be trapped in these sites (besides recombination) [205]:

1. $VBM_{TiO_2} \xrightarrow{e^-} trapping\ site \xrightarrow{e^-} reduction\ reaction$;
2. $VBM_{TiO_2} \xrightarrow{e^-} CBM_{TiO_2} \xrightarrow[relaxation\ of\ e^-]{} trapping\ site \xrightarrow{e^-} reduction\ reaction.$

It is worth noting that this kind of trapping is possible if the energy band alignment is done in such a way that the trapping center is positioned inside the energy bandgap of TiO_2. Additionally, if TiO_2 is doped with another semiconductor, the *CBM* of the dopant semiconductor must be at lower energy values than that of TiO_2.

Doping introduces the impurity levels (of the acceptor or donor) in the TiO_2 energy bandgap known as shallow or deep traps [206]. Here, the donor is a negatively charged ion (with an additional one or more electrons), and the acceptor is a positively charged ion (with an additional one or more vacancies). The position of the shallow donor level is near *CBM*, whereas the shallow acceptor level is near *VBM*, in the energy bandgap. On the contrary, the position of the deep donor level is near *VBM*, and deep acceptor level is near *CBM* [207]. These impurities might increase the photosensitivity under visible light irradiation for TiO_2. In this case, the electron can be excited from *VBM* and be caught by the acceptor level, where the transition from *VBM* to shallow acceptor trap requires a lower energy than the transition from *VBM* to *CBM*. Similarly, it is for the shallow donor trap, whereas the electron can be excited from the donor level to the *CBM*, and shallow transition occurs, which requires a lower photon energy, and this results in enhanced photoconductivity under visible light irradiation. The shallow traps of the donor level increase the concentration of free charge carriers instead of working as a trapping centre, whereas the shallow traps of the acceptor level act more as a trapping center for electrons excited from *VBM*. The deep traps work the same way, but higher energy (which is still lower than the energy bandgap of TiO_2) is required for the deep transition than for the shallow transition. Therefore, photocatalytic efficiency can be enhanced by the addition of the shallow donor or acceptor level in the TiO_2 energy bandgap, rather than the deep donor or the acceptor level.

The dopants or defects in the TiO_2 lattice create the Ti^{3+} species in Ti^{4+} and oxygen vacancies (O_V). As F. Amano *et al*. suggested, the increase in the Ti^{3+} species increases the photocatalytic efficiency, while the increase in the concentration of O_V decreases it [208]. The concentration of O_Vs is mainly attributed to the concentration of the acceptor dopants which act as a recombination centre. On the other hand, the Ti^{3+} species is attributed to the addition of donor sites, which increases the concentration of electrons followed by an enhanced photocatalytic activity. Thus we suggest that doping TiO_2 with higher valence cations leads to enhanced photocatalytic efficiency.

As previously mentioned, crystalline TiO_2 achieves a higher photocatalytic efficiency compared to a-TiO_2 even though the electronic structure in bulk is somewhat similar [209]. Therefore, it is worth noting that doping crystalline TiO_2

might lead to the amorphization of the TiO_2 structure. E. Khramov *et al*. drew the conclusion that the TiO_2 rutile phase is more susceptible to amorphization due to the modification by dopants than anatase [210]. This can be attributed to the denser structure of the TiO_2 rutile phase and its weaker Ti-O bonds compared to the TiO_2 anatase phase, which results in easier destruction of crystallites. Meanwhile, the TiO_2 anatase phase is less dense and is capable of forming interstitial defects inside the lattice. Thus, it is crucial to assess the effect of dopants on the TiO_2 crystalline structure [157, 211, 212].

Nevertheless, a-TiO_2 might also achieve a considerably high photocatalytic efficiency after the doping. The photoconductivity in bulk is similar to that in TiO_2 anatase and rutile phases [209]. Thus, doping the surface of a-TiO_2 might increase the surface conductivity, which would result in a higher photocatalytic efficiency. Moreover, choosing a donor-level dopant would result in additional electrons getting injected in the conduction band.

In their carefully designed study, S. Hu *et al*. found that covering Si, GaAs, and GaP with a-TiO_2 protects them from photo-corrosion and increases the diffusion of holes [18]. The presently discussed semiconductors have an energy bandgap suitable for water splitting under visible light irradiation, however, according to their redox potential, either photo-corrosion or photo-passivation occurs. Thus, covering them with a-TiO_2 eliminates the possibility of photo-corrosion or photo-passivation. This suggests a different kind of approach for TiO_2 application in photocatalytic water splitting. S. Hu *et al*.'s view is supported by S. Sun *et al*. who also suggest the utilization of a-TiO_2 as a protective layer for other photocatalysts [19]. They also suggest that a-TiO_2 used as a substrate increases the surface-enhanced Raman scattering (*SERS*) when a thin film is doped with Au *NP*. In other words, a-TiO_2 enhances the localized surface plasmon resonance (*LSPR*) [213] compared to crystalline TiO_2 because of its special energy band structure.

Interestingly, it was also observed that a mixture of TiO_2 anatase and rutile phases achieves a higher photocatalytic efficiency compared to single-phase TiO_2 [214]. S. Bakardjieva *et al*.'s findings support those of Z. Rui *et al*., as their study shows a correlation between the ratio of anatase/rutile in mixed-phase TiO_2 and the photocatalytic efficiency [215]. Their findings show that photocatalytic efficiency decreased with an increasing annealing temperature, but only until the anatase-to-rutile transition began. Without additional annealing, the sample of TiO_2 (100% of anatase phase) with a crystallite size of 3.5 nm achieved a rate constant $k = 0.0145$ min^{-1}, whereas, with the same sample annealed at 400 °C (crystallite size 20.2 nm and 100% anatase), the rate constant was 0.0037 min^{-1}. This shows a decrease in efficiency of more than 4 times. Furthermore, by increasing the annealing temperature to 600 °C, the phase transition to rutile phase begins, with 0.4% of rutile detected in the sample, and the rate constant slightly increases to 0.0045 min^{-1}. With a further increase of the annealing temperature to 825 °C, the rate constant reaches its peak value of 0.0195 min^{-1}. In this case, the concentration of anatase (77.4%) and rutile (22.6%) almost matches Degussa P25 (83% anatase and 17% rutile) which achieved a rate constant of 0.0203 min^{-1}. Moreover, they showed that the highest photocatalytic efficiency is reached when the particle size of anatase matches that of rutile (~59.8

nm for both). When the anatase-to-rutile transition ends (pure TiO_2 rutile), the photocatalytic efficiency drops below the mixed-phase TiO_2 efficiency (k = 0.0057 min^{-1}). This was explained by the efficient electron transition through the phases (from anatase to rutile). Moreover, the energy band alignment between the TiO_2 anatase phase and the TiO_2 rutile phase enables more efficient charge carrier separation. Additionally, a lower energy bandgap of the TiO_2 rutile phase widens the spectral selectivity of the sample, thus increasing the photosensitivity under visible light irradiation [216].

Given these points, the photocatalytic efficiency by doping crystalline TiO_2 or amorphous TiO_2 results in enhanced charge carrier separation or higher photosensitivity under visible light irradiation.

TiO_2 combined photocatalysts (hybrid photocatalysts)

Even though the application of TiO_2 is limited due to its wide energy bandgap, it still meets all the requirements: chemical stability against the photo corrosion, a great oxidation and reduction potential, and a wide energy bandgap generating an electron with sufficient energy to split water molecules. Thus, the issue of the wide energy bandgap and how it can be solved by combining it with other semiconductors shall be discussed in detail.

Here, H. Morisaki *et al*. drew attention to the structure of a hybrid TiO_2 photocatalyst (as a photoanode) by covering a solar cell (*pn* junction of Si) with a TiO_2 thin film [217]. In their study, a single junction solar cell was covered with a TiO_2 thin film where the latter was deposited on a *p*-type Si layer with a final structure being TiO_2/*p*-type Si/*n*-type Si/metal electrode. Such a structure would be able to widen the spectral selectivity to visible light irradiation. Here, the photons with an energy of 3.2 eV or higher would photo-generate charge carriers at the TiO_2 thin film, and photons with an energy of 1.2 up to 3.2 would be absorbed in the solar cell, photo-generating the charge carriers at the *pn* junction. Even though they reported that there is no potential barrier between the solar cell and TiO_2, it is debatable as the study made by A. J. Nozik [218] has shown otherwise. The author extensively analyzed the charge carrier separation and transfer throughout the system in metal-semiconductor and semiconductor-semiconductor interfaces. They presented that in order to eliminate the Schottky barrier at the *n*-type and *p*-type semiconductor interface, a metal electrode as an interlayer must be formed. Therefore, it may be suggested that the Schottky barrier might have formed at the TiO_2 and *p*-type Si heterojunction interface. T. Bak *et al*. agrees with J. Nozik *et al*.'s study stipulating that the structure proposed by H. Morisaki *et al*. did not show the full potential because of the barrier forming between the two semiconductors [219]. Additionally, S. Avasthi *et al*. presented clear *I-V* characteristics of TiO_2/*p*-type Si and TiO_2/*n*-type Si heterojunctions, thus showing that a Schottky barrier forms at the former, whereas an ohmic contact was formed at the latter [220]. G. Man *et al*.'s observations further corroborate S. Avasthi *et al*.'s findings by showing the energy band alignment dependence on the dopant density of either *p*-type Si or *n*-type Si [221]. Despite their study, the first one to utilize the data gathered from the *XPS* to engineer an energy band alignment at the heterojunction

was M. Perego *et al*. [222]. Their study shows an energy band alignment between TiO_2 and Si with three different interlayers of Si_3N_4, Al_2O_3 and Ti-rich SiO_x. However, no study on proving whether an ohmic contact was formed was presented, thus only suggesting that an interlayer between TiO_2 and Si might help align the band structures. Considering their study, as well as the structure presented by H. Morisaki *et al*., it should be noted that an interlayer must be transparent in the visible light region, and must not contribute to the light scattering, which could negatively affect the overall photocatalytic efficiency.

Besides, in their recent study, M. Koca *et al*. suggested deposition of polyphenylene (*PPh*) as an interlayer between *p*-type Si and TiO_2 with the objective to eliminate the Schottky barrier and enhance the transfer of charge carriers [223]. Regarding this issue, M. V. Mishin *et al*. suggested deposition of Au*NP* as an interlayer between TiO_2 and Si with the aim to improve the charge carrier transition between the two semiconductors [224]. Three different structures: TiO_2/Au*NP*/*n*-Si; TiO_2/Au*NP*/SiO_2/*n*-Si, and TiO_2/Au*NP*(SiO_2)/*n*-Si (where SiO_2 was an interlayer between Au*NP* and *n*-Si) were analyzed, resulting in either strong or weak rectifying behavior seen from I-V characteristics. Even though the structure showed better charge carrier separation and transfer compared to TiO_2/*n*-Si, it was still insufficient as an ohmic contact if it were preferable in such heterojunction. The above discussed studies have one thing in common: no deep analysis on the energy band alignment throughout the system was done. Considering the implementation of Au*NP*, T. Marino *et al*. proposed the idea of using TiO_2/Au as a photoanode and CeO_2/Au as a photocathode and vice versa [15]. They analyzed how different configurations affected the photocatalytic efficiency. The study suggests that TiO_2/Au is more efficient for reduction reactions (hydrogen generation), whereas CeO_2/Au is more efficient for oxidation reactions (oxygen generation). This can be attributed to the difference in the band edges of CeO_2. In vacuum, *CBM* and *VBM* of CeO_2 are at a more negative potential than the reduction and oxidation potentials of water. It follows that the discussed material is more suitable for reduction reactions. However, in water, *CBM* and *VBM* change and are at a more positive potential with *VBM* having a higher oxidation potential than that of TiO_2 [225]. In this case, the *CBM* and *VBM* of TiO_2 do not change much when measured in vacuum and in water, which proves that it is more reliable and stable as a photocatalyst.

Taking in mind the *pn* junction of Si, and the charge carrier transition based on the internal electric field, a somewhat similar structure can be manufactured by combining a *p*-type semiconductor with TiO_2 (which is an *n*-type semiconductor). X. Deng *et al*. demonstrated that a combination of *p*-type NiO and *n*-type TiO_2 nanotube arrays (*NTa*) enhances the charge carrier separation based on the internal electric field [226]. This structure achieved a higher photocatalytic efficiency in degradation of 4-chlorophenol with a result of 50% degradation in ~60 min, whereas the same degradation was achieved in ~130 min by using only TiO_2 *NTa* as a photocatalyst. Similarly, I. Yoo *et al*. studied the structure of TiO_2 *NRa*/CdS/NiO_x, where an interlayer of CdS improved the holes transition from TiO_2 to *p*-type NiO_x and suppressed the charge carrier recombination [227]. According to these studies, the formation of *pn* junction does actually enhance the charge carrier separation, which

eliminates or lowers the rates of recombination and results in a higher photocatalytic efficiency.

Nevertheless, combining two semiconductors that work as a photocatalyst when employed separately might also be an option. The work by J. Jia et al. suggests the combination of WO_3 and TiO_2 as a photocatalyst which is photo-active under visible light irradiation [228]. The low energy bandgap of WO_3 (~ 2.65 eV) and wide energy bandgap of TiO_2 (~ 3.44 eV) enable the photogeneration of charge carriers under UV-vis light irradiation. The authors went one step further by adding a Pt *NP* as an interlayer between the TiO_2 and WO_3, resulting in even higher photocatalytic efficiency. T. Munawar *et al*. study extend the work done by J. Jia *et al*. by adding an extra layer of CeO_2 in the TiO_2/WO_3 combination [13]. According to the energy band engineering of such structure, the photogenerated holes would drift from WO_3 to either TiO_2 or CeO_2, whereas photogenerated electrons would drift to WO_3 from TiO_2 and CeO_2. This way enhances the photoconversion efficiency. However, as C. W. Lai *et al*. study shows, it is important to evaluate the possible passivation of WO_3 on TiO_2 surface which might negatively affect the photocatalytic efficiency [229]. Such a layer might do the opposite and increase the recombination rates of the photogenerated charge carriers.

In terms of considering even more complex combinations, known as monolithic structures, in their 2018 paper, W. Cheng *et al*. reported a hybrid (monolithic) photoelectrochemical device with an efficiency of 19% in a water splitting application [230]. The monolithic structure of Rh doped TiO_2/GaInP/GaInAs/GaAs/RuO_x with interlayers of $AlInPO_x$ and AlInP was presented as an efficient photocatalyst where TiO_2 works as a cathode for hydrogen reduction reactions, and RuO_x serves as an anode for water oxidation reactions. By carefully engineering the energy band alignment throughout the system, an internal electric field was created where electrons were driven to the surface of TiO_2, and holes were driven in the opposite direction (to RuO_x). Thus an efficient charge carrier separation was achieved with the result of efficient water splitting reactions. Another study by W. Cul *et al*. shows efficient oxidation properties of a NiFe-*MOF*/TiO_2 structure where TiO_2 nanorods (TiO_2 *NR*) were deposited on *FTO* and doped by NiFe on the walls of *NR* [231]. Such energy band engineering enables the electron transfer in the path NiFe-*MOF* →TiO_2 → *FTO*→ Pt when the NiFe-*MOF*/TiO_2 *HPE* and the Pt counter electrode are connected via an external power source. Meanwhile, the photogenerated holes would drift from TiO_2 to NiFe-*MOF*, which, based on the effect between the Ni and Fe active states, accelerates water oxidation.

Many different co-doped TiO_2 systems were already presented in the previous chapter. Whilst some of these suggest co-doping with another semiconductor, others promote co-doping with nanoparticles of precious metals, such as Au, Ag, or Pt [81, 119–121, 133]. There is one thing shared by most studies – a combined structure as one photocatalyst. In other words, a photocatalyst and a co-catalyst are in close proximity to one another considering the structure at the atomic level. Taking in mind the purification of wastewater, decomposition of organic compounds is a one-way reaction, thus water splitting is a two-way reaction. In other words, the photogenerated oxygen (O_2) and hydrogen (H_2) can recombine by emitting heat as a by-product:

$$2H_2O \xleftrightarrow{Photocatalysis/heat} 2H_2 + O_2 \quad 1.17$$

Therefore, during photocatalytic water-splitting reactions, it is important to ensure the separation of photogenerated O_2 and H_2. In reality, it is convenient to measure and capture photogenerated hydrogen when the experiment is done in laboratory conditions. However, the design should be applicable for commercial use (at a larger scale of photocatalyst utilization). Thus, a photocatalyst (photoanode) and a co-catalyst (photocathode or cathode) should be separated. At some point, this might seem like a debatable idea, and it brings a challenge for charge carrier separation and the transfer between the (photo)anode and (photo)cathode (if required), but this gives more room for the engineering of a more efficient photocatalyst system. In other words, the (photo)anode could be engineered in such a way that it would provide only an oxidation reaction by splitting charge carriers, with the holes drifting to the surface of the (photo)anode. Whereas, the (photo)cathode might get engineered in such a way that it provides only reduction reactions by splitting charge carriers with electrons drifting to the surface of the (photo)cathode.

Taking in mind a photocatalyst system that contains a (photo)anode and a (photo)cathode as separate (photo)electrodes, it is worth noting that they should be connected through the external grid, which might result in the loss of the current. Therefore, at some point, monolithic structures where the (photo)anode and the (photo)cathode are in contact might be an alternative to that. However, the issues of the commercial use of such complex structures, their stability, and the cost of producing larger-scale photocatalysts are still in question. Moreover, the use of Pt as a counter electrode or Pt as a dopant with the objective to enhance the photocatalytic efficiency does not solve the problem of the cost. Thus, search for a cost-effective Pt-free counter electrode is fundamentally important.

1.5. Literature Review Summary

Photocatalysis is a simple yet complex type of catalysis. The efficiency of photocatalysis depends on the four processes occurring in parallel to each other: photogeneration, recombination, trapping of the photogenerated charge carriers, and redox reactions at the interface of the photocatalyst and the gas or the aqueous solution. The first parameter which describes the efficiency of a photocatalyst is the energy bandgap. In other words, the value of the energy bandgap is equal to the photon energy which is required to excite electrons from *VBM* to *CBM* [5]. During the excitation, the photogenerated charge carriers might be caught by the defect state inside the energy bandgap. This way, according to the position of the defect site in the energy bandgap, it can act as a trapping center or a recombination center (trap-assisted recombination) [29, 30]. If taking the recombination process from the equation, redox reactions take place on the surface of the photocatalyst [52]. in this context, electrons (as donors) and holes (as acceptors) participate in the reduction and oxidation reactions, respectively [8]. Therefore, a photon-activated chemical reaction occurs in the system called photocatalysis. The latter can be used in various applications, but

the most important ones nowadays are the ones which participate in environmental remediation: water and air purification, solar-to-energy conversion, or anti-bacterial coatings. Even though the applications are different, the chemical process behind them is similar – photodegradation of organic or inorganic compounds [58]. However, considering the solar-to-energy conversion, there are some limitations and issues to deal with: energy loss, cost-efficiency, and scalability. Whereas for water and air purification, *UV* irradiation can be used (in terms of the technological capability), for solar-to-energy conversion, visible-light-driven photocatalysis would be preferable. Therefore, another issue arises – the efficient photocatalyst with an energy bandgap of ~1.8 to 3.1 eV which would manifest photoactivity under visible light irradiation [93, 94]. In addition, there are other requirements for an efficient photocatalyst: thermodynamical stability against photo-corrosion, redox potentials at the required energy level (based on the application), non-toxicity, and eco-friendliness [57, 58]. Thus, several semiconductors can be considered as photocatalysts: TiO_2, ZrO_2, WO_3, NbO_2, Nb_2O_5, SnO_2, In_2O_3, Ga_2O_3, GeO_2 [9, 10]. However, most of them are denoted by a high energy bandgap or low thermodynamical stability [97, 98]. Thus, it is suggested that the application of a combined semiconductor (a monolithic structure) would be a better approach for solar-to-energy conversion. A number of photocatalysts listed in this chapter, their modifications, and combinations (**Table 1.1**) involve a range of different approaches towards manufacturing an efficient stand-alone photocatalyst or their combined systems. To conclude the results presented in **Table 1.1**, it is difficult to compare the results as different light sources, sacrificial agents, and photocatalysts with counter electrodes were used. The most important part here is the sacrificial agent as it increases the hydrogen concentration in the aqueous solution, which directly results in higher hydrogen generation if it were compared to hydrogen generation from water. Even though it is a sensible approach to manufacture an efficient and sustainable photocatalyst, thus, the best comparison between the introduced photocatalysts would be done by analyzing the efficiency under the same conditions. On the other hand, it was observed that one of the presently mentioned semiconductors stands out in many cases. Specifically, TiO_2 is used either as the main photocatalyst for oxidation or reduction reactions [15], or as a protective layer for other photocatalysts [19]. In terms of a short review of TiO_2 properties, it stands out as being thermodynamically stable against the photo-corrosion of both electrons and holes, and its redox potentials are at the preferable energy values: the reduction potential is more negative than that of H^+/H_2, and its oxidation potential is more positive than that of H_2O/O_2 [20]. Granted that, the search for cost-efficient photocatalysts is still ongoing, and the field is open for a discussion.

Therefore, in accordance with the previously outlined challenges of TiO_2 application for photocatalysis, such as the wide energy bandgap followed by photosensitivity only under *UV* irradiation and fast charge carrier recombination, this research focuses on various approaches towards enhancing the photocatalytic efficiency, and thus it overcomes the presently mentioned limitations. In this case, anatase phase TiO_2 was chosen as an efficient photocatalyst over the rutile phase TiO_2. This was proven by numerous research based on the energy band structure of rutile and anatase phase TiO_2 [95, 177, 204, 232]. Therefore, modifications of TiO_2 thin

films by doping it in bulk or on the surface which are intended either to reduce the recombination rates, or to increase the hot electron concentration, were carried out. Moreover, a different approach was done by combining two semiconductors (TiO_2 and Si) to enhance the photosensitivity under visible light irradiation and to reduce recombination rates. Such a combination was done by manufacturing a hybrid photoelectrode which, based on the internal electric field, should decrease the recombination rates at the TiO_2 layer, and enhance the photosensitivity under visible light irradiation.

2. Experimental Technique and Methodology

Even though TiO_2 thin films can be deposited by various types of techniques (as mentioned above in Section 1.4), only two of them – *RMS* and sol-gel spin-coating techniques – were chosen for this research. The latter two are different deposition techniques which enable comparative analysis of the properties of the deposited TiO_2 thin films. Furthermore, the *RMS* technique allows the deposition of amorphous or crystalline phase TiO_2 thin films on heat-sensitive or patterned substrates. Moreover, it enables an easy control of the process parameters, which results in the desirable dopant concentration or the desirable thin film thickness compared to the chemical deposition techniques. Whilst *RMS* stands out as a viable deposition technique, sol-gel spin-coating enables the deposition of highly porous TiO_2 thin films compared to *RMS*. Thus, a comparison of the two deposition techniques and the outcomes of the TiO_2 properties has been made together with the photocatalytic efficiency evaluation. Considering the properties of TiO_2 thin films, such analytical methods as *XRD*, *FE-SEM*, *XPS* and some others were used for the morphological, energy band and crystalline structure analysis, etc. Despite all that, the translation of *XPS* data proved as a viable technique for the energy band evaluation and the energy band alignment between the two semiconductors.

2.1. Reactive Magnetron Sputtering

TiO_2 thin films

The reactive magnetron sputtering technique is a viable method for depositing thin films on any substrate or surface. Additionally, this method allows the deposition on the patterned surface without damaging the pattern. In this study, Kurt J. Lesker *PVD*-75 system (**Fig. 2.1**) was used for the deposition of TiO_2 thin films. The vacuum system contains a 2-stage rotary vane fore-vacuum pump and a turbomolecular pump allowing to achieve the initial pressure of up to 10^{-5} Pa. Inside the chamber, four separate magnetrons are positioned, thus enabling parallel deposition of different materials. A substrate holder is fixated above the magnetrons, thereby enabling the sputtering-up deposition. Moreover, the ability to rotate the substrate holder allows the deposition of evenly distributed thin films. Nevertheless, the heating elements (which are above the substrate holder) allow the deposition at temperatures up to 300 °C.

Table 2.1. Specification sheet of *PVD*-75 system [233]

Vacuum system	2-stage: rotary pump and turbomolecular pump
Initial pressure	Up to 10^{-5} Pa
Deposition system	4 magnetrons controlled by the shutter
Power source	*DC* and *RF*
Gas flow	2 channels
Substrate fixation	Platen with a size up to 305 mm
Rotation speed	Up to 20 rpm
Heating	Up to 300 °C

Fig. 2.1. Physical vapor deposition system *Kurt J. Lesker PVD-75*

The deposition parameters are given in **Table 2.2**. During plasma activation and thin films deposition, argon (Ar) and oxygen (O_2) gases (99.999% purity) were used. TiO_2 thin films were deposited by using two titanium targets (99.995% purity) with a diameter of 50.8 mm and thickness of 6.35 mm. The vacuum chamber was filled with the Ar and O_2 gases with a ratio of 8/2, accordingly, reaching $6.6 \cdot 10^{-1}$ Pa. Additionally, the substrates were rotated at 8 *RPM* speed to achieve better uniformity of the deposited thin films. The deposition was done without additional heating, thus the deposited TiO_2 thin films were amorphous. The thickness of the deposited TiO_2 thin films was ~200 nm. To obtain a crystalline structure, either anatase or rutile, the samples were annealed under atmospheric pressure at high temperatures (500–900

°C). The annealing process consisted of three steps[3]: temperature increase (4 °C/min), soaking (10 h), and cooling (2.5 °C).

Table 2.2. Deposition parameters of TiO_2 thin films[4]

Vacuum system	2-stage: rotary pump and the turbomolecular pump
Initial pressure	Up to 10^{-3} Pa
Working pressure	$6.6 \cdot 10^{-1}$ Pa
Deposition system	2 magnetrons with titanium targets
Power source	*DC* (250 W)
Gas flow	2 channels (Ar and O_2 at ratio of 8:2)
Substrate fixation	Platen with a size up to 305 mm
Rotation speed	8 *RPM*
Heating	Without additional heating
Substrate[5]	Glass, quartz glass, alloy (304L), n-Si (100)

Metallic nanoparticles

The formation of Au*NP* on the surface of TiO_2 thin films was carried out in a similar way (**Fig. 2.2**). At first, a high vacuum of $4 \cdot 10^{-3}$ Pa was reached, and the chamber was filled with high purity (99.999%) Ar gas, which yielded $2 \cdot 10^{-1}$ Pa pressure. Au thin films were deposited on the surface of TiO_2 thin films by using a high purity (99.995%) Au cathode with a diameter of 50.8 mm. A growth rate of 9.66 nm/min was achieved during Au deposition by using a *DC* power supply at 50 W sputtering power. Thin films of 5; 7.5 and 10 nm thicknesses were formed on the surface of TiO_2. The solid-state dewetting (*SSD*) process was used for the formation of Au *NP* on the surface of the TiO_2 thin films. Therefore, the TiO_2/Au samples were annealed at 500 °C temperature in vacuum. The *SSD* of Au was done on as-deposited TiO_2 annealed at 500 °C and 900 °C temperature to analyze the *NP* formation based on the TiO_2 surface morphology and crystallinity.

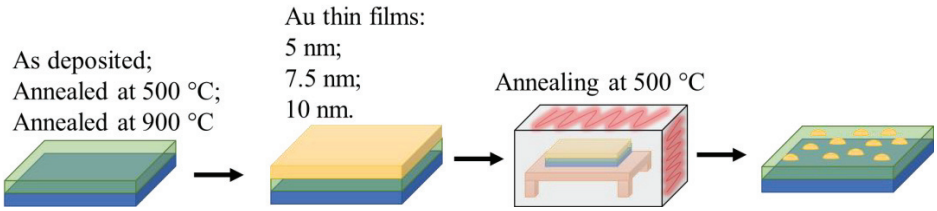

Fig. 2.2. Formation of Au*NP* on TiO_2 thin film surface by *SSD* method

[3] The annealing process was the same for all the TiO_2 thin films deposited by *RMS*, unless specified otherwise in the discussion about the specific results.
[4] The deposition parameters were the same for all the depositions done by *RMS* unless indicated otherwise in the discussion about the specific results.
[5] The substrate material used for the deposition of TiO_2 thin films differs based on the further analysis.

2.2. Thermal Evaporation System

A thermal evaporation system (**Fig. 2.3**) was used for coplanar gold electrode and aluminum electrode deposition on the samples. The required masks (**Fig. 2.20**) were set on the sample holder and the sample on top of it. A tungsten tub was used for the evaporation of a gold wire (~1.5 cm length gold wire for 70–80 nm thickness of a gold coplanar electrode). At first, the chamber was pumped up to 5–10 Pa by using a rotary pump, and, afterwards, by using a diffusion pump, the vacuum level of 10^{-3} Pa was reached. After that, by using a power supply, the current which flows through the tungsten tub was increased to 50–55 A (with a step of 0.1 A/s) to evaporate the gold wire. The same process was used for the deposition of Al electrodes on the back of the samples.

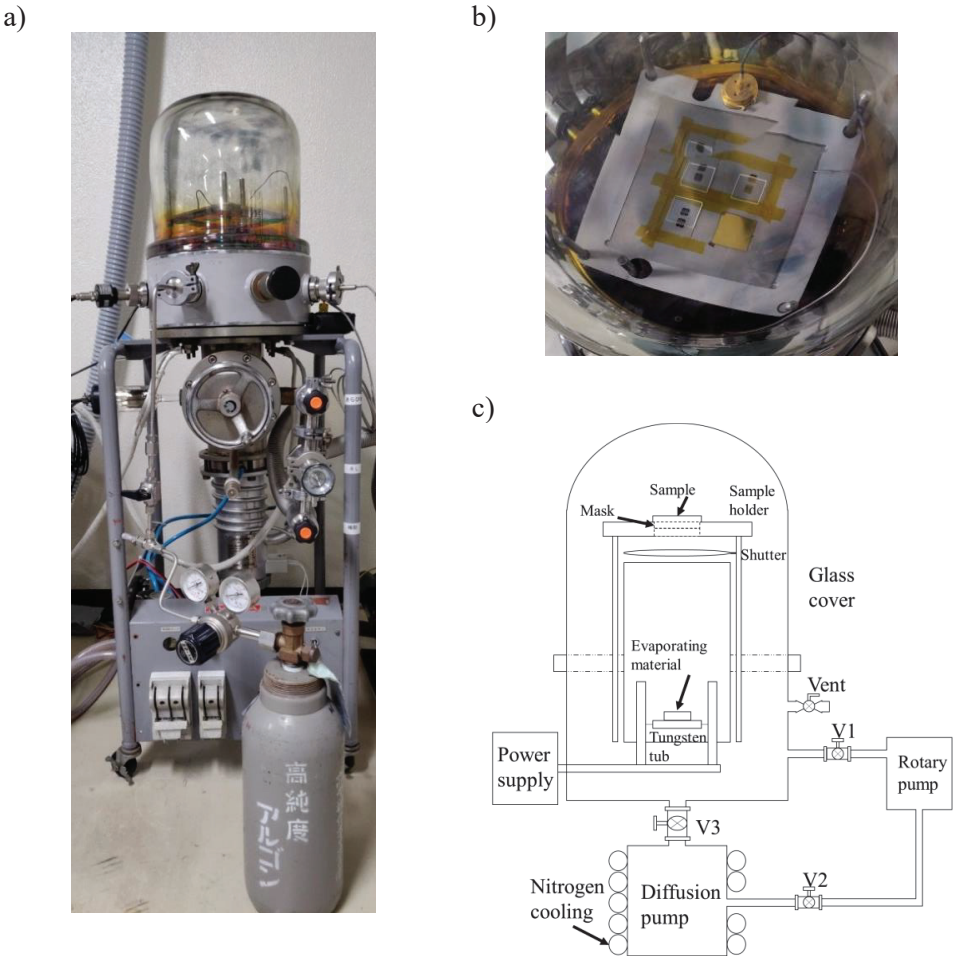

Fig. 2.3. Thermal evaporation system (a), sample holder with masks inside the chamber (b) and system schematics (c) where *V1* – a valve between the chamber and the rotary pump, *V2* – a valve between the rotary pump and the diffusion pump, *V3* – a valve between the diffusion pump and the chamber

2.3. Sol-gel Spin-coating

Sol-gel spin-coating enables the deposition of porous TiO_2 thin films from the solution. For this study, a photocatalytic hydrosol *STS-21* was bought from *Ishihara Sangyo Co*., Ltd. and spin-coated on Si substrates. According to the specification sheet (see data in **Table 2.3**), the photocatalytic hydrosol *STS-21* contains a TiO_2 anatase phase with a particle size of 20 nm and 40 wt.% concentration in the solution (pH 8.5).

Table 2.3. Commercially available photocatalytic hydrosols from STS series [234]

Hydrosol grade	TiO_2 concentration, wt.%	Particle size, nm	pH
STS-01	30	7	1.5
STS-02	30	7	1.5
STS-21	**40**	**20**	**8.5**

TiO_2 thin films were deposited on the Si substrate by the following parameters to achieve a thickness of around 650 to 750 nm: 2000 rotations per minute (rpm) speed, with a 10 s slope and the total spinning time of 60 s. After the deposition, the samples were moved to a furnace where the baking process at 150 °C for 30 min was set to minimize the stress induced by the further annealing process which was done under 600 °C for 60 min (**Fig. 2.4. (b)**). The difference in thickness is caused by the spin-coating deposition kinetics, which resulted in a slightly uneven distribution of the sol-gel on the surface of the Si substrate (the sides of the substrate were slightly thicker than the centre). However, this does not affect the final structure, as only the center part of the deposited TiO_2 was used as the active area.

a) b)

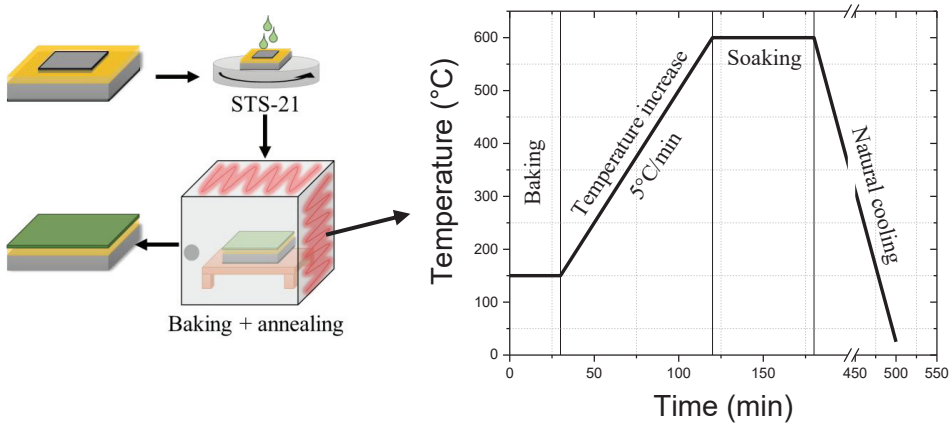

Fig. 2.4. TiO_2 deposition by spin-coating technique from STS-21 photocatalytic hydrosol: a) TiO_2 thin films deposition procedure, b) annealing program

2.4. Si Photocell Manufacturing Description

The manufacturing of the Si photocell, which shall be used as a substrate for TiO_2 deposition and metal cluster deposition, was carefully done by adhering to the following procedure:

1. At first, in order to maintain clean preparation of the Si photocells, *n*-type Si substrates (N_D = $10^{17\text{-}18}$ cm^{-3}) were cleaned by immersing them in an acidic solution (*Piranha* – H_2SO_4:H_2O_2, ratio 4 to 1, respectively). The native oxide layer which forms on the surface of Si under atmospheric pressure was removed by using buffered hydrofluoric acid (*BHF*).

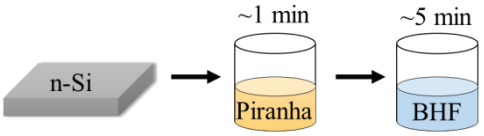

Fig. 2.5. Cleaning and oxide etching procedure of Si substrate

2. After that, in order to minimize the manufacturing errors which may have been caused by the boron and phosphorous diffusion process, the surface area around the active center must be covered in SiO_2. Therefore, a controlled wet oxidation process was performed for cleaned Si substrates. The samples were annealed at 1000 °C for 90 min, which resulted in ~500 nm SiO_2 layer on the surface.

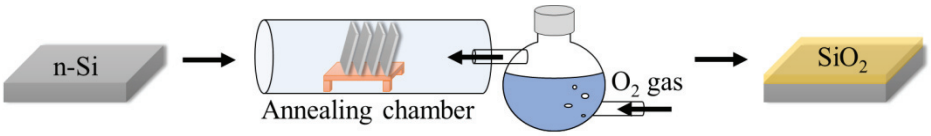

Fig. 2.6. Wet oxidation process to form a SiO_2 layer on Si substrate

3. In order to keep SiO_2 around the active centre, the lithography process by using a *DWL2000 – OAF* lithography system (*Heidelberg Instruments*, Germany) was performed. At first, hexamethyldisilane (*HMDS*) was spin-coated on the samples to increase the adhesion for the deposition of the photoresist (*OFPR*). The hardening of *OFPR* was done by baking the samples at 110 °C for 90 s. Then, the lithography procedure was operated by using a prepared mask (10 x 10 mm square). The development of the photoresist was done by immersing the samples into the *NMD* solution and distilled water for 1 min each (*NMD* for 1 minute → H_2O for 1 minute → H_2O for 1 minute). To finish the procedure, the samples were baked at 135 °C for 5 minutes.

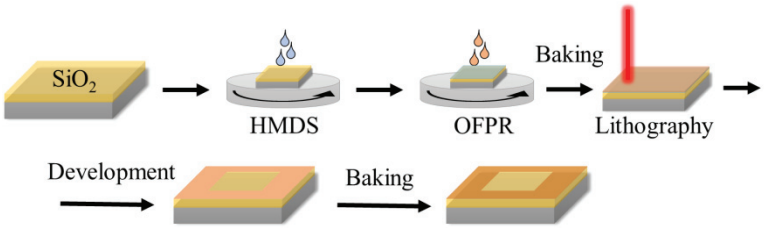

Fig. 2.7. Photoresist coating and lithography process on Si substrate

4. As a result of the lithography process, the area around the active center was covered in photoresist which acts as a shield during oxide etching. Therefore, the prepared samples were immersed in BHF for approximately 7 minutes to etch SiO_2 from the surface (SiO_2 etch rate ~700 Å/min). After that, *piranha* cleaning was done to remove the photoresist.

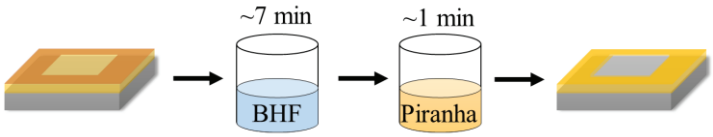

Fig. 2.8. Oxide etching and cleaning procedure after lithography process

5. Boron diffusion was done to form a *p*-type Si layer on the surface of the *n*-type Si substrate. To do this, a poly-boron film (*PBF*) was deposited on the surface by the spin-coating technique, and it was set into the annealing chamber where the baking process had been done beforehand at 600 °C for 30 minutes, and annealing was performed at 1000 °C for 60 minutes to achieve the dopant density of $N_A = 10^{20\text{-}21}$ cm^{-3}. The thickness of the doped p^+-Si layer was approximately 110 nm.

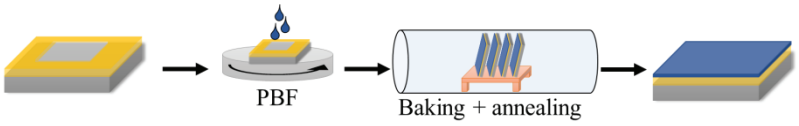

Fig. 2.9. Boron diffusion process

6. After boron diffusion, a lithography process (similar to the one described in step 3) and a cleaning/oxide etching process (similar to the one defined in step 4) were done.

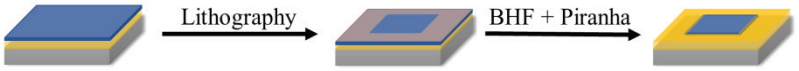

Fig. 2.10. Lithography process and cleaning/oxide etching procedure

7. Phosphorous diffusion was done to form a highly doped *n*-type Si layer on the top of the previously formed *p*-type Si and on the back of an *n*-type Si substrate. To perform this, *OCD* was spin-coated on the surface and on the back, while baking the samples at 150 °C for 3 min in between. Then, samples were transferred to the annealing chamber and baked at 600 °C for 30 min, followed by annealing at 900 °C for 10 min. The achieved dopant density in this step was $N_D = 10^{20\text{-}21}$ cm^{-3} with an *n*-type Si layer thickness of approximately 50 nm.

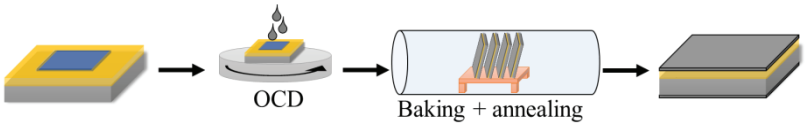

Fig. 2.11. Phosphorous diffusion process

8. The lithography and cleaning processes were done similarly to the strategy described in step 3 and step 4.

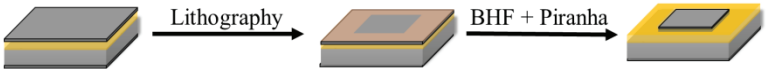

Fig. 2.12. Lithography process and cleaning/oxide etching procedure

The manufacturing of the Si photocell for a Pt-free photoelectrode was done similarly, but, instead of using n$^+$-Si as a substrate, p$^+$-Si with a dopant density of $N_A = 10^{17\text{-}18}$ cm^{-3} was chosen for the production. Phosphorous diffusion (similar to the one described in step 7) was done on the surface, and boron diffusion (similar to the one defined in step 5) was done on the back of the substrate. The final structure of the Si photocell for the photoanode and the Si photocell for the photocathode is shown in **Fig. 2.13**.

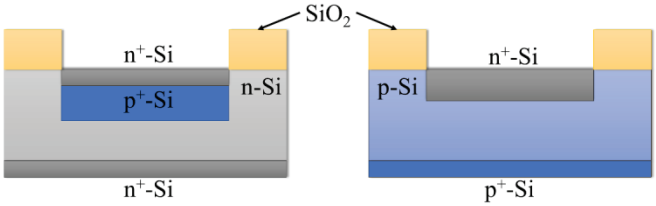

Fig. 2.13. Graphical representation of Si photocell cross-section for photoanode (left) and photocathode (right). *n*-Si – $N_D = 10^{17\text{-}18}$ cm^{-3}, n$^+$-Si – $N_D = 10^{20\text{-}21}$ cm^{-3}, *p*-Si – $N_A = 10^{17\text{-}18}$ cm^{-3}, p$^+$-Si – $N_A = 10^{20\text{-}21}$ cm^{-3}

In order to analyze the I-V characteristics of the prepared Si photocell under light irradiation, a different mask was used during the lithography process.

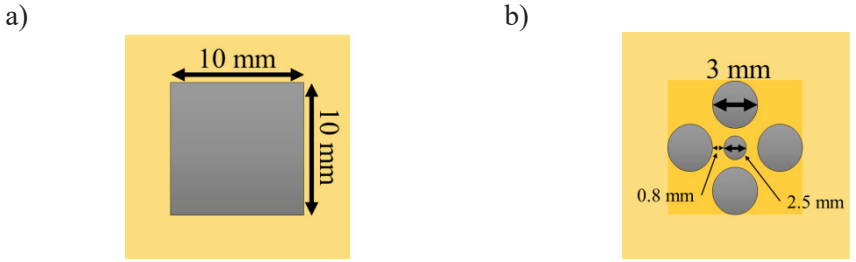

Fig. 2.14. Masks used during lithography process: a) for TiO_2 *HPE* system, b) for Si photocell analysis

2.5. Field Emission Scanning Electron Microscopy (*FE-SEM*)

The surface morphology and the cross-section of TiO_2 thin films were analyzed with a field emission electron microscope (*FE-SEM*, *JEOL*, Model: *JSM-7600F*) shown in **Fig. 2.15**. *FE-SEM* enables the analysis of the surface area and the cross-section of TiO_2 thin films at a resolution up to 1 nm and magnification up to 10^6 times (thus yielding an image size of 120 x 90 mm). *FE-SEM* is widely used in a range of scientific studies aiming to investigate and analyze nanoscale objects. Compared to the conventional *SEM*, *FE-SEM* enables to capture less electrostatically distorted, higher-quality images. A remarkable difference between *FE-SEM* and *SEM* is the electron generation system. *FE-SEM* uses a field emission gun which provides highly focused electron beams at a wide energy range and enables the analysis to be carried out at low potentials. Thus, the minimizing of the charging effect on dielectric materials is achieved; this also reduces the damage to the surface of a sensitive sample.

SEI resolution	1 nm (15 kV) 1.5 nm (1 kV)
Magnification	25 up to 10^6
Accelerating voltage	0.1 to 30 kV
Probe current	1 pA to 200 nA
Digital image size	1280x960 2560x1920 5120x3840

Fig. 2.15. *FE-SEM* JSM-7600F system [235]

The surface area was scanned at an acceleration voltage of 5 kV and magnification of 10 to $20 \cdot 10^3$. The images captured by using *FE-SEM* were analyzed with the *ImageJ* program to investigate the porosity, thickness, and the surface area. The porosity evaluation by the *ImageJ* program is preliminary as only the surface area is analyzed. The analysis is done by applying the thresholding procedure for *FE-SEM* images and carefully assigning the areas of pores and grains. The thickness was analyzed from the cross-sectional images based on the *FE-SEM* scanning parameters.

2.6. Atomic Force Microscopy (*AFM*)

Atomic force microscopy (Multifunction Probe Station *AFM5000 II* (*Hitachi High-Tech Co.*) and *AFM NanoWizard® 3* (*JPK Instruments*) were used for the analysis of the TiO_2 surface. This equipment was used for various types of analysis: Au clusters formation on the TiO_2 surface and TiO_2 deposited on the patterned surface. In general, *AFM* consists of three interconnected components: scanning equipment (1), a controller (2), and the operating system (3) (**Fig. 2.16**). In principle, the *AFM* operation is based on the tip-sample interaction force. The cantilever bends according to the surface area of the sample, and the bending is detected by using a laser diode and a photodetector. Primarily, there are two groups of operating modes: the contact and the dynamic (tapping) mode. In the contact mode, a tip is pressed onto the surface, therefore sweeping along the surface. On the other hand, in the dynamic mode, a cantilever vibrates, therefore tapping the surface as it moves along the line. Generally, the mode selection depends on the mechanical properties of the analyte: for hard solids, the contact mode is typically the optimal choice, however, for soft solids or organic compounds, the dynamic mode may be a better alternative. The following parameters were measured: surface roughness (R_q), average roughness (R_a) maximum height of peaks (h_{max}), average height (h_{mean}), skewness (R_{sk} shows whether the material is porous ($R_{sk} < 0$) or grainy ($R_{sk} > 0$). In addition, the nominal area, the full area, and the ratio nominal/full were calculated for patterned structures.

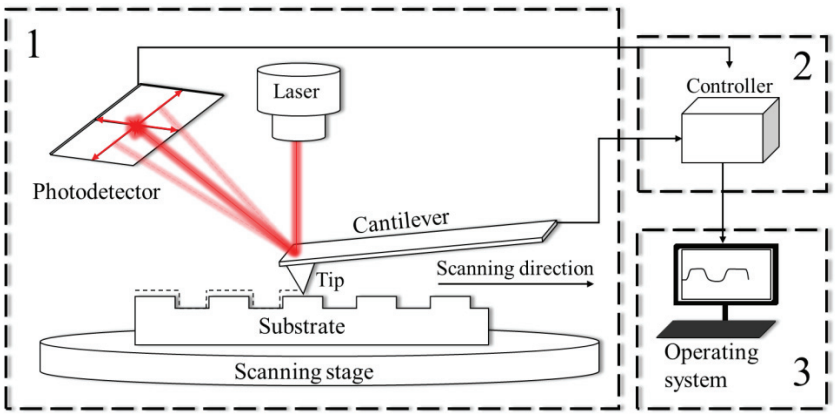

Fig. 2.16. Principal scheme of atomic force microscope. 1 – scanning equipment, 2 – control unit, 3 – computer with operating software

2.7. X-ray Diffraction (*XRD*)

X-ray diffractometry (*XRD*, *Rigaku RINT Ultima-III XR*) was used for the analysis of TiO_2 crystallography (**Fig. 2.17**). This equipment enables us to investigate the crystallite size and the degree of crystallization, density, roughness, structure refinement, multilayer thicknesses, depth-controlled or normal geometry phase identification, and to perform quantitative analysis. Along with the standard Bragg geometries, the *XRD* system enables us to do thin film analysis as well as grazing incidence diffraction or pole figure analysis, Rietveld analysis, the determination of

residual tensions, reflective and transmissive small-angle X-ray scattering, and reciprocal space mapping. The maximum rated output for this X-ray generator is 3 kW with a rated tube voltage and current from 20 to 60 kV and from 2 to 60 mA, accordingly. The goniometer radius is 285 mm, which allows measuring 2θ within a range of -3° to 162° with a minimum step size of 0.0001°. Scanning can be done by coupling θ_s and θ_d, or by switching to independent θ_s, θ_d scanning [236, 237].

Fig. 2.17. X-ray diffraction (*XRD, Rigaku RINT Ultima-III XR*)

The TiO_2 thin film analysis was done at 2θ angle within the range of 20° to 60° by using Cu Kα radiation of 1.541836 Å, at 2°/min speed and a 0.02° step. The selected scan range is optimal for the analysis of the TiO_2 crystal structure as it shows the main peaks for the TiO_2 anatase phase. The gathered data was analyzed by using the *Match!3* crystallographic analysis software using the *COD20210614* database. The crystallite size was evaluated from Scherrer's equation [238–240]:

$$D = \frac{K\lambda}{\beta \cos\theta}; \qquad 2.1$$

Here, D is the crystallite size, K is Scherrer constant, λ is the wavelength of the X-ray beam, β is the full width at half maximum (*FWHM)*, and θ is the Bragg's scattering angle.

2.8. X-ray Photoelectron Spectroscopy (*XPS*)

The electronic structure of the deposited TiO_2 thin films was analyzed by X-ray photoelectron spectroscopy (*XPS*, *Shimadzu*, *ESCA-3400*). The XPS spectra give valuable information about the chemical and electronic structure of TiO_2 thin films. The gathered data was fitted and analyzed via *MultiPak* data reduction software for

XPS. The spectra were calibrated according to the standard value of carbon C 1s peak (according to ASTM and ISO Standards [241, 242], which is at 284.8 eV). Ion sputtering was used in the case of the Si substrate analysis to decrease the amount of the native SiO_2 on the surface which forms in a matter of minutes after the cleaning procedure and could potentially affect the results. The valence band maximum (*VBM*) and the concentration of oxygen vacancies (O_V) were evaluated by translating the *XPS* data. The valence band offset (*VBO*), the conduction band minimum (*CBM*), and the conduction band offset (*CBO*) were calculated by using the following equations [108, 243, 244]:

$$VBO_{A/B} = \left(E_{CL\,(A)} - E_{CL\,(B)}\right)_{A/B} - [(E_{CL} - E_{VBM})_A - (E_{CL} - E_{VBM})_B]; \qquad 2.2$$

Here, *A* and *B* stand for two semiconductors whose heterojunction is being analyzed, E_{CL} is the binding energy of the core-level peak of material *A* or *B*. Therefore, *CBO* between materials *A* and *B* can be determined as follows:

$$CBO_{A/B} = E_{g(A)} - VBO_{A/B} - E_{g(B)}; \qquad 2.3$$

Here, E_g is the energy bandgap of *A* or *B* material.

These calculations enable us to investigate the conduction band discontinuity between the two semiconductors at their heterojunction.

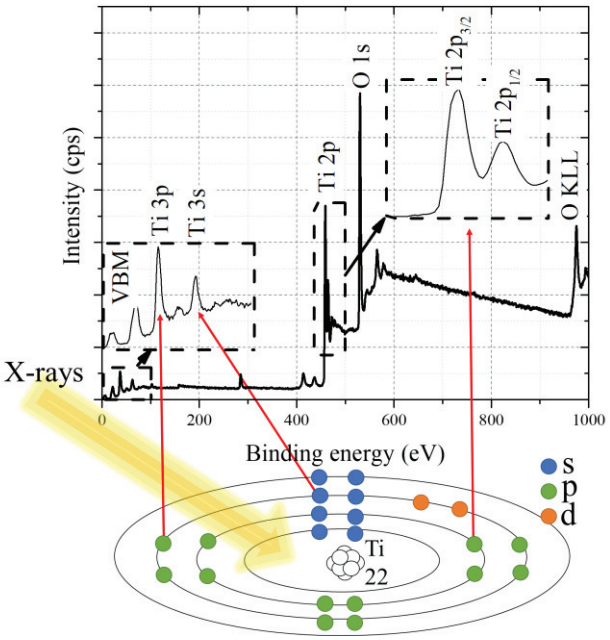

Fig. 2.18. Principal scheme of *XPS* measurement and *XPS* spectra of TiO_2 anatase phase with *VBM* and main TiO_2 peaks (Ti 2p)

Fig. 2.18 shows the core level peaks of TiO_2: Ti $2p_{3/2}$ at 458.9 eV (ref. 458.59 eV) and Ti $2p_{1/2}$ at 464.6 eV (ref. 464.31 eV) [245], together with O 1s at 530 eV.

VBM was measured at a high resolution (0.01 eV) for more accurate evaluation and further calculation of *VBO* and *CBO*.

2.9. *UV-VIS* Spectroscopy

The *UV*-vis spectrophotometer *JASCO V-630* was used for the measurement of the optical properties of TiO_2 thin films. The main hardware specifications are listed in **Table 2.4**:

Table 2.4. Technical sheet of spectrophotometer *JASCO V-630* [246]

Light source	Deuterium lamp: 190–350 nm Halogen lamp: 330–1100 nm
Detector	Silicon photodiode (S1337)
Wavelength range	190–1100 nm
Wavelength accuracy	±0.2 nm
Wavelength repeatability	±0.1 nm
Scanning speed	10–8000 nm/min
Spectral bandwidth	1.5 nm (fixed)

The optical system of the spectrophotometer *JASCO V-63* is shown in **Fig. 2.19**. The light source, which consists of two lamps (a deuterium lamp (190–350 nm) and a halogen lamp (330–1100 nm)), is directed into the diffraction grating (monochromator). The diffraction grating disperses light into its component wavelengths. By controlling the angle between the light source and the monochromator, different parts of the light spectrum are then directed through the exit slit to the rotating disc. Here, the light splits into two beams: one flows through the sample (the sample beam), and the second one flows through the reference sample (the reference beam). With a help of mirrors, those beams are again directed to the rotating disc and to the detector where the intensity of the reference beam is considered as 100%, and the intensity of the sample beam is equated to the reference beam. For the final part, the gathered data is processed by specialized software in a computer (*PC*).

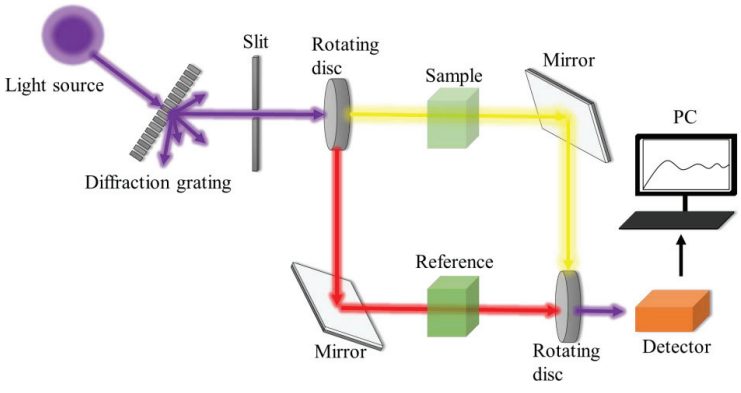

Fig. 2.19. Schematic representation of spectrophotometer *JASCO V-630*

The optical transmission was measured for TiO_2 deposited on a glass or quartz glass substrate at wavelengths between 300 and 800 nm. Such a range was chosen according to the possible application of TiO_2 thin films: the photogeneration of hydrogen under UV-Vis light irradiation. Thus, measurements below 300 or above 800 nm wavelength do not give valuable information. According to the gathered data, the thickness of thin films (d) can be calculated by the following equation [247, 248]:

$$\mathrm{d} = \frac{\lambda_1 \lambda_2}{2(\lambda_1 n_2 - \lambda_2 n_1)}; \quad 2.4$$

Here, $\lambda_{1,2}$ is the wavelength at the first and second maxima, and $n_{1,2}$ is the refractive index which is calculated by the following equation:

$$n = \sqrt{N + \sqrt{N^2 - {n_s}^2}}; \quad 2.5$$

Here, n_s is the refractive index of the substrate, and N is the complex refractive index which can be determined as follows:

$$N = 2n_s \left(\frac{T_M - T_m}{T_M T_m}\right) + \frac{n_s^2 + 1}{2}; \quad 2.6$$

Here, T_M and T_m are the upper and lower tangent envelopes of the transmission spectra.

The optical bandgap (E_g) evaluation was done by using the Tauc relation [249, 250]:

$$\alpha \mathrm{h}\nu^{\frac{1}{\mathrm{n}}} = \beta(\mathrm{h}\nu - \mathrm{E_g}); \quad 2.7$$

Here, α is the absorption coefficient, $h\nu$ is the photon energy, n is a power factor of the transition mode which depends on the nature of the material, which, for the TiO_2 anatase phase, is 2[6], β is the band tailing parameter, E_g is the optical energy bandgap.

Therefore, from the plot of $(\alpha h\nu)^{(1/n)}$ versus $(h\nu)$, the E_g can be evaluated by extrapolating the straight line in a specific region, which intercepts the $h\nu$-axis and gives the value of E_g. Moreover, by assuming that the refractive index of non-porous anatase phase TiO_2 is $n_d = 2.52$ [251], the porosity of the deposited TiO_2 thin films can be calculated with the following equation:

$$P = \left(1 - \frac{n^2 - 1}{n_d^2 - 1}\right) \cdot 100(\%); \quad 2.8$$

2.10. Dark Current Measurements

A position of the Fermi energy level in a semiconductor can be found by experimental measurements of the dark current dependence on the reciprocal

[6] For direct bandgap – 1/2; indirect – 2; direct with the forbidden transition – 3/2, indirect – 3

temperature. This way, the activation energy (E_A) which, in general, is the distance between the Fermi energy level and *CBM* can be calculated by the Arrhenius equation [238, 252]:

$$\Delta E = \frac{k}{q}\left(\frac{T_1 T_2}{T_1 - T_2}\right) \ln\left(\frac{I_1}{I_2}\right), \qquad 2.9$$

Here, ΔE is the difference between E_F and *CBM* (activation energy E_A), T_1 and T_2 are the temperatures at which current I_1 and I_2 were measured, k is the Boltzmann constant ($1.38 \cdot 10^{-23}$ m^2 kg/s^{-2}K^{-1}), and q is the electron charge ($1.60 \cdot 10^{-19}$ C).

In order to calculate the activation energy (E_A), the dark current dependence on the temperature was measured. Therefore, the coplanar gold (Au) electrode was deposited on the surface of TiO_2 thin film by using a thermal evaporation system and a mask (**Fig. 2.20**). The unique structure of the coplanar electrode results in a higher surface area for the electron flow. Then, the coplanar electrode was connected to the external power source to measure the current flow. The sample was set on a heater in the chamber (similarly to that shown in **Fig. 2.21**) filled with nitrogen gas, and the temperature was increased slowly by using a temperature controller. I-V characteristics were measured by using a *Keithley* picoammeter/voltage source. From the data in the current dependence on the reciprocal temperature plot, E_A can be calculated by using Eq. 2.9.

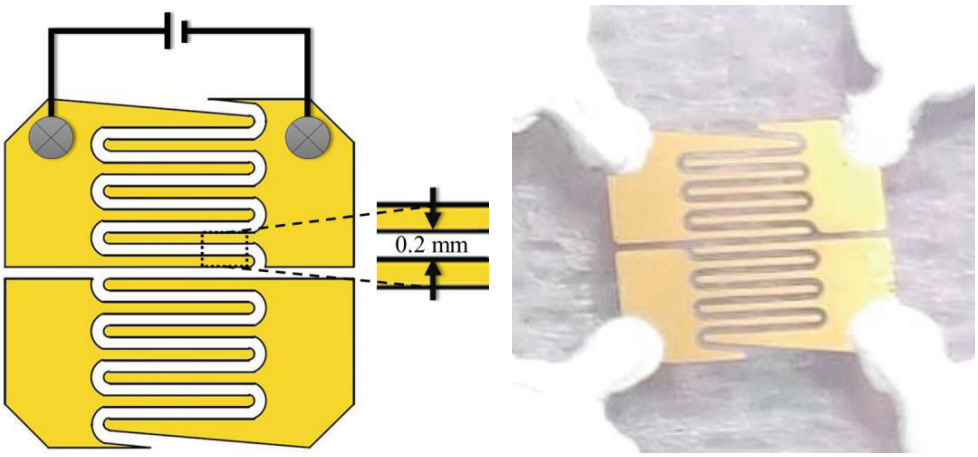

Fig. 2.20. Graphical illustration of coplanar electrode (left) and deposited coplanar electrode (right) and its connection to an external power source via silver paste. Electrode length is 18.5 mm; gap between the electrodes is 0.2 mm

2.11. I-V Characteristics of Si Photocells

I-V characteristics of the prepared multi-layered Si substrate were measured in a controlled environment by using the measurement setup shown in **Fig. 2.21**. For the sake of comparison, a commercially available photodiode Si *PIN S6775* (manufactured by *Hamamatsu Photonics K. K.*) was employed under the same conditions. I-V measurements were performed under two conditions: dark and under

UV irradiation (Mercury lamp, *Toshiba Light-Tech. Co. Ltd.*, Toscure). The *UV* light intensity was controlled by using *UV* light filters and measured with a *UV* power meter (*LT Ilutron YK-35UV*). Continuous irradiation with *UV* light slightly increases the temperature; therefore, a sample was set on the cooler which was connected to a temperature controller (*TC*) and a water supply system (*CS*) to maintain room temperature (25 °C). For this particular measurement, a multi-layered Si substrate was prepared by using a different mask during the lithography process (**Fig. 2.14 (b)**). The measurements under two different conditions (dark and light) are important as measurements in the dark give information about shunt resistance (R_{Sh}), series resistance (R_S), and diode saturation current (I_S). Meanwhile, under light irradiation, such parameters as open-circuit voltage (V_{OC}) and short-circuit current (I_{SC}) can be measured (**Fig. 2.21 (b)**). Moreover, it is hard to control the concentration of the photogenerated charge carriers, and any fluctuation in light may give noise in the photogenerated current, which is crucial in the microampere and nano ampere range.

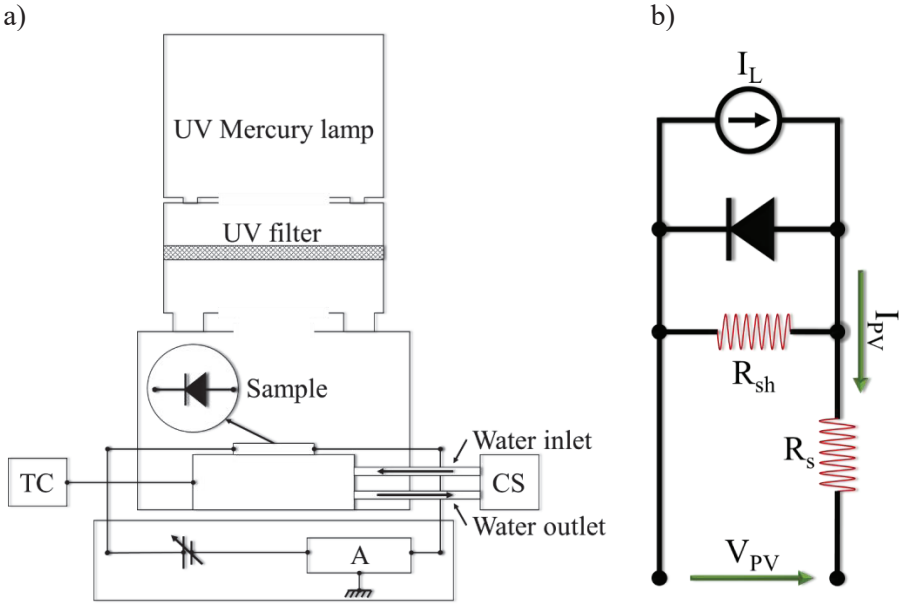

Fig. 2.21. Schematics of I-V measurement equipment (a), circuit diagram (b). *TC* – temperature controller, *CS* – cooling system, A – ammeter (*Keithley* Picoammeter/Voltage source 6487)

2.12. I-V Characteristics of TiO_2/Si Heterojunction

To ensure the accuracy for further measurements of the prepared TiO_2/Si heterojunction and TiO_2/Si *HPE*, two key points must be ensured:

- The metal electrode which is being deposited on the back of the Si substrate must show ohmic contact at the junction, thus minimally contributing to the series resistance (R_s) of TiO_2 *HPE*. To this matter, an Al electrode was deposited on the back as it shows the ohmic behavior at the junction with *n*-type Si (**Fig. 2.22 (a)**) [253].

- The junction of the metal electrode, which is being deposited on the TiO_2 surface, and TiO_2 should affect R_s as minimally as possible. To this matter, either of two metals can be used: Au or Al, featuring approximately $R_{s(Au)}$ = 1.2 kΩ and $R_{s(Al)}$ = 0.9 kΩ, accordingly [254]. Therefore, an Au electrode was deposited on the surface of a TiO_2 thin film as it shows the ohmic behavior (**Fig. 2.22 (b)**).

Contacts exhibiting the rectifying behavior can negatively affect I-V measurements and result in false statements as the current flow would be limited by the Schottky barrier, quantum tunnelling, or current leakage.

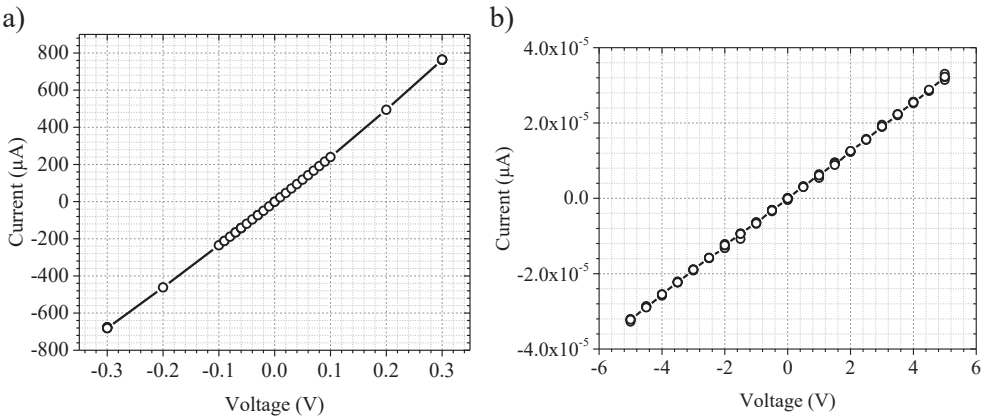

Fig. 2.22. I-V characteristics of contact between a) TiO_2 and Au electrode and b) *n*-type Si and Al electrode

The conduction bands between the two semiconductors – TiO_2 and *n*-Si – must be aligned in order to have minimal contribution to R_s. However, it is difficult to measure the resistance at the heterojunction interface. Therefore, the heterojunction was modified by doping the *n*-type Si surface with phosphorus (thus increasing the free charge carrier concentration). Moreover, regarding the ability of Si to oxidize in a matter of minutes even under atmospheric pressure, it is important to carefully clean the Si surface from any contaminants and SiO/SiO_2 so that to avoid a SiO/SiO_2 interlayer between TiO_2 and *n*-Si. Each parameter specifies the requirement to minimize the overall series resistance of TiO_2 *HPE*.

2.13. (Photo)electrochemical Analysis

The photodegradation of oxalic acid ($H_2C_2O_4$) was measured by using Mg, Cu, and Ni-doped a-TiO_2 as photocatalysts. The changes in the concentration of carbon in the solution were measured by the total organic compound (*TOC*) analyzer (*Shimadzu*, *TOC-L*, *Shimadzu Corp*., Japan) according to the EN 1484:2002 procedure. In order to eliminate the possible errors, the average concentration of carbon was evaluated from three measurements. The withdrawn samples of oxalic acid were not returned based on the *TOC* analysis, as the sample solution was evaporated. Therefore, photodegradation might be slightly affected by the decrease in the total volume of oxalic acid in the measurement setup. However, since the volume of the taken sample

was low, the effect is considered to be negligibly low, and consequently it was not analyzed.

The photodegradation of organic dyes was measured under *UV* irradiation by using TiO_2/Au*NP* as a photocatalyst. Here, Rhodamine B (RhB) solution of $1 \cdot 10^{-5}$ mol/l concentration was used, and photodegradation was evaluated from *UV*-vis measurements by implying a decrease in absorbance at a specific wavelength is equivalent to the degradation of dyes. Since the deposited TiO_2 is denoted by a wide energy bandgap, additionally, oxygen gas was set to flow in RhB solution with a flow rate of 60 ml/min to enhance the photocatalytic degradation. The increase in photocatalytic degradation gives a better perspective on the photocatalytic properties of the formed structures. After *UV*-vis analysis, the withdrawn sample solution was returned to the measurement in order to eliminate the possible influence of the decreased total volume of RhB to photodegradation.

Electrochemical analysis for TiO_2/Si *HPE* and Pt or Pt-free *CE* was set in three different electrolyte solutions with various pH levels:

- A mixture of 0.05 mol/l concentration citric acid monohydrate ($C_6H_8O_7.H_2O$) and 0.5 mol/l concentration ammonium acetate ($C_2H_7NO_2$) was used as an acidic solution with a pH of 4.8.
- A mixture of 0.5 mol/l concentration potassium chloride (KCl) and 0.5 mol/l concentration ammonium acetate ($C_2H_7NO_2$) was used as a neutral solution with a pH of 6.2.
- A mixture of 0.05 mol/l concentration sodium hydroxide (NaOH) and 0.5 mol/l concentration ammonium acetate ($C_2H_7NO_2$) was used as an alkaline solution with a pH of 8.8.

The electrochemical measurements with TiO_2/Si *HPE* as the photoanode and Pt as the counter electrode or Pt-free as the counter photoelectrode were immersed into the solutions and connected to the external power source (*Keithley* Picoammeter/voltage source) to measure the photogenerated current. These measurements, similarly to I-V measurements of multi-layered Si, were conducted under two conditions: dark and under *UV* irradiation.

3. Results and Discussion

3.1. Investigation of the Structure and Morphology of the formed TiO_2 Thin Films

3.1.1. Morphology Investigation of the Formed TiO_2 Thin Films

Morphology analysis of the deposited TiO_2 thin films was done by analyzing the *FE-SEM* images presented in **Fig. 3.1**. (TiO_2 thin films deposited by the sol-gel spin-coating technique) and **Fig. 3.2** (TiO_2 thin films deposited by the *RMS* technique). TiO_2 thin films were baked at 150 °C for 30 minutes and annealed at various temperatures (800, 850, 875, 900, 950, 1000 °C) with the objective to investigate the changes in the microstructure. According to the surface images in **Fig. 3.1**, the grain size increases from ~80 nm to almost 350 nm as the annealing temperature increases. The calculations were done by analyzing the surface images with the *ImageJ* software. Even though the densification over all the film occurs with an increased annealing temperature, from the cross-section images (at temperatures of 950 and 1000 °C), it can be seen that a very thin (~20–25 nm) and even layer forms at the surface of a substrate. Considering the previously mentioned Si diffusion into the TiO_2 lattice, it can be stated that this thin layer might be a mixture of TiO_x (possibly anatase phase TiO_2) and Si/SiO_2 [192]. Unfortunately, as this layer is too thin in comparison with the full thickness of the films, it is hard to investigate it further with *XRD* analysis. In this case, either *XPS* or *SIMS* (Secondary Ion Mass Spectrometry) should be used for depth profiling. On the other hand, this would be an important study if a composite material of rutile phase TiO_2 and Si could be manufactured for photocatalytic application, and this is not the case in the present study. Furthermore, the effect of densification on the microstructure of TiO_2 thin films can be observed from the images in **Fig. 3.1**.

The densification of TiO_2 thin films with an increased annealing temperature, or, in other words, the changes in porosity, was analyzed from the cross-sectional images presented in **Fig. 3.1**. Densification occurs with an increased annealing temperature, as the porosity decreases from 35.87% (800 °C) to 16.28% (1000 °C), as listed in **Table 3.1**. Even though such analysis could be affected by the sample preparation technique (cutting the sample before *FE-SEM* measurement), the result somewhat agrees with the images presented above.

Table 3.1. Calculated porosity of TiO_2 thin films based on the annealing temperature. Calculations were done by using the cross-section images in **Fig. 3.1**.

Annealing temperature	800 °C	850 °C	875 °C	900 °C	950 °C	1000 °C
Porosity	35.87%	31.87%	25.14%	20.90%	19.56%	16.28%

However, further investigation is needed to accurately analyze the concentration of pores. This can be done by several methods, and one of the simplest options is gas sorption [202, 255], where, usually N_2, Ar or CO_2 is used, or else X-Ray and neutron scattering porosimetry is employed [256].

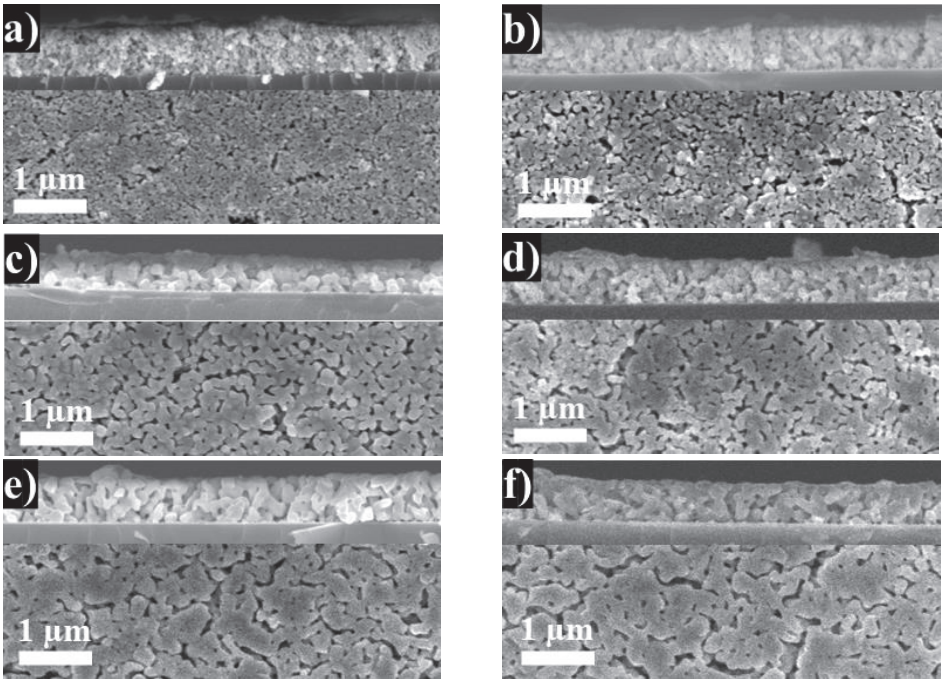

Fig. 3.1. *FE-SEM* surface and cross-section images of TiO_2 thin films deposited on *n*-type Si substrate by the sol-gel spin-coating technique and annealed at different temperatures for 1 hour: a) 800 °C; b) 850 °C; c) 875 °C; d) 900 °C; e) 950 °C and f) 1000 °C. Accelerating voltage – 5 kV, magnification – 20k (the white bar indicates 1 µm)

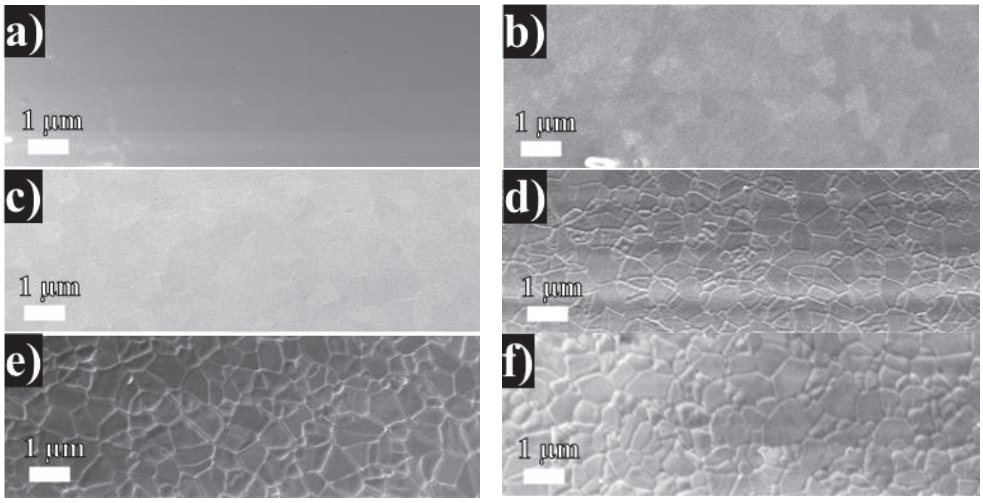

Fig. 3.2. *FE-SEM* surface images of TiO_2 thin films deposited on *n*-type Si substrate by *RMS* technique and annealed at different temperatures for 1 hour: a) as-deposited; b) 750 °C; c) 850 °C; d) 950 °C; e) 1000 °C; f) 1200 °C. Accelerating voltage – 5 kV, magnification – 10k (the white bar indicates 1 µm)

Analogous analysis was done for TiO_2 thin films deposited by the *RMS* technique. In this case, no baking was done before the annealing process, as it is not important according to the deposition kinetics. On the basis of **Fig. 3.2 (a)**, a TiO_2 thin film was deposited evenly on the substrate without any visible cracks or grain structures. The formation of grain structures was observed when TiO_2 thin films were annealed at 750 °C temperature with slightly visible grain boundaries. With annealing temperatures increased to 950, 1000, 1200 °C, the grain boundaries became more visible (**Fig. 3.2 (d, e, f)**). This is a result of an increase in the tensile residual stress caused by the high annealing temperature [257].

The surface and depth microstructure plays a crucial role in photocatalysis as it affects the surface area, which directly affects the photocatalytic efficiency [258–260]. The higher is the surface area, the higher is the photocatalytic efficiency as more surface is in contact with the solution [261]. However, considering the porous material, it is important to take into consideration whether the solution would be able to reach the inner parts of thin films, or it will react only on the surface level. Moreover, if the porous structure is columnar, the photocatalytic efficiency increases even more if columns are aligned with the internal electric field [262]. Thus, the electrons would be given additional mobility alongside the columns, and the scattering or recombination processes would be minimized. Therefore, when preparing stand-alone TiO_2 thin films as a photocatalyst or a composite monolithic structure of a photocatalyst, it is important to take into account the morphology and how it might affect the further photocatalytic efficiency. Nevertheless, the properties of the deposited thin films also depend on the deposition technique [263–265].

3.1.2. Structural Properties of the Formed TiO_2 Thin Films

The *XRD* measurements were set for TiO_2 deposited by the sol-gel spin-coating technique from commercially available STS-21 hydrosol (**Fig. 3.3**) and for TiO_2 deposited by the *RMS* technique (**Fig. 3.4**). TiO_2 deposited from STS-21 hydrosols was dried at 150 °C for 30 min to form as-deposited TiO_2 thin films. According to the *XRD* spectra, TiO_2 deposited by the sol-gel spin-coating technique contains the anatase phase with a dominant {101} facet at $2\theta = 25.30°$, and the following {004} facet at 37.82°, {200} at 48.12°, {103} at 37.06°, {112} at 38.58°, {105} at 54.02° and {211} at 55.08° [168]. Such results were expected as STS-21 hydrosol already contains TiO_2 anatase phase particles (based on the specification sheet); see **Table 2.3**. TiO_2 thin films deposited by the *RMS* technique and without additional annealing are amorphous (a-TiO_2) (**Fig. 3.4**). According to the *XRD* spectra, no peaks corresponding to either TiO_2 anatase or TiO_2 rutile phase were detected.

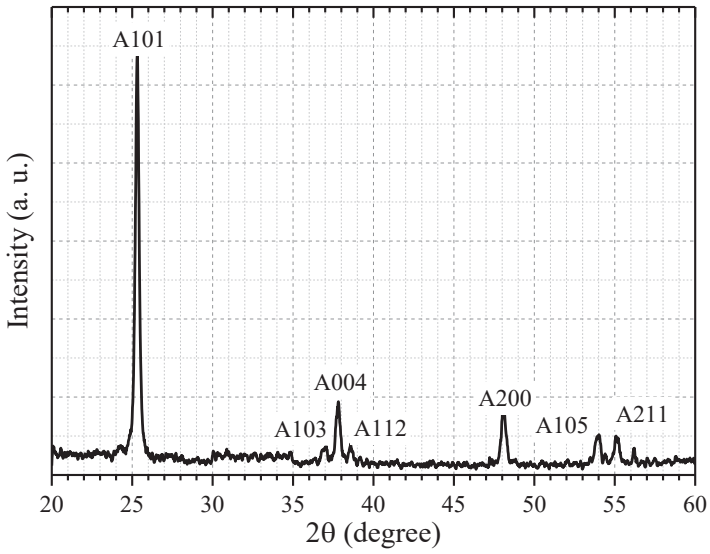

Fig. 3.3. *XRD* spectra of TiO_2 deposited by the sol-gel spin-coating technique from STS-21 hydrosol and dried at 150 °C. A – peaks attributed to TiO_2 anatase phase

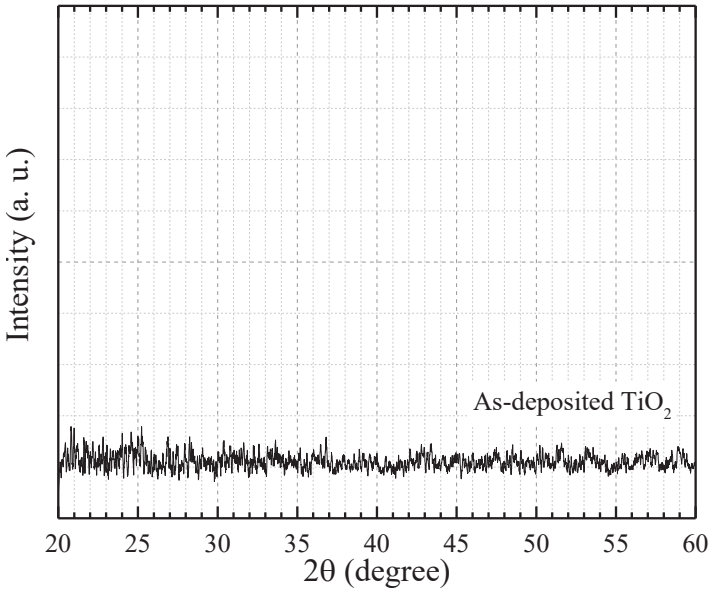

Fig. 3.4. *XRD* spectra of TiO_2 deposited by the *RMS* technique without additional annealing

The effect of the deposition parameters was investigated for TiO_2 thin films by annealing the samples at various temperatures. TiO_2 thin films were deposited by the sol-gel spin-coating and physical vapor deposition techniques as described in Sections **2.1** and **2.3**. According to the *XRD* results (**Fig. 3.5**), the phase transition from the anatase phase to rutile begins at ~850 °C with at least 5% of the rutile phase detected

in the thin film. Considering that the solution used for TiO_2 thin films deposition already contains the anatase phase, the temperature for the phase transition is much higher than the average 600 °C temperature reported in other articles for the amorphous-to-anatase-to-rutile or anatase-to-rutile transition [266–270]. Thin films annealed at 800 °C temperature for 60 min have a dominant facet {101} at 25.32° (ref. 25.28°) and secondary facets {103}, {004}, {112}, {200}, {105} and {211} at 37.08° (ref. 36.87°), 37.84° (ref. 37.68°), 38.70° (ref. 38.52°), 48.12° (ref. 48.01°), 53.94° (ref. 53.74°) and 55.12° (ref. 55.03°), accordingly. A slight shift of ~0.04 to 0.21° at the peaks may be caused by the stress induced by the annealing process [192]. With the increased annealing temperature (at 850 °C), the rutile facets {110} at 27.44° (ref. 27.36°) and {220} at 56.24° (ref. 56.45°) appear with only ~5% of the rutile phase in TiO_2 thin films. At the annealing temperature of 875 °C, the intensity of the peaks for the above mentioned facets slightly increases, and one new facet {211} at 54.56° (ref. 54.15°) appears with a higher intensity peak compared to the previous ones. By further increasing the annealing temperature, the other rutile facets {101}, {200}, {111}, {210} and {211} appear at 36.08° (ref. 35.96°), 39.22° (ref. 39.06°), 41.24° (ref. 41.11°), 44.02° (ref. 43.90°) and 54.40° (ref. 54.15°), accordingly. A similar shift (as it was detected for the anatase phase) in the peak positions can be observed for the rutile phase. The intensity of the dominant rutile facet {110} increases with an increased temperature followed by the decrease in intensity for the dominant anatase facet {101}. The phase transition ends at 1000 °C where no anatase was detected in the TiO_2 thin film. The above mentioned references were taken from the open database *RRUFF Project* [271] (anatase ID: R070582 and rutile ID: R060745). The calculated average (see Equation 2.1) crystallite size of the TiO_2 anatase phase increases from 45.1 nm (annealed at 800 °C) to 62.11 nm (annealed at 1000 °C). A similar tendency was observed during the formation of the TiO_2 rutile phase: 52.39 nm (annealed at 850 °C) and 75.74 nm (annealed at 1000 °C). This increase in the average crystallite size can be explained by the increase in crystallization resulting in the decrease of the crystal defects [272]. Other authors reported that an increase in the crystallite size may be caused by the densification due to a high annealing temperature (which can also be observed in the *FE-SEM* images **Fig. 3.1**) [273].

The observed effect where the phase transition requires enormously high annealing temperatures can be attributed to the material of the substrate on which TiO_2 was deposited [274]. According to S. Miszczak et al., phase transition from amorphous to the anatase phase ends at ~500 °C, and, from anatase to the rutile phase, it ends at ~800, 850, or 1000 °C while depositing on 304L steel, Co-Cr-Mo alloy or Si substrate, accordingly. Moreover, another study reported Si diffusion into the TiO_2 lattice, which, according to the authors, might slow down the phase transition from the anatase phase to the rutile phase [192]. This observation was done by *XPS* analysis which detected higher concentrations of Si with increased annealing temperatures of TiO_2. Considering the *XPS* detection depth (which is around 10 nm), the thickness of TiO_2 (which was ~40–70 nm), and while taking in mind the densification of thin films under high annealing temperatures, there is a high chance of Si diffusion into the TiO_2 lattice. Another study states that Si locks the Ti-O species at the interface, thus

preventing the nucleation process which is necessary for the phase transition to take place [170].

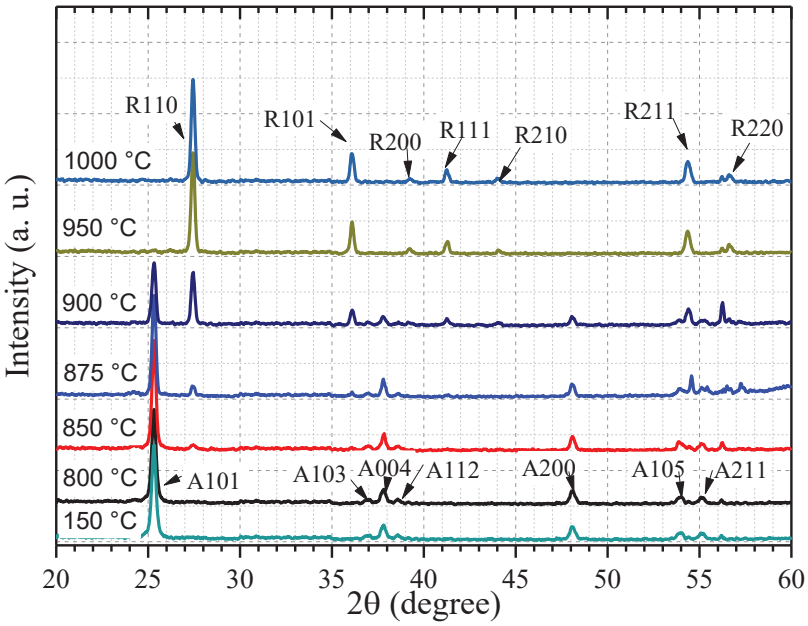

Fig. 3.5. *XRD* pattern of TiO_2 thin films deposited by the sol-gel spin-coating technique using a commercially available STS-21 hydrosol and annealed at different temperatures for 60 min: 800 °C; 850 °C; 875 °C; 900 °C; 950 °C; 1000 °C. For a comparison, as-deposited (dried at 150 °C for 30 min) TiO_2 pattern is added from **Fig. 3.3**. A – peaks attributed to TiO_2 anatase phase, R – peaks attributed to TiO_2 rutile phase

At the interface of Ti/Si (Ti/SiO_2)[7], Ti atoms are substituted into the tetrahedral SiO_2 lattice, which results in the formation of tetrahedral Ti sites. Taking into account that the TiO_2 anatase-to-rutile transition is reconstructive and requires the breaking of the weakest Ti-O bonds, the interaction between the octahedral and tetrahedral Ti sites is the reason for the delayed transition process. Therefore, a higher activation energy (a higher temperature) is required to drive the phase transition process. Nevertheless, the diffusion of Si atoms into the TiO_2 lattice violates the Moss rule [254, 275], which explains the interrelation between the energy bandgap and the high-frequency refractive index for semiconductors or dielectrics [276]. It states that materials with a high refractive index feature lower energy bandgaps and vice versa:

$$n^4 E_g = constant \qquad 3.1$$

Here, n – refractive index and E_g – energy bandgap. At first, this relation was proposed mainly for photoconductors with a constant of ~95 eV. However, the list of

[7] Considering the natural oxide layer of several nanometres, which forms in the matter of minutes on the Si substrate in atmospheric ambience

semiconductors was expanded, and the values of the presently discussed constant slightly vary between them [277, 278].

Furthermore, the *XRD* pattern for TiO_2 thin films deposited by *RMS* and annealed at different temperatures (for 60 min) shows that even higher annealing temperatures are required for the anatase to rutile phase transition (**Fig. 3.6**). It is worth noting that, in this particular case, the amorphous-to-anatase-to-rutile phase transition occurs because as-deposited TiO_2 thin films are amorphous. According to the *XRD* spectra, two dominant anatase facets of {101} and {004} at 25.38° (ref. 25.28°) and 37.88° (ref. 37.68°) appear when samples are annealed at 750 °C temperature. The dominant facet {004} overcomes the other dominant facet {101} when the annealing temperature increases, as it can be observed from the slightly increased peak intensity for {004}, compared to {101}. However, the rutile phase did not appear until the annealing temperature reached 1200 °C. It can be stated that the anatase-to-rutile phase transition began between 950 and 1200 °C, which is the double value compared to the average phase transition temperature.

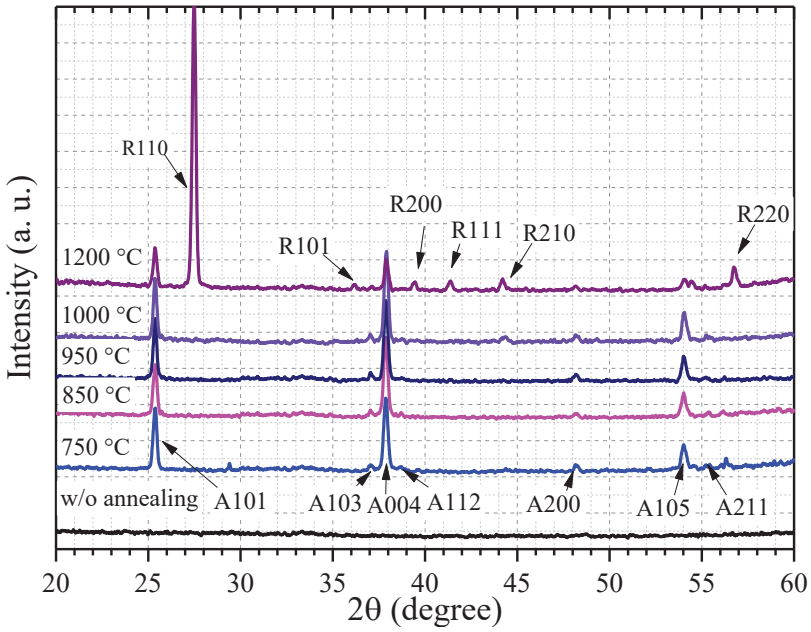

Fig. 3.6. *XRD* spectra of TiO_2 thin films deposited by the *RMS* technique and annealed at different temperatures: 750 °C; 850 °C; 950 °C; 1000 °C; 1200 °C. For a comparison, as-deposited (without annealing) TiO_2 pattern is added from **Fig. 3.4**. A – peaks attributed to TiO_2 anatase phase, R – peaks attributed to TiO_2 rutile phase

Even though the dominant rutile facet {110} with the highest intensity peak was detected at 27.48° (ref. 27.36°), two anatase facets {101} and {004} were still observed. The above used references were taken from the open database *RRUFF Project* [271] (anatase ID: R070582 and rutile ID: R060745). The average crystallite size was calculated for these samples as well. Likewise, for TiO_2 deposited by the sol-

gel spin-coating technique, in this case, the average crystallite size increased with an increased annealing temperature as well. The average crystallite size of the anatase phase was estimated to be 37.17 nm (annealed at 750 °C), and increased to 44.85 nm (annealed at 1000 °C). However, during the phase transition, the crystallite size for the anatase phase decreased to 35.00 nm (annealed at 1200 °C), while the crystallite size of the TiO_2 rutile phase was estimated to be around 45.27 nm (annealed at 1200 °C). Such a crystallization process was expected for TiO_2 deposited by the *RMS* technique on the *n*-type Si substrate according to the previous results of TiO_2 deposited by sol-gel spin-coating on the same substrate. The increase in the required annealing temperature for the TiO_2 anatase-to-rutile transition may be attributed to a low thickness of the deposited thin films. As E. Blanco *et al*. suggested, Si diffusion into the TiO_2 lattice occurs under high annealing temperatures [192]. However, the presently mentioned study analyzed Si diffusion into TiO_2 deposited by the sol-gel spin-coating technique. Thus, diffusion is much easier into a porous structure, compared to a dense one. In our study, TiO_2 thin films deposited by the *RMS* technique yield low-to-zero porosity (i.e., no visible porosity was observed from the TiO_2 surface images taken with *FE-SEM*), which might eliminate the diffusion of Si. Moreover, the thickness of the TiO_2 thin films deposited by the sol-gel spin-coating technique was ~700 nm, while those deposited by *RMS* were ~200 nm. When taking into consideration that *n*-type Si substrates were used in both cases and by considering that Si diffusion takes place during the annealing process, it can be suggested that the temperature required for the phase transition is inversely proportional to the thickness of thin films. Nevertheless, an additional study and more profound analysis are required to understand the TiO_2 phase transition dependence on the substrate material.

Additionally, TiO_2 was deposited by the *RMS* technique on glass and quartz glass substrates. According to the *XRD* spectra (**Fig. 3.7**), an amorphous TiO_2 structure forms before annealing, and, after annealing, TiO_2 anatase with a dominant {101} facet and a low-intensity TiO_2 rutile {110} facet were observed. The crystalline structure changes when TiO_2 is annealed at 900 °C. Here, the first dominant TiO_2 anatase {004} facet followed by the {101} facet were detected with a lower TiO_2 rutile {220} facet. According to the XRD spectra, regarding TiO_2 thin films deposited on the Si substrate and annealed at 950 °C temperature, no rutile peak was observed at all (**Fig. 3.6**). Whereas, for TiO_2 deposited on quartz glass and annealed at 500 °C and 900 °C, comparably high intensity rutile peaks were observed at 27.64° (ref. 27.36°) and 54.08° (ref. 54.25°), accordingly (**Fig. 3.7**). Moreover, TiO_2 thin films deposited on the quartz glass substrate have a dominant anatase {004} facet, compared to the dominant {101} facet when deposited on the Si substrate. Therefore, the dependence of crystallization and phase transition on the substrate material is undeniable.

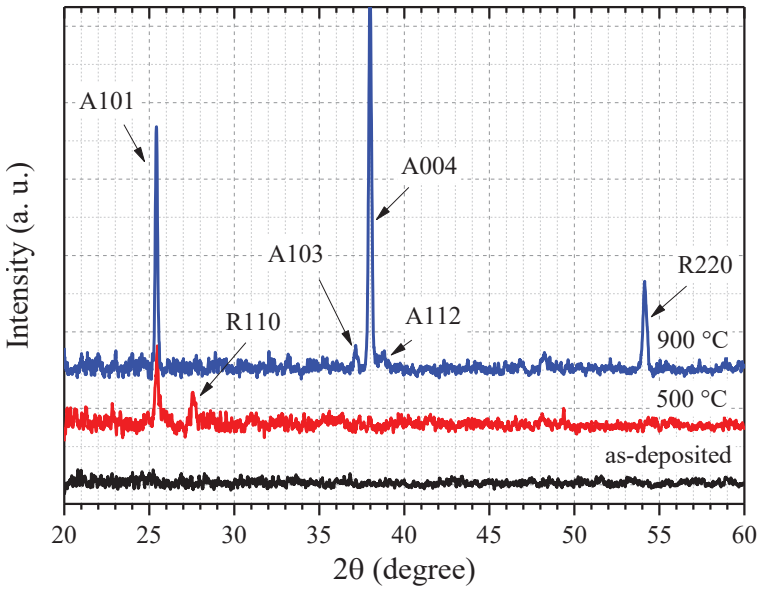

Fig. 3.7. *XRD* spectra of TiO_2 thin films annealed at different temperatures: as-deposited on glass substrate; 500 °C on glass substrate; 900 °C on quartz glass substrate [200]

The anatase-to-rutile phase transition in TiO_2 is reconstructive. The phase transition occurs by breaking the minimum number of Ti-O bonds and results in the lowest disturbance of the oxygen substructure [163, 259]. This means that the phase transition occurs at the weakest Ti-O bonds, which requires a lower activation energy. As a review study by D. A. H. Hanaor *et al*. suggests, any impurities or defects weaken the Ti-O bonds and allow an easier TiO_2 anatase-to-rutile phase transition [163]. Moreover, Y. Iida *et al*. analyzed the anatase-to-rutile transition dependence on the dopants [259]. They observed that CuO had the strongest effect on the anatase-to-rutile phase transition, thus lowering the required annealing temperature for the phase transition to begin. The opposite was observed when WO_3 and Na_2O were added to TiO_2. Thus, it can be suggested that not all impurities have the same effect on the TiO_2 anatase-to-rutile phase transition. Moreover, the authors suggested that the phase transition begins with rutile nucleation on the surface of the sample or where impurities or defects are located, and then spreads inside the lattice. Considering the single-crystal transformation, in the presence of any kind of impurities, the rutile {200} facet grows in parallel to the anatase {112} facet [279]. On the other hand, rutile might grow on the interface between the two {112} facets in pure anatase [280, 281]. However, there is no agreement as to how exactly the recrystallization process works. Thus, it is clear that the TiO_2 phase transition is a more complex process, and it requires an additional more extensive study.

Considering the crystallization of deposited TiO_2 thin films during the annealing process, another study was done to analyze the growth kinetics based on the oxygen partial pressure and the total pressure ratio instead of the annealing temperature. In this case, TiO_2 was deposited on a Si substrate by the *RMS* technique by changing the oxygen partial pressure and the total pressure ratio (p_{O_2}/p_{tot}). The mechanism behind

this ratio is that with an increased p_{tot}, the density of the gas particles (in the deposition chamber) increases as well. This results in a higher probability of collision between the gas particles, followed by an increased acceleration [282]. Additionally, the gas flow ratio has an effect on the phase development in TiO_2 thin films. The concentration of negative oxygen ions (O^-) in the chamber increases with the increased p_{O_2}/p_{tot} ratio [283]. Consequently, O^- together with Ti atoms is being accelerated towards the substrate, and the bombardment of the surface may cause the formation of the TiO_2 rutile phase at low temperatures [284–286]. However, it might be attributed to the decreased kinetic energy of Ti atoms, as the migration of Ti atoms occurs, which causes the densification of the microstructure (the density of the TiO_2 anatase phase is 3.89 g/cm^3, the TiO_2 rutile phase density is 4.25 g/cm^3) [161]. Another study suggests that the TiO_2 rutile phase formation originates from the generation of oxygen vacancies caused by Ti^+ and Ar^+ bombardment [283]. Different mechanics were observed for the TiO_2 anatase phase formation, as a higher p_{tot} value is required [287]. Even though these results are debatable, the p_{O_2}/p_{tot} ratio together with the growth rate dependence on the oxygen flow rate has to be taken into account during low-temperature crystalline TiO_2 formation [288].

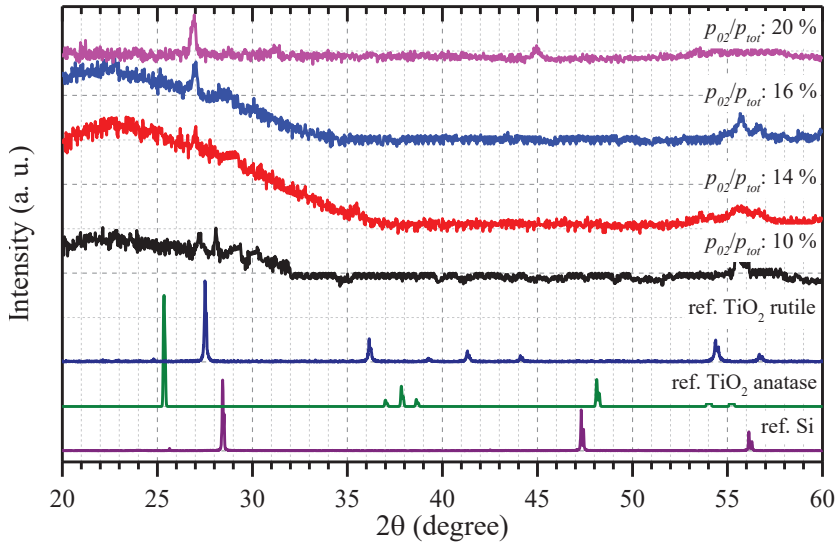

Fig. 3.8. *XRD* spectra of TiO_2 thin films deposited under different p_{02}/p_{tot} ratios [189]. Reference spectra were taken from the database with an ID 050145.3 for Si [289], R070582 for TiO_2 anatase [290], and 050417.2 for TiO_2 rutile [291]. The elimination of the Si peak was done during *XRD* analysis to avoid any interference with TiO_2 data

What concerns the *XRD* spectra (**Fig. 3.8**), the TiO_2 rutile phase with a dominant {110} facet at 26.94° (ref. 27.95°) was detected when thin films were deposited at p_{O_2}/p_{tot} = 20 % without additional annealing. With the decreased p_{O_2}/p_{tot} ratio, changes in the crystalline structure can be observed. The peak position shifts to 27.29° with decreased p_{O_2}/p_{tot} = 10%, which suggests an increase in the tensile stress during the deposition process. In accordance with the previously stated deposition

mechanism, the TiO_2 anatase phase should appear with a decreased p_{O_2}/p_{tot} ratio. However, the corresponding peak of {101} facet at 25.35° for the TiO_2 anatase phase might be hidden under the 'hump' signal of amorphous TiO_2. Nevertheless, this study suggests an alternative deposition method of crystalline TiO_2 on heat-sensitive substrates.

3.1.3. Optical Properties (UV-Vis) of TiO_2 Thin Films

The optical properties of TiO_2 thin films deposited by the *RMS* and sol-gel spin-coating techniques were measured with a *UV*-vis spectrometer (**Fig. 3.11 (a)** and **Fig. 3.9 (a)**, respectively). To this matter, TiO_2 thin films were deposited on the quartz glass substrate. Considering the TiO_2 thin films deposition by the sol-gel spin-coating technique, the deposition parameters were calibrated to achieve the same thin film thickness as the ones deposited on the *n*-type Si substrate. This was not the case for the TiO_2 thin films deposited by *RMS*, as mainly TiO_2 deposited on quartz glass was used as the final structure for photocatalytic measurements. The thickness of the deposited TiO_2 thin films was measured with a profilometer, which resulted in slightly uneven distribution of the thickness all over the sample ranging from ~680 (at the centre) to ~715 nm (at the sides). The thickness at the center was up to 50 nm thinner than the thickness of the substance deposited on the edge of the *n*-type Si substrate. However, what concerns the E_g dependence on the thickness (density) (**Fig. 3.10**), 50 nm does not significantly affect E_g.

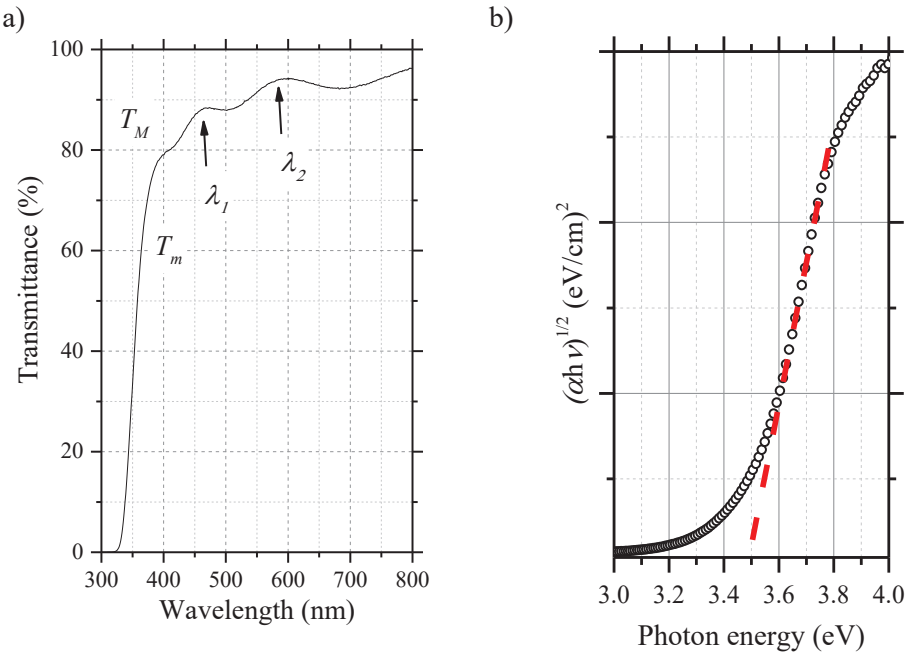

Fig. 3.9. Optical transmittance spectrum of TiO_2 deposited by the sol-gel spin-coating technique (a) and optical energy bandgap evaluation from Tauc relation (b). T_M and T_m are the upper and lower tangent envelopes of the transmission spectra, $\lambda_{1,2}$ is the wavelength at the first and second maxima

According to the results, thin films are transparent in near-*UV* (327–400 nm), with the transparency increasing from several percent to 80% and showing high transparency (80 to 95%) within the visible light region (400 to 700 nm). This is an important factor for manufacturing complex monolithic structures for photocatalytic applications. Based on the equations listed in Section **0**, the refractive index of n = ~2.16 was calculated. This is in the range, as TiO_2 usually has a refractive index of 2 to 2.5, respectively, to the density of thin films. A study shows that TiO_2 thin films with a porosity of 40.91% and 20.67% had a refractive index of 2.04 and 2.29, accordingly [160]. Moreover, TiO_2 thin films with a porosity of 53.5% and 65.2% feature a refractive index of ~1.80 and 1.62 [171]. In this case, with regard to the calculated refractive index, the estimated porosity of P = 31.37% is expected. The plot based on the *Tauc* relation (**Fig. 3.9 (b)**) was used for E_g evaluation, which is ~3.5 eV. Usually, E_g for the TiO_2 anatase phase is in the range of 3.2 to 3.5 eV [292]. Moreover, E_g exhibits an exponential dependency on the thickness of TiO_2. Therefore, E_g can be modified by changing the deposition parameters and increasing the 'thickness' of the deposited TiO_2 thin films. However, this could result in a decrease in transparency [293]. Such a decrease of E_g with an increased thin film thickness can be explained by the increased density of localized states. Moreover, scattering and light absorbance increases with an increased thickness [294]. This is especially the case for porous thin films. Nevertheless, the exponential decrease in E_g can be related to the increase of the crystallite size, which causes the quantum confinement effect [295–297]. On the other hand, this can also be attributed to the increased density of oxygen vacancies [298]. In our case, this requires an additional study and further measurements to analyze such phenomena and prove or challenge the findings published by others. This may be done in future projects.

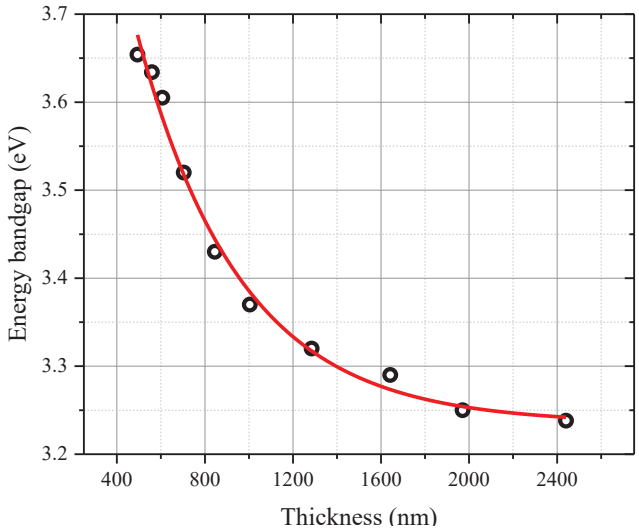

Fig. 3.10. E_g dependence on the thickness of TiO_2 thin films.TiO_2 deposited by the sol-gel spin-coating technique, baked at 150 °C for 30 min and annealed at 800 °C for 60 min. Different thickness values were achieved by changing the spin-coating parameters: slope (0–15 s), *RPM* (2000–8000) and spinning time (30–40 s)

Analogous measurement was done for TiO_2 deposited by the *RMS* technique. The thickness of TiO_2 thin films deposited by *RMS* was ~200 nm. The deposition parameters of as-deposited TiO_2 thin films were used for various applications: doping TiO_2 with Mg, Cu, and Ni; deposition on the patterned structure and for Au*NP* and Ag*NP* formation on the surface. However, for the latter, as-deposited TiO_2 and TiO_2 annealed at 500 °C and 900 °C temperatures was used. According to the transmittance spectra, the transmittance of TiO_2 thin films decreases with an increased annealing temperature (**Fig. 3.11 (a)**). As-deposited TiO_2 shows a considerably high transparency in the visible light region (>75–90%), with a slight decrease at around 500–525 nm wavelength with a transmittance of <80%. After the annealing, the transparency in the 600 to 800 nm wavelength is similar for all the samples. Whereas, at the lower wavelength, the transparency is up to 15% lower with an increased annealing temperature.

The optical energy bandgap (E_g) was evaluated analogically as for the previous samples (**Fig. 3.11 (b)**). E_g is considerably high for all the three samples, which results in ~3.75 eV (for as-deposited TiO_2); ~3.65 eV (for TiO_2 annealed at 500 °C) and ~3.70 eV (for TiO_2 annealed at 900 °C). When considering that TiO_2 thin films annealed at 500 °C and 900 °C contain the anatase phase, the evaluated E_g is higher than the reported average values for the TiO_2 anatase phase [292]. The slight increase in the energy bandgap when TiO_2 was annealed at 900 °C (compared to the samples annealed at 500 °C) can be attributed to densification followed by a decrease in thickness. The explanation behind the TiO_2 thin film thickness and the energy bandgap width was already explained above in this section. Further investigation on the energy bandgap formation in TiO_2 deposited by the RMS technique shall be carried out in future studies.

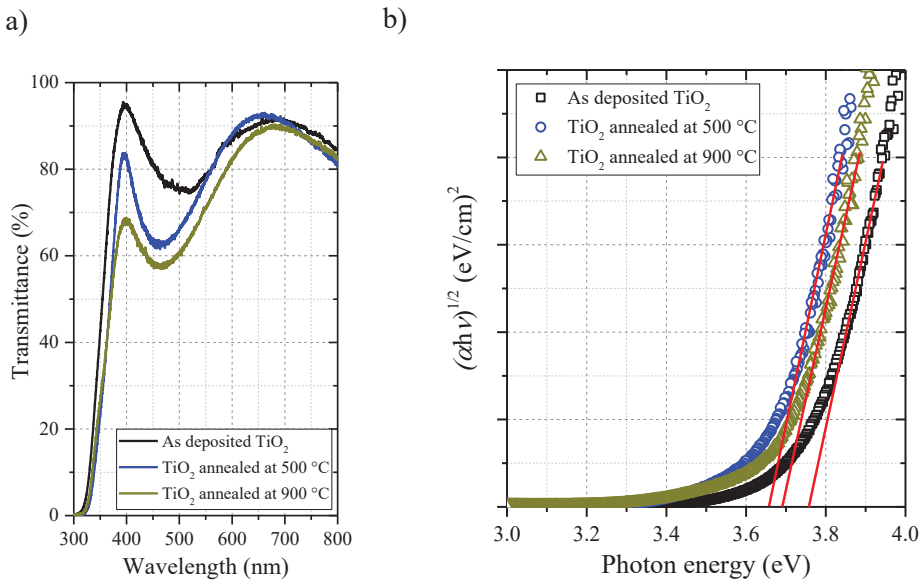

Fig. 3.11. Optical transmittance spectrum (a) and optical energy bandgap evaluation from Tauc relation (b)

3.1.4. Chemical and Electrical Properties of the Formed TiO_2 Thin Films

XPS analysis was done for the TiO_2 thin films deposited by the sol-gel spin-coating technique and annealed at 800 °C (the anatase phase) and 1000 °C (the rutile phase); see **Fig. 3.12**. The backgrounds were subtracted by using the Tougaard method, and the deconvolution of the peaks was calculated by the sum of Gaussian functions. The Chi-square represents the fitting parameter: the closer it is to 1, the better fitting procedure was done. The core-level peaks for the TiO_2 anatase phase was observed at 458.86±0.03° for *Ti* $2p_{3/2}$ (ref. 458.59° [299]) and 464.21±0.08° for *Ti* $2p_{1/2}$ (ref. 464.31° [299]) binding energies. The slight shift in the binding energy for the TiO_2 rutile phase was observed as the core level peaks are at 458.29±0.03° for *Ti* $2p_{3/2}$ (ref. 458.46° [299]) and 463.70±0.07° *Ti* $2p_{1/2}$ (ref. 464.23° [299]). The reason for the shift in the spin-orbit components may be caused by the oxygen vacancies (O_{VS}) formed during the crystallization process, which results in breaking the weakest Ti-O bonds [300–302].

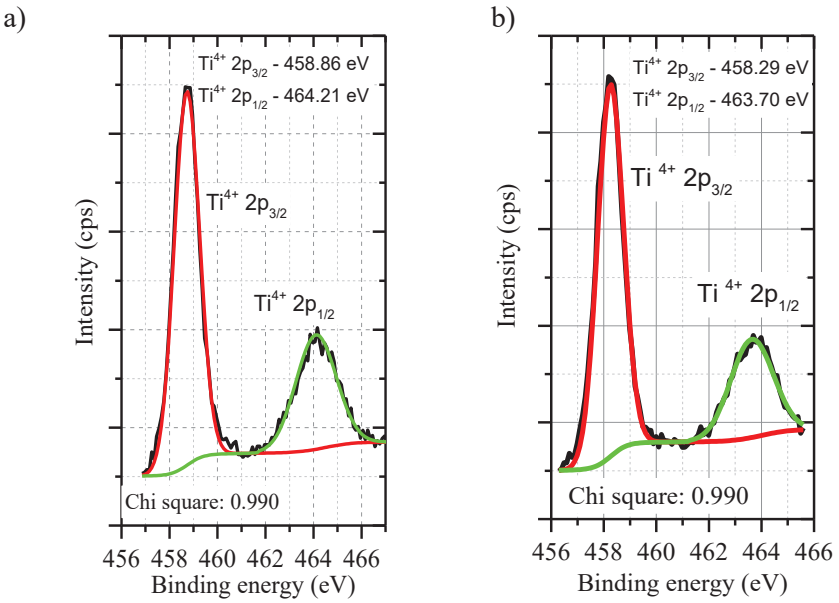

Fig. 3.12. *XPS* spectra of the TiO_2 core peak position: a) TiO_2 anatase phase; b) TiO_2 rutile phase. Chi-square ~0.99

The *O 1s* peak, which represents the Ti-O bond, gives more information on the electronic structure of TiO_2 phases. It is defined as the main characteristic which defines the electronic properties of TiO_2. To be more specific, the concentration of oxygen vacancies (O_{VS}) can be calculated by translating the *XPS* data from the *O 1s* peak. Considering the two TiO_2 phases, anatase tends to exhibit a higher concentration of O_{VS} (a higher number of point defects) than rutile [174]. Therefore, this results in a decrease of the recombination rates as point defects introduce new electronic states in E_g. The point defects affect the value of E_F ($E_F = E_A$), which is the distance between

E_C and the upper layer of the defective states. The Fermi energy level for the TiO_2 anatase phase, based on the concentration of O_Vs, is in the range of 0.4 to 1 eV, while, for the TiO_2 rutile phase, it is around 1 eV [175–178, 303]. The peaks at the binding energy 529.92±0.11° (ref. 530.00° [304]) and 531.05±0.13° (ref. 531.30° [305]) are attributed to the lattice oxygen (O_L) and non-lattice oxygen (oxygen vacancies) (O_V) for the TiO_2 anatase phase, accordingly. For the TiO_2 rutile phase, the peaks of O_L and O_V were at binding energies 529.31±0.14° (ref. 530.50°) [304] and 531.44±0.05° (ref. 531.30°) [305], accordingly. O_A here represents the adsorbed oxygen (**Fig. 3.13**). According to the measurements, the calculated values of ΔTi-O (the difference between Ti $2p_{3/2}$ and O 1s) are 71.06 eV (ref. ~71.40 eV [304]) (for the TiO_2 anatase phase) and 71.02 eV (ref. 71.60 eV [304]) (for the TiO_2 rutile phase).

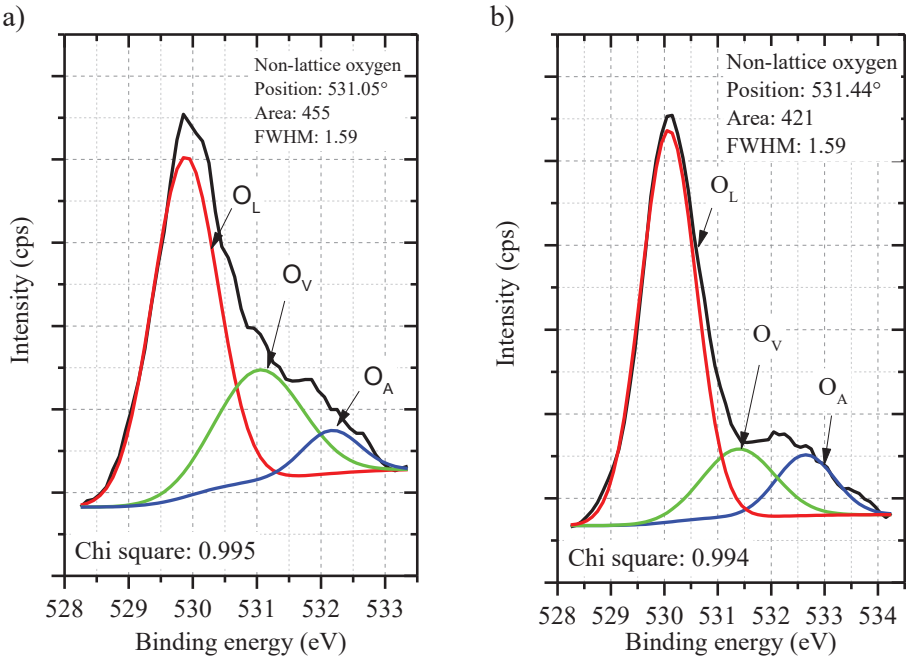

Fig. 3.13. *XPS* spectra of the O core peak (*O 1s*) position: a) TiO_2 anatase phase; b) TiO_2 rutile phase

Even though it was complicated to distinguish Ti^{3+} $2p_{3/2}$ (ref. 457.30–457.80°) [299, 304] and Ti^{3+} $2p_{1/2}$ (ref. 460.40°)[305] from the *Ti 2p* scan, the *O 1s* scan (**Fig. 3.13**) gives a reasonable approximation on the concentration of O_V in the TiO_2 anatase and rutile phases. Based on the calculated parameters (area and *FWHM*) of the O_V peaks (**Fig. 3.13**), it shows that the TiO_2 anatase phase has a higher concentration of non-lattice oxygen compared to the TiO_2 rutile phase. This is in agreement with the previous statement that the TiO_2 anatase phase offers a better photocatalytic efficiency compared to the rutile phase based on the point defects appearing in the crystal structure in the course of the crystallization process.

Electrical properties

In order to estimate the E_A of TiO_2 thin films, the dark-current dependence on the reciprocal temperature was measured (**Fig. 3.14 (b and c)**). The coplanar gold electrode was deposited on the surface of the TiO_2 thin film and connected to an external power source by connecting a Cu wire with Ag paste to an Au electrode. To ensure the accuracy of the dark-current measurement, the contact between the coplanar electrode and the TiO_2 thin film must exhibit the ohmic behavior. Therefore, I-V characteristics were measured (**Fig. 3.14 (a)**). The current was measured in the lateral direction. Thus, the current values (even under a high applied voltage) were in the picoampere range. The estimated values of E_A for the TiO_2 anatase phase are E_A = 0.472 eV, and, for the rutile phase, they are E_A = 0.902 eV. This falls within the range of the reported values for both TiO_2 anatase (with an average of 0.4 eV) and rutile (with an average of 0.8 eV) phases [175–178, 303].

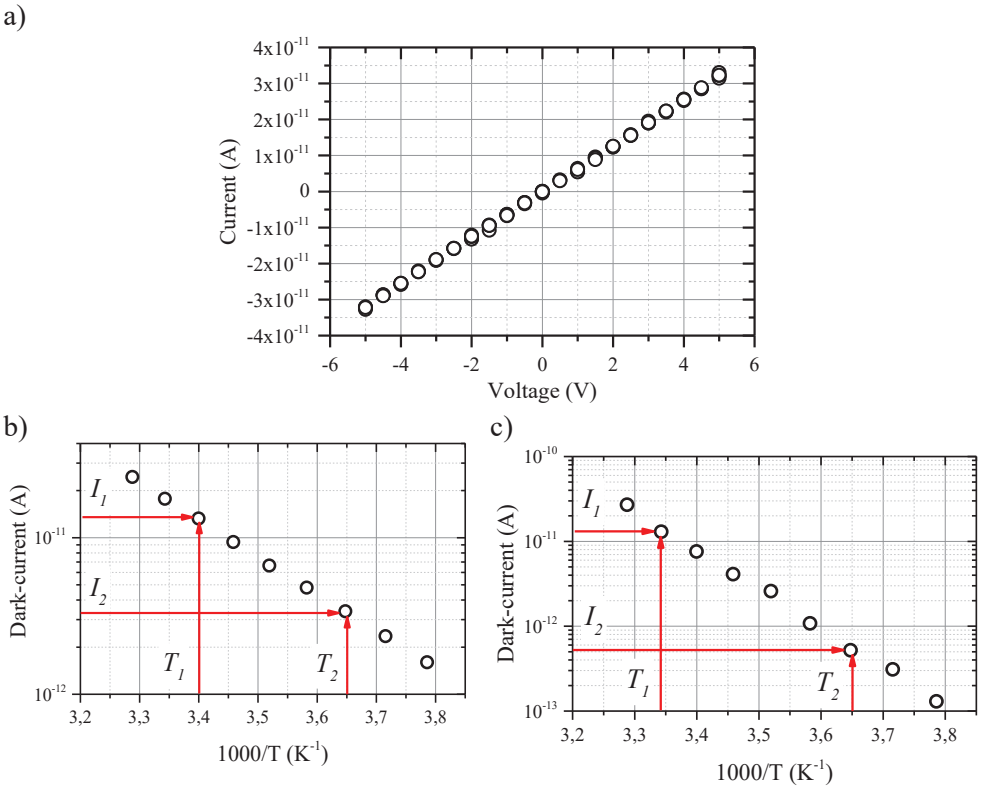

Fig. 3.14. The I-V characteristics between Au coplanar electrode and TiO_2 (deposited by the sol-gel spin-coating technique) (a) and semi-log plot of the dark-current dependence on reciprocal temperature for the estimation of activation energy (E_A): b) TiO_2 anatase phase; c) TiO_2 rutile phase

The point defects in TiO_2 dictate the value of E_A; for that reason, E_A may slightly differ in the deeper layers of the thin film. Moreover, when considering the Si

diffusion into the TiO_2 lattice and that point defects are mainly O_{VS} and Ti^{3+}, E_A may also be different at the TiO_2 and Si heterojunction interface [306–308].

Photocatalytic properties

Since the photodegradation of a solution happens mainly on the surface of a photocatalyst, surface area modification is one of the ways to consider for improving efficiency. The deposition of a-TiO_2 was done on the patterned structure to increase the surface area. At first, a patterned structure was made by the photolithography process on a glass substrate followed by the *RMS* deposition of a-TiO_2 (without additional annealing). Preparing a crystalline structure TiO_2 is difficult to this particular matter, whereas a photoresist (with which a patterned structure was made) may get damaged during the annealing process. Therefore, the surface area may get uncontrollably changed. Moreover, thin films deposited by the *RMS* technique repeat the structure of the substrate. Therefore, such deposition techniques as sol-gel spin-coating would not be a viable choice. A visual representation of the prepared structures is shown in **Fig. 3.15**.

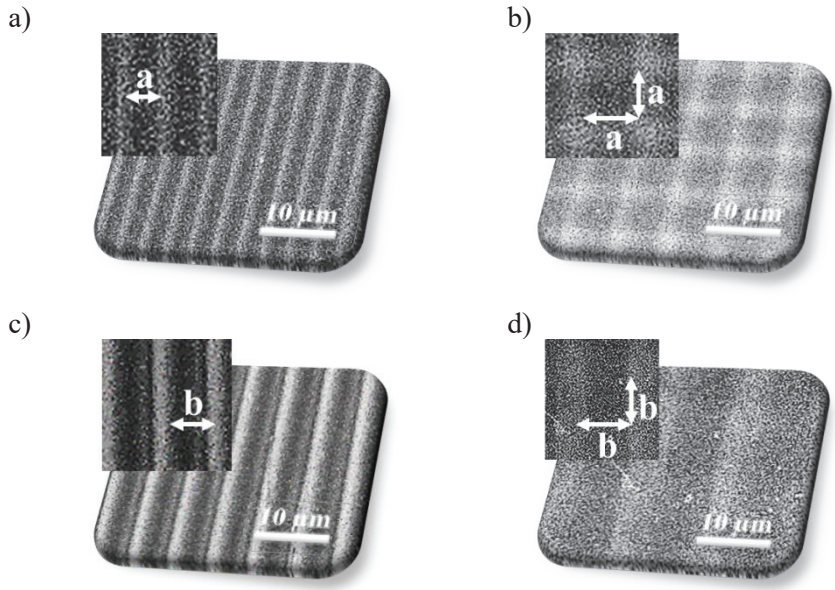

Fig. 3.15. *SEM* images of a) line pattern and b) grid pattern with a period of ~3 µm; c) line pattern and d) grid pattern with a period of ~5 µm. 'a' and 'b' markings in the picture measure ~3 and ~5 µm, respectively) [186]

The photocatalytic efficiency directly depends on the surface area of the prepared photocatalyst [309]. TiO_2 thin films deposited through a mesh showed a higher efficiency compared to plain TiO_2. Moreover, thin films deposited through a mesh with a smaller aperture achieved the highest photocatalytic efficiency [310]. Thus, it was expected that a patterned structure with a smaller period might result in

a similar way. The data from the photodegradation measurements is shown in **Fig. 3.16**.

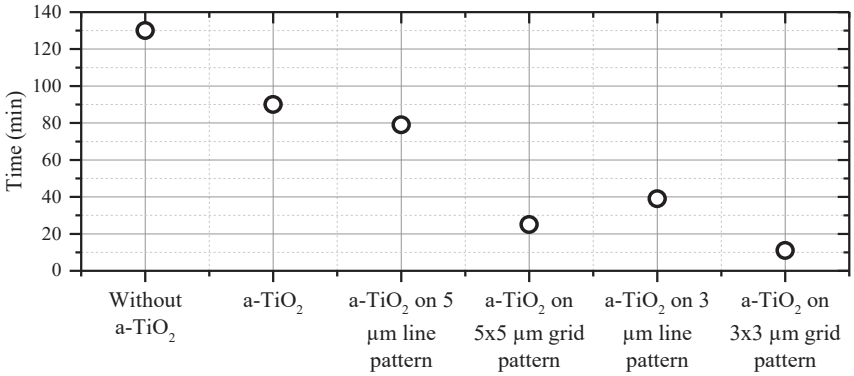

Fig. 3.16. Time required for methylene blue to reach 50% decolorization under *UV* irradiation with and without photocatalyst [186]

The photodegradation of methylene blue shows that the highest photocatalytic efficiency is reached when using a-TiO_2 deposited on the grid pattern with a period of 3 µm (50% decolorization was reached in 11 min). In comparison, the same 50% decolorization level was reached in 25 min when using a-TiO_2 deposited on the grid pattern with a period of 5 µm. For a-TiO_2 deposited on the glass substrate (without a pattern) the 50% decolorization level of methylene blue was reached only after 90 min. Additionally, the data shows that the grid pattern is more efficient compared to the line pattern. a-TiO_2 deposited on a ~3 µm grid pattern shows a 3-time higher photocatalytic efficiency over a-TiO_2 deposited on a ~3 µm line pattern. This suggests an alternative method for enhancing the TiO_2 photocatalytic efficiency. Considering the TiO_2 deposition on heat-sensitive substrates, a study on how the deposition parameters affect the crystalline structure has already been carried out previously. Thus, the TiO_2 anatase or TiO_2 rutile phase deposition on a heat-sensitive patterned structure could be done without additional annealing.

In addition, the substrate on which TiO_2 has been deposited could directly or indirectly affect the photocatalytic efficiency [261]. J. Yu *et al*. reached a conclusion that TiO_2 thin films deposited on fused quartz achieved a higher apparent rate constant compared to TiO_2 deposited on soda-lime glass [261]. This was explained by sodium and calcium diffusion into the TiO_2 lattice, which resulted in increased recombination rates of the photogenerated charge carriers by forming additional recombination centres. Moreover, their study shows that the thickness of TiO_2 thin films also directly affects the photocatalytic efficiency, and this is attributed to the increased surface area and number of active centres [261]. Moreover, the surface microstructure of a substrate affects the growth kinetics and morphology of TiO_2 during the deposition process. Therefore, the presently discussed property of a substrate would have an indirect effect on the photocatalytic efficiency. On the other hand, depositing an *n*-type semiconductor on a *p*-type semiconductor would create an internal electric field, which would increase the probability of the charge carrier separation, and this directly

affects the photocatalytic efficiency [311]. Nevertheless, the morphology of TiO_2 has a direct effect on the photocatalytic efficiency [258]. As T. D. Nguyen-Phan *et al*. highlighted, the highest apparent rate constant was reached with the mixed-phase TiO_2. Their study shows that the apparent rate constant increases with the increased wt.% of the rutile phase in TiO_2 thin films and reaches the peak value with 94.8 wt.%. The reason behind this is explained by the charge carrier separation at the interface of the TiO_2 anatase and rutile phases.

Given these points, TiO_2 thin films can be characterized as transparent in the visible light region, and it slightly differs depending on the deposition technique, which affects the thin films morphology. TiO_2 deposited by the sol-gel spin-coating technique achieved higher transparency compared to TiO_2 deposited by *RMS*. Additionally, the difference in the density of deposited thin films is undeniable; it can be elaborated from the surface images taken by *FE-SEM*. Furthermore, the optical energy bandgap has a declining exponential dependence on the thickness of TiO_2 thin films (**Fig. 3.10**). In terms of the optical energy bandgap of TiO_2 thin films deposited by the *RMS* technique (~3.65 to 3.75 eV with a thickness of ~200 nm), the latter may rather depend on the thickness than on the morphology. This suggests that, at first, the thickness of the deposited TiO_2 thin films should be optimized in order to achieve a lower optical energy bandgap.

Moreover, the analysis of crystallization shows that the TiO_2 anatase-to-rutile or amorphous-to-anatase-to-rutile phase transition depends on the substrate material. The average annealing temperature for the TiO_2 anatase-to-rutile phase transition to occur is around 600 to 800 °C [161–163]. In our study, the TiO_2 anatase-to-rutile transition begins at ~850 °C (for TiO_2 deposited from STS-21 hydrosol) and ~500 °C to 1000 °C (for TiO_2 deposited by *RMS*), based on the substrate material. Such phenomena are attributed to the Si diffusion into the TiO_2 lattice, as E. Blanco *et al*. suggested [192]. It should also be considered that the substrate material could also contribute (either positively or negatively) to the photocatalytic efficiency of TiO_2 [261]. Nevertheless, the study of growth kinetics based on the deposition parameters shows that crystal phase TiO_2 can be deposited without additional annealing. Here, the control of the gas flow rate and the control of the partial oxygen pressure and the total pressure ratio result in different growth kinetics. This is attributed to the density of gas particles and their probability to collide with each other, which would result in acceleration [282]. The formation of the TiO_2 rutile phase is preferable at low p_{tot} and room temperature, as the low kinetic energy of Ti atoms is manifested, which results in the structure densification, whereas it is conversely for the TiO_2 anatase phase [161]. Also, based on the calculated parameters (the area and *FWHM*) of the O_V peaks (**Fig. 3.13**), it shows that the TiO_2 anatase phase is denoted by a higher concentration of non-lattice oxygen, compared to the TiO_2 rutile phase. This is in agreement with the previous statement that the TiO_2 anatase phase exhibits a better photocatalytic efficiency compared to the rutile phase; this assumption is based on the point defects appearing in the crystal structure during the crystallization process.

3.1.5. Summary of the Results

To conclude, differences between TiO_2 deposited by the *RMS* and sol-gel spin-coating techniques are evident. TiO_2 thin films deposited by the *RMS* technique feature a denser structure compared to the ones deposited from STS-21 hydrosol by the spin-coating technique as shown by the surface images captured by *FE-SEM*. The densification of the structure occurs at high annealing temperatures for TiO_2 deposited from STS-21 hydrosol, which results in a larger grain size and a lower thickness level. Whereas, for TiO_2 deposited by *RMS* and annealed at high temperatures, the grain boundaries become more visible with an increased temperature. This may be caused by the stress induced during the annealing process. Considering photocatalytic applications, it can be assumed that the photocatalytic efficiency depends on the surface area of TiO_2 thin films. As seen from the obtained results, a higher surface area leads to a higher photocatalytic efficiency.

3.2. Modifications of TiO_2

As elaborated in the previous section, TiO_2, as a photocatalyst, can be modified by various methods to increase the photocatalytic efficiency by modifying E_g, the microstructure or the surface, or by increasing sensitivity under visible light irradiation.

3.2.1. Modifications Based on Doping a-TiO_2

Hence, the electronic structure of amorphous TiO_2 (a-TiO_2) is somewhat similar to crystalline TiO_2; thus it is considered a viable alternative [209]. Therefore, a modification of a-TiO_2 was made by doping it with Mg, Cu, and Ni nanoclusters (*NC*). In this particular case, a-TiO_2 was deposited on stainless steel alloy (Alloy 304L). The deposition was done by the *RMS* technique, and various dopant concentrations in a-TiO_2 were achieved by controlling the shutter of the magnetron (of a specific dopant). The thickness of the doped a-TiO_2 thin films was ~100 nm. Since the *XRD* technique is not able to detect such low concentrations of dopants, the concentration was measured by the *XPS* technique (**Fig. 3.18**). Moreover, *XRD* spectra do not change much with an increased dopant concentration as the substrate peaks overlap with dopants (**Fig. 3.17**), and only spectra of a-TiO_2/Mg*NC* (0.9 wt.%); a-TiO_2/Cu*NC* (0.6 wt.%), and a-TiO_2/Ni*NC* (0.5 wt.%) are shown below.

The corresponding peak for the Mg {102}[312] facet overlaps with Austenite {111} (Alloy 304L) at 43.45°, and additional peaks of Martensite/Ferrite {110} at 44.60° and Austenite {200} at 50.58° were detected [313, 314]. The peaks of Alloy 304L were observed at a-TiO_2/Cu (0.6 wt.%) spectra where the peaks overlap; it was observed similarly to the a-TiO_2/Mg (0.9 wt.%) scan. Cu {111} at 43.54°, Cu {200} at 51.75° and low intensity Cu {220} at 75.12° were detected [315]. The *XRD* scan of a-TiO_2/Ni (0.5 %) shows Ni {111} and Ni {200} peaks at 43.65° and 50.79°, respectively [312, 314]. Alloy 304L contains up to 12% Ni [316], thus, lower intensity peaks of Alloy 304L were detected in the a-TiO_2/Ni*NC* (0.5 wt.%) scan. Further analysis would be required in order to analyze a significant decrease of the

Martensite/Ferrite {110} peak in a-TiO_2/Ni*NC*. However, the substrate has no effect on the photocatalytic efficiency itself, thus no further analysis of this aspect was done.

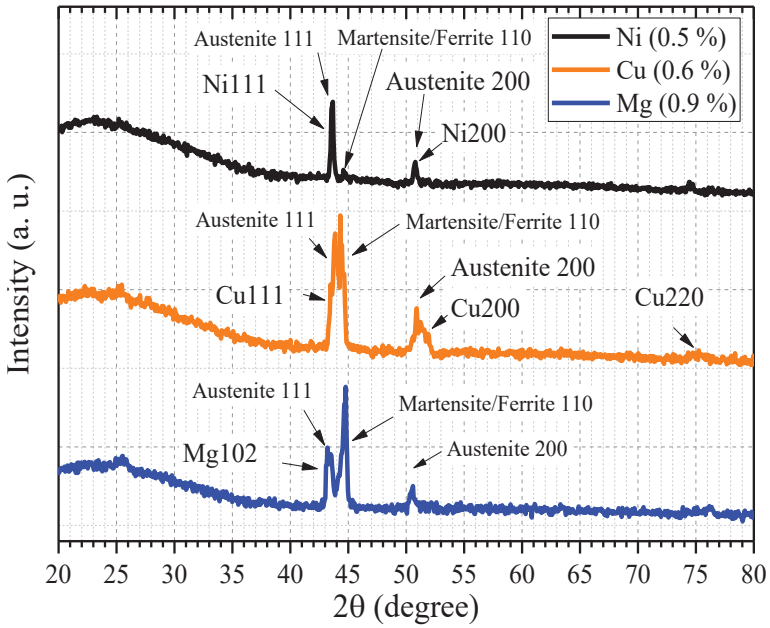

Fig. 3.17. *XRD* spectra of a-TiO_2 thin films doped with Mg, Cu, Ni *NC*. Stainless steel (Alloy 304L) was used as a substrate

XPS analysis was done for the presently discussed samples. From the wide scan of a-TiO_2/Mg*NC* (**Fig. 3.18 (a)**), Mg 1s peak is at 1303.97 eV (ref. 1303 eV for metal Mg and 1304.5 eV for native oxide [317]). For Ni-doped a-TiO_2, Ni 2p peak is at 853.09 eV (ref. metal Ni at 852.60 eV, NiO at 853.7 eV [317]) (**Fig. 3.18 (c)**). It is difficult to distinguish the Cu and CuO peaks from the *XPS* spectra of TiO_2/Cu*NC*, as these peaks are at the same binding energy of 933 eV (**Fig. 3.18 (b)**).

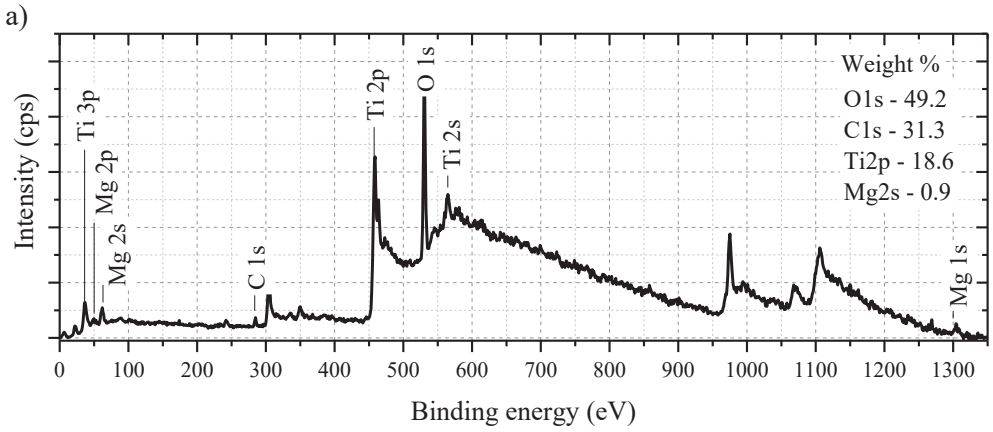

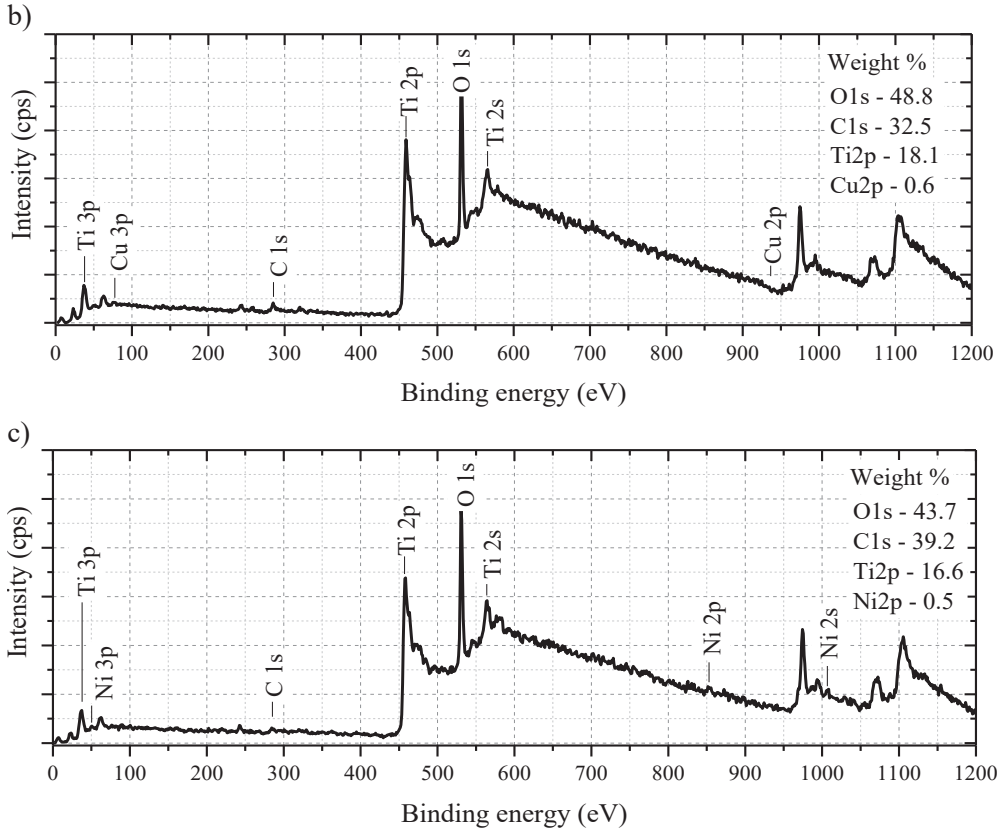

Fig. 3.18. *XPS* spectra (wide scan) of a-TiO_2/Mg*NC* (a); a-TiO_2/Cu*NC* (b); a-TiO_2/Ni*NC* (c)

Because of the low concentration of a dopant in a-TiO_2, it is difficult to state whether metal oxides formed in the lattice. Thus, narrow scans were done in order to analyze the structure more precisely. For metal oxides, O 1s is in a range of 529–530 eV. This was observed from the narrow scans of the O 1s peak, where low intensity peaks of metal oxides were detected: MgO – 529.34 eV (ref. 529.4 eV [318]), CuO – 529.08 eV (ref. 529.5–529.8 eV [319]) and NiO – 529.34 eV (ref. 529.8 eV [320]). The dopants create point defects in the TiO_2 lattice, which was observed in the narrow scan of Ti 2p: for a-TiO_2/Mg*NC*, Ti^{3+} $2p_{3/2}$ was detected at 457.05 eV; a-TiO_2/Cu*NC* at 457.05 eV; a-TiO_2/Ni*NC* at 457.40 eV (ref. 457.3 eV [299]). However, the formation of Ti^{3+} could also be associated with the deposition of a-TiO_2 [305], thus negating the effect of the dopant. Even though the results are debatable, according to the deposition parameters, where the gas ratio of 80/20 for Ar/O_2 was used, it is considered that at least a low concentration of the deposited dopants was oxidized. The full data of the peak positions, *FWHM,* and the area in % is shown in **Table 3.2**.

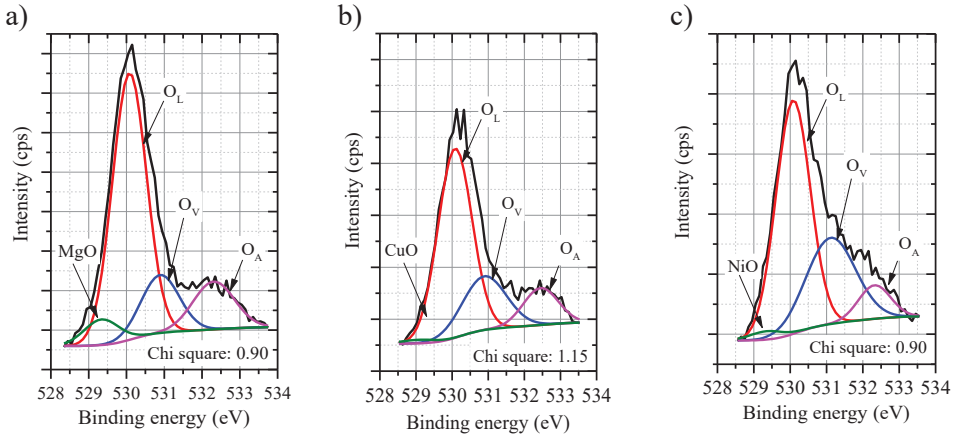

Fig. 3.19. *XPS* spectra (narrow scan) of O 1s peak: a) a-TiO_2/Mg*NC*; b) a-TiO_2/Cu*NC*; c) a-TiO_2/Ni*NC*

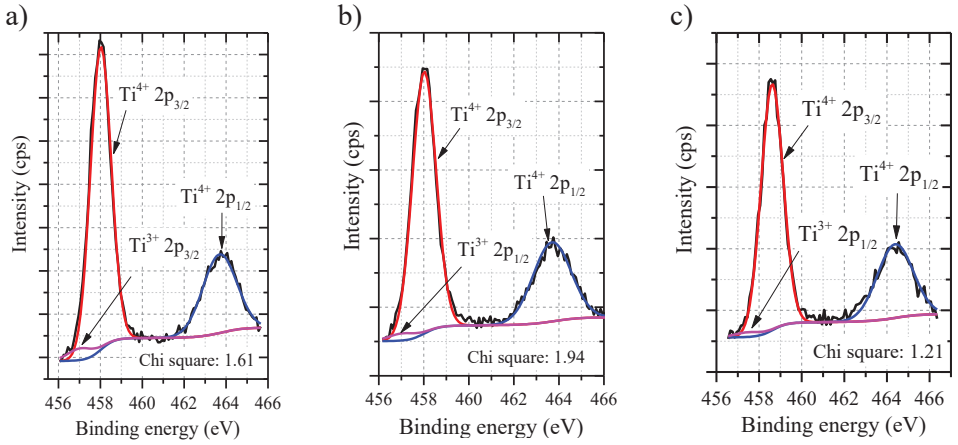

Fig. 3.20. *XPS* spectra (narrow scan) of Ti 2p peak: a) a-TiO_2/Mg*NC*; b) a-TiO_2/Cu*NC*; c) a-TiO_2/Ni*NC*

The calculated values of ΔTi-O (the difference between the Ti $2p_{3/2}$ (Ti^{4+} and Ti^{3+}) and O 1s) agree with the V. V. Atuchin *et al.*'s study [304]. As their study shows, ΔTi-O is higher in doped TiO_2. In our study, ΔTi-O (Ti^{3+}) is 73.03 eV (for TiO_2/Mg*NC*); 73.03 eV (for TiO_2/Cu*NC*) and 72.77 eV (for TiO_2/Ni*NC*) (see **Table 3.2**). Whereas, for pure TiO_2, the anatase and rutile phases are 71.06 eV (ref. 71.4 eV [304]) and 71.02 eV (ref. 71.60 eV [304]), respectively. Furthermore, V. V. Atuchin *et al*. observed a slight correlation between ΔTi-O (Ti^{4+} and Ti^{3+}) and the Ti-O bond length [304]. Their study shows that Ti-O bond lengths increase with increased ΔTi-O (Ti^{3+}) in doped TiO_2, whereas no particular correlation was observed for ΔTi-O (Ti^{4+}) and pure TiO_2 phases.

Table 3.2. Positions of core-level peaks for Ti 2p and O 1s of a-TiO_2/Mg*NC*, a-TiO_2/Cu*NC,* and a-TiO_2/Ni*NC*. O_L – lattice oxygen (TiO_2); O_V – non-lattice oxygen (oxygen vacancies); O_A – adsorbed oxygen (O_2^-; O^{2-}; O^- or OH^-); ΔTi-O – difference between O 1s (O_L) and Ti $2p_{3/2}$ (of Ti^{4+} and Ti^{3+}). *FWHM* range for metal oxides: 0.9–1.7 eV; for O 1s of metal oxides: 1.0–1.4 eV.

Compound	Chemical state	Position, *BE*, eV	*FWHM*, eV	Area	Chi-square	Chemical state	Position, *BE*, eV	*FWHM*, eV	Area	Chi-square	ΔTi-O, eV
a-TiO_2/MgNC	Ti^{3+} $2p_{3/2}$	457.05	1.41	3.15%	1.61	O_L	530.08	1.06	64.18%	0.90	73.03
	Ti^{4+} $2p_{3/2}$	458.01	1.16	67.94%		O_V	530.89	1.19	15.63%		72.07
	Ti^{4+} $2p_{1/2}$	463.69	1.61	28.90%		O_A	532.31	1.29	13.89%		
						MgO	529.34	1.09	6.30%		
a-TiO_2/CuNC	Ti^{3+} $2p_{3/2}$	457.05	1.41	2.02%	1.54	O_L	530.08	1.11	63.15%	1.15	73.03
	Ti^{4+} $2p_{3/2}$	458.01	1.24	66.12%		O_V	530.89	1.43	23.06%		72.07
	Ti^{4+} $2p_{1/2}$	463.69	1.98	31.86%		O_A	532.45	1.14	12.64%		
						CuO	529.08	1.06	1.15%		
a-TiO_2/NiNC	Ti^{3+} $2p_{3/2}$	457.40	0.69	1.47%	1.21	O_L	530.17	1.09	61.06%	1.14	72.77
	Ti^{4+} $2p_{3/2}$	458.10	1.18	65.62%		O_V	531.15	1.19	17.93%		72.07
	Ti^{4+} $2p_{1/2}$	463.80	1.98	32.91%		O_A	532.15	1.29	14.23%		
						NiO	529.34	0.90	6.78%		

As mentioned above, the formation of Ti^{3+} can also be associated with the formation of a-TiO_2. However, according to V. V. Atuchin *et al*., an increase in ΔTi-O (Ti^{3+}), compared to pure TiO_2 phases, can also be attributed to the dopants. Nevertheless, *XPS* study of a single crystal is required for better evaluation of ΔTi-O.

The photodegradation of oxalic acid solution under *UV-C* light irradiation was measured when doped a-TiO_2 was used as a photocatalyst. The measurement results are presented in **Table 3.3**. For comparison, the apparent rate constant for oxalic acid degradation under *UV-C* light irradiation without a photocatalyst was measured and calculated with a result of $0.80 \cdot 10^{-3}$ min^{-1}. Thus, self-degradation is considered as negligibly low to influence further measurements with a photocatalyst. The highest photodegradation efficiency was observed when using a-TiO_2/Cu*NC* (0.6 %), followed by a-TiO_2/Mg*NC* (0.9%) as the second highest, and the a-TiO_2/Ni*NC* (0.5%) as the third highest. With a further increase of Cu wt.% in TiO_2, the photocatalytic efficiency is negatively affected, as the measurement data shows a significant reduction in the apparent rate constant (wt.% 0.6→3.4 resulted in k_{app} reduction from 22.21→6.31 $\cdot 10^{-3}$ min^{-1}). A similar result was observed by decreasing the Cu concentration in TiO_2 to 0.3 wt.%, with a result of k_{app} reduction from 22.21 to 13.73 $\cdot 10^{-3}$ min^{-1}. Analogous tendencies were observed for Mg and Ni: Mg wt.% 0.9→1.0, k_{app} 18.66→10.15$\cdot 10^{-3}$ min^{-1}; Ni wt. % 0.5→1.4, k_{app} 13.17→5.19$\cdot 10^{-3}$ min^{-1}.

Table 3.3. Dopant concentration in a-TiO_2 thin films [195]

Without photocatalyst	k_{app} = 0.80 $\cdot 10^{-3}$ min^{-1}	a-TiO_2 (stand-alone)	k_{app} = 11.60 $\cdot 10^{-3}$ min^{-1}		
a-TiO_2/Mg*NC*		a-TiO_2/Cu*NC*		a-TiO_2/Ni*NC*	
Concentration, wt. %	k_{app}, min^{-1} ($\cdot 10^{-3}$)	Concentration, wt. %	k_{app}, min^{-1} ($\cdot 10^{-3}$)	Concentration, wt. %	k_{app}, min^{-1} ($\cdot 10^{-3}$)
0.9	18.66	0.3	13.73	0.5	13.17
1.0	10.15	0.6	22.21	1.4	5.19
4.1	4.74	3.4	6.31	3.6	2.14
14.1	2.27	4.5	6.46	11.6	1.70
17.5	0.92	8.4	4.32	17.9	1.52
		13.5	1.11	20.2	1.14
		21	0.73		

As shown by the data presented in **Fig. 3.21**, an exponential drop in k_{app} with an increased dopant concentration in a-TiO_2 can be observed. The highest photodegradation level was achieved when the dopant concentration was up to 1%. The dopants in a-TiO_2 act as charge carrier traps.

Consequently, a higher amount of dopants in TiO_2 increases the number of active traps, which results in a higher photocatalytic efficiency. However, a high number of active traps might result in a low distance between them, thus increasing the chance of recombination between the active traps [321–323]. However, if the concentration of the dopant in the TiO_2 lattice is too low, it results in a low amount of active centres. Thus, the correlation between the dopant cluster size, their concentration, and the photocatalytic efficiency requires extensive research [324].

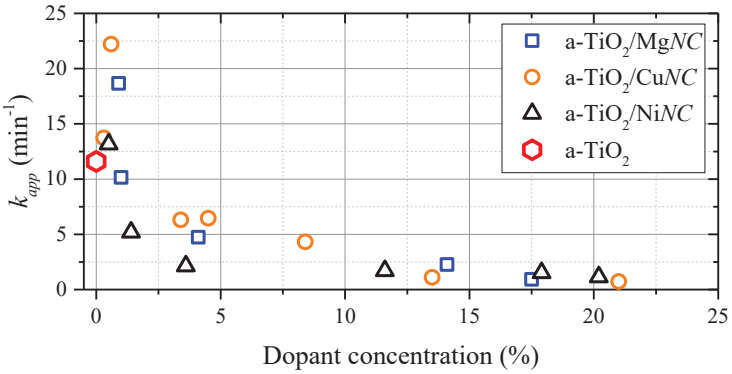

Fig. 3.21. Apparent rate constant dependence on the dopant concentration in a-TiO_2 thin films

The dark current dependence on the reciprocal temperature was measured (**Fig. 3.22**), where TiO_2 was doped with a specific amount of Mg, Ni, and Cu dopants on the surface. The deposition of doped TiO_2 was done by the *RMS* technique, where, alongside Ti cathodes, Mg, Ni, and Cu (separately) cathodes were used for a specific time to produce a mixture. Even though in this particular case TiO_2 was amorphous, according to the studies, amorphous TiO_2 attracts similar interest alongside the anatase or rutile phase TiO_2 as an alternative [179, 325, 326]. Furthermore, a previous study shows that doping crystalline TiO_2 might lead to the amorphization of the structure [210]. Amorphous TiO_2 is denoted by wider E_g which is not suitable for visible light photocatalysis, but it has a similar electronic structure to the TiO_2 anatase phase [209]. When taking in mind the point defects, amorphous TiO_2 has a higher concentration of O_{VS}; however, they appear mostly under the surface (in the deeper layers), which results in much higher E_g compared to crystalline TiO_2 [18]. However, it is still debatable whether amorphous or crystalline structure TiO_2 is a better candidate for photocatalytic application, and this field of study requires further investigation [209, 326, 327].

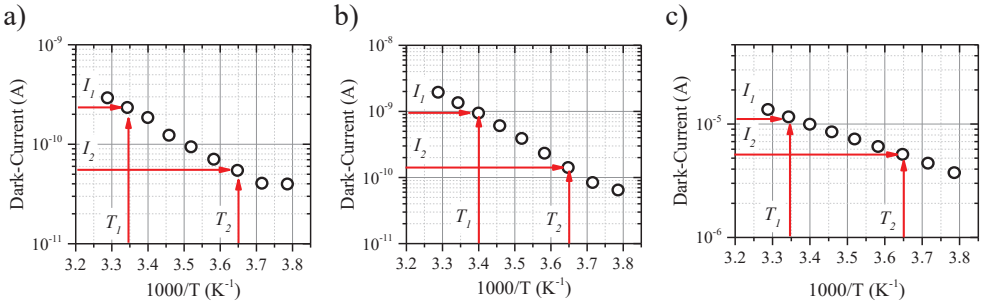

Fig. 3.22. Semi-log plot of the dark-current dependence on reciprocal temperature: a) TiO_2/Mg (10 nm); b) TiO_2/Ni (10 nm); c) TiO_2/Cu (10 nm)

According to the dark-current dependence on the reciprocal temperature, the estimated E_A value for TiO_2/Mg (10 nm) is 0.60 eV, for TiO_2/Ni (10 nm) – E_A = 0.64

eV, and, for TiO_2/Cu (10 nm), E_A = 0.23 eV. As the dark-current measurement is set on the surface of the sample, and by considering that doping was done for the surface levels of TiO_2, it is a good approximation as to how dopants would affect the E_A in the deeper layers of TiO_2. When comparing the calculated values, only TiO_2/Cu (10 nm) shows a positive change in the activation energy, as E_A is ~0.24 eV lower than the pure TiO_2 anatase phase.

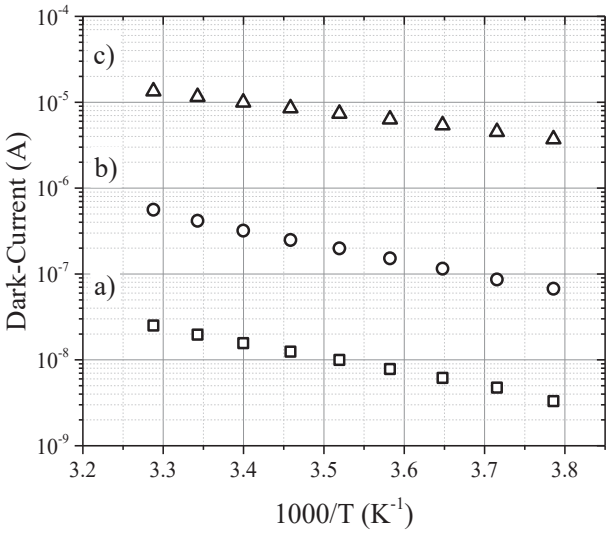

Fig. 3.23. Semi-log plot of the dark-current dependence on reciprocal temperature: a) TiO_2/Cu (<5 nm); b) TiO_2/Cu (5 nm); c) TiO_2/Cu (10 nm)

Additionally, the effect of how the concentration of Cu in the TiO_2 surface lattice changes E_A was analyzed (**Fig. 3.23**). The calculated values for TiO_2/Cu (<5 nm), TiO_2/Cu (5 nm) and TiO_2/Cu (10nm) were E_A = 0.37, 0.34 and 0.23 eV, respectively. Taking into account that the dopant concentration is somewhat equal to the concentration of the point defects, a higher number of the latter leads to a higher photocatalytic efficiency. On the contrary, too many point defects can also lead to a decrease in efficiency, as the distance between the point defects becomes smaller, and the recombination process occurs [324].

Considering the dopant material, the outcome of the measurements can be attributed to the energy band alignment between a-TiO_2 and Mg, Cu, Ni *NC*. Specifically, doping a-TiO_2 with a small amount of Mg creates shallow traps of electrons and holes in the a-TiO_2 energy bandgap [328]. Thus, the recombination rates of charge carriers get reduced. Additionally, Mg dopants on the surface of a-TiO_2 can act as an electron donor, thus affecting the surface charge properties, which results in an increased photodegradation process near the surface [329]. Likewise, CuO forms on the surface of a-TiO_2 when doping it with Cu. It is considered that this might decrease the photocatalytic efficiency as the number of the active centres diminishes [330]. However, a small amount of dopants may result in high dispersion of CuO throughout the surface, thus decreasing the charge carrier recombination rates [331,

332]. Similarly, doping a-TiO_2 with Ni causes an increase or decrease (based on the concentration of Ni) of the active centres in TiO_2 [333]. The Ni dopant separates and transfers the charge carries, thus acting as a co-catalyst during the process, which results in the decrease of the charge carriers' recombination rates [334].

Table 3.4. Work function of a-TiO_2, Mg, Cu, Ni [335–337] and barrier height at a-TiO_2/Mg; a-TiO_2/Cu, and a-TiO_2/Ni heterojunction interface

	a-TiO_2	Mg	$\Phi_{TiO_2} - \Phi_{Mg}$	Cu	$\Phi_{TiO_2} - \Phi_{Cu}$	Ni	$\Phi_{TiO_2} - \Phi_{Ni}$
Work function (Φ, eV)	4.4	3.66	-0.74	4.53 – 5.10	0.13–0.50	5.04 – 5.35	0.64–0.82

The work function of a-TiO_2 and dopants is presented in **Table 3.4**. In terms of the barrier height (the difference between the work functions) at the a-TiO_2 and Me (Mg, Cu, Ni) heterojunction, the amount of energy which is required for an electron to overcome it is the lowest for a-TiO_2/Mg*NC*, followed by a-TiO_2/Cu*NC* and a-TiO_2/Ni*NC*. In this case, the electron flow is possible without any barrier in the direction of Mg*NC* to TiO_2, whereas, for Cu*NC* and Ni*NC*, a potential barrier is formed. Based on this, Mg doped TiO_2 should achieve a higher photocatalytic efficiency. However, according to the XPS data, a higher amount of Mg dopants was oxidized. This leads to a lower concentration of O_vs, compared to Cu*NC*. Thus, a simple evaluation of the energy band alignment between the two materials and *XPS* measurements could suggest the correct outcome of the practical measurements.

Granted that, the gathered data on the photodegradation of oxalic acid suggests that the optimal dopant concentration in TiO_2 should be less than 1 wt.% to enhance the photocatalytic efficiency. Despite that, the energy band alignment (the barrier height at the metal-semiconductor heterojunction interface) might yield a relatively accurate assumption of how the dopant might affect the photocatalytic efficiency of TiO_2.

3.2.2. Modifications Based on Au*NP* Formation on the Surface of TiO_2

The formation of Au clusters on the top of TiO_2 thin films was done by the solid-state dewetting (*SSD*) process. The deposited TiO_2 thin films (on fused quartz substrate) were annealed at 500 °C and 900 °C temperatures, and as-deposited TiO_2 was used as well for Au*NP* formation on the surface.

The *SSD* process occurs when a solid-state thin film is heated (annealed at a specific temperature). The dewetting process depends on the initial thin film thickness and the annealing temperature [338]. Such a dependency can be observed from the below presented images in **Fig. 3.24**, where the formation of Au*NP* during the *SSD* process occurred. The initial thicknesses of Au (h_{Au}) thin films (before the *SSD* process) were 5, 7.5, and 10 nm. Moreover, the dependency of the initial annealing temperature of TiO_2 thin films (before Au thin film deposition) can be observed as well. Therefore, it may be suggested that *SSD* depends on the surface morphology.

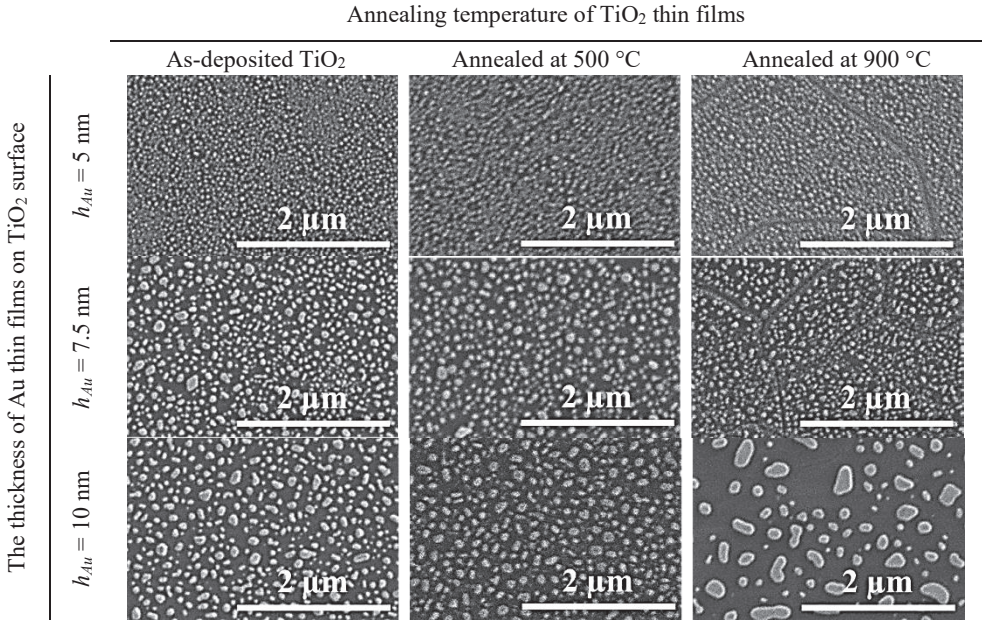

Fig. 3.24. *FE-SEM* images of TiO_2/Au*NP* surface annealed at 500 °C

Table 3.5. Au*NP* characteristics on the surface of TiO_2 thin films [200]

Sample structure	Surface density[8], µm^{-2}	Average diameter of Au*NP*, nm	Circularity	Distance between Au*NPs*, nm
As-deposited TiO_2/Au*NP* (h_{Au} = 5 nm)	316.4±0.1	33.3±0.1	0.91±0.01	11.9±0.1
Annealed at 500 °C TiO_2/Au*NP* (h_{Au} = 5 nm)	258.8±0.1	37.2±0.1	0.89±0.01	13.7±0.1
Annealed at 900 °C TiO_2/Au*NP* (h_{Au} = 5 nm)	245.6±0.1	38.1±0.1	0.89±0.01	13.7±0.1
As-deposited TiO_2/Au*NP* (h_{Au} = 7.5 nm)	218.1±0.1	40.1±0.1	0.90±0.01	14.7±0.1
Annealed at 500 °C TiO_2/Au*NP* (h_{Au} = 7.5 nm)	129.5±0.1	54.4±0.1	0.85±0.01	16.5±0.1
Annealed at 900 °C TiO_2/Au*NP* (h_{Au} = 7.5 nm)	113.4±0.1	51.1±0.1	0.77±0.01	22.3±0.1
As-deposited TiO_2/Au*NP* (h_{Au} = 10 nm)	82.8±0.1	59.8±0.1	0.85±0.01	27.4±0.1
Annealed at 500 °C TiO_2/Au*NP* (h_{Au} = 10 nm)	114.9±0.1	52.8±0.1	0.86±0.01	19.3±0.1
Annealed at 900 °C TiO_2/Au*NP* (h_{Au} = 10 nm)	33.2±0.1	86.8±0.1	0.80±0.01	45.6±0.1

The characteristics of Au*NP* and its distribution data is shown in **Table 3.5**. The density of Au*NP* decreases from ~316.4 µm^{-2} to ~82.8 µm^{-2} with the initial thickness of Au thin films being increased from 5 up to 10 nm. A similar dependency was

[8] Quantity of nanoparticles per unit area

observed by annealing TiO_2 thin films at higher temperatures. The density of Au*NP* (with an initial thickness of 5 nm) decreased from ~316.4 to 245.8 μm^{-2}, when comparing as-deposited TiO_2 and TiO_2 annealed at 900 °C. Analogically, a similar change in the characteristics was observed for Au with an initial thickness of 7.5 nm. However, a different tendency is observed for Au with an initial thickness of 10 nm. The increase in density (up to 114.9 μm^{-2}) was observed when Au*NP* was formed on TiO_2 annealed at 500 °C, compared to 82.8 μm^{-2} (for as-deposited TiO_2) and a decrease in density (down to 33.2 μm^{-2}) with a further increase in the annealing temperature. The *SSD* process on amorphous TiO_2 is affected by the additional crystallization of a-TiO_2 [339]. This can also be attributed to the dewetting of Au on the crystalline structure, as high temperatures affect the TiO_2 microstructure.

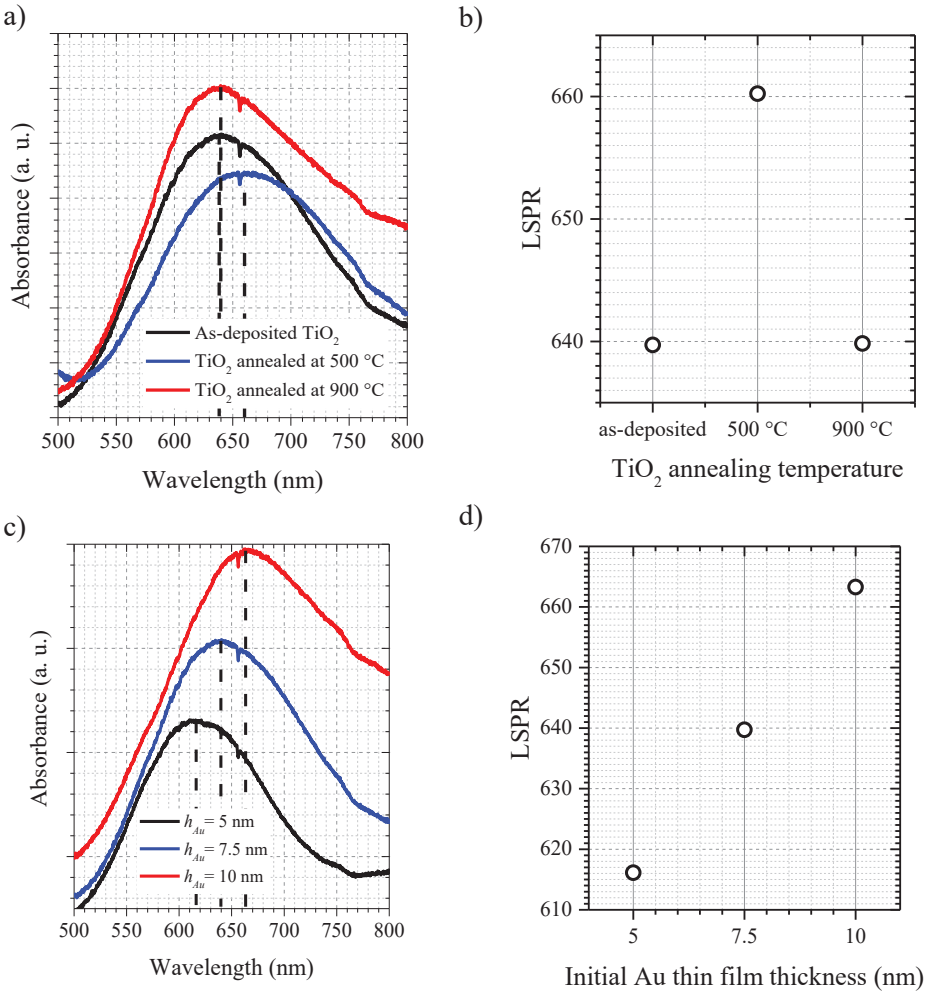

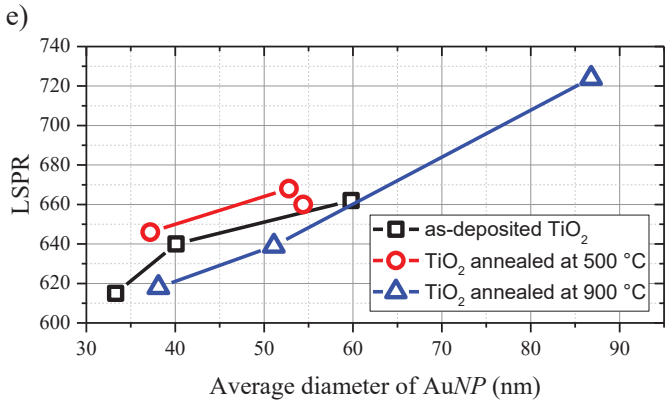

Fig. 3.25. Absorbance spectra of TiO_2/Au*NP* (with an initial thickness of 7.5 nm) thin films annealed at different temperatures (a), LSPR dependence on TiO_2 annealing temperature (b), absorbance spectra of (as-deposited) TiO_2/Au*NP* with a different initial thickness of Au thin films, (d) LSPR dependence on the initial thickness of Au thin films on TiO_2 surface, and (e) LSPR dependence on the average diameter of Au*NP* [200]

According to **Fig. 3.25**, the *LSPR* (localized surface plasmon resonance) of TiO_2/Au*NP* (h_{Au} = 7.5 nm) shifts to a lower wavelength with an increased annealing temperature of TiO_2 (with as-deposited TiO_2 standing out). Thus, a shift in *LSPR* can be attributed to the increased crystallite size of TiO_2. Additionally, a shift to higher wavelengths was observed with an increased initial thickness of Au thin films on the TiO_2 surface. Depositing a thicker Au thin film results in larger clusters during the *SSD* process, thus extending *LSPR* to larger wavelengths (**Fig. 3.25** (e)) [339].

The photodegradation of Rhodamine B (RhB) was measured under *UV* light illumination by using prepared TiO_2 and TiO_2/Au*NP* samples as photocatalysts (**Fig. 3.26**). The results show the time required for RhB to reach 50% decolorization. Even though the photodegradation of RhB (without a photocatalyst) under *UV* irradiation was detected as 50% decolorization was reached in 126 min, an increase in the photodegradation efficiency was observed when using a photocatalyst. The 50% decolorization level was reached in ~121, ~118, and ~101 min when a-TiO_2, TiO_2 annealed at 500 °C and TiO_2 annealed at 900 °C were used, respectively, as a photocatalyst. The highest photodegradation rates were observed with TiO_2 annealed at 500 °C and 900 °C with Au*NP* (h_{Au} = 10 nm) on the surface. The 50% decolorization level of RhB was reached in ca. 78 min for both cases. In general, the tendency of an increased photocatalytic efficiency is observed when using TiO_2/Au*NP* compared to stand-alone TiO_2. The 50% decolorization level of RhB in less than 30 min was observed when using a spongelike TiO_2 structure with Au nanoparticles deposited on top [340]. Thus, an increased surface area dramatically increases the photodegradation rates. Additionally, 50% decolorization was reached in ~30 min when using Pt nanoparticles (at a concentration of 0.75 to 1%) on TiO_2 surface [341]. This suggests that Au nanoparticles may be a viable and more economically favorable alternative compared to Pt. The photocatalytic efficiency dependence on the surface area was analyzed and discussed above.

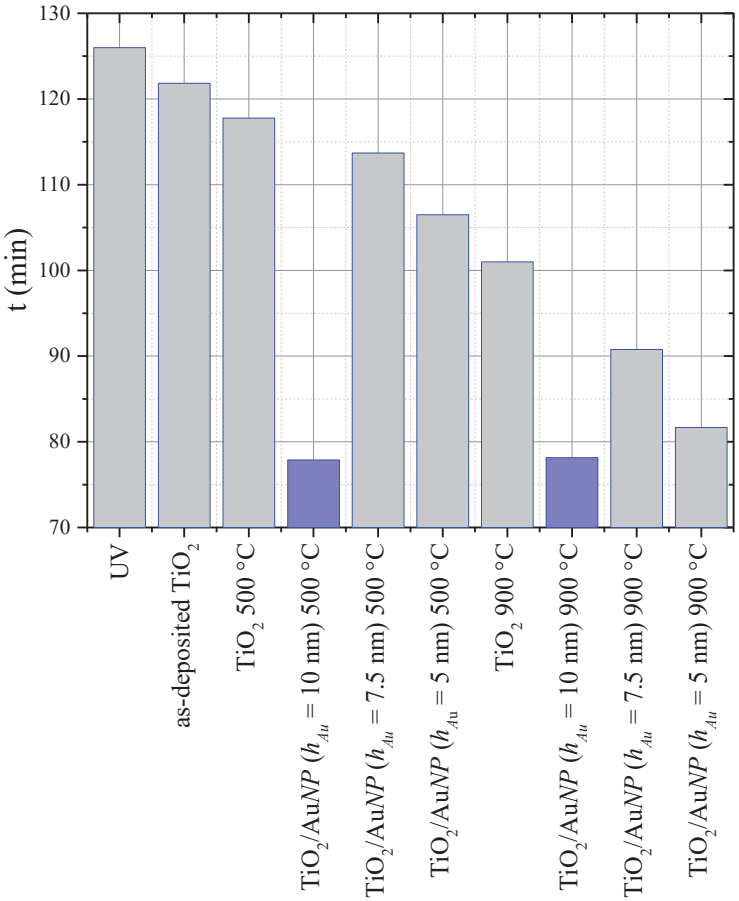

Fig. 3.26. Time required for Rhodamine B to reach 50% decolorization while under *UV* irradiation with and without a photocatalyst

Given these points, TiO_2 annealed at 900 °C (E_g = 3.70 eV) achieves a higher photocatalytic efficiency compared to as-deposited (E_g = 3.75 eV) and annealed at 500 °C (E_g = 3.65 eV) TiO_2. Even though the energy bandgap of TiO_2 annealed at 500 °C is slightly lower, the difference in the efficiency compared to TiO_2 annealed at 900 °C can be attributed to the surface area, which, for the latter, was higher due to the surface morphology. Even though no particular correlation between the properties of the formed Au*NP* (**Table 3.5**) and the photocatalytic efficiency of TiO_2/Au*NP* was observed, it is perspicuous that Au*NP* deposited on the TiO_2 surface positively affects the photocatalytic efficiency (**Fig. 3.26**). Further investigation on these particular results shall be carried out in further studies to understand the interrelationship between Au formation on the TiO_2 surface and the photocatalysis efficiency.

3.2.3. Summary of the Results

The evaluated photocatalytic efficiency and its dependence on the dopant concentration in the TiO_2 lattice suggests that the optimal concentration of dopants may be in the range of 0.1 to 1 wt.%. Thus, when doping TiO_2 to enhance the photocatalytic efficiency, a range of different concentrations has to be analyzed. Here, the highest photocatalytic efficiency was reached with 0.6 wt.% Cu in the TiO_2 lattice, followed by 0.9 wt.% Mg and 0.5 wt.% Ni. However, no statement can still be given whether Cu is a better dopant than Mg and Ni in terms of enhancing the photocatalytic efficiency, as, for the latter, only one point (0.9 and 0.5) of a concentration lower than 1 wt.% was analyzed, whereas, for Cu – 0.3 and 0.6 wt.% values were examined. Moreover, according to the measurements of the dark-current dependence on the reciprocal temperature for the above mentioned structures, the lowest activation energy (0.23 eV) forms in Cu-doped TiO_2, whereas, for Mg and Ni-doped TiO_2, it is 0.60 and 0.64 eV, respectively. Additionally, the amount of Cu in TiO_2 affects the activation energy. This attributes to the creation of point defects in the TiO_2 lattice [324]. Nevertheless, the electrical properties, such as the work function and the formed barrier at the metal-semiconductor interface, must be taken into account. The evaluated barrier height between Cu and TiO_2 is in the range of 0.13 to 0.50 eV, whereas, for TiO_2/Mg, it equals -0.74 eV, and TiO_2/Ni exhibits 0.64 to 0.82 eV. Moreover, the *XPS* study shows that the highest O_v concentration is detected in Cu doped TiO_2, followed by Ni- and Mg-doped TiO_2. Thus, the *XPS* study may be an effective way to evaluate how the dopant may affect the photocatalytic efficiency of TiO_2 thin films.

Additionally, the formation of gold nanoparticles on the surface of TiO_2 results in an increased photocatalytic efficiency compared to plain TiO_2. Even though the deposited and annealed TiO_2 thin films resulted in the formation of the anatase phase and rutile/anatase mixture, the evaluated optical energy bandgap was considerably high (~3.65 to 3.75 eV). The highest photocatalytic efficiency was reached when using TiO_2 thin films annealed at 500 and 900 °C temperature with Ag*NP* (h_{Au} = 10 nm) on the surface, compared to as-deposited TiO_2 and annealed TiO_2. However, no particular correlation between the parameters of Au*NP* and the photocatalytic efficiency was observed.

3.3. Formation and Investigation of a Hybrid Photoelectrode

3.3.1. Implementation of a Substrate Material for Charge Carrier Transfer: Energy Band Alignment between TiO_2 and n-Si

Manufacturing a multi-layered (monolithic) structure as a photocatalyst requires the determination of the energy band alignment throughout the layers. Therefore, ab-initio calculations using the data gathered from the *XPS* spectra, together with optical measurements, with which E_g was estimated, were carried out. Since this study requires high precision, the *XPS* measurements at the Fermi energy level region were done at a resolution of 0.01 eV. The evaluation of *VBM* at this region is done by doing two linear fits: one at the last peak near the Fermi energy level region, and the other one on the baseline in the Fermi energy level region (**Fig. 3.27** and **Fig. 3.29**). The intersection of the two lines presented on the x-axis indicates a value of *VBM* which is 3.21±0.01 eV for the TiO_2 anatase phase.

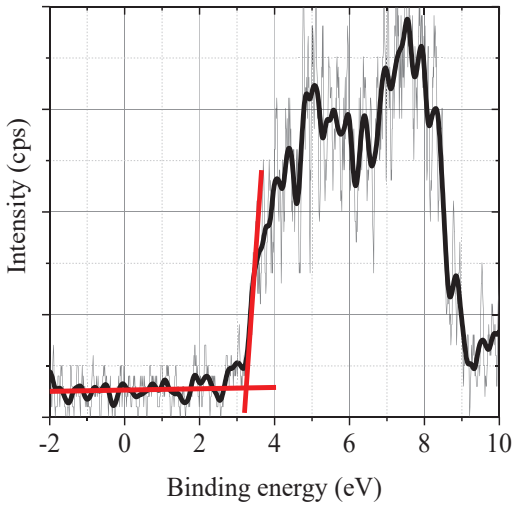

Fig. 3.27. *XPS* spectra of TiO_2 anatase phase thin film at the Fermi energy level region. The intersection of the two lines represented on the x-axis gives a value of *VBM*. The gray curve represents raw scan data, the black curve is the smoothed scan data for more accurate *VBM* evaluation

Analogically, *XPS* analysis was set for three differently doped *n*-type Si substrates: $N_D = 10^{15\text{-}16}$; $10^{17\text{-}18}$; $10^{20\text{-}21}$ cm^{-3}. The full spectra of *n*-type Si are presented in **Fig. 3.28 (a)**. As mentioned above, the *XPS* spectra were calibrated according to the *C 1s* peak (which is at 284.8 eV). The *n*-type Si substrates were cleaned in *Piranha* and in *BHF* solution to avoid any contaminants and the native oxide layer on the surface of the substrates. However, a native oxide layer forms on the surface of Si under atmospheric ambient in a matter of minutes. Thus, it was considered negligibly thin to affect further results. The narrow scan of the Si 2p region (**Fig. 3.28 (b)**) contains two peaks: at 99.5 eV (ref. 99.4 eV) [245, 342] and 101.77 eV, which corresponds to elemental (pure) Si and Si lattice oxide (the native oxide layer),

accordingly [343]. A slight shift to the lower energy values in ΔE_L was detected as the dopant density in *n*-type Si was increasing (**Fig. 3.28 (c)**). According to the *XPS* spectra of the core level Si 2p peak, the binding energy difference between Si 2p and *VBM* was ΔE_L = 98.89±0.01 eV (for *n*-Si with $N_D = 10^{15\text{-}16}$ cm^{-3}), ΔE_L = 98.73±0.01 eV (for *n*-Si with $N_D = 10^{17\text{-}18}$ cm^{-3}) and ΔE_L = 98.60±0.01 eV (for *n*-Si with $N_D = 10^{20\text{-}21}$ cm^{-3}).

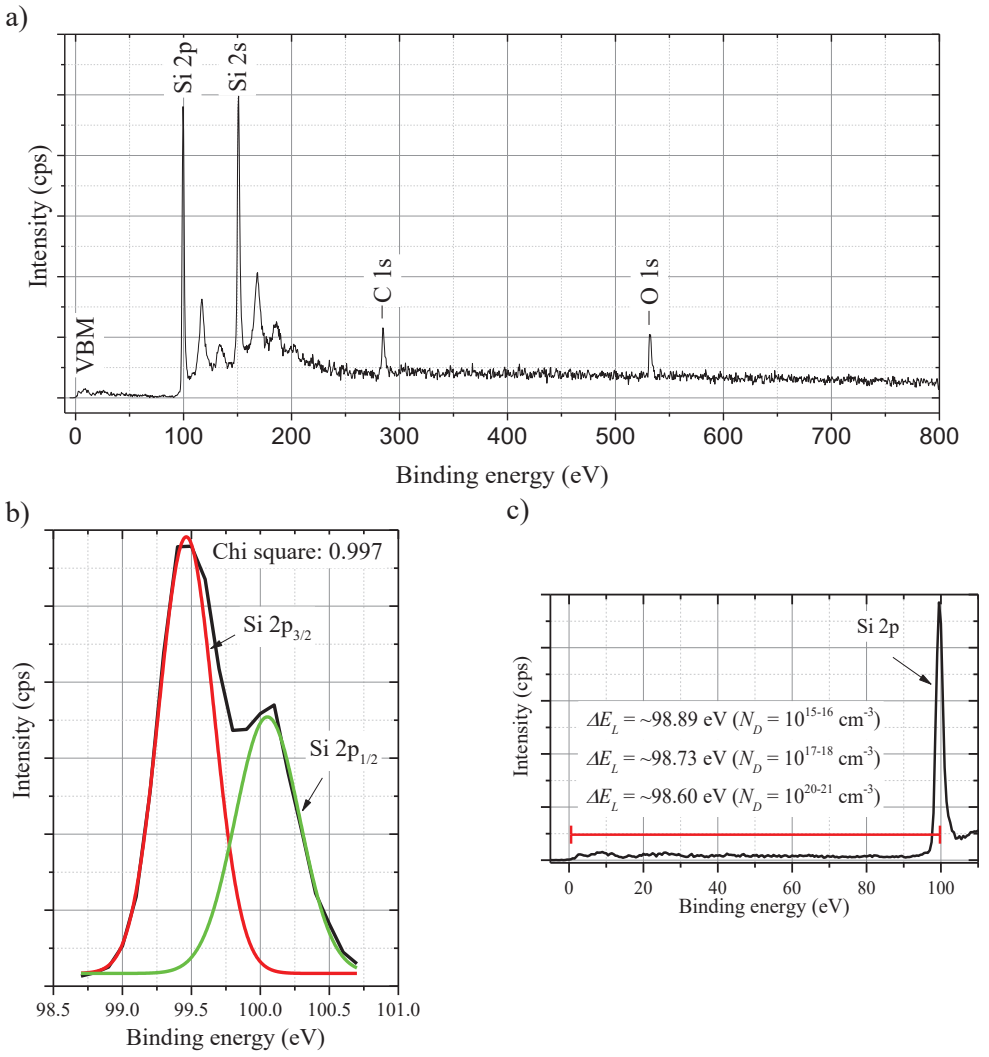

Fig. 3.28. *XPS* spectra of *n*-type Si substrate (a) and core level Si 2p peak (b) together with ΔE_L (c) for *n*-type Si substrates

A slight shift in ΔE_L was caused by the shift in *VBM* with an increased dopant density in the *n*-type Si substrate. As a narrow scan of the Fermi energy region shows (**Fig. 3.29**), the values of *VBM* for *n*-type Si substrates are 0.61±0.01 eV (for *n*-Si with $N_D = 10^{15\text{-}16}$ cm^{-3}), 0.77±0.01 eV (for *n*-Si with $N_D = 10^{17\text{-}18}$ cm^{-3}) and 0.90±0.01 eV

(for *n*-Si with $N_D = 10^{20\text{-}21}$ cm^{-3}). Further calculations were done by using a previously measured E_g = 3.5 eV for TiO_2 anatase phase, and the standard E_g = 1.12 eV for Si was used. Thus, *VBOs* for TiO_2/*n*-Si ($N_D = 10^{15\text{-}16}$ cm^{-3}) was 2.60 eV, TiO_2/*n*-Si ($N_D = 10^{17\text{-}18}$ cm^{-3}) was 2.44 eV, and TiO_2/*n*-Si ($N_D = 10^{20\text{-}21}$ cm^{-3}) was 2.31 eV.

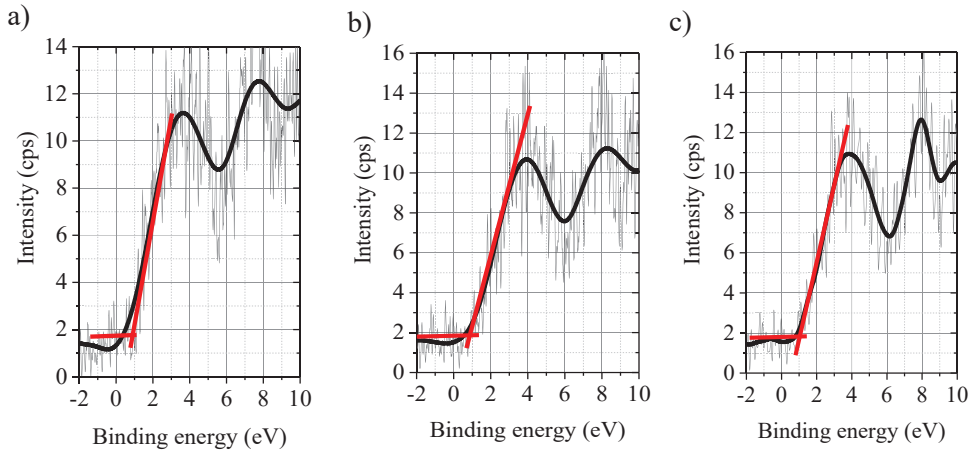

Fig. 3.29. *XPS* spectra of *n*-type Si substrate at the Fermi energy level region: a) $N_D = 10^{15\text{-}16}$ cm^{-3}; b) $N_D = 10^{17\text{-}18}$ cm^{-3}; c) $N_D = 10^{20\text{-}21}$ cm^{-3}. The gray curve represents raw scan data, the black curve is smoothed scan data for more accurate *VBM* evaluation

According to the calculated *VBO* and measured E_g values, *CBOs* for TiO_2/*n*-Si ($N_D = 10^{15\text{-}16}$ cm^{-3}) was -0.22 eV, TiO_2/*n*-Si ($N_D = 10^{17\text{-}18}$ cm^{-3}) was -0.06 eV, and TiO_2/*n*-Si ($N_D = 10^{20\text{-}21}$ cm^{-3}) was +0.07 eV. The negative value of *CBO* indicates that the *CBM* of *n*-Si is at a higher energy level than that of TiO_2, and vice versa. These calculations offer approximate understanding of how the energy band aligns without taking E_F into consideration. Therefore, visual representation of energy band alignment between the two semiconductors provides better understanding (**Fig. 3.30**).

E_F for TiO_2 was measured by the dark-current dependence on the temperature (as $E_A = E_F$), while, for *n*-Si, it was taken from the already known data which represents the E_F value according to the dopant density [344–346]. At the heterojunction, E_{FS} are at the same energy values for both the semiconductor (the energy band alignment), and the depletion layer occurs. Here, the barrier (built-in potential V_{bi}) at the heterojunction is equal to *CBO*. Based on the previous calculations and the visual representation, in the first case scenario (**Fig. 3.30 (a)**), the current flow from TiO_2 to *n*-Si, or the electron flow from *n*-Si to TiO_2 should occur under applied forward bias. However, under reverse bias, the electron flow would be rejected by V_{bi}. With an increased dopant density, V_{bi} becomes lower; therefore, the electron flow would be possible both ways (from TiO_2 to *n*-Si and vice versa), as shown in **Fig. 3.30 (b** and **c)**.

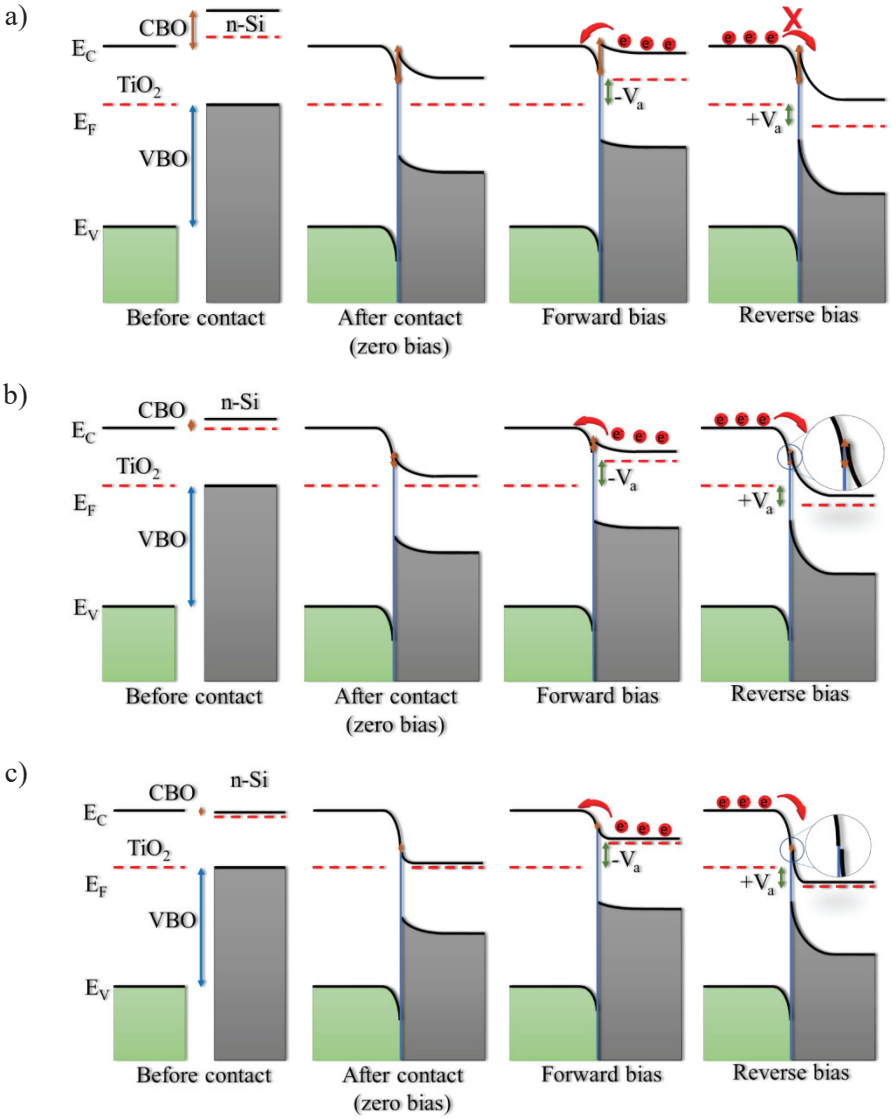

Fig. 3.30. Visual representation of the energy band alignment between TiO_2 anatase phase and *n*-type Si: a) $N_D = 10^{15\text{-}16}$ cm^{-3}; b) $N_D = 10^{17\text{-}18}$ cm^{-3}; c) $N_D = 10^{20\text{-}21}$ cm^{-3}. Forward bias ($-V_a$) corresponds to positive bias connected to TiO_2 and negative bias to *n*-Si, and the opposite is observed for reverse bias ($+V_a$)

Even though the energy band alignment based on the data gathered from *XPS* analysis is reliable, *I-V* measurements were set to prove it (**Fig. 3.31**). As suggested previously, the TiO_2/*n*-Si ($N_D = 10^{15\text{-}16}$ cm^{-3}) heterojunction acts as a Schottky junction (the rectification behavior) under forward bias with a knee voltage of ~1.5 V, and the current increases to almost 15 μA with the applied forward bias of 10 V. On the contrary, the current under reverse bias (up to -10 V) is suppressed to the nA scale (**Fig. 3.31 (a)**).

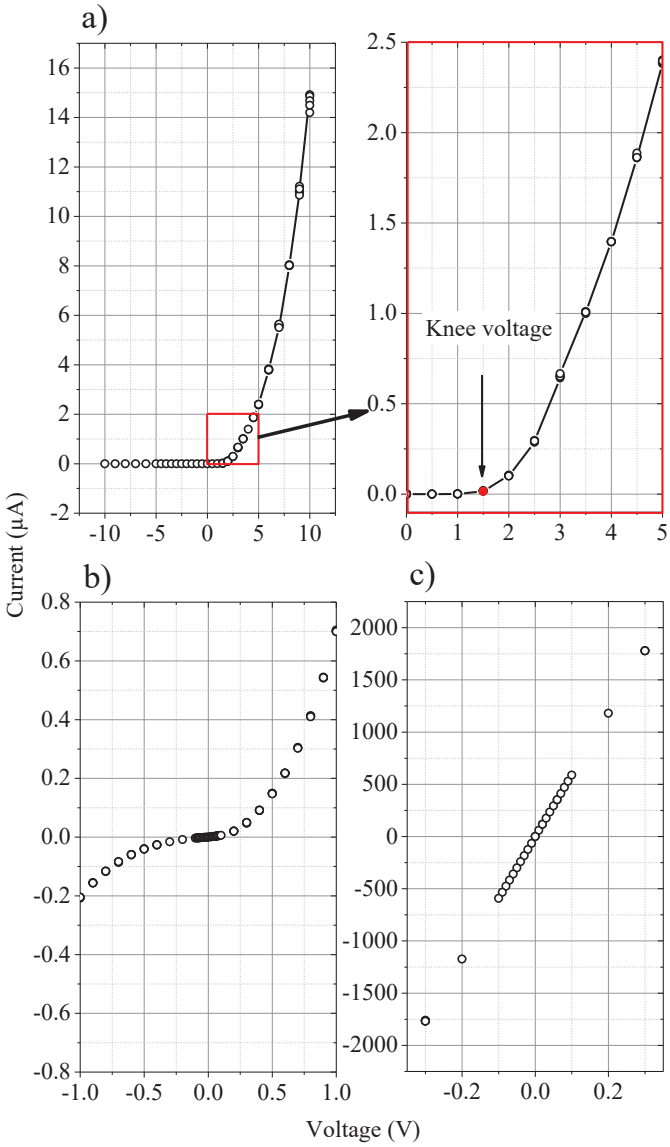

Fig. 3.31. I-V characteristics of TiO_2/*n*-Si heterojunction when *n*-Si with a dopant density of: a) $N_D = 10^{15\text{-}16}$ cm^{-3}; b) $N_D = 10^{17\text{-}18}$ cm^{-3}; c) $N_D = 10^{20\text{-}21}$ cm^{-3} [107]

With an increased dopant density, changes in the I-V characteristics were observed. The heterojunction of TiO_2/*n*-Si ($N_D = 10^{17\text{-}18}$ cm^{-3}) shows a weak rectification behavior with a knee voltage around +0.1 eV, whereas the breakdown voltage was -0.1 eV (**Fig. 3.31 (b)**). Thus, this data is in agreement with the previous calculations. The current increases to almost 0.8 μA and -0.2 μA with 1 V of applied forward and reverse bias, accordingly. Thus, asymmetrical characteristics are observed. The ohmic contact was formed between TiO_2 and *n*-Si ($N_D = 10^{20\text{-}21}$ cm^{-3}), as seen from the I-V graph in **Fig. 3.31 (c)** with the current increasing to almost 2000

μA with the applied forward bias of only 0.3 V. Moreover, the characteristics are symmetrical as the behavior is the same under forward bias and under reverse bias. The rectification behavior may occur because of the relatively wide depletion layer and *CBO* in TiO_2 and the low doped *n*-type Si as a similar behavior was observed in other studies [110, 306]. However, with an increased dopant density, the depletion layer becomes narrow and *CBO* decreases, which results in the electron flow proceeding in both directions. The study on the energy band alignment according to the ab initio calculations from the data gathered by *XPS* analysis has proven to be a reliable method for designing monolithic photocatalysts. Moreover, as the study shows, the energy band alignment is essential for the TiO_2/*n*-Si heterojunction interface [220, 221].

3.3.2. Investigation of the Formed Hybrid Photoelectrode

After examining the conduction band discontinuity in the TiO_2 and *n*-type Si heterojunction interface, a design model of TiO_2 *HPE* was manufactured (**Fig. 3.32**). According to the structure of TiO_2 *HPE*, the internal electric field drives the electrons to the back of the sample, while holes will drift towards the TiO_2 surface, thus decreasing the chance of recombination. A similar process occurs at the Pt-free *CE*, where, based on the internal electric field, electrons will drift to the surface of Pt-free *CE* and holes in the opposite direction. This design should not only decrease the rate of recombination, but also increase the sensitivity of TiO_2 *HPE* under visible light irradiation.

When considering photocatalysis under *UV-vis* light irradiation, low-energy photons from the visible light range passing through the TiO_2 layer will create an electron-hole pair at the *pn* junction (No. 4 in **Fig. 3.32 (a)**). Meanwhile, higher energy photons from the *UV* light range would be absorbed by TiO_2 and create an electron-hole pair at this layer (No. 1 in **Fig. 3.32 (a)**). According to the direction of the internal electric field, holes from the *pn* junction (No. 4 in **Fig. 3.32 (a)**) would drift to the heavily doped *pn* junction (Nos. 2–3 in **Fig. 3.32 (a)**), where they will recombine with an electron from the TiO_2 layer. Therefore, an electron from the *pn* junction (No. 4 in **Fig. 3.32 (a)**) will drift to the Al electrode on the back of TiO_2 *HPE*, where it is connected to a Cu wire, while holes in the TiO_2 layer will be forced to drift to the surface of TiO_2. Then, correspondingly, an electron-hole pair will be created at the *pn* junction of Pt-free *CE*, and, based on the internal electric field, holes will drift to the back of Pt-free *CE*, where they will recombine with an electron from TiO_2 *HPE*. Meanwhile, electrons will drift to the surface of Pt-free *CE*, where they will be trapped by Au or Ag (or other metallic clusters).

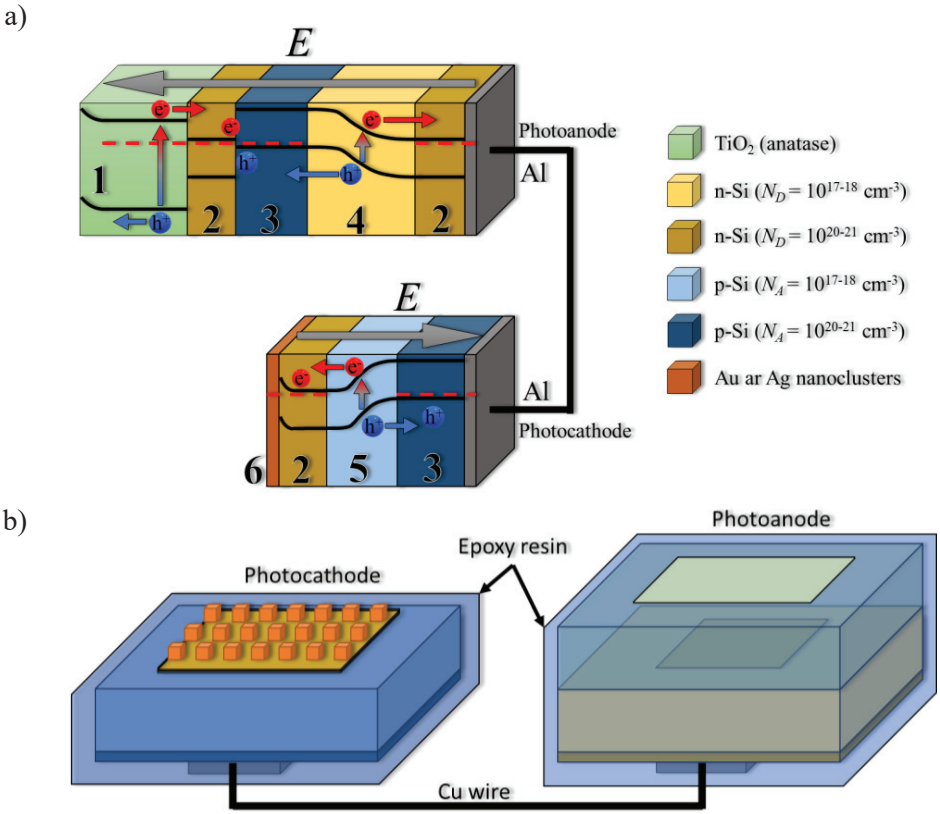

Fig. 3.32. Visual representation of TiO_2 *HPE* and Pt-free *CE* system. a) energy band alignment throughout the layers of TiO_2 *HPE* and Pt-free *CE*; b) final structure of the system prepared for photocatalytic efficiency evaluation. Here, 1 – TiO_2 anatase phase; 2 – *n*-Si ($N_D = 10^{20\text{-}21}$ cm^{-3}); 3 – *p*-Si ($N_A = 10^{20\text{-}21}$ cm^{-3}); 4 – *n*-Si ($N_D = 10^{17\text{-}18}$ cm^{-3}); 5 – *p*-Si ($N_A = 10^{20\text{-}21}$ cm^{-3}); 6 – Au or Ag clusters; E – internal electric field; Al – aluminum electrode

The photoelectrochemical study of TiO_2 *HPE* vs. Pt *CE* was set in three different pH levels: acidic (pH 4.8); neutral (pH 6.2); alkaline (pH 8.8) (**Fig. 3.33**). The *UV* irradiation with an intensity of 0.8 mW/cm^2 was used for all the measurements. The photocurrent density of 0.064; 0.145 and 0.052 $\mu A/cm^2$ at zero bias was observed for acidic, neutral, and alkaline solutions, respectively.

Additionally, the V_{OC} values of 0.91; 0.98, and 0.26 V were achieved when TiO_2 *HPE* vs. Pt was immersed in acidic, neutral, and alkaline solutions. The photocurrent with the applied forward bias dramatically increased in the dark and under *UV* irradiation when the alkaline solution was used, compared to the acidic and neutral solutions. The current increases up to 0.4 $\mu A/cm^2$ (in the dark), whereas the photocurrent increased up to 0.8 $\mu A/cm^2$ (under *UV* irradiation) with the applied forward bias of 1 V and TiO_2 *HPE* vs. Pt *CE* in the alkaline solution. However, under the same conditions, the current (when using the acidic solution) increases up to 0.3 $\mu A/cm^2$ (in the dark), while the photocurrent increases up to 0.017 $\mu A/cm^2$ (under *UV* irradiation) (which is close to V_{OC}).

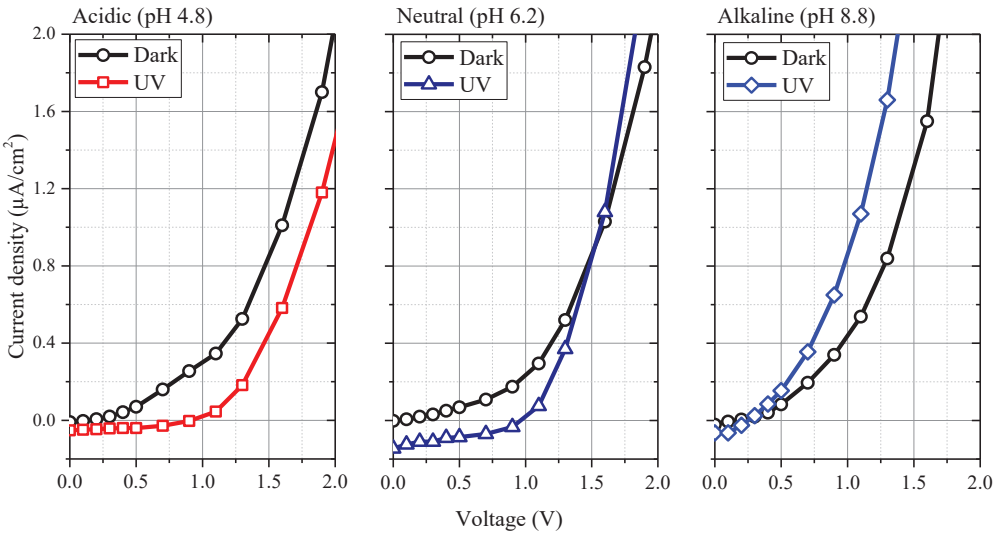

Fig. 3.33. Photoelectrochemical analysis of TiO_2 *HPE* vs. Pt *CE* immersed in three different pH solutions and set under *UV* irradiation [347]

Considering the low light intensity used in this study, the photogenerated current is viable for the TiO_2 *HPE* system. Thus, it is expected that *UV*-vis irradiation would increase the photogenerated current to higher values. A study on stand-alone TiO_2 shows a photocurrent of ~0.3 to 0.6 μA/cm^2 under *UV* irradiation of 3 mW/cm^2 [348, 349]. Meanwhile, under 100 mW/cm^2 intensity (AM 1.5G illumination), the observed photogenerated current was up to 0.2 mA/cm^2 for TiO_2 with an energy bandgap of ~3.15 eV [350]. Moreover, the photocurrent is related to the solution's pH, as, with an increased applied forward bias, the photocurrent increases more when photocatalysts are immersed in the alkaline solution, compared to the acidic ones [351]. Even though it is difficult to analyze the photogenerated current dependence on the pH value due to the fact that it depends on the active photocatalyst [352], the increase in the photocurrent can be attributed to the concentration of OH radicals. OH radicals act as a charge carrier in the circuit of the photocatalyst and the solution [351]. Whilst using TiO_2 as a photocatalyst, the highest photodegradation of methylene blue was reached with pH 6, and there was no difference when using ZnO as a photocatalyst [353]. When considering the photocatalytic efficiency dependence on pH, while using TiO_2 as a photocatalyst, a pH value of 11.5 for Orange II and pH 3 for methyl orange showed the highest photodegradation rates [354, 355]. The process behind these differences can be attributed to the amphoteric behavior of the TiO_2 surface. The surface charge properties of TiO_2 change with a change of the solution's pH. In other words, the pH value affects the sorption-desorption process on the TiO_2 surface and dictates the chance of the photogenerated charge carriers' separation [356–358].

On the grounds of the previous results, further photoelectrochemical analysis of TiO_2 *HPE* and platinum-free *CE* was set in a solution with pH 6.2 (**Fig. 3.34**). Whereas, the structure of Pt-free *CE* is different compared to Pt, an increase in the photogenerated current under *UV* irradiation was observed. The photocurrent

increases to 0.185 μA/cm^2 (for Pt-free *CE* with Au*NP*) and 0.25 μA/cm^2 (for Pt-free *CE* with Ag*NP*) with V_{OC} of ~0.68 V for both *CE*s. Moreover, the photocurrent increases exponentially with an increased forward bias to 2 V: up to 45 μA/cm^2 (for Pt-free *CE* with Au*NP*) and up to 105 μA/cm^2 (for Pt-free *CE* with Ag*NP*). This is 10 to 100 times higher compared to Pt *CE*. Such a difference in the photogenerated current while using Pt-free *CE* is associated with additional electrons injected into the TiO_2 *HPE*/Pt-free *CE* circuit from the *pn* junction at *CE*.

Additional measurements were done to analyze the stability of the TiO_2 *HPE* and platinum-free *CE*s system (**Fig. 3.34 (c)**). The measurement was set under zero applied bias for up to 60 min to observe if are any fluctuations can be observed in the photogenerated current. As seen from the graph, all the three systems offered high stability, with fluctuations of ~0.004 to 0.008 μA/cm^2.

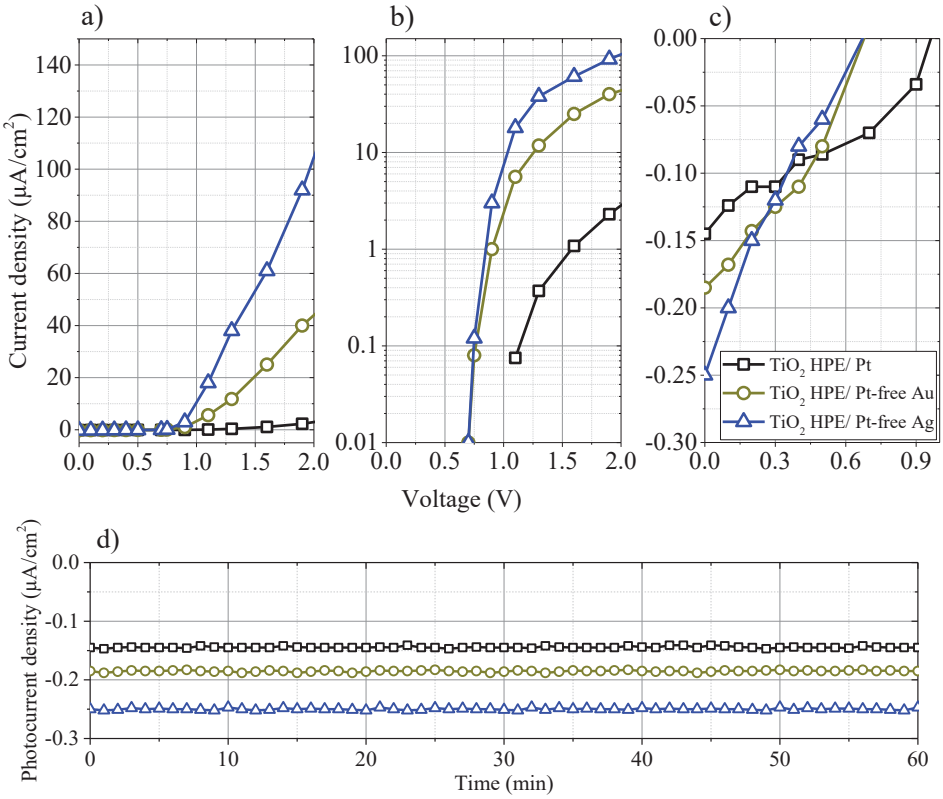

Fig. 3.34. Photoelectrochemical analysis of TiO_2 *HPE* vs. Pt and Pt-free *CE* in neutral solution under *UV* irradiation. a) J-V measurement; b) semi-log plot of J-V measurement; c) close-up graph of (a); d) photogenerated current at zero bias in time [347]

The difference between the Pt-free *CE*s is attributed to the work function of Au (~5.1 to 5.47 eV) and Ag (~4.26 to 4.73 eV). Nevertheless, the depletion layer which forms at the Au or Ag and *n*-type Si heterojunction plays a secondary role in the charge carrier transportation. Based on the calculations, the depletion layer for Au and the *n*-type Si heterojunction (W = 1.11–4.13 nm, with a built-in potential of 1.05 to 1.42 eV)

is higher compared to Ag and the *n*-type Si heterojunction (W = 0.36–2.72 nm with the built-in potential of 0.21 to 0.68 eV) (**Fig. 3.35**).

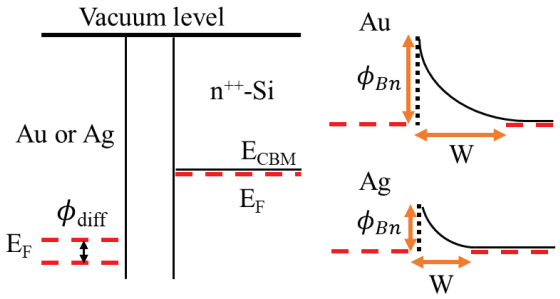

Fig. 3.35. Visual representation of *n*-type Si and Au or Ag heterojunction

3.3.3. Summary of the Results

The ab-initio calculations for the energy band alignment between TiO_2 and n-type Si show that alignment can be done by increasing the dopant's density in n-type Si. Even though there are suggestions of adding an interlayer between TiO_2 and Si for the energy band alignment [222], it might negatively affect the overall photocatalytic efficiency of TiO_2/Si *HPE*. The calculated *CBO* between TiO_2 and Si substrates of various n-types is in agreement with the further I-V characteristics showing that the ohmic contact forms between TiO_2 and the n-type Si substrate with a dopant density of $10^{20\text{-}21}$ cm^{-3}, whereas a weak and strong rectifying behavior was observed for the n-type Si substrate with a dopant density of $10^{17\text{-}18}$ cm^{-3} and $10^{15\text{-}16}$ cm^{-3}, respectively. This suggests that the ab-initio calculations from the data gathered by *XPS* are reliable and can be used for the energy band alignment before the formation of combined structures.

To conclude, the energy band alignment is crucial in designing a monolithic photocatalyst or a hybrid photoelectrode of two semiconductors. The data gathered from the *XPS* study, along with the implemented analysis based on this study, can be considered relatively accurate for the energy band alignment before the actual preparation of the photocatalyst. Considering a photocatalytic application and photogenerated charge carrier separation, the internal electric field which occurs based on the structure of the photocatalyst must be considered beforehand in order to enhance the charge carrier separation. Consequently, the proposed and analyzed conceptual design of TiO_2/Si *HPE* shows a considerably good photocatalytic efficiency based on the photogenerated current under *UV* irradiation, where TiO_2/Si *HPE* vs. a platinum electrode achieved a photocurrent density of ~0.145 $\mu A/cm^2$. An increase in photocurrent density was observed when using a platinum-free photoelectrode as the counter electrode, which resulted in ~0.25 $\mu A/cm^2$ (where Ag clusters were deposited on the Pt-free photoelectrode surface) and ~0.185 $\mu A/cm^2$ (where Au clusters were deposited on Pt-free photoelectrode surface). The difference in the photocurrent density between the two platinum-free photoelectrodes can be attributed to the barrier height and depletion layer which forms at the Si and Au (W =

1.11 – 4.13 nm; $\phi_{Au/Si}$ = 1.05–1.42 eV) or Ag (W = 0.36–2.72 nm; $\phi_{Ag/Si}$ = 0.21–0.68 eV) interface.

However, further analysis still has to be done under simulated solar light irradiation to reach the full potential of the prepared structure. Nevertheless, a conceptual design of a platinum-free photoelectrode has been proposed and analyzed, which resulted in a higher photocurrent compared to the platinum electrode. This suggests that a platinum-free photoelectrode, which consists of a Si photocell and Ag nanoparticles on the surface, may be a cost-effective alternative for the platinum electrode.

CONCLUSIONS

1. The optical bandgap of the deposited TiO_2 thin films depends on the thin film thickness rather than on the morphology. The results show an exponential decline with increased thin film thickness from ~3.8 eV for ~200 nm to ~3.25 eV for ~2400 nm. Thus, it suggests that the wide energy bandgap of TiO_2 can be optimized by controlling the thickness of the deposited thin film. However, a more profound analysis and additional measurements are still required for better understanding of such phenomena in our case.

2. TiO_2 thin films deposited by *RMS* and from STS-21 hydrosol by spin-coating on Si substrate require an annealing temperature of ~850 to 1000 °C for the phase transition to begin. Moreover, the dependence of the as-deposited TiO_2 structure on the deposition parameters by *RMS* suggested that the TiO_2 anatase phase or the TiO_2 rutile phase can be formed without additional annealing. TiO_2 thin films deposited by setting the p_{O_2}/p_{tot} ratio of 20% resulted in an as-deposited TiO_2 rutile phase, rather than in an amorphous phase.

3. The study of the TiO_2 anatase phase and the TiO_2 rutile phase shows that the latter contains a lower concentration of oxygen vacancies (on the grounds of *XPS* analysis) than the former. This was proven by the dark-current dependence on the reciprocal temperature measurements with a result of the activation energy of 0.472 and 0.902 eV for TiO_2 anatase and rutile phases, respectively.

4. The photocatalytic efficiency of TiO_2 thin films increases up to 8 times when a 3x3 grid pattern is used, compared to plain TiO_2. The 50% decolorization of methylene blue was reached in 90 min with a-TiO_2 and in 11 min with a-TiO_2 deposited on a 3x3 μm grid pattern. With an increased size of the period to the 5x5 grid, the efficiency slightly decreased, thus ultimately reaching 50% decolorization in 25 min.

5. The apparent rate constant has an exponential decline with an increased Mg, Cu, and Ni dopant concentration in TiO_2. The evaluated Fermi energy level was 0.60 eV (for TiO_2/Mg); 0.64 eV (for TiO_2/Ni) and 0.23 eV (for TiO_2/Cu). Moreover, on the basis of the work function, the barrier at the interface is 0.74; 0.13–0.50 and 0.64–0.82 eV at the TiO_2/Mg; TiO_2/Cu; and TiO_2/Ni interface, respectively. The photocatalytic degradation of oxalic acid shows that the highest apparent rate constant was achieved with TiO_2/Cu*NC* (0.6 wt.%), followed by TiO_2/Mg*NC* (0.9 wt.%) and TiO_2/Ni*NC* (0.5 wt.%).

6. Au*NP* formation on the TiO_2 surface enhances the photocatalytic activity, which resulted in 50% decolorization of RhodamineB in less than 80 min for TiO_2/Au*NP* (h_{Au} = 10 nm), whereas, for TiO_2, the same decolorization was reached in over 120 min.

7. The energy band alignment between TiO_2 and Si photocell was done by increasing the dopant density to $N_D = 10^{20\text{-}21}$ cm^{-3} in the n-type Si layer. The formed TiO_2/Si *HPE* and platinum-free photoelectrode with Ag clusters on the surface resulted in a photocurrent density of ~0.25 μA/cm^2, whereas for a platinum-free photoelectrode with Au clusters, the value was ~0.185 μA/cm^2, and for the platinum electrode it was 0.145 μA/cm^2.

SANTRAUKA

ĮVADAS

Fotokatalizė gali būti pritaikoma daugelyje sričių; tačiau svarbiausia tai, jog šis procesas gali tiesiogiai ar netiesiogiai prisidėti prie klimato kaitos kontrolės. Remiantis teršalų koncentracijos ore didėjimu bėgant metams, didžiausias dėmesys šiuo metu skiriamas oro bei vandens valymo mechanizmams, paremtiems fotokatalizės procesu, ar kitiems tvarios energijos gavybos būdams [1–4]. Pagrindiniai fotokatalizės metu vykstantys procesai yra krūvininkų fotogeneracija, jų rekombinacija arba sustabdymas, taip pat oksidacijos-redukcijos reakcijos. Pirmieji trys procesai vyksta fotokatalizatoriaus (puslaidininkio) viduje, kai fotonas, kurio energija yra lygi draustinės juostos pločiui arba už jį didesnė, sutikęs kelyje elektroną, jį sužadina ir sugeneruoja elektronų-skylių poras. Elektronai gali laisvai judėti puslaidininkyje, iki kol savo kelyje sutinka priešingo krūvio dalelę (įvyksta rekombinacija) arba jie „pagaunami“ taškinių defektų, kuriuose jų judėjimas yra ribojamas [5–7]. Kita vertus, oksidacijos-redukcijos reakcijos vyksta medžiagos paviršiuje, t. y. sąlytyje tarp tirpalo (elektrolito) ir fotokatalizatoriaus. Šio proceso našumas priklauso nuo krūvininkų rekombinacijos, aktyvaus paviršiaus ploto bei fotokatalizatoriaus oksidacijos-redukcijos potencialų [8].

Pagrindiniai ir plačiai straipsniuose sutinkami puslaidininkiai yra TiO_2, ZrO_2, WO_3, NbO_2, Nb_2O_5, SnO_2, In_2O_3, Ga_2O_3, GeO_2 ir Fe_2O_3 [9, 10]. Atsižvelgiant į tai, jog išvardytų puslaidininkių fotokatalizinis našumas yra sąlygiškai nedidelis, siūloma formuoti jų kombinacijas. Šiuo atveju svarbiausia atsižvelgti į energinių juostų išsidėstymą ir sulygiavimą per visą struktūrą (jeigu ji sudaryta iš dviejų ar daugiau puslaidininkių). Atvejais, kai energinių juostų sulyginimas nėra įmanomas, tai galima padaryti į struktūrą įterpiant plonus metalo ar kito puslaidininkio sluoksnius. Kruopščiai atrinkus tinkamus puslaidininkius ir suformavus daugiasluoksnes fotokatalizines struktūras susidaro vidinis elektrinis laukas, kuris gali pagerinti fotokatalizinio proceso našumą padidindamas krūvininkų atskyrimo tikimybę (skylės judės elektrinio lauko kryptimi, o elektronai – priešinga kryptimi) [11, 12]. Remiantis T. Munawar ir kt. atliktu tyrimu, kombinuota $TiO_2/WO_3/CeO_2$ sistema pasižymėjo geresnėmis fotokatalizinėmis savybėmis nei atskiri jos komponentai: TiO_2 ar WO_3 [13]. Šį padidėjusį našumą autoriai aiškina krūvininkų atskyrimu dėl susidariusio vidinio elektrinio lauko. Negana to, D. Chen ir kt. pateikė išsamų palyginimą tarp TiO_2, TiO_2/rGO (rGO – redukuotas grafeno oksidas) ir TiO_2/*NS*rGO (*NS* – nanosferiniai) naudojant platiną kaip bendrąjį katalizatorių [14]. Pirmuoju atveju (TiO_2/rGO) fotogeneruotieji krūvininkai būdavo sėkmingai atskiriami TiO_2 ir rGO sandūroje, tačiau, autorių nuomone, rekombinacija vis dar galėjo įvykti rGO pusėje. Tokiu atveju buvo pasiūlyta pakeisti pluoštinę rGO struktūrą į nanosferinius darinius. Buvo manoma, kad tokiu atveju *NS*-rGO ne tik dalyvautų atskiriant krūvininkus, tačiau ir taptų krūvininkų spąstais sulaikydami juos vidiniuose nanosferų sluoksniuose. Norint tiksliai išmatuoti rekombinacijos procesą reikalingos brangios sistemos arba sudėtingi matavimai. Negana to, fotokatalizės proceso metu, vykstant rekombinacijos procesui, lygiagrečiai vyksta ir cheminės reakcijos bei fizikiniai

procesai, kurie gali daryti įtaką rekombinacijos matavimams. Tokiu atveju, energinių juostų sulyginimas daugiasluoksnėje struktūroje gali suformuoti prielaidą, kaip elektrono-skylės pora elgsis vienu ar kitu atveju. Taip pat svarbu nuspręsti, kokiems procesams bus naudojamas fotokatalizatorius. Kitaip tariant, fotokatalizatorius gali būti naudojamas kaip fotoanodas (oksidacijos reakcijoms) arba fotokatodas (redukcijos reakcijoms). Šiuo atveju T. Marino ir kt. atliko tyrimą, kurio metu naudojo TiO_2/Au kaip fotoanodą ir CeO_2/Au kaip fotoanodą ir fotokatodą, taip pat atvirkščiai [15]. Remiantis autorių pateiktais rezultatais, didžiausias fotokatalizinis efektyvumas (beveik 7 kartus didesnis) yra pasiekiamas TiO_2/Au naudojant kaip fotoanodą, o CeO_2/Au – kaip fotokatodą, bet ne atvirkščiai. Tai nenuostabu, nes TiO_2 pasižymi ypatingomis oksidacinėmis savybėmis, ir jo panaudojimas fotoanodo struktūroje sąlygoja geresnį našumą. Dažnu atveju platinos elektrodas yra naudojamas kaip katodas, ant kurio vyksta redukcijos reakcijos [16, 17]. Vis dėlto, nepaisant gerų redukcinių savybių, platinos kaina yra per didelė, kad ši medžiaga būtų naudojama komerciškai. Tokiu atveju ieškoma alternatyvų, kurios kainos ir našumo santykiu pranoktų platinos elektrodą. Taip pat, remiantis atliekamų tyrimų gausa ir jų tikslais, plačiausiai tiriamas ar naudojamas puslaidininkis yra TiO_2. Jis naudojamas kaip pagrindinis fotokatalizatorius arba kaip apsauginis sluoksnis kitiems fotokatalizatoriams [18, 19]. Toks didelis dėmesys jam skiriamas būtent dėl to, kad TiO_2 pasižymi neįprastomis oksidacinėmis savybėmis, taip pat yra termodinamiškai stabilus ir atsparus fotokorozijai [20]. Verta paminėti, jog norint lyginti skirtingas fotokatalizines struktūras svarbu išlaikyti tas pačias matavimo sąlygas: šviesos šaltinis ir jo galingumas, elektrolito ar organinių dažų koncentracija. Remiantis kitų mokslininkų atliktais tyrimais vandenilio fotogeneravimui iš vandens naudojant fotokatalizatorių, į vandenį papildomai įmaišomas tam tikras kiekis „aukojamo“ tirpalo. Jis padidina vandenilio jonų koncentraciją tirpale, dėl to gautas galutinis sistemos našumas vandenilio gavybai gali skirtis nuo realių rezultatų – vandenilio gavyba iš gryno vandens (be priemaišų).

Remiantis pateikta informacija, šioje disertacijoje pagrindinis dėmesys skiriamas TiO_2 plonoms dangoms bei jų modifikacijoms, skirtoms fotokatalizės proceso pritaikymui. Tyrimai buvo atlikti stengiantis išlaikyti nekintančias sąlygas, kai taikomos skirtingos matavimo metodikos. Šioje disertacijoje ištirta TiO_2 kristalizacijos ir morfologijos priklausomybė nuo formavimo metodikų ir formavimo parametrų. Negana to, atliktos kelios TiO_2 modifikacijos norint padidinti fotokatalizinį efektyvumą. Šiuo atveju TiO_2 buvo legiruojamas kitais metalais, formuojamos nanostruktūros ant paviršiaus ir formuojamas hibridinis TiO_2/Si fotoelektrodas. Taip pat suformuotas fotokatodas, neturintis savyje platinos, kaip alternatyva platinai. Suformuotos struktūros buvo tiriamos pasitelkiant FE-SEM, XRD, XPS, AFM, I-V, taip pat fotolaidumo ir tirpalų fotodestrukcijos matavimo metodikas.

Disertacijos tikslas

Šio darbo tikslas – ištirti skirtingus TiO_2 modifikavimo metodus norint pagerinti fotokatalizines savybes.

Norint pasiekti šį tikslą, buvo iškelti ir išspręsti tokie uždaviniai.

1. Suformuoti plonasluoksnes TiO_2 struktūras taikant fizikinį garų nusodinimo ir zolių-gelių metodą nusodinant TiO_2 dangas iš tirpalo.
2. Išanalizuoti plonasluoksnių TiO_2 dangų kristalines bei morfologines savybes ir jų priklausomybę nuo formavimo parametrų.
3. Suformuoti modifikuotas TiO_2 plonasluoksnes struktūras ir ištirti jų fotokatalizinį efektyvumą, taip pat atlikti lyginamąją analizę su grynu TiO_2.
4. Atlikti energinių juostų analizę TiO_2 ir Si sandūroje, taip pat, remiantis gautais rezultatais, suformuoti hibridinį TiO_2 fotoelektrodą. Papildomai suformuoti platinos savyje neturintį fotokatodą ir ištirti bendros sistemos fotokatalizines savybes.

Darbo naujumas

Magniu, variu ir nikeliu legiruotų TiO_2 plonasluoksnių struktūrų formavimas RMS metodu, taip pat priemaišų koncentracijos optimizavimas TiO_2 struktūroje, siekiant padidinti fotokatalizinį efektyvumą. Fotokatalizės proceso efektyvumo nustatymas išlaikant tas pačias matavimo sąlygas, kai siekiama ištirti priemaišų ir jų koncentracijos įtaką TiO_2 fotokatalizinėms savybėms. Papildomai atliktas aukso nanodarinių formavimas RMS metodu ant plonasluoksnių TiO_2 struktūrų paviršiaus, apskaičiuota šių nanodarinių formavimosi priklausomybė nuo formavimo parametrų ir TiO_2 morfologijos. Taip pat atliktas fotokatalizinių savybių matavimas ir nustatyta, kaip jos priklauso nuo suformuotų aukso nanodarinių parametrų. Galiausiai suformuotas hibridinis TiO_2/Si fotoelektrodas ir platinos savyje neturintis fotokatodas kaip alternatyva platinos elektrodui, taip pat ištirtos suformuotų struktūrų fotokatalizinės savybės.

1. EKSPERIMENTINĖ ĮRANGA

1.1. Plonų titano dioksido dangų formavimas

Titano dioksido plonų dangų formavimas buvo atliekamas dviem skirtingais metodais: taikant fizikinį garų nusodinimą (reaktyvųjį magnetroninį dulkinimą) ir zolių-gelių metodą (naudojant STS-21 TiO_2 hidrozolį [234]). Fizikinio garų nusodinimo metu buvo naudojama Kurto J. Leskerio sistema [233]. Plonos titano dioksido dangos buvo formuojamos naudojant du titano katodus (99,995 % grynumo), suformuojant apie 200 nm storio dangas. Suformuotos dangos pasižymėjo amorfine TiO_2 struktūra, tačiau papildomas iškaitinimas aukštoje temperatūroje (apie 500–900 °C) inicijuodavo kristalizacijos procesą TiO_2 struktūroje, išgaunant anatazo ar rutilo struktūras. Antra vertus, formuojant plonas TiO_2 dangas zolių-gelių metodu, suformuotos dangos (be papildomo iškaitinimo) pasižymėjo anatazo struktūra. Papildomas iškaitinimas (esant 800–1000 °C temperatūrai) leisdavo suformuoti anatazo-rutilo mišinį ar rutilo struktūras.

1.2. Nanodarinių formavimas ant TiO_2 paviršiaus

Aukso nanodariniai buvo formuojami taikant jau minėtą Kurto J. Leskerio fizikinį garų nusodinimo metodą. Šiuo atveju buvo naudojamas vienas Au katodas (99,995 % grynumo), norint suformuoti skirtingo storio plonus Au sluoksnius. Nanodarinių formavimas buvo atliekamas taikant iškaitinimo aukštoje temperatūroje procedūras. Šiuo atveju, plonos Au dangos (5, 7,5 ir 10 nm storio), suformuotos ant plonų TiO_2 dangų, buvo kaitinamos vakuume 60 minučių esant 500 °C temperatūrai.

1.3. Suformuotų struktūrų analizės metodai

Paviršiaus morfologija buvo tiriama taikant elektrinio lauko emisijos skenuojamosios elektroninės mikroskopijos metodą (FE-SEM, JEOL, JSM-7600F) [235]. Šio metodo dėka buvo galima ištirti suformuotų dangų paviršiaus ir skerspjūvio morfologiją. Gautos nuotraukos buvo analizuojamos „ImageJ“ programine įranga.

Suformuotų plonų TiO_2 dangų struktūrinė analizė atlikta taikant rentgeno spindulių difrakcijos metodą (XRD, Rigaku RINT Ultima-III XR) [237]. Gauti duomenys apdoroti naudojant „Match!3“ programinę įrangą ir „COD20210614“ duomenų bazę. Plonų TiO_2 dangų cheminė struktūra bei elektrinės savybės buvo tiriamos rentgeno spindulių fotoelektroninės spektroskopijos metodu, o gauti duomenys analizuojami „MultiPak“ programine įranga.

Suformuotų aukso nanodarinių analizė buvo atliekama pasitelkiant atominių jėgų mikroskopijos metodą. Šiuo metodu įvertinti ir apskaičiuoti suformuotų nanodarinių parametrai (forma, skersmuo, aukštis, pasiskirstymas ir kt.).

Terminis garų nusodinimo metodas buvo taikomas suformuoti plokštuminiam (angl. *co-planar*) aukso elektrodui ant plonų TiO_2 dangų. Vėliau pasitelkus suformuotą elektrodą buvo tiriama tamsinės srovės priklausomybė nuo temperatūros. Gauti duomenys leidžia apskaičiuoti suformuotų dangų elektronų aktyvacijos energiją.

Ultravioletinės ir regimosios šviesos spektroskopijos metodu buvo tiriamos suformuotų plonų TiO_2 dangų (grynų ir modifikuotų) optoelektroninės savybės, tokios kaip šviesos pralaidumas, draustinės juostos plotis, taip pat struktūrinės savybės, tokios kaip porėtumas.

I-V matavimai buvo atliekami norint ištirti elektrines TiO_2 ir *n*-tipo Si sandūros savybes, taip pat suformuoto Si fotoelemento elektrines savybes. Remiantis gautais rezultatais buvo formuojamas hibridinis TiO_2 fotoelektrodas.

Hibridinio TiO_2 fotoelektrodo formavimui buvo taikomas 9 žingsnių procesas: (1) *n*-tipo silicio plokštelės (priemaišų koncentracija $10^{17–18}$ cm^{-3}) valymas „piranijos“ ir buferiniame hidrofluorido tirpaluose; (2) apsauginis oksido sluoksnio (SiO_2) formavimas ant *n*-tipo silicio plokštelės (apie 500 nm storio); (3) kompiuterinė litografija, formuojant aktyvų fotoelektrodo plotą, kurį supa apsauginis SiO_2 sluoksnis; (4) pakartotinis valymas kaip (1) žingsnyje; (5) paviršiaus legiravimas boru (priemaišų koncentracija $10^{20–21}$ cm^{-3}), formuojant *p*-laidumo sluoksnį ant *n*-tipo silicio plokštelės; (6) pakartojami (3) ir (1) žingsniai; (7) paviršiaus ir dugno legiravimas fosforu (priemaišų koncentracija $10^{20–21}$ cm^{-3}), formuojant *n*-laidumo sluoksnį ant p-laidumo sluoksnio paviršiaus, taip pat plokštelės apačios; (8) pakartojami (3) ir (1) žingsniai; (9) formuojamas plonas TiO_2 sluoksnis ant paviršiaus. Analogiškai buvo atliekamas priešinio fotoelektrodo formavimas (Si fotoelemento pagrindu), tačiau buvo naudojamas *p*-tipo silicio pagrindas ir jo paviršius legiruotas fosforu, vėliau suformuojant aukso bei sidabro nanodarinius ant paviršiaus.

Oksalo rūgšties fotodestrukcijos matavimai buvo atliekami naudojant magniu, variu ir nikeliu legiruotas TiO_2 dangas, nustatant šių dangų fotokatalizinį aktyvumą. Anglies kiekio nustatymui ir jo pakitimui buvo atliekami organinės anglies matavimai (TOC-L, Šimadzu, Japonija), remiantis EN 1484:2002 procedūra. Organinių dažų (rodamino B vandeninio tirpalo) fotodestrukcijos matavimai buvo taikomi norint ištirti plonų TiO_2 dangų su aukso nanodariniais fotokatalizines savybes. Šiuo atveju buvo tiriamas rodamino B tirpalo skaidrumas bėgant laikui. Fotoelektrocheminiai matavimai su skirtingos *p*H tirpalais (4,8, 6,2 ir 8,8), buvo atliekami naudojant hibridinį TiO_2 fotoelektrodą kartu su Si fotoelemento pagrindu sukurtu priešiniu fotoelektrodu ir platinos katodu.

2. REZULTATAI IR JŲ APTARIMAS

2.1. Suformuotų plonų TiO_2 dangų morfologijos ir optinių savybių tyrimas

Zolių-gelių metodu suformuotos plonos TiO_2 dangos (storis apie 672,3 nm) pasižymi dideliu šviesos pralaidumu (80–95 %) regimosios šviesos diapazone (400–800 nm) (**1 pav. (a)**). Taip pat nustatyta, jog draustinės juostos eksponentiškai mažėja, didėjant plonų dangų storiui (arba, kitaip tariant, tankiui) (**1 pav. (b)**). Antra vertus, fizikiniu garų nusodinimo metodu suformuotos plonos TiO_2 dangos (storis apie 200 nm) pasižymi santykinai mažesniu šviesos pralaidumu regimosios šviesos diapazone (**2 pav. (a)**) ir didesniu draustinės juostos pločiu (**2 pav. (b)**). Tačiau, remiantis anksčiau paminėta draustinės juostos pločio priklausomybe nuo dangos tankio, panašu, jog ši priklausomybė yra analogiška ir dangoms, suformuotoms kitais metodais. Negana to, draustinės juostos plotis nežymiai skiriasi lyginant amorfinę bei kristalinę TiO_2 struktūrą (remiantis Tauco priklausomybe (**2 pav. (b)**). Tikėtina, jog tiek zolių-gelių metodu, tiek fizikiniu garų nusodinimo metodu suformuotų plonų TiO_2 dangų draustinės juostos plotis priklauso nuo suformuotų dangų tankio. Dažnu atveju kristalinės anatazo struktūros TiO_2 dangų draustinės juostos plotis gali siekti nuo 3,2 iki 3,5 eV [292]. Tačiau pateiktuose šaltiniuose nėra įvertinamas dangos storis, tankis ar porėtumas.

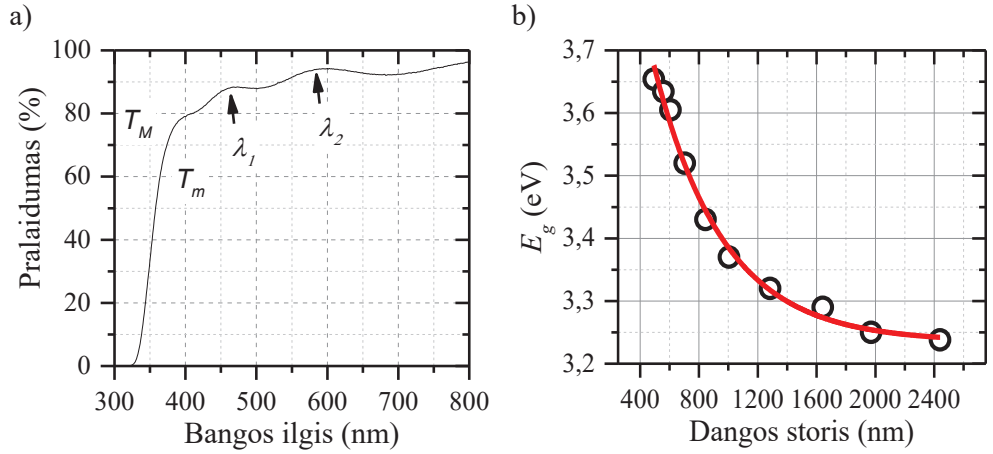

1 pav. Šviesos pralaidumo spektras (a) ir optinės draustinės juostos pločio (E_g) priklausomybė nuo TiO_2 dangų storio (b). T_M ir T_m – kreivės tangento maksimumas ir minimumas, atitinkamai; $\lambda_{1,2}$ – bangos ilgis ties pirmuoju ir antruoju maksimumais

Negana to, galima pastebėti, jog draustinės juostos plotis sumažėja, kai plonos TiO_2 dangos iškaitintos 500 °C temperatūroje, tačiau vėl šiek tiek padidėja, kai iškaitinimo temperatūra pakyla iki 900 °C. Toks draustinės juostos pokytis gali būti sąlygotas kristalizacijos proceso (pirmuoju atveju), kai amorfinė TiO_2 struktūra kristalizuojasi į anatazo fazę. Tačiau antruoju atveju draustinės juostos padidėjimui gali daryti įtaką plonų dangų sutankėjimas, t. y. storio sumažėjimas (remiantis anksčiau pateiktais rezultatais).

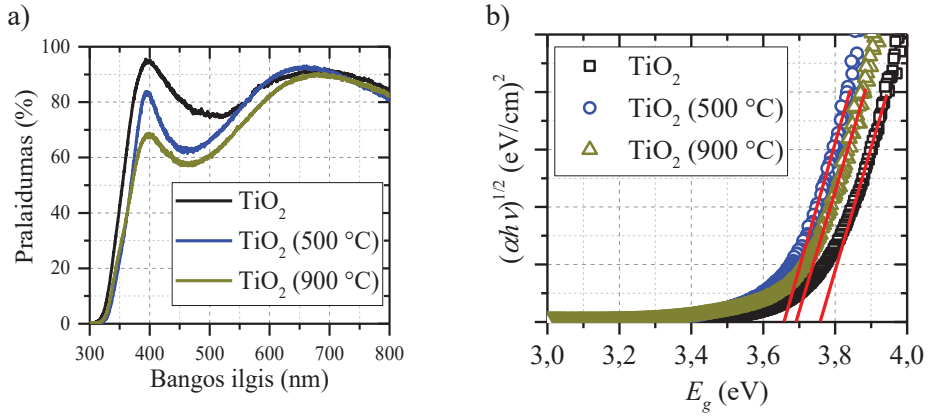

2 pav. Šviesos pralaidumo spektras (a) ir optinės draustinės juostos (E_g) įvertinimas per Tauco priklausomybę (b)

Rentgeno spindulių difrakcijos matavimai atlikti su plonomis TiO_2 dangomis, kurios formuotos zolių-gelių metodu, taip pat iškaitintos skirtingose temperatūrose (**3 pav.**). Šis tyrimas atliktas siekiant plačiau išanalizuoti plonų TiO_2 dangų kristalizacijos kinetiką. Papildomai yra pateikiamos suformuotų dangų paviršiaus ir skerspjūvio FE-SEM nuotraukos.

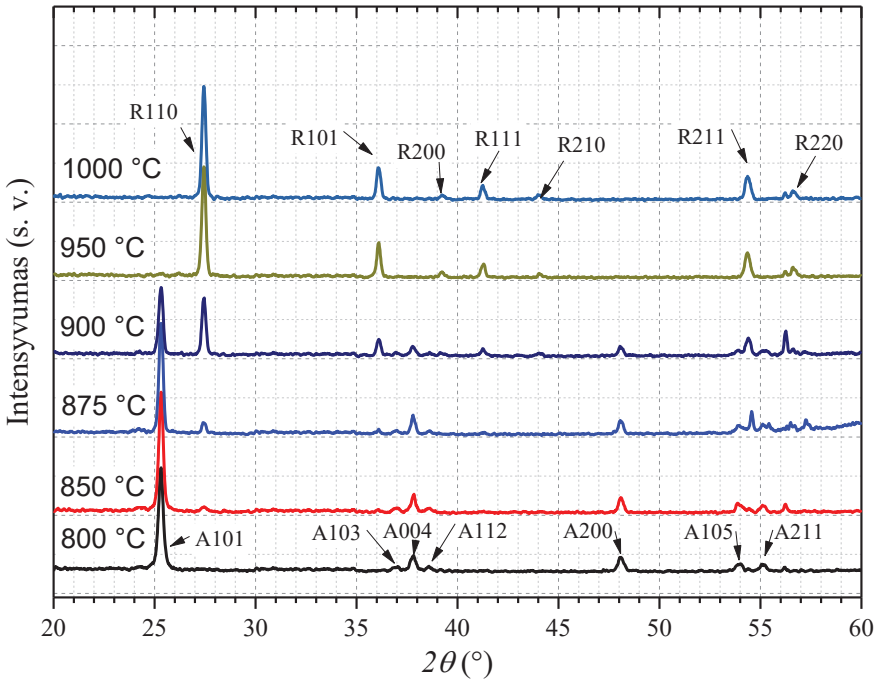

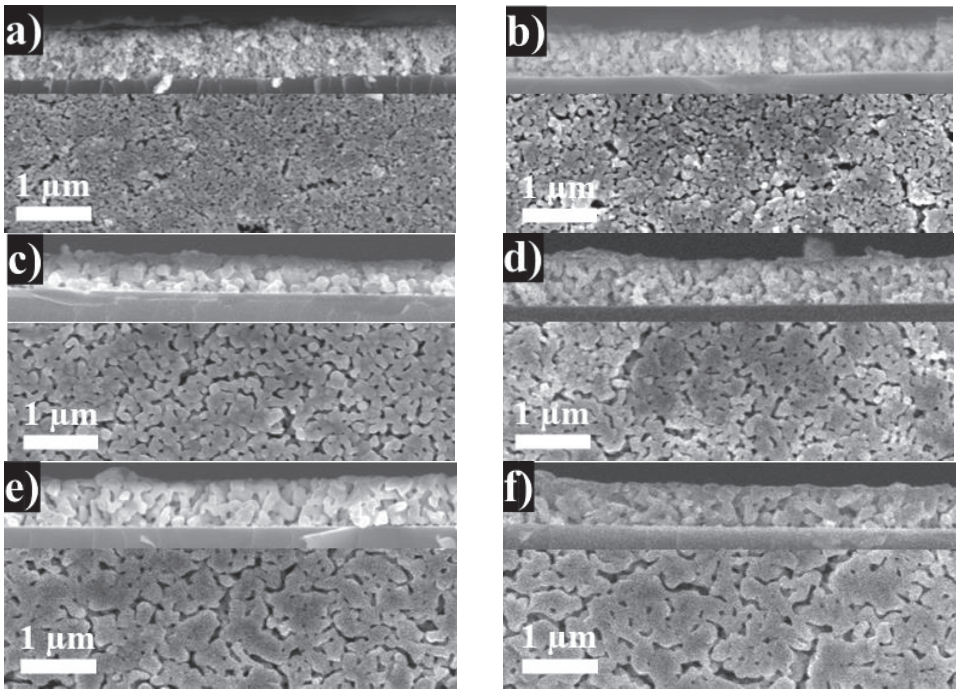

3 pav. Zolių-gelių metodu suformuotų plonų TiO_2 dangų XRD spektras ir atitinkamų dangų paviršiaus bei skerspjūvio nuotraukos. Dangos iškaitintos skirtingose temperatūrose: a) 800 °C; b) 850 °C; c) 875 °C; d) 900 °C; e) 950 °C; f) 1000 °C. Čia A atitinka anatazo fazę, o R – rutilo fazę

Remiantis gautais rezultatais, TiO_2 fazės perėjimas iš anatazo į rutilą prasideda ties 850 °C temperatūra, kai maža dalis rutilo fazės (apie 5 %) buvo užfiksuota XRD spektre. Galutinis fazės perėjimas įvyksta, kai plonos TiO_2 dangos yra iškaitinamos sąlygiškai didelėje 1000 °C temperatūroje. Negana to, STS-21 hidrozolis yra sudarytas iš TiO_2 anatazo fazės miltelių. Taigi didelė temperatūra, reikalinga įvykti rekristalizacijai iš anatazo fazės į rutilo fazę, yra neįprasta remiantis kitų mokslininkų atliktais tyrimais [271, 273]. Vis dėlto mokslininko S. Miszczako ir jo kolegų atliktas tyrimas parodė, jog TiO_2 kristalizacija ar rekristalizacija gali priklausyti nuo padėklo, ant kurio TiO_2 dangos yra formuojamos [274]. Remiantis šių mokslininkų pasiektais rezultatais, amorfiniam TiO_2 kristalizuotis į anatazo fazę reikia 500 °C temperatūros, nepaisant to, koks padėklas yra naudojamas. Tačiau rekristalizacijos procesui, kurio metu anatazo fazę pakeičia rutilo fazė, reikia 800 °C temperatūros, jeigu naudojamas padėklas yra plieno lydinys (304L); 850 °C temperatūros, jeigu naudojamas padėklas yra Co-Cr-Mo lydinys; ir 1000 °C temperatūros, jeigu naudojamas padėklas yra silicio lydinys. Šie rezultatai atitinka mūsų gautus rezultatus, kai TiO_2 rekristalizacijai iš anatazo fazės į rutilo fazę reikalinga 1000 °C temperatūra. Toks skirtumas gali būti paaiškintas padėklo medžiagos difuzija į TiO_2 esant didelei iškaitinimo temperatūrai. Remiantis E. Blanco ir jo kolegų atliktais tyrimais, kai formuojamos plonos TiO_2 dangos ant silicio padėklų, pastebima silicio difuzija į TiO_2 struktūrą [192]. Šis tyrimas atliktas taikant

XPS analizę, kurios metu nustatyta, kad silicio koncentracija TiO_2 struktūroje padidėja, didėjant iškaitinimo temperatūrai. J. G. Yu ir jo kolegos savo straipsnyje teigia, kad TiO_2 rekristalizacijos procesas gali būti sulėtinamas dėl Si difuzijos į TiO_2 gardelę, taip „užrakinant“ ryšius tarp titano ir deguonies atomų [170]. Žinant, jog rekristalizacijos procesas vyksta per ryšių nutraukimus ir naujus susijungimus, tai paaiškintų, kodėl yra reikalinga didesnė iškaitinimo temperatūra (analogiškai didesnė aktyvacijos energija ryšių nutraukimui) naudojant silicio padėklus [165, 284]. Maža to, galima atkreipti dėmesį į pateiktas TiO_2 dangų paviršiaus ir skerspjūvio FE-SEM nuotraukas, kuriose nesunku įžvelgti ploną (apie 20– 25 nm storio) sluoksnį tarp padėklo ir TiO_2, kuris šiek tiek išsiskiria savo struktūra (**3 pav. (e), (f)**). Tikėtina, jog šis plonas sluoksnis gali būti sudarytas iš anatazo fazės kristalų, tačiau norint tuo įsitikinti reikia atlikti papildomus tyrimus. Kadangi tolimesni tyrimai atlikti naudojant plonas TiO_2 dangas, iškaitintas 800 °C temperatūroje, šis fazės perėjimas ir naujos struktūros susidarymas ties 950–1000 °C iškaitinimo temperatūra šalia padėklo nebuvo tiriamas.

Analogiškas tyrimas atliktas formuojant plonas TiO_2 dangas fizikiniu garų nusodinimo metodu. Šiuo atveju pastebėta, kad rekristalizacijos procesas prasideda tik tarp 950 ir 1200 °C temperatūros (**4 pav.**). Skirtumas tarp dangų, suformuotų zolių-gelių metodu ir fizikiniu garų nusodinimo metodu, yra dangos storis (pirmuoju atveju apie 700 nm, antruoju – apie 200 nm) ir porėtumas. Remiantis tuo, jog dangos buvo formuojamos ant tų pačių padėklų, manoma, kad Si difuzija daro didesnę įtaką plonesnėms dangoms, nors lengviau pasireiškia porėtose dangose. Negana to, remiantis pateiktomis plonų TiO_2 dangų paviršiaus FE-SEM nuotraukomis, stebimas grūdelių struktūros susidarymas esant didelėms iškaitinimo temperatūros vertėms. Tai gali būti sąlygota liekamųjų įtempių, susidarančių dėl didelės temperatūros [257].

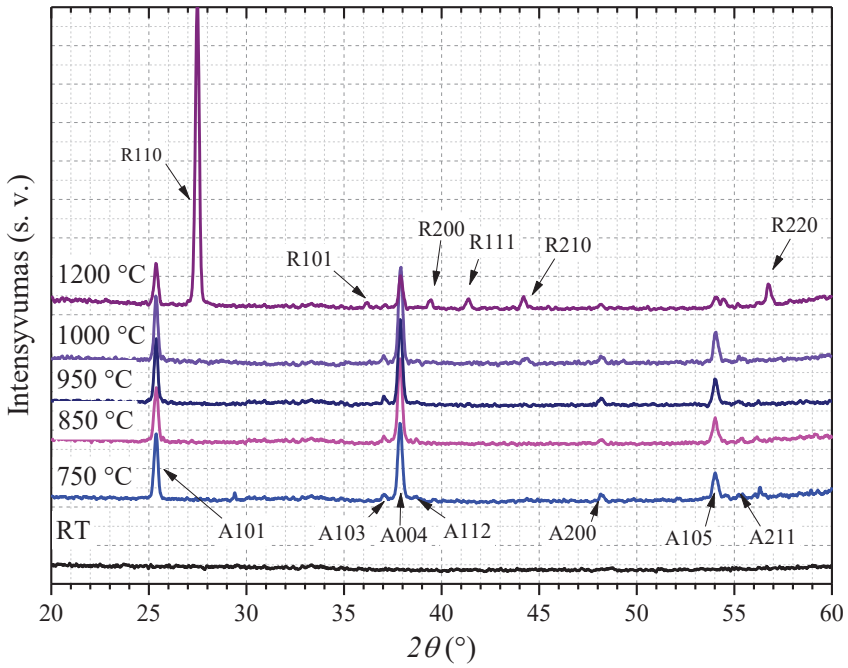

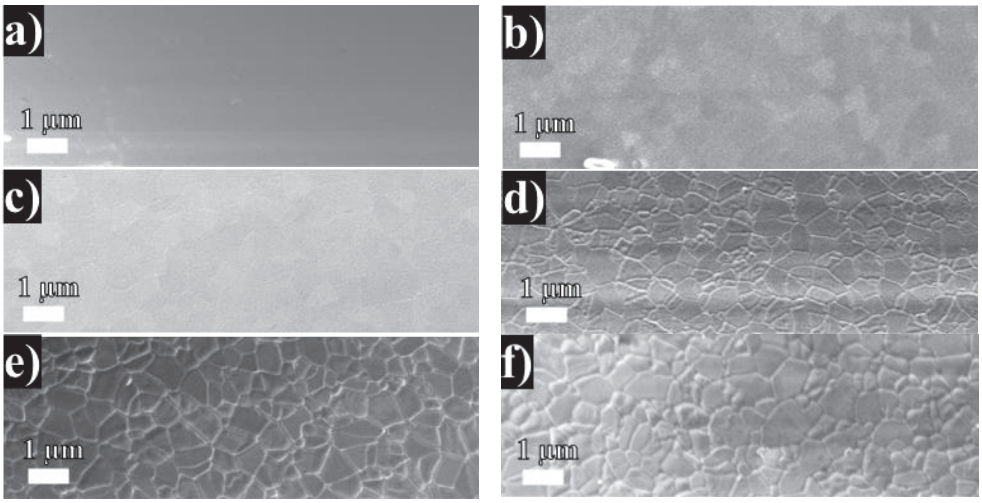

4 pav. Fizikiniu garų nusodinimo metodu suformuotų plonų TiO_2 dangų XRD spektras ir atitinkamų dangų paviršiaus bei skerspjūvio nuotraukos. Dangos iškaitintos skirtingose temperatūrose: a) be papildomo iškaitinimo (RT), °C; b) 750 °C; c) 850 °C; d) 950 °C; e) 1000 °C; f) 1200 °C. Čia A atitinka anatazo fazę, o R – rutilo fazę

2.2. Cheminės ir elektrinės suformuotų plonų TiO_2 dangų savybės

Suformuotų plonų TiO_2 dangų cheminės ir elektrinės struktūros tyrimas atliktas lyginant anatazo (iškaitinimo temperatūra 800 °C) ir rutilo (iškaitinimo temperatūra 1000 °C) kristalines fazes. Remiantis gautais XPS rezultatais pastebėta, jog pagrindinės TiO_2 smailės (Ti 2p) padėtis (rutilo fazėje) kiek pasislenka link mažesnės ryšio energijos (**5 pav. (a), (b)**) lyginant su anatazo faze. Toks poslinkis gali būti dėl rekristalizacijos proceso, kurio metu nutrūksta silpniausi Ti-O ryšiai ir susikuria nauji [300–302]. Visgi daugiau informacijos galima išgauti iš pagrindinės deguonies (O 1s) smailės, jos padėties bei struktūros. Kitaip tariant, kaip tik šioje smailėje esanti laisvųjų deguonies atomų smailė ir jos plotas netiesiogiai nusako elektrines TiO_2 savybes bei fotokatalizinį aktyvumą: didesnė laisvųjų deguonies atomų koncentracija TiO_2 struktūroje reiškia mažesnę aktyvacijos energiją ir kartu mažesnę energiją, reikalingą elektronui peršokti iš Fermi energijos lygmens į laidumo juostą. Šiuo atveju, remiantis XPS matavimais, TiO_2 anatazo fazė turi didesnę laisvųjų deguonies atomų koncentraciją (**5 pav. (c)**) lyginant su rutilo faze (**5 pav. (d)**). Tai patvirtinta atlikus papildomus tamsinės srovės priklausomybės nuo temperatūros tyrimus. Šių tyrimų metu išmatuota ir nustatyta, jog elektronų aktyvacijos energija yra apie 0,472 eV (anatazo fazė) (**5 pav. (e)**) ir 0,902 eV (rutilo fazė) (**5 pav. (f)**). Tai atitinka ankstesnių tyrimų nustatytas vertes šioms fazėms [177–180, 310].

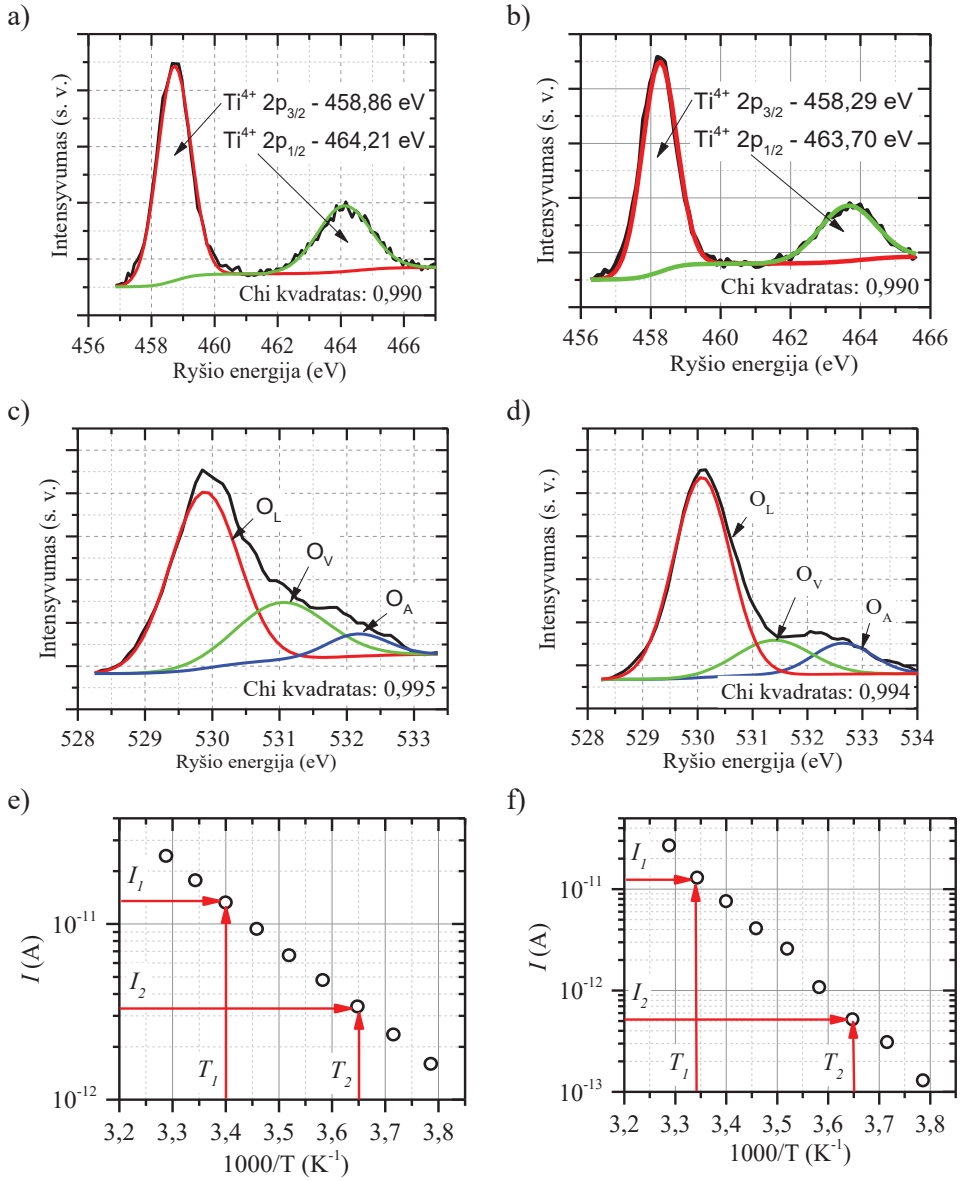

5 pav. Plonų TiO_2 dangų XPS spektrai: a) Ti 2p smailė (anatazo fazė); b) Ti 2p smailė (rutilo fazė); c) pagrindinė deguonies O 1s smailė (anatazo fazė); d) pagrindinė deguonies O 1s smailė (rutilo fazė). Tamsinės srovės priklausomybė nuo temperatūros (e) anatazo fazė ir (f) rutilo fazė

2.3. Legiruotų plonų TiO_2 dangų savybės

Analogiški XPS matavimai atlikti su legiruotomis plonomis TiO_2 dangomis. Plonos TiO_2 dangos legiruotos magniu, variu ir nikeliu. Tyrimų metu nustatyta, jog formuojant legiruotas TiO_2 struktūras, priemaišos taip pat sudaro metalo oksidų junginius (**6 pav. (a), (b), (c)**). Negana to, priemaišos padidina taškinių defektų

koncentraciją TiO_2 struktūroje, tai galime pastebėti iš pagrindinės TiO_2 Ti 2p smailės sudėties. Nors Ti^{3+} gali susidaryti dėl amorfinės TiO_2 struktūros, nurodyto piko intensyvumo skirtumas pagal priemaišas leidžia manyti, jog taškiniai defektai, kurie sąlygoja Ti^{3+} susidarymą, galėjo atsirasti ir dėl priemaišų [305]. Ryšio energijos skirtumas tarp pagrindinės TiO_2 ir deguonies smailių atitinka V. V. Atuchino ir jo kolegų pateiktas vertes [304]. Šių mokslininkų tyrimas rodo, kad ryšio energija tarp minėtų smailių padėčių yra didesnė legiruotame TiO_2 lyginant su grynu TiO_2. Negana to, pastebėta, kad jungtis tarp Ti ir O atomų (Ti^{3+}) ilgėja didėjant priemaišų koncentracijai, to nebuvo pastebėta tarp Ti^{4+} ir O 1s.

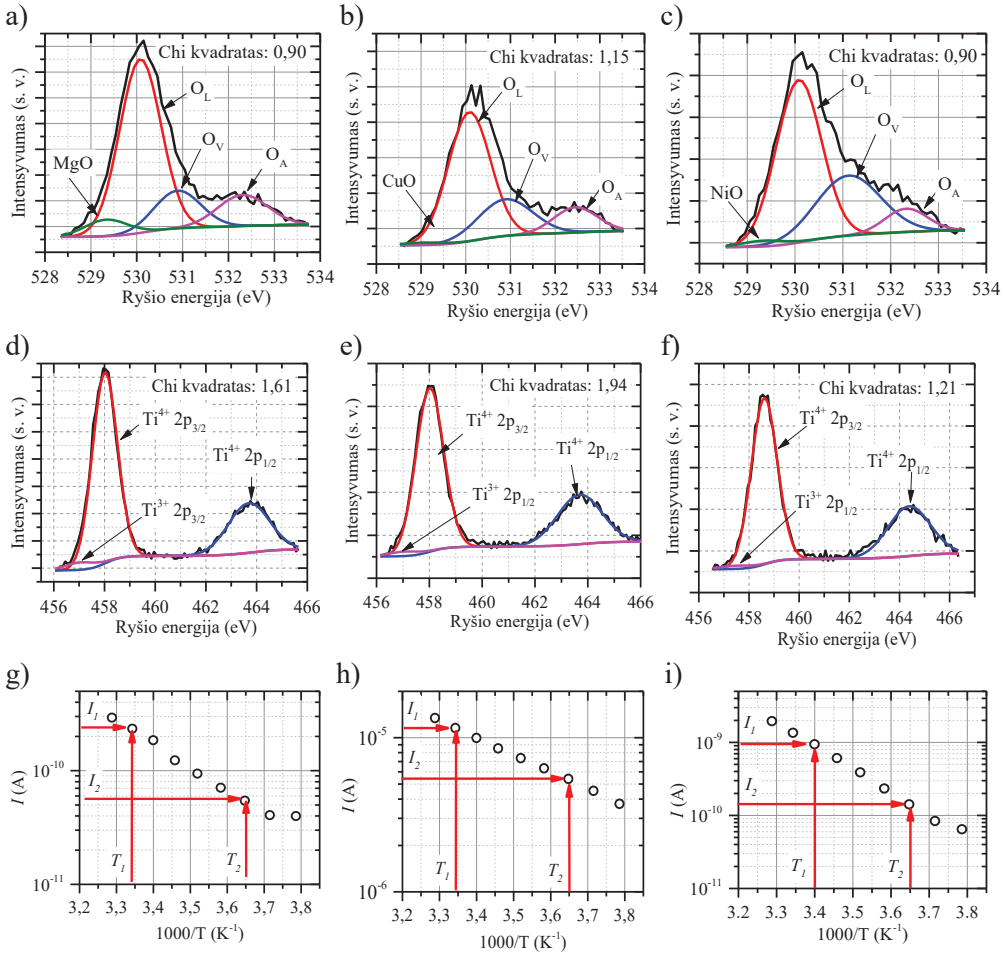

6 pav. Legiruotų TiO_2 dangų XPS spektrai. Pagrindinės deguonies O 1s ir TiO_2 Ti 2p smailės (a), (d) – TiO_2/Mg*NC*; (b), (e) – TiO_2/Cu*NC*; (c), (f) – TiO_2/Ni*NC*, atitinkamai. Tamsinės srovės priklausomybė nuo temperatūros: g) TiO_2/Mg*NC*; h) TiO_2/Cu*NC*; i) TiO_2/Ni*NC*

Tamsinės srovės priklausomybės nuo temperatūros matavimas leido įvertinti, kaip keičiasi Fermi energijos lygmens padėtis TiO_2 draustinėje juostoje esant skirtingoms priemaišoms. Šiuo atveju apskaičiuota aktyvacijos energija suformuotose struktūrose yra 0,60 eV (TiO_2/Mg); 0,23 eV (TiO_2/Cu); 0,64 eV (TiO_2/Ni). Nors šis

matavimas atliekamas suformuotų struktūrų paviršiuje ir matuojama paviršinė srovė, galima manyti, jog analogiškos savybės būdingos ir gilesniems sluoksniams.

Negana to, taip pat, kaip formuojant dviejų ar daugiau puslaidininkių struktūras yra reikalingas energinių juostų sulyginimas, taip ir šiuo atveju galima apskaičiuoti priemaišų ir TiO_2 sandūros susidariusio barjero aukštį (**1 lentelė**). Skaičiavimai atlikti naudojant ankstesniuose straipsniuose pateiktas elektrono darbo funkcijos vertes. TiO_2 ir Mg sandūroje susidariusio barjero aukštis gali siekti iki 0,74 eV; tarp TiO_2 ir Cu – nuo 0,13 iki 0,50 eV; tarp TiO_2 ir Ni – nuo 0,64 iki 0,82 eV.

1 lentelė. Apskaičiuotas sandūros barjero aukštis, remiantis elektrono darbo funkcijos vertėmis [335–337]

	a-TiO_2	Mg	$\Phi_{TiO_2} - \Phi_{Mg}$	Cu	$\Phi_{TiO_2} - \Phi_{Cu}$	Ni	$\Phi_{TiO_2} - \Phi_{Ni}$
Darbo funkcija (Φ, eV)	4,4	3,66	-0,74	4,53–5,10	0,13–0,50	5,04–5,35	0,64–0,82

Remiantis pateiktais rezultatais galima manyti, jog TiO_2 legiravimas variu turėtų žymiau pagerinti fotokatalizines savybes nei legiravimas magniu ar nikeliu. Fotokatalizinio aktyvumo tyrimas parodė, jog fotodestrukcijos greičio konstanta yra didžiausia naudojant TiO_2/Cu*NC* struktūrą, kurioje Cu priemaišų koncentracija yra apie 0,6 %, toliau eina TiO_2/Mg*NC* su 0,9 % priemaišų koncentracija ir TiO_2/Ni*NC* su 0,5 % priemaišų koncentracija. Negana to, nustatyta, kad geriausias fotokatalizinis aktyvumas yra pasiekiamas, kai priemaišų koncentracija TiO_2 struktūroje neviršija 1 % (**7 pav.**). Žinoma tai, jog priemaišos sukuria taškinius defektus, o didėjant jų koncentracijai sąlygiškai gerėja fotokatalizinis aktyvumas. Per didelė minėtų defektų koncentracija gali taip pat padidinti krūvių rekombinacijos tikimybę dėl per mažo atstumo tarp defektų [324]. Remiantis pateiktais rezultatais galima teigti, jog teoriniai skaičiavimai iš dalies patvirtina praktinius rezultatus, o juos atlikti galima prieš formuojant vienas ar kitas struktūras, kad įsitikintume, kaip iš tiesų bus paveiktos TiO_2 fotokatalizinės savybės.

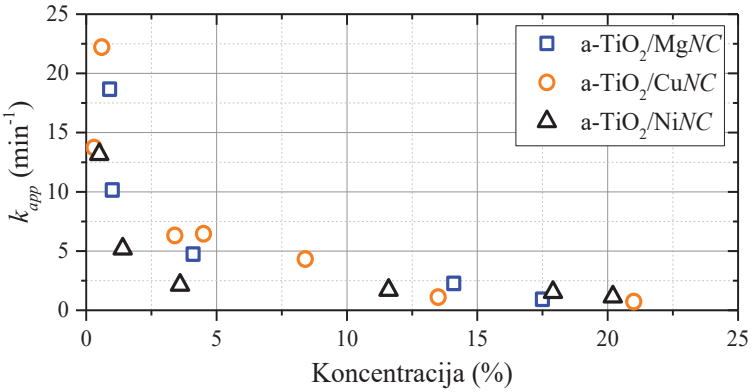

7 pav. Fotodestrukcijos greičio konstantos priklausomybė nuo priemaišų koncentracijos TiO_2 struktūroje [195]

2.4. Fotokatalizinės plonų TiO_2 dangų su paviršiuje suformuotais aukso nanodariniais savybės

Formuojant aukso nanodarinius ant TiO_2 paviršiaus nustatyta nanodarinių susiformavimo priklausomybė nuo pradinio Au sluoksnio storio, taip pat nuo TiO_2 paviršiaus struktūros (remiantis skirtinga iškaitinimo temperatūra) (**8 pav.**). Nanodarinių tankis sumažėja nuo 316,4 μm^{-2} iki 82,8 μm^{-2}, didėjant pradiniam Au sluoksnio storiui. Dar panaši priklausomybė nustatyta tuo atveju, kai prieš formuojant plonas Au dangas ant TiO_2 paviršiaus šis buvo iškaitintas skirtingose temperatūrose (nanodarinių tankis mažėja didėjant iškaitinimo temperatūrai). Tokiu atveju tankis sumažėja nuo 316,4 μm^{-2} iki 245,8 μm^{-2}, formuojant NP ant neiškaitinto TiO_2 ir iškaitinto 900 °C temperatūroje, atitinkamai. Tačiau priešinga priklausomybė pastebėta, kai 10 nm storio Au sluoksnis buvo suformuotas ant neiškaitinto TiO_2 ir TiO_2, iškaitinto 500 °C temperatūroje. Šiuo atveju stebėtas nanodarinių tankio padidėjimas nuo 82,8 μm^{-2} iki 114,9 μm^{-2}. Remiantis tuo, jog formuojant Au nanodarinius struktūros buvo kaitinamos 500 °C temperatūroje apie 60 min, galima teigti, jog TiO_2 struktūroje (nepaisant ankstesnio iškaitinimo) taip pat vyko rekristalizacijos procesai, kurie galėjo daryti įtaką nanodarinių formavimui [339].

Fotokatalizinių savybių tyrimas su suformuotomis TiO_2/Au*NP* dangomis atliktas tiriant rodamino B vandeninio tirpalo skilimą. Tyrimo metu nustatyta, kad 50 % tiriamojo tirpalo yra suskaidoma per mažiau nei 80 min naudojant TiO_2/Au*NP*, kai pradinis plonas Au sluoksnis yra 10 nm storio, o TiO_2 iškaitintas 500 °C ir 900 °C temperatūroje (**9 pav.**). Per kiek daugiau nei 80 min 50 % tirpalo suskyla naudojant TiO_2/Ag*NP* (pradinis plonos Au dangos storis apie 5 nm). Nors 900 °C temperatūroje iškaitinto TiO_2 draustinės juostos plotis yra kiek didesnis (apie 3,70 eV) nei iškaitinto 500 °C (apie 3,65 eV) ir mažesnis nei neiškaitinto (apie 3,75 eV), geresnis fotokatalizinis aktyvumas gali būti sąlygotas didesnio TiO_2 paviršiaus ploto (**8 pav.**). Nors didžiausios fotodestrukcijos greitis pasiektas naudojant TiO_2/Au*NP* (kai pradinis Au sluoksnio storis yra 10 nm), nepastebėta, ar fotokatalizinės savybės priklauso nuo Au nanodarinių formos ir dydžio.

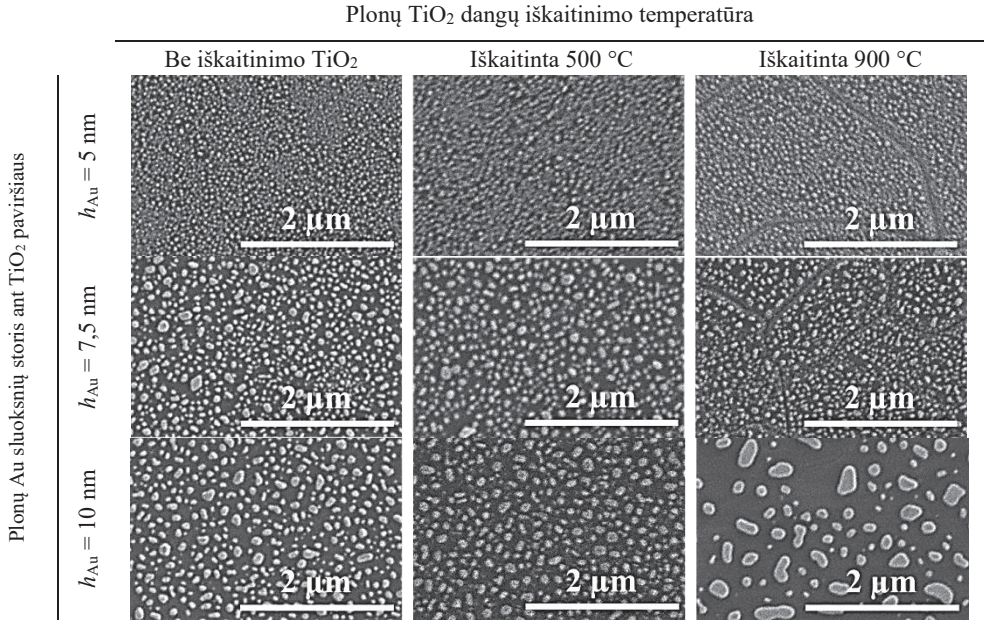

8 pav. TiO_2/Ag*NP* struktūrų FE-SEM paviršiaus nuotraukos [200]

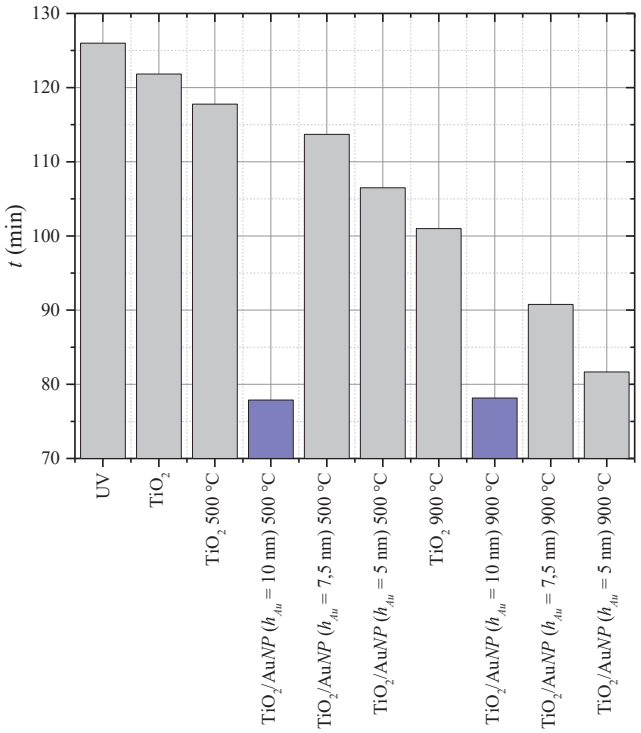

9 pav. Laikas, per kurį rodamino B vandeninis tirpalas pasiekė 50 % koncentraciją fotodestrukcijos metu naudojant atitinkamas struktūras kaip fotokatalizatorius

2.5. Hibridinis TiO_2 fotoelektrodas ir Si fotoelemento pagrindu sukurtas priešinis fotoelektrodas

Formuojant dviejų ar daugiau puslaidininkių struktūrą fotokataliziniam panaudojimui svarbu sulyginti energines juostas. Sėkmingas energinių juostų sulyginimas gali sąlygoti geresnes krūvių atskyrimo ar rekombinacijos sumažinimo tikimybes. Dėl šios priežasties buvo atliktas tyrimas, kurio metu nustatyta sandūros laidumo priklausomybė nuo priemaišų koncentracijos (N_D) *n*-tipo Si padėkle. Tyrimas apima valentinės juostos regiono XPS (**10 pav. (a), (b), (c), (d)**) ir I-V charakteristikos matavimus (**10 pav. (e), (f), (g)**). Jų metu išmatuotas ir apskaičiuotas valentinės ir laidumo juostų poslinkis tarp TiO_2 ir *n*-tipo silicio. Remiantis apskaičiuotomis valentinės juostos poslinkio vertėmis tarp TiO_2 ir *n*-tipo silicio, kurios yra 0,61 eV (*n*-Si priemaišų koncentracija $N_D = 10^{15–16}$ cm^{-3}); 0,77 eV ($N_D = 10^{17–18}$ cm^{-3}); 0,90 eV ($N_D = 10^{20–21}$ cm^{-3}), ir išmatuotu TiO_2 (~3,5 eV) bei *n*-Si (~1,12 eV) draustinės juostos pločiu, buvo apskaičiuotas laidumo juostų poslinkis. Šiuo atveju jis yra -0,22 eV ($N_D = 10^{15–16}$ cm^{-3}); -0,06 eV ($N_D = 10^{17–18}$ cm^{-3}); +0,07 eV ($N_D = 10^{20–21}$ cm^{-3}). Neigiamas laidumo juostos poslinkis reiškia, kad *n*-tipo Si laidumo juosta yra aukštesniame energiniame lygmenyje lyginant su TiO_2, ir atvirkščiai. Žinant, jog dviejų puslaidininkių sandūroje Fermi energijos lygmuo susilygina, tai reikštų, jog neigiamas laidumo juostų poslinkis sukuria papildomą potencialinį barjerą tarp TiO_2 ir *n*-tipo silicio, kurį elektronai turi pereiti. O štai teigiamas laidumo juostų poslinkis nurodo, kad šis barjeras nesusidaro, ir sandūros laidumas turėtų būti ominis. Norint įsitikinti XPS matavimų ir skaičiavimų metu gautais rezultatais, buvo atlikti I-V charakteristikos matavimai, matuojant elektros srovės priklausomybę nuo įtampos, statmenai sandūrai. Pastebėta, jog sandūroje tarp TiO_2 ir *n*-Si ($N_D = 10^{15–16}$ cm^{-3}) elektros srovės tekėjimas galimas tik viena kryptimi, o priešinga kryptimi keliant įtampą (net iki -10 V), nebuvo užfiksuotas srovės tekėjimas. Padidinus priemaišų koncentraciją *n*-tipo Si padėkle iki $N_D = 10^{17–18}$ cm^{-3} ir sumažėjus potencialiniam barjerui, srovės tekėjimas galimas abiem kryptimis; tačiau srovės stiprio priklausomybė nuo įtampos nėra tiesioginė, o I-V charakteristikos matavimų kreivė yra asimetriška. Tačiau padidinus priemaišų koncentraciją *n*-Si padėkle iki $N_D = 10^{20–21}$ cm^{-3} sandūra pasižymi ominiu kontaktu ir simetriška I-V charakteristika, kai srovės stipris tiesiogiai proporcingas įtampai. Negana to, pastebėtas sąlyginis srovės stiprio padidėjimas esant tai pačiai įtampai, tačiau skirtingiems padėklams. Tai reiškia, kad kai naudojamas *n*-Si ($N_D = 10^{15–16}$ cm^{-3}), srovės stipris esant 10 V įtampai padidėja iki maždaug 15 μA; su *n*-Si ($N_D = 10^{17–18}$ cm^{-3}) srovės stipris esant 1 V įtampai, pasiekia apie 0,8 μA ir toliau eksponentiškai didėja; su *n*-Si ($N_D = 10^{20–21}$ cm^{-3}) srovės stipris esant 0,3 V įtampai padidėja iki 2000 μA. Praktiniai matavimai patvirtina teoriniais skaičiavimais prieitas išvadas dėl energinių juostų sulyginimo. Panašūs rezultatai buvo gauti ir kitų mokslininkų atliktuose tyrimuose [112, 313]. Nepaisant to, energinių juostų sulyginimą tarp dviejų skirtingų puslaidininkių galima atlikti įterpiant papildomą ploną metalo ar puslaidininkio sluoksnį [222]. Tačiau, remiantis tolimesniu šio energinių juostų sulyginimo panaudojimu, tai gali daryti neigiamą įtaką šviesos pralaidumui, o kartu ir fotokatalizinėms savybėms.

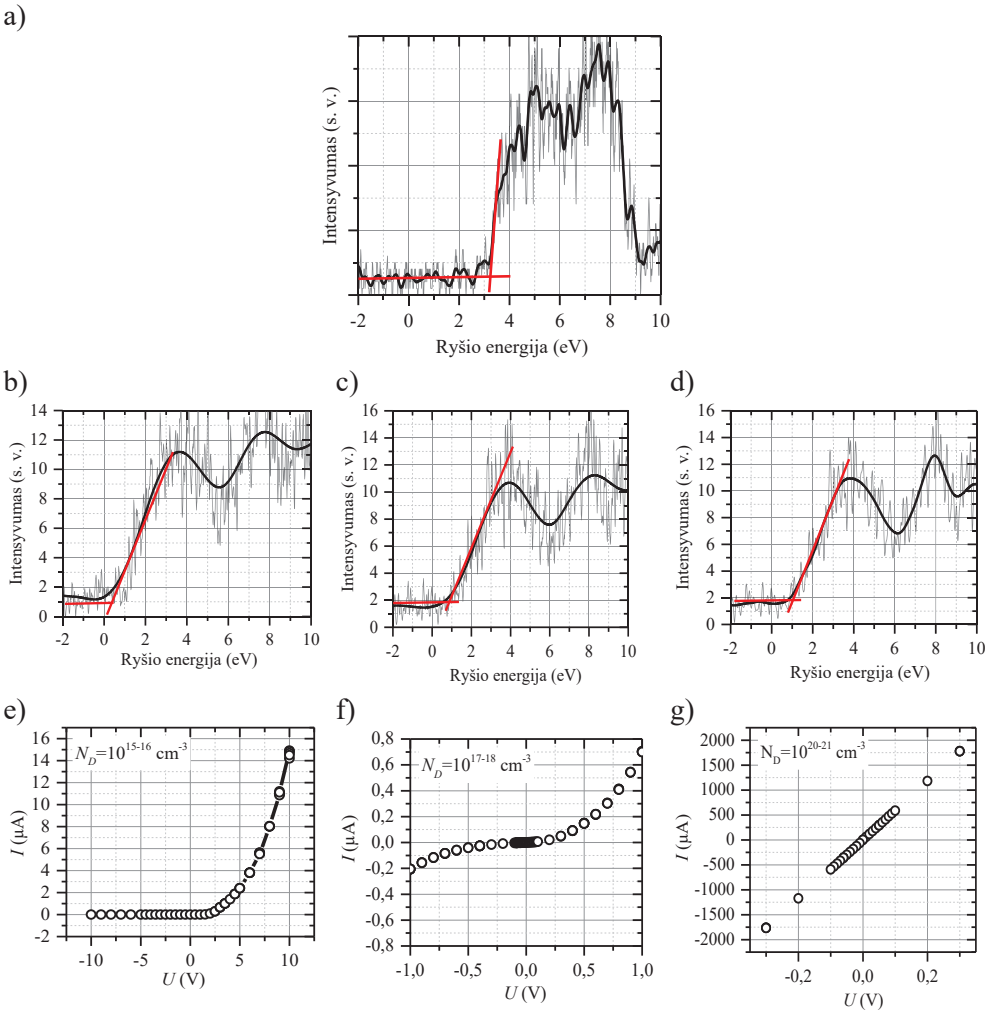

10 pav. Plonų TiO_2 dangų (a) ir *n*-tipo silicio (b), (c), (d) (su skirtinga priemaišų koncentracija) XPS spektrai ties valentinės juostos regionu, taip pat I-V charakteristikos atitinkamai struktūrai, kai *n*-Si priemaišų koncentracija: e) $N_D = 10^{15–16}$ cm^{-3}; f) $N_D = 10^{17–18}$ cm^{-3}; g) $N_D = 10^{20–21}$ cm^{-3} [107]

Remiantis pateiktų matavimų rezultatais, sukurtas hibridinio TiO_2 fotoelektrodo dizainas ir suformuota struktūra. Taip pat analogiškai suformuotas priešinis fotoelektrodas (Si fotoelemento pagrindu) (**11 pav.**). Remiantis pateiktu grafiniu hibridinio TiO_2 fotoelektrodo ir priešinio fotoelektrodo atvaizdu, taip pat suformuota struktūra, ši sistema galėtų radikaliai padidinti sugeneruotų krūvių atskyrimo tikimybę. Suformuotos struktūros dėka sukurtas vidinis elektrinis laukas elektronus ir skyles nukreiptų priešingomis kryptimis: TiO_2 sluoksnyje sugeneruoti elektronai tekėtų į *n*-Si sluoksnį ($N_D = 10^{20–21}$ cm^{-3}), o štai skylės tekėtų į TiO_2 paviršių; *pn* sandūroje sugeneruoti elektronai tekėtų link aliuminio elektrodo, suformuoto ant hibridinio TiO_2 fotoelektrodo dugno, o skylės būtų nukreiptos į *n*-Si sluoksnį ($N_D = 10^{20–21}$ cm^{-3}), kuriame įvyktų krūvininkų rekombinacija. Tuo metu vidinio

elektrinio lauko dėka priešinio fotoelektrodo struktūroje sugeneruoti krūvininkai būtų nukreipti skirtingomis kryptimis: skylės judėtų link aliuminio elektrodo, suformuoto ant fotoelektrodo dugno, kuriame įvyktų krūvininkų rekombinacija; sugeneruoti elektronai būtų nukreipti į priešinio fotoelektrodo paviršių, ant kurio suformuoti aukso ar sidabro nanodariniai. Manoma, jog šitaip būtų pasiekiamas fotojautrumas regimosios šviesos diapazone ir krūvininkų rekombinacijos sumažinimas iki minimalių verčių.

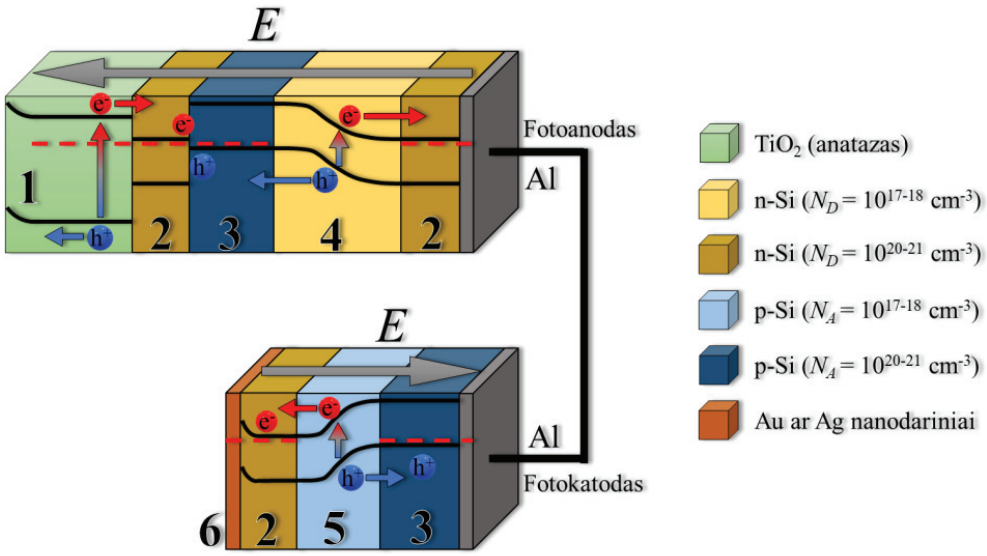

11 pav. Grafinis hibridinio TiO_2/Si fotoelektrodo ir Si fotoelemento pagrindu sukurto priešinio fotoelektrodo sistemos atvaizdas su pažymėta vidinio elektrinio lauko kryptimi (E), taip pat elektronų (e^-) ir skylių (h^+) judėjimo kryptimi. Čia: 1) TiO_2 sluoksnis; 2) n-tipo Si sluoksnis ($N_D = 10^{20–21}$ cm^{-3}); 3) p-tipo Si ($N_A = 10^{20–21}$ cm^{-3}); 4) n-tipo Si ($N_D = 10^{17–18}$ cm^{-3}); 5) p-tipo Si ($N_A = 10^{20–21}$ cm^{-3}); 6) Au arba Ag nanodariniai; Al – aliuminio elektrodas

Manoma, jog priešinis fotoelektrodas turėtų pakeisti brangų platinos katodą, kuris yra plačiai naudojamas analogiškuose tyrimuose. Dėl šios priežasties atlikti fotosrovės tankio matavimai naudojant platinos elektrodą, priešinį fotoelektrodą su aukso ir sidabro nanodariniais (**12 pav.**). Remiantis gautais rezultatais pastebėta, jog fotosrovės tankis naudojant platinos elektrodą yra apie 0,145 μA/cm^{-2}. Tačiau naudojant priešinį fotoelektrodą su aukso nanodariniais ant paviršiaus, fotosrovės tankis padidėja beveik 27,5 % (iki 0,185 μA/cm^2) lyginant su platinos elektrodu. Negana to, atlikti tyrimai, kuriuose buvo naudojamas priešinis fotoelektrodas su sidabro nanodariniais ant paviršiaus, parodė, jog fotosrovės tankis šiuo atveju padidėja beveik 72,4 % (iki 0,25 μA/cm^2). Šis fotosrovės tankių skirtumas tarp skirtingų priešinių fotoelektrodų gali būti sąlygotas potencialinio barjero (ϕ) ir nuskurdinto sluoksnio (W) susidarymu tarp aukso ar sidabro nanodarinių ir n-tipo Si ($N_D = 10^{20–21}$ cm^{-3}) sluoksnio. Šiuo atveju potencialinio barjero aukštis tarp n-Si ir Au yra apie 1,05–1,42 eV, o nuskurdintas sluoksnis – 1,11–4,13 nm; tarp n-Si ir Ag šios

vertės yra 0,21–0,68 eV ir 0,36–2,72 nm, atitinkamai. Taigi elektrono perėjimas iš *n*-tipo Si sluoksnio į suformuotus nanodarinius yra „lengvesnis“ sidabro nanodarinių atveju.

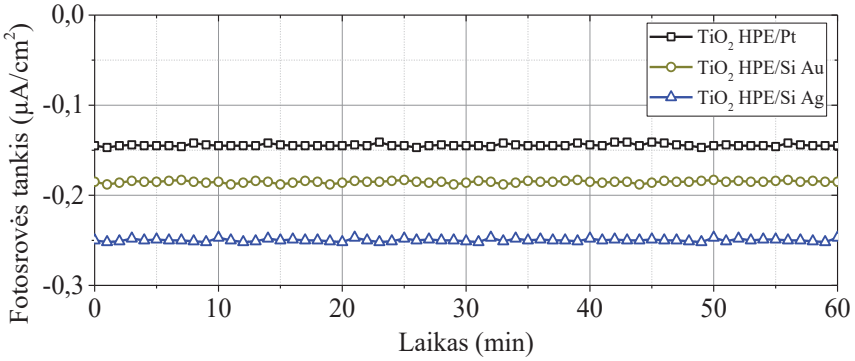

12 pav. Fotosrovės tankio stabilumo matavimai laike, naudojant UV spinduliuotę. Čia TiO_2 HPE/Pt yra hibridinio TiO_2 fotoelektrodo ir platinos katodo sistema; TiO_2 HPE/Si Au ar TiO_2 HPE/Si Ag yra hibridinio TiO_2 fotoelektrodo ir priešinio fotoelektrodo su aukso ar sidabro nanodariniais sistema

3. IŠVADOS

1. Nustatyta, jog draustinės juostos plotis plonose TiO_2 dangose, suformuotose taikant zolių-gelių metodą, labiau priklauso nuo dangos morfologinių parametrų (t. y. tankio, kuris sąlygiškai priklauso nuo suformuotos dangos storio), nei nuo kristalinės TiO_2 fazės. Šiuo atveju nustatyta, jog draustinės juostos plotis sumažėja nuo 3,8 eV iki 3,25 eV, storiui padidėjus nuo 200 nm iki 2400 nm. Tačiau papildoma analizė būtina norint nuodugniau išnagrinėti šią priklausomybę.
2. Nustatyta, jog formuojant plonas TiO_2 dangas fizikiniu garų nusodinimo bei zolių-gelių metodu, reikalingos didelės iškaitinimo temperatūros (apie 850–1000 °C) rekristalizacijos procesui (fazės perėjimui iš anatazo į rutilo) įvykti.
3. Atliktų XPS matavimų dėka nustatyta, jog TiO_2 anatazo fazė pasižymi didesne laisvųjų deguonies atomų koncentracija (didesne taškinių defektų koncentracija) nei TiO_2 rutilo fazė. Atlikti tamsinės srovės priklausomybės nuo temperatūros matavimai, kai aktyvacijos energija ~0,472 eV ir 0,902 eV buvo nustatyta anatazo ir rutilo fazėms, atitinkamai, patvirtina XPS matavimų metu pateiktas prielaidas.
4. Fotodestrukcijos greičio konstanta eksponentiškai mažėja didėjant priemaišų (Mg, Cu, Ni) koncentracijai TiO_2 struktūroje. Nustatyta aktyvacijos energija šioms struktūroms (TiO_2/Mg – 0,60 eV; TiO_2/Cu – 0,23 eV; TiO_2/Ni – 0,64 eV) ir potencialinio barjero aukštis (0,74, 0,13–0,50 ir 0,64–0,82 eV, atitinkamai). Didžiausia fotodestrukcijos greičio konstanta buvo nustatyta TiO_2/Cu*NC* sistemai su 0,6 % Cu koncentracija TiO_2 struktūroje, toliau eina TiO_2/Mg*NC* su 0,9 % Mg koncentracija ir TiO_2/Ni*NC* su 0,5 % koncentracija.
5. Nustatyta, jog aukso nanodarinių formavimas ant TiO_2 paviršiaus pagerina fotokatalizines TiO_2 savybes. Rodamino B vandeninio tirpalo fotodestrukcija iki 50 % buvo pasiekta per mažiau nei 80 min naudojant TiO_2/Au*NP* (su pradiniu 10 nm Au sluoksnio storiu), o tuo atveju naudojant tik TiO_2, analogiškas rezultatas buvo pasiektas vos per daugiau nei 120 min.
6. Energinių juostų sulyginimas buvo atliktas prieš formuojant hibridinį TiO_2 fotoelektrodą ir nustatyta, jog *n*-tipo Si sluoksnis su priemaišų koncentracija $N_D = 10^{20–21}$ cm^{-3} sudaro ominį kontaktą su TiO_2. Negana to, suformuotas hibridinis TiO_2 fotoelektrodas ir priešinis fotoelektrodas su aukso bei sidabro nanodariniais ant paviršiaus pasiekė 24,5 % (0,185 μA/cm^2) ir 72,4 % (0,25 μA/cm^2) didesnį fotosrovės tankį lyginant su platinos elektrodu (0,145 μA/cm^2).

REFERENCES

1. NASA. Carbon Dioxide | Vital Signs – Climate Change: Vital Signs of the Planet. *NASA Global Climate Change*. 2019. [Accessed 28 January 2022]. Available from: https://climate.nasa.gov/vital-signs/carbon-dioxide/
2. NASA/GISS. *Global Temperature | Vital Signs – Climate Change: Vital Signs of the Planet*. 2019. [Accessed 28 January 2022]. Available from: https://climate.nasa.gov/vital-signs/global-temperature/
3. NASA. Arctic Sea Ice Extent | Vital Signs – Climate Change: Vital Signs of the Planet. *NASA Global Climate Change*. [Accessed 28 January 2022]. Available from: https://climate.nasa.gov/vital-signs/arctic-sea-ice/
4. NASA. Ice Sheets | Vital Signs – Climate Change: Vital Signs of the Planet. *NASA Global Climate Change*. 2019. [Accessed 28 January 2022]. Available from: https://climate.nasa.gov/vital-signs/ice-sheets/
5. FRAVVENTURA, M. C., SIEBBELES, L. D. A., & SAVENIJE, T. J. Mechanisms of photogeneration and relaxation of excitons and mobile carriers in anatase TiO_2. *Journal of Physical Chemistry C*. 2014. 118, (14), 7337–7343. ISSN 19327455.
6. VALDOVINOS, S. M., & GUREVICH, Y. G. Hall effect: the role of nonequilibrium charge carriers. Revista Mexicana de Fisica. 2011. 57, (4), 368–374. ISSN 0035001X.
7. HANEEF, H. F., ZEIDELL, A. M., & JURCHESCU, O. D. Charge carrier traps in organic semiconductors: A review on the underlying physics and impact on electronic devices. *Royal Society of Chemistry*. 2020. 8, 759-787. ISSN 1473-7604.
8. ATHANASEKOU, C. P., LIKODIMOS, V., & FALARAS, P. Recent developments of TiO_2 photocatalysis involving advanced oxidation and reduction reactions in water. *Journal of Environmental Chemical Engineering*. 2018. 6, (6), 7386–7394. ISSN 22133437.
9. KUDO, A., & MISEKI, Y. Heterogeneous photocatalyst materials for water splitting. *Chemical Society Reviews*. 2009. 38, (1), 253–278. ISSN 03060012.
10. CHEN, X., SHEN, S., GUO, L., & MAO, S. S. Semiconductor-based photocatalytic hydrogen generation. *Chemical Reviews*. 2010. 110, (11), 6503–6570. ISSN 00092665.
11. HARRISON, S., & HAYNE, M. Photoelectrolysis Using Type-II Semiconductor Heterojunctions. *Scientific Reports*. 2017. 7, (1), 1–11. ISSN 20452322.
12. ZHU, Y., WAN, T., WEN, X., CHU, D., & JIANG, Y. Tunable Type I and II heterojunction of CoO_x nanoparticles confined in g-C_3N_4 nanotubes for photocatalytic hydrogen production. *Applied Catalysis B: Environmental*. 2019. 244, 814–822. ISSN 09263373.
13. MUNAWAR, T., MUKHTAR, F., NADEEM, M. S., MANZOOR, S., ASHIQ, M. N., MAHMOOD, K., BATOOL, S., HASAN, M., & IQBAL, F. Fabrication of dual Z-scheme TiO_2-WO_3-CeO_2 heterostructured nanocomposite with enhanced photocatalysis, antibacterial, and

electrochemical performance. *Journal of Alloys and Compounds*. 2022. 898, 162779. ISSN 09258388.
14. CHEN, D., ZOU, L., LI, S., & ZHENG, F. Nanospherical like reduced graphene oxide decorated TiO_2 nanoparticles: An advanced catalyst for the hydrogen evolution reaction. *Scientific Reports*. 2016. 6, (1), 1–8. ISSN 20452322.
15. MARINO, T., FIGOLI, A., MOLINO, A., ARGURIO, P., & MOLINARI, R. Hydrogen and oxygen evolution in a membrane photoreactor using suspended nanosized Au/TiO_2 and Au/CeO_2. *ChemEngineering*. 2019. 3, (1), 1–12. ISSN 23057084.
16. SAWYER, D. T., & INTERRANTE, L. V. Electrochemistry of dissolved gases. II. Reduction of oxygen at platinum, palladium, nickel and other metal electrodes. *Journal of Electroanalytical Chemistry*. 1961. 2, (4), 310–327. ISSN 00220728.
17. CHEN, R., YANG, C., CAI, W., WANG, H. Y., MIAO, J., ZHANG, L., CHEN, S., & LIU, B. Use of Platinum as the Counter Electrode to Study the Activity of Nonprecious Metal Catalysts for the Hydrogen Evolution Reaction. *American Chemical Society*. 2017. 2, (5), 1070-1075. ISSN 0002-7863.
18. HU, S., SHANER, M. R., BEARDSLEE, J. A., LICHTERMAN, M., BRUNSCHWIG, B. S., & LEWIS, N. S. Amorphous TiO_2 coatings stabilize Si, GaAs, and GaP photoanodes for efficient water oxidation. *Science*. 2014. 344, (6187), 1005–1009. ISSN 10959203.
19. SUN, S., SONG, P., CUI, J., & LIANG, S. Amorphous TiO_2 nanostructures: Synthesis, fundamental properties and photocatalytic applications. *Catalysis Science and Technology*. 2019. 9, (16), 4198–4215. ISSN 20444761.
20. SMITH, W. A., SHARP, I. D., STRANDWITZ, N. C., & BISQUERT, J. Interfacial band-edge energetics for solar fuels production. *Energy Environ. Sci.* 2015, 8, (10), 2851-2862. ISSN 1754-5692.
21. CONFERENCE OF THE PARTIES. *Decision-/CP.26 Glasgow Climate Pact*. 2021. [Accessed 29 January 2022]. Available from: https://www.ipcc.ch/report/ar6/wg1/.
22. UNFCCC & UN. The Glasgow Climate Pact. In : *2021 United Nations Climate Change Conference (COP26)*. 2021. [Accessed 29 January 2022]. Available from: https://ukcop26.org/cop26-presidency-outcomes-the-climate-pact/
23. AMETA, R., SOLANKI, M. S., BENJAMIN, S., & AMETA, S. C. Photocatalysis. *Advanced Oxidation Processes for Wastewater Treatment: Emerging Green Chemical Technology*. 2018. 135–175. ISBN 978-0-12-810499-6.
24. REYNOLDS, S., BRINZA, M., BENKHEDIR, M. L., & ADRIAENSSENS, Photoconductivity in materials research. *Springer Handbook of Electronic and Photonic Materials*. Springer, Cham, 2017. 1-1. ISBN 9780387291857.
25. HONG, N. H. Introduction to Nanomaterials: Basic Properties, Synthesis, and Characterization. *Nano-sized Multifunctional Materials: Synthesis, Properties and Applications*. 2019. 1–19. ISBN 9780128139349.

26. MANIAS, S. N. Fully Controlled Semiconductor Devices. *Power Electronics and Motor Drive Systems*. 2017. 695–805. ISBN 978-0-12-811798-9.
27. CHOI, W. S., SEO, S. S. A., & LEE, H. N. Optoelectronics: Optical properties and electronic structures of complex metal oxides. *Epitaxial Growth of Complex Metal Oxides*. 2015. 331–363. ISBN 9780081029466.
28. GUREVICH, Y. G., LOGVINOV, G. N., VOLOVICHEV, I. N., ESPEJO, G., TITOV, O. Y., & MERIUTS, A. The Role of Non-Equilibrium Carriers in Formation of Thermo-E.M.F. in Bipolar Semiconductors. *Physica Status Slidi (B)*. 2002. 231, (1), 278-293. ISSN 0370-1972.
29. KLIMOV, V. I. Mechanisms for Photogeneration and Recombination of Multiexcitons in Semiconductor Nanocrystals: Implications for Lasing and Solar Energy Conversion. *Journal of Physical Chemistry B*. 2006. 110, (34), 16827–16845. ISSN 15206106.
30. PROCTOR, C. M., KUIK, M., & NGUYEN, T. Q. Charge carrier recombination in organic solar cells. *Progress in Polymer Science*. 2013. 38, (12), 1941–1960. ISSN 0079-6700.
31. AGRAWAL, G. P., & DUTTA, N. K. Recombination Mechanisms in Semiconductors. *Semiconductor Lasers*. 1993. 74–146. ISBN 9781461304814.
32. HUBBARD, S. Recombination. *Photovoltaic Solar Energy*. 2017. 39–46. ISBN 9781118927489.
33. N HALL, B. R. Recombination processes in semiconductors. *The Institution of Electrical Engineers.* 1960. 3047, 923-931.
34. ROTHENBERGER, G., MOSER, J., GRATZEL, M., SERPONE, N., & SHARMA, D. K. Charge carrier trapping and recombination dynamics in small semiconductor particles. *American Chemical Society*. 1985. 107, (26), 8054-8059. ISSN 1520-5126.
35. OHTANI, B., BOWMAN, R. M., JR, D. P. C., KOMINAMI, H., NOGUCHI, H., & UOSAKI, K. Femtosecond Diffuse Reflectance Spectroscopy of Aqueous Titanium (IV) Oxide Suspension: Correlation of Electron-Hole Recombination Kinetics with Photocatalytic Activity. *Chemistry Letters*. 1998. 27, (7), 579-580. ISSN 2717-1892.
36. KATOH, R., MURAI, M., & FURUBE, A. Transient absorption spectra of nanocrystalline TiO_2 films at high excitation density. *Chemical Physics Letters*. 2010. 500, (4–6), 309–312. ISSN 00092614.
37. PETERS, J. A., LIU, Z., YU, R., MCCALL, K. M., HE, Y., KANATZIDIS, M. G., & WESSELS, B. W. Carrier recombination mechanism in CsPbB_{3} revealed by time-resolved photoluminescence spectroscopy. *Physical Review B*. 2019. 100, (23), 235305. ISSN 24699969.
38. Time-Resolved Photoluminescence (TRPL) | PicoQuant. . [Accessed 9 February 2022]. Available from: https://www.picoquant.com/applications/category/materials-science/time-resolved-photoluminescence
39. LAUTH, J., KINGE, S., & SIEBBELES, L. D. A. Ultrafast Transient Absorption and Terahertz Spectroscopy as Tools to Probe Photoexcited States

and Dynamics in Colloidal 2D Nanostructures. *Zeitschrift fur Physikalische Chemie*. 2017. 231, (1), 107–119. ISSN 09429352.
40. SINTON, R. A., CUEVAS, A., & STUCKINGS, M. Quasi-steady-state photoconductance, a new method for solar cell material and device characterization. In : *Conference Record of the IEEE Photovoltaic Specialists Conference*. IEEE, 1996. 457–460. ISSN 1608371.
41. ASADA, T., ICHIKAWA, Y., & KATO, M. Carrier lifetime measurements in semiconductors through the microwave photoconductivity decay method. *Journal of Visualized Experiments*. 2019. 2019, (146), e59007. ISSN 1940087X.
42. KATO, T., TAI, K. F., YAGIOKA, T., KAMADA, R., & SUGIMOTO, H. Recombination analysis of CIGS solar cells using temperature and illumination dependent open-circuit voltage measurement. *26th International Photovoltaic Science and Engineering Conference*. 2016. 1–4.
43. FAN, H. Y. Effect of Traps on Carrier Injection in Semiconductors. *Physical Review*. 1953. 92, (6), 1424. ISSN 0031899X.
44. KASH, J. A., ZACHAU, M., MENDEZ, E. E., HONG, J. M., & FUKUZAWA, T. Fermi-Dirac distribution of excitons in coupled quantum wells. *Physical Review Letters*. 1991. 66, (17), 2247–2250. ISSN 00319007.
45. LITVIN, A. I., & SIMONZHENKOV, S. D. Computation of Fermi-Dirac functions. *Computational Mathematics and Mathematical Physics*. 1991. 31, (8), 100–103. ISSN 09655425.
46. MARTÍNEZ-DUART, J. M., MARTÍN-PALMA, R. J., & AGULLÓ-RUEDA, F. Survey of Solid State Physics. *Nanotechnology for Microelectronics and Optoelectronics*. 2006. 21–53. ISBN 978-0-08-044553-3.
47. BROGLIA, R. A. Nuclear Models and Methods. *Encyclopedia of Condensed Matter Physics*. 2005. 118–131. ISBN 9780122276101.
48. PATHRIA, R. K., & BEALE, P. D. Ideal Fermi systems. *Statistical Mechanics*. 2022. 247–290. ISBN 9780081026922.
49. POOLE, C. P., PROZOROV, R., FARACH, H. A., & CRESWICK, R. J. Properties of the normal state. *Superconductivity*. 2014. 1–31. ISBN 978-0-12-409509-0.
50. LEE, J., YEO, H., & KIM, Y. H. Quasi-Fermi level splitting in nanoscale junctions from ab initio. *Proceedings of the National Academy of Sciences of the United States of America*. 2020. 117, (19), 10142–10148. ISSN 10916490.
51. REDDY, P., HOFFMANN, M. P., KAESS, F., BRYAN, Z., BRYAN, I., BOBEA, M., KLUMP, A., TWEEDIE, J., KIRSTE, R., MITA, S., GERHOLD, M., COLLAZO, R., & SITAR, Z. Point defect reduction in wide bandgap semiconductors by defect quasi Fermi level control. *Journal of Applied Physics*. 2016. 120, (18), 185704. ISSN 10897550.
52. HARRIS, D. C. *Quantitative Chemical Analysis - 8th edition*. 2010. ISBN 978-1429263092.
53. BARKE, H.-D., HAZARI, A., & YITBAREK, S. Redox Reactions. *Misconceptions in Chemistry*. 2009. 207–234. ISBN 978-3540709886.

54. MARCUS, R. A. On the Theory of Oxidation-Reduction Reactions Involving Electron Transfer. III. Applications to Data on the Rates of Organic Redox Reactions. *The Journal of Chemical Physics*. 2004. 26, (4), 872. ISSN 0021-9606.
55. SZABÓ, M., BELLÉR, G., KALMÁR, J., & FÁBIÁN, I. The Kinetics and Mechanism of Complex Redox Reactions in Aqueous Solution: The Tools of the Trade. *Advances in Inorganic Chemistry*. 2017. 70, 1–61. ISSN 08988838.
56. MAEDA, K., & DOMEN, K. Photocatalytic water splitting: Recent progress and future challenges. *Journal of Physical Chemistry Letters*. 2010. 1, (18), 2655–2661. ISSN 19487185.
57. VAN-HUY NGUYEN, DAI-VIET N. VO, S. N. *Nanostructured Photocatalysts: From Fundamental to Practical Applications*. 2021. ISBN 9780128230077.
58. ZHANG, J., TIAN, B., WANG, L., XING, M., & LEI, J. *Photocatalysis: fundamentals, materials and applications*. 2018. ISBN 9811321132.
59. KHAN, M. M. Principles and mechanisms of photocatalysis. *Photocatalytic Systems by Design*. 2021. 1–22. ISBN 978-0-12-820532-7.
60. SAHARAN, V. K., PINJARI, D. V., GOGATE, P. R., & PANDIT, A. B. Advanced Oxidation Technologies for Wastewater Treatment: An Overview. *Industrial Wastewater Treatment, Recycling and Reuse*. 2014. 141–191. ISBN 9780444634030.
61. MOUSSET, E., LOH, W. H., LIM, W. S., JARRY, L., WANG, Z., & LEFEBVRE, O. Cost comparison of advanced oxidation processes for wastewater treatment using accumulated oxygen-equivalent criteria. *Water research*. 2021. 200. ISSN 1879-2448.
62. STEFAN, M. I. Advanced Oxidation Processes for Water Treatment - Fundamentals and Applications. *Water Intelligence Online*. 2017. 16, 9781780407197. ISSN 1476-1777.
63. BELVER, C., BEDIA, J., GÓMEZ-AVILÉS, A., PEÑAS-GARZÓN, M., & RODRIGUEZ, J. J. Semiconductor Photocatalysis for Water Purification. *Nanoscale Materials in Water Purification*. 2018. 581–651. ISBN 9780128139271.
64. BODZEK, M., & RAJCA, M. Photocatalysis in the treatment and disinfection of water. Part I. Theoretical backgrounds. *Ecological Chemistry and Engineering S*. 2012. 19, (4), 489–512. ISSN 18986196.
65. HSIAO, C. Y., LEE, C. L., & OLLIS, D. F. Heterogeneous photocatalysis: Degradation of dilute solutions of dichloromethane (CH_2Cl_2), chloroform ($CHCl_3$), and carbon tetrachloride (CCl_4) with illuminated TiO_2 photocatalyst. *Journal of Catalysis*. 1983. 82, (2), 418–423. ISSN 0021-9517.
66. PRUDEN, A. L., & OLLIS, D. F. Photoassisted heterogeneous catalysis: The degradation of trichloroethylene in water. *Journal of Catalysis*. 1983. 82, (2), 404–417. ISSN 0021-9517.
67. KAMAT, P. V., HUEHN, R., & NICOLAESCU, R. A "Sense and Shoot" Approach for Photocatalytic Degradation of Organic Contaminants in Water. *Journal of Physical Chemistry B*. 2001. 106, (4), 788–794. ISSN 10895647.

68. KHODJA, A. A., SEHILI, T., PILICHOWSKI, J. F., & BOULE, P. Photocatalytic degradation of 2-phenylphenol on TiO_2 and ZnO in aqueous suspensions. *Journal of Photochemistry and Photobiology A: Chemistry*. 2001. 141, (2–3), 231–239. ISSN 1010-6030.
69. RAO, M. V., RAJESHWAR, K., PAL VERNEKER, V. R., & DUBOW, J. Photosynthetic production of H_2 and H_2O_2 on semiconducting oxide grains in aqueous solutions. *Journal of Physical Chemistry*. 1980. 84, (15), 1987–1991. ISSN 00223654.
70. SPATHIS, P., & POULIOS, I. The corrosion and photocorrosion of zinc and zinc oxide coatings. *Corrosion Science*. 1995. 37, (5), 673–680. ISSN 0010938X.
71. HUY, T. H., BUI, D. P., KANG, F., WANG, Y. F., LIU, S. H., THI, C. M., YOU, S. J., CHANG, G. M., & PHAM, V. V. SnO_2/TiO_2 nanotube heterojunction: The first investigation of NO degradation by visible light-driven photocatalysis. *Chemosphere*. 2019. 215, 323–332. ISSN 0045-6535.
72. KHASAWNEH, O. F. S., PALANIANDY, P., PALANIANDY, P., AHMADIPOUR, M., MOHAMMADI, H., & BIN HAMDAN, M. R. Removal of acetaminophen using Fe_2O_3-TiO_2 nanocomposites by photocatalysis under simulated solar irradiation: Optimization study. *Journal of Environmental Chemical Engineering*. 2021. 9, (1), 104921. ISSN 22133437.
73. RÖSCH, C., KOHAJDA, T., RÖDER, S., VON BERGEN, M., & SCHLINK, U. Relationship between sources and patterns of VOCs in indoor air. *Atmospheric Pollution Research*. 2014. 5, (1), 129–137. ISSN 1309-1042.
74. BOONEN, E., & BEELDENS, A. Recent photocatalytic applications for air purification in Belgium. *Coatings*. 2014. 4, (3), 553–573. ISSN 20796412.
75. HU, Z., XU, T., LIU, P., & JIN, G. Developed photocatalytic semi-flexible pavement for automobile exhaust purification using iron-doped titanium dioxide. *Construction and Building Materials*. 2020. 262, 119924. ISSN 09500618.
76. HASSAN, M. M., DYLLA, H., ASADI, S., MOHAMMAD, L. N., & COOPER, S. Laboratory Evaluation of Environmental Performance of Photocatalytic Titanium Dioxide Warm-Mix Asphalt Pavements. *Journal of Materials in Civil Engineering*. 2012. 24, (5), 599–605. ISSN 0899-1561.
77. HASSAN, M., MOHAMMAD, L. N., ASADI, S., DYLLA, H., & COOPER, S. Sustainable Photocatalytic Asphalt Pavements for Mitigation of Nitrogen Oxide and Sulfur Dioxide Vehicle Emissions. *Journal of Materials in Civil Engineering*. 2013. 25, (3), 365–371. ISSN 0899-1561.
78. STEFANOV, B. Photocatalytic TiO_2 thin films for air cleaning. Effect of facet orientation, chemical functionalization, and reaction conditions. *Acta Universitatis Upsaliensis*, 2015. [Accessed 29 January 2022]. Available from: https://uu.diva-portal.org/smash/get/diva2:862338/FULLTEXT01.pdf
79. HAY, S. O., OBEE, T., LUO, Z., JIANG, T., MENG, Y., HE, J., MURPHY, S. C., & SUIB, S. The viability of photocatalysis for air purification. *Molecules*. 2015. 20, (1), 1319–1356. ISSN 14203049.
80. MAVRIKOS, A., PAPOULIS, D., TODOROVA, N., PAPAILIAS, I.,

TRAPALIS, C., PANAGIOTARAS, D., CHALKIAS, D. A., STATHATOS, E., GIANNI, E., SOMALAKIDI, K., SYGKRIDOU, D., & KOMARNENI, S. Synthesis of Zn/Cu metal ion modified natural palygorskite clay – TiO_2 nanocomposites for the photocatalytic outdoor and indoor air purification. *Journal of Photochemistry and Photobiology A: Chemistry*. 2022. 423, 113568. ISSN 10106030.

81. PRAKASH, J., SUN, S., SWART, H. C., & GUPTA, R. K. Noble metals-TiO_2 nanocomposites: From fundamental mechanisms to photocatalysis, surface enhanced Raman scattering and antibacterial applications. *Applied Materials Today*. 2018. 11, 82–135. ISSN 2352-9407.
82. KELLY, K. L., CORONADO, E., ZHAO, L. L., & SCHATZ, G. C. The optical properties of metal nanoparticles: The influence of size, shape, and dielectric environment. *Journal of Physical Chemistry B*. 2003. 107, (3), 668–677. ISSN 10895647.
83. PETRYAYEVA, E., & KRULL, U. J. Localized surface plasmon resonance: Nanostructures, bioassays and biosensing—A review. *Analytica Chimica Acta*. 2011. 706, (1), 8–24. ISSN 0003-2670.
84. ANKER, J. N., HALL, W. P., LYANDRES, O., SHAH, N. C., ZHAO, J., & VAN DUYNE, R. P. Biosensing with plasmonic nanosensors. *Nature Materials*. 2008. 7, (6), 442–453. ISSN 1476-4660.
85. KARAGOZ, S., KIREMITLER, N. B., SAKIR, M., SALEM, S., ONSES, M. S., SAHMETLIOGLU, E., CEYLAN, A., & YILMAZ, E. Synthesis of Ag and TiO_2 modified polycaprolactone electrospun nanofibers (PCL/TiO_2-Ag NFs) as a multifunctional material for SERS, photocatalysis and antibacterial applications. *Ecotoxicology and Environmental Safety*. 2020. 188, 109856. ISSN 0147-6513.
86. SUBHAN, M. A., JHUMA, S. S., SAHA, P. C., AHMED, J., ASIRI, A. M., RIFAT, T. P., RAIHAN, T., AZAD, A. K., & RAHMAN, M. M. Photocatalysis, enhanced anti-bacterial performance and discerning thiourea sensing of $Ag_2O{\cdot}SnO_2{\cdot}TiO_2$ hetero-structure. *Journal of Environmental Chemical Engineering*. 2020. 8, (4), 104051. ISSN 22133437.
87. KILL TWO BIRDS WITH ONE STONE | meaning in the Cambridge English Dictionary. . [Accessed 29 January 2022]. Available from: https://dictionary.cambridge.org/dictionary/english/kill-two-birds-with-one-stone
88. KULESZA, P. J., RUTKOWSKA, I. A., & WADAS, A. *Electrocatalytic and photoelectrochemical reduction of carbon dioxide in aqueous media: Toward generation of fuels and utility chemicals*. 2018. ISBN 9780128098943.
89. CENTI, G., & PERATHONER, S. *Green Carbon Dioxide: Advances in CO_2 Utilization*. 2014. ISBN 9781118831922.
90. GUZMÁN, H., FARKHONDEHFAL, M. A., TOLOD, K. R., HERNÁNDEZ, S., & RUSSO, N. Photo/electrocatalytic hydrogen exploitation for CO_2 reduction toward solar fuels production. *Solar Hydrogen Production: Processes, Systems and Technologies*. 2019. 365–418. ISBN 9780128148549.
91. RACKLEY, S. A. CO_2 utilization and other sequestration options. *Carbon*

Capture and Storage. 2017. 577–591. ISBN 978-0-12-812041-5.
92. CHOU, H. L., HWANG, B. J., & SUN, C. L. Catalysis in Fuel Cells and Hydrogen Production. *New and Future Developments in Catalysis: Batteries, Hydrogen Storage and Fuel Cells*. 2013. 217–270. ISBN 9780444538802.
93. DINCER, I., & ZAMFIRESCU, C. Hydrogen Production by Photonic Energy. *Sustainable Hydrogen Production*. 2016. 309–391. ISBN 978-0-12-801563-6.
94. NAVARRO YERGA, R. M., ALVAREZ-GALVÁN, M. C., VAQUERO, F., ARENALES, J., & FIERRO, J. L. G. Hydrogen Production from Water Splitting Using Photo-Semiconductor Catalysts. *Renewable Hydrogen Technologies: Production, Purification, Storage, Applications and Safety*. 2013. 43–61. ISBN 9780444563521.
95. PATTANAIK, P., & SAHOO, M. K. TiO_2 photocatalysis: progress from fundamentals to modification technology. *Desalination and Water Treatment*. 2014. 52, (34–36), 6567–6590. ISSN 19443986.
96. MOMA, J., & BALOYI, J. Modified Titanium Dioxide for Photocatalytic Applications. *Photocatalysts - Applications and Attributes*. 2018. 79374. ISBN 978-1-78985-476-3.
97. ANANDAN, S., IKUMA, Y., & NIWA, K. An Overview of Semi-Conductor Photocatalysis: Modification of TiO_2 Nanomaterials. *Solid State Phenomena*. 2010. 162, 239–260. ISSN 1662-9779.
98. CASTELLOTE, M., & BENGTSSON, N. Applications of Titanium Dioxide Photocatalysis to Construction Materials. *Applications of Titanium Dioxide Photocatalysis to Construction Materials*. 2011. 5–10. ISBN 978-94-007-1296-6.
99. HU, W., & YANG, J. Two-dimensional van der Waals heterojunctions for functional materials and devices. *Royal Society of Chemistry*. 2017. 5, 12289-12297. ISSN 2050-7534.
100. ZHOU, H., QU, Y., ZEID, T., & DUAN, X. Towards highly efficient photocatalysts using semiconductor nanoarchitectures. *Energy and Environmental Science*. 2012. 5, (5), 6732–6743. ISSN 17545692.
101. MIKHAILOVA, M. P., MOISEEV, K. D., & YAKOVLEV, P. Y. Interface-induced optical and transport phenomena in type II broken-gap single heterojunctions. *Semicond. Sci. Technol.* 2004. 19, R109. ISSN 0268-1242.
102. SRIVASTAVA, P. K., HASSAN, Y., GEBREDINGLE, Y., JUNG, J., KANG, B., YOO, W. J., SINGH, B., & LEE, C. Van der Waals Broken-Gap p-n Heterojunction Tunnel Diode Based on Black Phosphorus and Rhenium Disulfide. *ACS Applied Materials and Interfaces*. 2019. 11, (8), 8266–8275. ISSN 19448252.
103. SCHMICKLER, W., SANTOS, E. The semiconductor-electrolyte interface. *Interfacial Electrochemistry.* 2010. 117-131. ISBN 978-3-642-04936-1.
104. SAAD, M., & KASSIS, A. Effect of interface recombination on solar cell parameters. *Solar Energy Materials and Solar Cells*. 2003. 79, (4), 507–517. ISSN 09270248.
105. MAHATO, S., BISWAS, D., GERLING, L. G., VOZ, C., & PUIGDOLLERS, J. Analysis of temperature dependent current-voltage and capacitance-voltage

characteristics of an Au/V_2O_5/n -Si Schottky diode. *AIP Advances*. 2017. 7, (8). ISSN 21583226.
106. GÄRTNER, W. W. Depletion-layer photoeffects in semiconductors. *Physical Review*. 1959. 116, (1), 84–87. ISSN 0031899X.
107. KAVALIUNAS, V., HATANAKA, Y., NEO, Y., LAUKAITIS, G., & MIMURA, H. Conduction Band Discontinuity in n-type Si/TiO_2 Heterojunction Interfaces . *ECS Journal of Solid State Science and Technology*. 2021. 10, (1), 015005. ISSN 2162-8769.
108. KRAUT, E. A., GRANT, R. W., WALDROP, J. R., & KOWALCZYK, S. P. Semiconductor core-level to valence-band maximum binding-energy differences: Precise determination by x-ray photoelectron spectroscopy. *Physical Review B*. 1983. 28, (4), 1965–1977. ISSN 01631829.
109. SAH, C. T., NOYCE, R. N., & SHOCKLEY, W. Carrier Generation and Recombination in P-N Junctions and P-N Junction Characteristics. *Proceedings of the IRE*. 1957. 45, (9), 1228–1243. ISSN 00968390.
110. HEIKKILÄ, M., PUUKILAINEN, E., RITALA, M., & LESKELÄ, M. Effect of thickness of ALD grown TiO_2 films on photoelectrocatalysis. *Journal of Photochemistry and Photobiology A: Chemistry*. 2009. 204, (2–3), 200–208. ISSN 10106030.
111. SATO, N. Electrocthemistry of Semiconductors. *Tetsu-to-Hagane*. 1990. 76, (9), 1423–1436. ISSN 0021-1575.
112. CORONADO, J. M., FRESNO, F., HERNÁNDEZ-ALONSO, M. D., & PORTELA, R. Design of advanced photocatalytic materials for energy and environmental applications. *Green Energy and Technology*. 2013. 71. ISSN 18653537.
113. REYES-CORONADO, D., RODRÍGUEZ-GATTORNO, G., ESPINOSA-PESQUEIRA, M. E., CAB, C., DE COSS, R., & OSKAM, G. Phase-pure TiO_2 nanoparticles: anatase, brookite and rutile. *Nanotechnology*. 2008. 19, 145605–145610. ISSN 0957-4484.
114. XU, Q., ZHANG, L., CHENG, B., FAN, J., & YU, J. S-Scheme Heterojunction Photocatalyst. *Chem*. 2020. 6, (7), 1543-1559. ISSN 2451-9294.
115. AHMAD, Z. Basic concepts in corrosion. *Principles of Corrosion Engineering and Corrosion Control*. 2006. 9–56. ISBN 9780080480336.
116. CHEN, S., & WANG, L. W. Thermodynamic oxidation and reduction potentials of photocatalytic semiconductors in aqueous solution. *Chemistry of Materials*. 2012. 24, (18), 3659–3666. ISSN 08974756.
117. POURBAIX, M. *Atlas of Electrochemical Equilibria in-Aqueous Solutions*. 1974. ISBN 9780080109855.
118. IM, Y., KANG, S., KIM, K. M., JU, T., HAN, G. B., PARK, N. K., LEE, T. J., & KANG, M. Dynamic hydrogen production from methanol/water photo-splitting using core@shell-structured CuS@TiO_2 catalyst wrapped by high concentrated TiO_2 Particles. *International Journal of Photoenergy*. 2013. 2013. ISSN 1110662X.
119. SARAVANAN, R., MANOJ, D., QIN, J., NAUSHAD, M., GRACIA, F.,

LEE, A. F., KHAN, M. M., & GRACIA-PINILLA, M. A. Mechanothermal synthesis of Ag/TiO_2 for photocatalytic methyl orange degradation and hydrogen production. *Process Safety and Environmental Protection*. 2018. 120, 339–347. ISSN 0957-5820.

120. BIAN, Z., TACHIKAWA, T., ZHANG, P., FUJITSUKA, M., & MAJIMA, T. Au/TiO_2 superstructure-based plasmonic photocatalysts exhibiting efficient charge separation and unprecedented activity. *Journal of the American Chemical Society*. 2014. 136, (1), 458–465. ISSN 00027863.
121. WU, F., HU, X., FAN, J., LIU, E., SUN, T., KANG, L., HOU, W., ZHU, C., & LIU, H. Photocatalytic Activity of Ag/TiO_2 Nanotube Arrays Enhanced by Surface Plasmon Resonance and Application in Hydrogen Evolution by Water Splitting. *Plasmonics*. 2013. 8, (2), 501–508. ISSN 15571955.
122. ZHU, C., LIU, C., FU, Y., GAO, J., HUANG, H., LIU, Y., & KANG, Z. Construction of CDs/CdS photocatalysts for stable and efficient hydrogen production in water and seawater. *Applied Catalysis B: Environmental*. 2019. 242, 178–185. ISSN 0926-3373.
123. CUI, G., WANG, W., MA, M., XIE, J., SHI, X., DENG, N., XIN, J., & TANG, B. IR-Driven Photocatalytic Water Splitting with WO_2-Na_xWO_3 Hybrid Conductor Material. *Nano Letters*. 2015. 15, (11), 7199–7203. ISSN 15306992.
124. JIANG, D., SUN, Z., JIA, H., LU, D., & DU, P. A cocatalyst-free CdS nanorod/ZnS nanoparticle composite for high-performance visible-light-driven hydrogen production from water. *Journal of Materials Chemistry A*. 2015. 4, (2), 675–683. ISSN 20507496.
125. LU, X., WANG, G., XIE, S., SHI, J., LI, W., TONG, Y., & LI, Y. Efficient photocatalytic hydrogen evolution over hydrogenated ZnO nanorod arrays. *Chemical Communications*. 2012. 48, (62), 7717–7719. ISSN 1364548X.
126. ZHU, S., YAO, F., YIN, C., LI, Y., PENG, W., MA, J., & ZHANG, D. Fe_2O_3/TiO_2 photocatalyst of hierarchical structure for H_2 production from water under visible light irradiation. *Microporous and Mesoporous Materials*. 2014. 190, 10–16. ISSN 13871811.
127. ZOU, X., WANG, P. P., LI, C., ZHAO, J., WANG, D., ASEFA, T., & LI, G. D. One-pot cation exchange synthesis of 1D porous CdS/ZnO heterostructures for visible-light-driven H_2 evolution. *Journal of Materials Chemistry A*. 2014. 2, (13), 4682–4689. ISSN 20507488.
128. WANG, X., LIU, G., LU, G. Q., & CHENG, H. M. Stable photocatalytic hydrogen evolution from water over ZnO-CdS core-shell nanorods. *International Journal of Hydrogen Energy*. 2010. 35, (15), 8199–8205. ISSN 03603199.
129. YANG, G., YAN, W., ZHANG, Q., SHEN, S., & DING, S. One-dimensional CdS/ZnO core/shell nanofibers via single-spinneret electrospinning: Tunable morphology and efficient photocatalytic hydrogen production. *Nanoscale*. 2013. 5, (24), 12432–12439. ISSN 20403364.
130. PARK, H., CHOI, W., & HOFFMANN, M. R. Effects of the preparation method of the ternary CdS/TiO_2/Pt hybrid photocatalysts on visible light-

induced hydrogen production. *Journal of Materials Chemistry*. 2008. 18, (20), 2379–2385. ISSN 09599428.
131. PARK, H., KIM, Y. K., & CHOI, W. Reversing CdS preparation order and its effects on photocatalytic hydrogen production of CdS/Pt-TiO_2 hybrids under visible light. *Journal of Physical Chemistry C*. 2011. 115, (13), 6141–6148. ISSN 19327447.
132. FANG, J., XU, L., ZHANG, Z., YUAN, Y., CAO, S., WANG, Z., YIN, L., LIAO, Y., & XUE, C. Au@TiO_2-CdS ternary nanostructures for efficient visible-light-driven hydrogen generation. *ACS Applied Materials and Interfaces*. 2013. 5, (16), 8088–8092. ISSN 19448244.
133. TANAKA, A., HASHIMOTO, K., & KOMINAMI, H. Visible-light-induced hydrogen and oxygen formation over Pt/Au/WO_3 photocatalyst utilizing two types of photoabsorption due to surface plasmon resonance and band-gap excitation. *Journal of the American Chemical Society*. 2014. 136, (2), 586–589. ISSN 00027863.
134. PAN, Y. X., ZHUANG, H., HONG, J., FANG, Z., LIU, H., LIU, B., HUANG, Y., & XU, R. Cadmium Sulfide Quantum Dots Supported on Gallium and Indium Oxide for Visible-Light-Driven Hydrogen Evolution from Water. *ChemSusChem*. 2014. 7, (9), 2537–2544. ISSN 1864564X.
135. MARTHA, S., REDDY, K. H., & PARIDA, K. M. Fabrication of In_2O_3 modified zno for enhancing stability, optical behaviour, electronic properties and photocatalytic activity for hydrogen production under visible light. *Journal of Materials Chemistry A*. 2014. 2, (10), 3621–3631. ISSN 20507488.
136. XIA, T., WALLENMEYER, P., ANDERSON, A., MUROWCHICK, J., LIU, L., & CHEN, X. Hydrogenated black ZnO nanoparticles with enhanced photocatalytic performance. *RSC Advances*. 2014. 4, (78), 41654–41658. ISSN 20462069.
137. GURYLEV, V., SU, C. Y., & PERNG, T. P. Hydrogenated ZnO nanorods with defect-induced visible light-responsive photoelectrochemical performance. *Applied Surface Science*. 2017. 411, 279–284. ISSN 0169-4332.
138. FENG, W., LIN, L., LI, H., CHI, B., PU, J., & LI, J. Hydrogenated TiO_2/ZnO heterojunction nanorod arrays with enhanced performance for photoelectrochemical water splitting. *International Journal of Hydrogen Energy*. 2017. 42, (7), 3938–3946. ISSN 0360-3199.
139. LI, L. L., LI, L. L., SUN, T., YU, X., LONG, L., XU, L., & YAN, J. Novel $H_3PW_{12}O_{40}$/TiO_2-g-C_3N_4 type-II heterojunction photocatalyst with enhanced visible-light photocatalytic properties. *Journal of Solid State Chemistry*. 2019. 274, (February), 152–161. ISSN 1095726X.
140. LU, C., GUO, F., YAN, Q., ZHANG, Z., LI, D., WANG, L., & ZHOU, Y. Hydrothermal synthesis of type II $ZnIn_2S_4$/$BiPO_4$ heterojunction photocatalyst with dandelion-like microflower structure for enhanced photocatalytic degradation of tetracycline under simulated solar light. *Journal of Alloys and Compounds*. 2019. 811, 151976. ISSN 09258388.
141. MILLS, A. An overview of the methylene blue ISO test for assessing the activities of photocatalytic films. *Applied Catalysis B: Environmental*. 2012.

128, 144–149. ISSN 09263373.
142. NAKATA, K., & FUJISHIMA, A. TiO_2 photocatalysis: Design and applications. *Journal of Photochemistry and Photobiology C: Photochemistry Reviews*. 2012. 13, (3), 169–189. ISSN 13895567.
143. FUJISHIMA, A., ZHANG, X., & TRYK, D. A. TiO_2 photocatalysis and related surface phenomena. *Surface Science Reports*. 2008. 63, (12), 515–582. ISSN 01675729.
144. FUJISHIMA, A., & HONDA, K. Electrochemical photolysis of water at a semiconductor electrode. *Nature*. 1972. 238, (5358), 37–38. ISSN 00280836.
145. Dimensions. TiO_2 Photocatalysis publications. [Accessed 1 February 2022]. Available from: https://app.dimensions.ai/discover/publication?search_mode=content&search_text=tio2 photocatalysis&search_type=kws&search_field=full_search
146. TICHONOVAS, M., KRUGLY, E., JANKUNAITE, D., RACYS, V., & MARTUZEVICIUS, D. Ozone-UV-catalysis based advanced oxidation process for wastewater treatment. *Environmental Science and Pollution Research*. 2017. 24, (21), 17584–17597. ISSN 16147499.
147. SIDARAVICIUTE, R., KRUGLY, E., DABASINSKAITE, L., VALATKA, E., & MARTUZEVICIUS, D. Surface-deposited nanofibrous TiO_2 for photocatalytic degradation of organic pollutants. *Journal of Sol-Gel Science and Technology*. 2017. 84, (2), 306–315. ISSN 0928-0707.
148. MONDAL, K., & SHARMA, A. Photocatalytic Oxidation of Pollutant Dyes in Wastewater by TiO_2 and ZnO nano-materials – A Mini-review. *Nanoscience & Technology for Mankind*. 2015. 36–72.
149. PELAEZ, M., NOLAN, N. T., PILLAI, S. C., SEERY, M. K., FALARAS, P., KONTOS, A. G., DUNLOP, P. S. M. M., HAMILTON, J. W. J. J., BYRNE, J. A. A., O'SHEA, K., ENTEZARI, M. H., & DIONYSIOU, D. D. A review on the visible light active titanium dioxide photocatalysts for environmental applications. *Applied Catalysis B: Environmental*. 2012. 125, 331–349. ISSN 0926-3373.
150. ZHAO, J., & YANG, X. Photocatalytic oxidation for indoor air purification: a literature review. *Building and Environment*. 2003. 38, (5), 645–654. ISSN 0360-1323.
151. WANG, J., JI, G., LIU, Y., GONDAL, M. A., & CHANG, X. Cu_2O/TiO_2 heterostructure nanotube arrays prepared by an electrodeposition method exhibiting enhanced photocatalytic activity for CO_2 reduction to methanol. *Catalysis Communications*. 2014. 46, 17–21. ISSN 15667367.
152. DEY, G. R. Chemical Reduction of CO_2 to Different Products during Photo Catalytic Reaction on TiO_2 under Diverse Conditions: an Overview. *Journal of Natural Gas Chemistry*. 2007. 16, (3), 217-226. ISSN 1003-9953.
153. NOWOTNY, J., BAK, T., NOWOTNY, M. K., & SHEPPARD, L. R. TiO_2 surface active sites for water splitting. *Journal of Physical Chemistry B*. 2006. 110, (37), 18492–18495. ISSN 15206106.
154. YU, J., QI, L., & JARONIEC, M. Hydrogen production by photocatalytic water splitting over Pt/TiO_2 nanosheets with exposed (001) facets. *Journal of*

Physical Chemistry C. 2010. 114, (30), 13118–13125. ISSN 19327447.
155. KHAN, S. U. M., AL-SHAHRY, M., & INGLER, W. B. Efficient photochemical water splitting by a chemically modified n-TiO_2. *Science*. 2002. 297, (5590), 2243–2245. ISSN 00368075.
156. ELFANAOUI, A., ELHAMRI, E., BOULKADDAT, L., IHLAL, A., BOUABID, K., LAANAB, L., TALEB, A., & PORTIER, X. Optical and structural properties of TiO_2 thin films prepared by sol-gel spin coating. *International Journal of Hydrogen Energy*. 2011. 36, (6), 4130–4133. ISSN 03603199.
157. ZALESKA, A. Doped-TiO_2: A Review. *Recent Patents on Engineering*. 2008. 2, (3), 157–164. ISSN 18722121.
158. ETACHERI, V., DI VALENTIN, C., SCHNEIDER, J., BAHNEMANN, D., & PILLAI, S. C. Visible-light activation of TiO_2 photocatalysts: Advances in theory and experiments. *Journal of Photochemistry and Photobiology C: Photochemistry Reviews*. 2015. 25, 1–29. ISSN 1389-5567.
159. TAHERNIYA, A., & RAOUFI, D. The annealing temperature dependence of anatase TiO_2 thin films prepared by the electron-beam evaporation method. *Semiconductor Science and Technology*. 2016. 31, (12), 1–9. ISSN 13616641.
160. TAHERNIYA, A., & RAOUFI, D. Thickness dependence of structural, optical and morphological properties of sol-gel derived TiO_2 thin film. *Materials Research Express*. 2019. 6, (1). ISSN 20531591.
161. KOTAKE, H., JIA, J., NAKAMURA, S., OKAJIMA, T., & SHIGESATO, Y. Tailoring the crystal structure of TiO_2 thin films from the anatase to rutile phase. *Journal of Vacuum Science & Technology A: Vacuum, Surfaces, and Films*. 2015. 33, (4), 41505. ISSN 0734-2101.
162. KANDIEL, T. A., ALKAIM, A. F., ROBBEN, L., ALKAIM, A. F., & BAHNEMANN, D. Brookite versus anatase TiO_2 photocatalysts: Phase transformations and photocatalytic activities. *Photochem. Photobiol. Sci*. 2013. 12. ISSN 1474-905X.
163. HANAOR, D. A. H. H., & SORRELL, C. C. *Review of the anatase to rutile phase transformation*. 2011. ISBN 0022-2461.
164. DIEBOLD, U. The surface science of titanium dioxide. *Surface Science Reports.* 2003. 48, (5-8), 53-229. ISSN 0167-5729.
165. KAVAN, L., GRÄTZEL, M., GILBERT, S. E., KLEMENZ, C., & SCHEEL, H. J. Electrochemical and photoelectrochemical investigation of single-crystal anatase. *Journal of the American Chemical Society*. 1996. 118, (28), 6716–6723. ISSN 00027863.
166. NOSHEEN, S., GALASSO, F. S., & SUIB, S. L. Role of Ti-O bonds in phase transitions of TiO_2. *Langmuir*. 2009. 25, (13), 7623–7630. ISSN 07437463.
167. LOW, I. M., ALBETRAN, H., PRIDA, V. M., VEGA, V., MANURUNG, P., & IONESCU, M. A comparative study on crystallization behavior, phase stability, and binding energy in pure and Cr-doped TiO_2 nanotubes. *Journal of Materials Research.* 2013. 28, (3), 304-312. ISSN 2044-5326.
168. CROMER, D. T., & HERRINGTON, K. The Structures of Anatase and Rutile. *Journal of the American Chemical Society*. 1955. 77, (18), 4708–4709. ISSN

15205126.
169. DETTE, C., PÉREZ-OSORIO, M. A., KLEY, C. S., PUNKE, P., PATRICK, C. E., JACOBSON, P., GIUSTINO, F., JUNG, S. J., & KERN, K. TiO_2 Anatase with a Bandgap in the Visible Region. *Nano Letters*. 2014. 14, (11), 6533–6538. ISSN 1530-6984.
170. YU, J. G., YU, H. G., CHENG, B., ZHAO, X. J., YU, J. C., & HO, W. K. The Effect of Calcination Temperature on the Surface Microstructure and Photocatalytic Activity of TiO_2 Thin Films Prepared by Liquid Phase Deposition. *Journal of Physical Chemistry B*. 2003. 107, (50), 13871–13879. ISSN 15206106.
171. ABDELLATIF, S., SHARIFI, P., KIRAH, K., GHANNAM, R., KHALIL, A. S. G., ERNI, D., & MARLOW, F. Refractive index and scattering of porous TiO_2 films. *Microporous and Mesoporous Materials*. 2018. 264, 84–91. ISSN 13871811.
172. SHANG, C., ZHAO, W.-N., & LIU, Z.-P. Searching for new TiO_2 crystal phases with better photoactivity. *Journal of Physics: Condensed Matter*. 2015. 27, (13), 134203. ISSN 0953-8984.
173. DE ANGELIS, F., DI VALENTIN, C., FANTACCI, S., VITTADINI, A., & SELLONI, A. Theoretical Studies on Anatase and Less Common TiO_2 Phases: Bulk, Surfaces, and Nanomaterials. *Chemical Reviews*. 2014. 114, (19), 9708–9753. ISSN 0009-2665.
174. MA, Y., WANG, X., JIA, Y., CHEN, X., HAN, H., & LI, C. Titanium dioxide-based nanomaterials for photocatalytic fuel generations. *American Chemical Society*. 2014, 114, (19), 9987-10043. ISSN 0002-7863.
175. SETVIN, M., FRANCHINI, C., HAO, X., SCHMID, M., JANOTTI, A., KALTAK, M., VAN DE WALLE, C. G., KRESSE, G., & DIEBOLD, U. Direct view at excess electrons in TiO_2 rutile and anatase. *Physical Review Letters*. 2014. 113, (8), 086402. ISSN 10797114.
176. KLETT, J., ZIEGLER, J., RADETINAC, A., KAISER, B., SCHÄFER, R., JAEGERMANN, W., URBAIN, F., BECKER, J. P., SMIRNOV, V., & FINGER, F. Band engineering for efficient catalyst-substrate coupling for photoelectrochemical water splitting. *Physical Chemistry Chemical Physics*. 2016. 18, (16), 10751–10757. ISSN 14639076.
177. WEN, B., HAO, Q., YIN, W. J., ZHANG, L., WANG, Z., WANG, T., ZHOU, C., SELLONI, A., YANG, X., & LIU, L. M. Electronic structure and photoabsorption of Ti^{3+} ions in reduced anatase and rutile TiO_2. *Physical Chemistry Chemical Physics*. 2018. 20, (26), 17658–17665. ISSN 14639076.
178. WANG, Z., WEN, B., HAO, Q., LIU, L. M., ZHOU, C., MAO, X., LANG, X., YIN, W. J., DAI, D., SELLONI, A., & YANG, X. Localized Excitation of Ti^{3+} Ions in the Photoabsorption and Photocatalytic Activity of Reduced Rutile TiO_2. *Journal of the American Chemical Society*. 2015. 137, (28), 9146–9152. ISSN 15205126.
179. LIU, H. Y., HSU, Y. L., SU, H. Y., HUANG, R. C., HOU, F. Y., TU, G. C., & LIU, W. H. A comparative study of amorphous, anatase, rutile, and mixed phase TiO_2 films by mist chemical vapor deposition and ultraviolet

photodetectors applications. *IEEE Sensors Journal*. 2018. 18, (10), 4022–4029. ISSN 1530437X.
180. NIEMELÄ, J. P., MARIN, G., & KARPPINEN, M. Titanium dioxide thin films by atomic layer deposition: A review. *Semiconductor Science and Technology*. 2017. 32, 093005. ISSN 02681242.
181. ULLATTIL, S. G., & PERIYAT, P. Sol-Gel Synthesis of Titanium Dioxide. *Advances in Sol-Gel Derived Materials and Technologies*. 2017. 271–283. ISSN 2364-0049.
182. BATTISTON, G. A., GERBASI, R., GREGORI, A., PORCHIA, M., CATTARIN, S., & RIZZI, G. A. PECVD of amorphous TiO_2 thin films: Effect of growth temperature and plasma gas composition. *Thin Solid Films*. 2000. 371, (1), 126–131. ISSN 00406090.
183. BESSERGENEV, V. G., KHMELINSKII, I. V., PEREIRA, R. J. F., KRISUK, V. V., TURGAMBAEVA, A. E., & IGUMENOV, I. K. Preparation of TiO_2 films by CVD method and its electrical, structural and optical properties. *Vacuum*. 2002. 64, (3–4), 275–279. ISSN 0042207X.
184. BERNARDI, M. I. B., LEE, E. J. H., LISBOA-FILHO, P. N., LEITE, E. R., LONGO, E., & VARELA, J. . TiO_2 thin film growth using the MOCVD method. *Materials Research*. 2001. 4, (3), 223–226. ISSN 1980-5373.
185. JILANI, A., ABDEL-WAHAB, M. S., & HAMMAD, A. H. Advance Deposition Techniques for Thin Film and Coating. *Modern Technologies for Creating the Thin-film Systems and Coatings*. 2017. ISBN 978-953-51-3004-8.
186. SIDARAVICIUTE, R., KAVALIUNAS, V., PUODZIUKYNAS, L., GUOBIENE, A., MARTUZEVICIUS, D., & ANDRULEVICIUS, M. Enhancement of photocatalytic pollutant decomposition efficiency of surface mounted TiO_2 via lithographic surface patterning. *Environmental Technology and Innovation*. 2020. 19, 100983. ISSN 23521864.
187. SUCIU, R. C., ROŞU, M. C., SILIPAŞ, T. D., BIRIŞ, A. R., BRATU, I., & INDREA, E. TiO_2 thin films prepared by spin coating technique. *Revue Roumaine de Chimie*. 2011. 607–612. ISSN 0035-3930.
188. WU, C. Y., LEE, Y. L., LO, Y. S., LIN, C. J., & WU, C. H. Thickness-dependent photocatalytic performance of nanocrystalline TiO_2 thin films prepared by sol-gel spin coating. *Applied Surface Science*. 2013. 280, 737–744. ISSN 01694332.
189. KAVALIUNAS, V., SESTAKAUSKAITE, A., SRIUBAS, M., & LAUKAITIS, G. Influence of Deposition Parameters on the Structure of TiO_2 Thin Films Prepared by Reactive Magnetron Sputtering Technique. *Recent Advances in Technology Research and Education.* 2019. 49–57. ISBN 978-3-319-99834-3.
190. SINGH, P., KUMAR, A., & KAUR, D. Substrate effect on texture properties of nanocrystalline TiO_2 thin films. *Physica B: Condensed Matter*. 2008. 403, (19–20), 3769–3773. ISSN 09214526.
191. MISZCZAK, S., & PIETRZYK, B. Anatase-rutile transformation of TiO_2 sol-gel coatings deposited on different substrates. *Ceramics International*. 2015.

41, (6), 7461–7465. ISSN 02728842.
192. BLANCO, E., DOMÍNGUEZ, M., GONZÁLEZ-LEAL, J. M., MÁRQUEZ, E., OUTÓN, J., & RAMÍREZ-DEL-SOLAR, M. Insights into the annealing process of sol-gel TiO_2 films leading to anatase development: The interrelationship between microstructure and optical properties. *Applied Surface Science*. 2018. 439, 736–748. ISSN 01694332.
193. ANDERSON, C., & BARD, A. J. Improved photocatalytic activity and characterization of mixed TiO_2/SiO_2 and TiO_2/Al_2O_3 materials. *Journal of Physical Chemistry B*. 1997. 101, (14), 2611–2616. ISSN 15206106.
194. LOPEZ, L., DAOUD, W. A., DUTTA, D., PANTHER, B. C., & TURNEY, T. W. Effect of substrate on surface morphology and photocatalysis of large-scale TiO_2 films. *Applied Surface Science*. 2013. 265, 162–168. ISSN 01694332.
195. KAVALIUNAS, V., KRUGLY, E., SRIUBAS, M., MIMURA, H., LAUKAITIS, G., & HATANAKA, Y. Influence of Mg, Cu, and Ni dopants on amorphous TiO_2 thin films photocatalytic activity. *Materials*. 2020. 13, (4), 886. ISSN 19961944.
196. QUESADA-GONZÁLEZ, M., BOSCHER, N. D., CARMALT, C. J., & PARKIN, I. P. Interstitial Boron-Doped TiO_2 Thin Films: The Significant Effect of Boron on TiO_2 Coatings Grown by Atmospheric Pressure Chemical Vapor Deposition. *ACS Applied Materials and Interfaces*. 2016. 8, (38), 25024–25029. ISSN 19448252.
197. KHAIRY, M., & ZAKARIA, W. Effect of metal-doping of TiO_2 nanoparticles on their photocatalytic activities toward removal of organic dyes. *Egyptian Journal of Petroleum*. 2014. 23, (4), 419–426. ISSN 20902468.
198. KHORE, S. K., KADAM, S. R., NAIK, S. D., KALE, B. B., & SONAWANE, R. S. Solar light active plasmonic $Au@TiO_2$ nanocomposite with superior photocatalytic performance for H2 production and pollutant degradation. *New Journal of Chemistry*. 2018. 42, (13), 10958–10968. ISSN 13699261.
199. CHOI, W., TERMIN, A., & HOFFMANN, M. R. The role of metal ion dopants in quantum-sized TiO_2: Correlation between photoreactivity and charge carrier recombination dynamics. *Journal of Physical Chemistry*. 1994. 98, (51), 13669–13679. ISSN 00223654.
200. SRIUBAS, M., KAVALIŪNAS, V., BOČKUTĖ, K., PALEVIČIUS, P., KAMINSKAS, M., RINKEVIČIUS, Ž., RAGULSKIS, M., & LAUKAITIS, G. Formation of Au nanostructures on the surfaces of annealed TiO_2 thin films. *Surfaces and Interfaces*. 2021. 25. ISSN 24680230.
201. YAO, Y., LI, G., CISTON, S., LUEPTOW, R. M., & GRAY, K. A. Photoreactive TiO_2/carbon nanotube composites: Synthesis and reactivity. *Environmental Science and Technology*. 2008. 42, (13), 4952–4957. ISSN 0013936X.
202. FATIMAH, I. Preparation of TiO_2-SiO_2 via sol-gel method: Effect of Silica precursor on Catalytic and Photocatalytic properties. *IOP Conference Series: Materials Science and Engineering*. 2017. 172, (1), 012025. ISSN 1757-899X.
203. LUI, G., LIAO, J. Y., DUAN, A., ZHANG, Z., FOWLER, M., & YU, A. Graphene-wrapped hierarchical TiO_2 nanoflower composites with enhanced

photocatalytic performance. *Journal of Materials Chemistry A*. 2013. 1, (39), 12255–12262. ISSN 20507488.
204. OHTANI, B. Titania Photocatalysis beyond Recombination: A Critical Review. *Catalysts*. 2013. 3, 942–953. ISSN 2073-4344.
205. MOHAMED, H. H., & BAHNEMANN, D. W. The role of electron transfer in photocatalysis: Fact and fictions. *Applied Catalysis B: Environmental*. 2012. 128, 91–104. ISSN 09263373.
206. WANG, S., DING, Z., CHANG, X., XU, J., & WANG, D. H. Modified Nano-TiO_2 Based Composites for Environmental Photocatalytic Applications. *Catalysts 2020, Vol. 10, Page 759*. 2020. 10, (7), 759. ISSN 20734344.
207. LI, X., YU, J., LOW, J., FANG, Y., XIAO, J., & CHEN, X. Engineering heterogeneous semiconductors for solar water splitting. *Journal of Materials Chemistry A*. 2015. 3, (6), 2485–2534. ISSN 20507496.
208. AMANO, F., TOSAKI, R., SATO, K., & HIGUCHI, Y. Effects of donor doping and acceptor doping on rutile TiO_2 particles for photocatalytic O_2 evolution by water oxidation. *Journal of Solid State Chemistry*. 2018. 258, 79–85. ISSN 0022-4596.
209. KAUR, K., & SINGH, C. V. Amorphous TiO_2 as a photocatalyst for hydrogen production: a DFT study of structural and electronic properties. *Energy Procedia*. 2012. 29, 291–299. ISSN 18766102.
210. KHRAMOV, E., KOTOLEVICH, Y., GARCÍA RAMOS, J. C., PESTRYAKOV, A., ZUBAVICHUS, Y., & BOGDANCHIKOVA, N. Amorphization of Degussa nanosized TiO_2 caused by its modification. *Fuel*. 2018. 234, 312–317. ISSN 00162361.
211. CHOI, J., PARK, H., & HOFFMANN, M. R. Effects of single metal-ion doping on the visible-light photoreactivity of TiO_2. *Journal of Physical Chemistry C*. 2010. 114, (2), 783–792. ISSN 19327447.
212. MALATI, M. A., & WONG, W. K. Doping TiO_2 for solar energy applications. *Surface Technology*. 1984. 22, (4), 305-322. ISSN 1001-3660.
213. CHEN, X. J., CABELLO, G., WU, D. Y., & TIAN, Z. Q. Surface-enhanced Raman spectroscopy toward application in plasmonic photocatalysis on metal nanostructures. *Journal of Photochemistry and Photobiology C: Photochemistry Reviews*. 2014. 21, 54–80. ISSN 13895567.
214. RUI, Z., WU, S., PENG, C., & JI, H. Comparison of TiO_2 Degussa P25 with anatase and rutile crystalline phases for methane combustion. *Chemical Engineering Journal*. 2014. 243, 254–264. ISSN 1385-8947.
215. BAKARDJIEVA, S., ŠUBRT, J., ŠTENGL, V., DIANEZ, M. J., & SAYAGUES, M. J. Photoactivity of anatase–rutile TiO_2 nanocrystalline mixtures obtained by heat treatment of homogeneously precipitated anatase. *Applied Catalysis B: Environmental*. 2005. 58, (3–4), 193–202. ISSN 0926-3373.
216. HURUM, D. C., AGRIOS, A. G., GRAY, K. A., RAJH, T., & THURNAUER, M. C. Explaining the enhanced photocatalytic activity of Degussa P25 mixed-phase TiO_2 using EPR. *Journal of Physical Chemistry B*. 2003. 107, (19), 4545–4549. ISSN 15206106.

217. MORISAKI, H., WATANABE, T., IWASE, M., & YAZAWA, K. Photoelectrolysis of water with TiO_2-covered solar-cell electrodes. *Applied Physics Letters*. 1976. 29, (6), 338–340. ISSN 00036951.
218. NOZIK, A. J. Photochemical diodes. *Applied Physics Letters*. 1977. 30, (11), 567–569. ISSN 00036951.
219. BAK, T., NOWOTNY, J., REKAS, M., & SORRELL, C. C. Photo-electrochemical properties of the TiO_2-Pt system in aqueous solutions. *International Journal of Hydrogen Energy*. 2002. 27, (1), 19–26. ISSN 03603199.
220. AVASTHI, S., MCCLAIN, W. E., MAN, G., KAHN, A., SCHWARTZ, J., & STURM, J. C. Hole-blocking titanium-oxide/silicon heterojunction and its application to photovoltaics. *Applied Physics Letters*. 2013. 102, (20). ISSN 00036951.
221. MAN, G., SCHWARTZ, J., STURM, J. C., & KAHN, A. Electronically Passivated Hole-Blocking Titanium Dioxide/Silicon Heterojunction for Hybrid Silicon Photovoltaics. *Advanced Materials Interfaces*. 2016. 3, (15), 1600026. ISSN 21967350.
222. PEREGO, M., SEGUINI, G., SCAREL, G., FANCIULLI, M., & WALLRAPP, F. Energy band alignment at TiO_2 Si interface with various interlayers. *Journal of Applied Physics*. 2008. 103, (4). ISSN 00218979.
223. KOCA, M., KUDAŞ, Z., EKINCI, D., & AYDOĞAN. Performance improvement of n-TiO_2/p-Si heterojunction by forming of n-TiO_2/polyphenylene/p-Si anisotype sandwich heterojunction. *Materials Science in Semiconductor Processing*. 2021. 121, (May 2020), 105436. ISSN 13698001.
224. MISHIN, M. V., VOROBYEV, A. A., KONDRATEVA, A. S., KOROLEVA, E. Y., KARASEOV, P. A., BESPALOVA, P. G., SHAKHMIN, A. L., GLUKHOVSKOY, A. V., WURZ, M. C., & FILIMONOV, A. V. The mechanism of charge carrier generation at the TiO_2/n-Si heterojunction activated by gold nanoparticles. *Semiconductor Science and Technology*. 2018. 33, (7). ISSN 13616641.
225. PARK, K. W., & KOLPAK, A. M. Optimal methodology for explicit solvation prediction of band edges of transition metal oxide photocatalysts. *Communications Chemistry*. 2019. 2, (1), 1–10. ISSN 23993669.
226. DENG, X., ZHANG, H., MA, Q., CUI, Y., CHENG, X., LI, X., XIE, M., & CHENG, Q. Fabrication of p-NiO/n-TiO_2 nano-tube arrays photoelectrode and its enhanced photocatalytic performance for degradation of 4-chlorphenol. *Separation and Purification Technology*. 2017. 186, 1–9. ISSN 18733794.
227. YOO, I. han, KALANUR, S. S., & SEO, H. A nanoscale p–n junction photoelectrode consisting of an NiOx layer on a TiO_2/CdS nanorod core-shell structure for highly efficient solar water splitting. *Applied Catalysis B: Environmental*. 2019. 250, 200–212. ISSN 09263373.
228. JIA, J., TANIYAMA, K., IMURA, M., KANAI, T., & SHIGESATO, Y. A visible-light active TiO_2 photocatalyst multilayered with WO_3. *Physical Chemistry Chemical Physics*. 2017. 19, (26), 17342–17348. ISSN 14639076.

229. LAI, C. W., & SREEKANTAN, S. Preparation of hybrid WO_3-TiO_2 nanotube photoelectrodes using anodization and wet impregnation: Improved water-splitting hydrogen generation performance. *International Journal of Hydrogen Energy*. 2013. 38, (5), 2156–2166. ISSN 03603199.
230. CHENG, W. H., RICHTER, M. H., MAY, M. M., OHLMANN, J., LACKNER, D., DIMROTH, F., HANNAPPEL, T., ATWATER, H. A., & LEWERENZ, H. J. Monolithic Photoelectrochemical Device for Direct Water Splitting with 19% Efficiency. *ACS Energy Letters*. 2018. 3, (8), 1795–1800. ISSN 23808195.
231. CUI, W., BAI, H., SHANG, J., WANG, F., XU, D., DING, J., FAN, W., & SHI, W. Organic-inorganic hybrid-photoanode built from NiFe-MOF and TiO_2 for efficient PEC water splitting. *Electrochimica Acta*. 2020. 349, 136383. ISSN 00134686.
232. HASHIMOTO, K., IRIE, H., & FUJISHIMA, A. TiO_2 photocatalysis: A historical overview and future prospects. *Japanese Journal of Applied Physics, Part 1: Regular Papers and Short Notes and Review Papers*. 2005. 44, (12), 8269–8285. ISSN 00214922.
233. Kurt J. Lesker Company | PRO Line PVD 75 – Versatile Sputtering, Electron Beam, & Thermal Evaporation Deposition Platform. [Accessed 7 February 2022]. Available from: https://www.lesker.com/newweb/vacuum_systems/deposition_systems_pvd_prolinepvd75.cfm
234. Photocatalytic Titanium Dioxide | Products | Chemical Manufacturer, ISHIHARA SANGYO KAISHA,LTD. [Accessed 19 May 2021]. Available from: https://www.iskweb.co.jp/eng/products/functional05.html
235. JEOL LTD. JSM-7600F Schottky Field Emission Scanning Electron Microscope | Products | JEOL Ltd. [Accessed 2 March 2021]. Available from: https://www.jeol.co.jp/en/products/detail/JSM-7600F.html
236. Rigaku Ultima III XRD | Materials Research Facility. . [Accessed 17 November 2021]. Available from: https://mrf.research.unt.edu/rigaku-ultima-iii-xrd
237. X-ray diffractometer - Rigaku Smart lab. [Accessed 17 November 2021] https://scientificservices.eu.
238. MIURA, K., & MAKI, T. A simple method for estimating f(E) and k_0(E) in the distributed activation energy model. *Energy and Fuels*. 1998. 12, (5), 864–869. ISSN 08870624.
239. INGHAM, B., & TONEY, M. F. X-ray diffraction for characterizing metallic films. *Metallic Films for Electronic, Optical and Magnetic Applications: Structure, Processing and Properties*. 2013. 3–38. ISBN 9780857090577.
240. BISHNOI, A., KUMAR, S., & JOSHI, N. Wide-Angle X-ray Diffraction (WXRD). *Microscopy Methods in Nanomaterials Characterization*. 2017. 313–337. ISBN 9780323461412.
241. ASTM E1523 - 15 Standard Guide to Charge Control and Charge Referencing Techniques in X-Ray Photoelectron Spectroscopy. [Accessed 17 November 2021]. Available from:

https://www.astm.org/Standards/E1523.htm
242. ISO - ISO 19318:2004 - Surface chemical analysis — X-ray photoelectron spectroscopy — Reporting of methods used for charge control and charge correction. . [Accessed 17 November 2021]. Available from: https://www.iso.org/standard/33783.html
243. BERSCH, E., DI, M., CONSIGLIO, S., CLARK, R. D., LEUSINK, G. J., & DIEBOLD, A. C. Complete band offset characterization of the $HfO_2/SiO_2/Si$ stack using charge corrected x-ray photoelectron spectroscopy. *Journal of Applied Physics*. 2010. 107, (4). ISSN 00218979.
244. ZHANG, D., YANG, M., GAO, H., & DONG, S. Translating XPS Measurement Procedure for Band Alignment into Reliable Ab Initio Calculation Method. *Journal of Physical Chemistry C*. 2017. ISSN 19327455.
245. GAITHERSBURG, M. NIST X-ray Photoelectron Spectroscopy (XPS) Database Main Search Menu. [Accessed 6 May 2021]. Available from: https://srdata.nist.gov/xps/main_search_menu.aspx
246. JASCO INTERNATIONAL CO., L. *JASCO UV-Vis/NIR Spectrophotometer V-600 series*. [Accessed 6 May 2021] Available from: https://jascoinc.com/wp-content/uploads/2017/08/V630_Leaflet.pdf
247. SÁNCHEZ-GONZÁLEZ, J., DÍAZ-PARRALEJO, A., ORTIZ, A. L., & GUIBERTEAU, F. Determination of optical properties in nanostructured thin films using the Swanepoel method. *Applied Surface Science*. 2006. 252, (17), 6013–6017. ISSN 01694332.
248. VIEZBICKE, B. D., PATEL, S., DAVIS, B. E., & BIRNIE, D. P. Evaluation of the Tauc method for optical absorption edge determination: ZnO thin films as a model system. *physica status solidi (b)*. 2015. 252, (8), 1700–1710. ISSN 1521-3951.
249. HOSSEINI, A., IÇLI, K., ÖZENBAŞ, M., & ERÇELEBI. Fabrication and characterization of spin-coated TiO_2 films. *Energy Procedia*. 2014. 60, (C), 191–198. ISSN 18766102.
250. HASAN, M. M., HASEEB, A. S. M. A., SAIDUR, R., & MASJUKI, H. H. Effects of annealing treatment on optical properties of anatase TiO_2 thin films. *World Academy of Science, Engineering and Technology*. 2009. 40, (April), 221–225. ISSN 2010376X.
251. KAROUI, M. Ben, KADDACHI, Z., & GHARBI, R. Optical properties of nanostructured TiO_2 thin films. *Journal of Physics: Conference Series*. 2015. 596, (1). ISSN 17426596.
252. WORASAWAT, S., TASAKI, K., HATANAKA, Y., NEO, Y., MIMURA, H., & PECHARAPA, W. Growth of ZnO nano-rods and its photoconductive characteristics on the photo-catalytic properties. In : *Materials Today: Proceedings*. 2019. 17, (4), 1379–1385. ISSN 2214-7853.
253. HAIMING GUO. Electrical Properties of Junction Structure in Silicon Devcies. *University of Pittsburgh Thesis*. 2018. 1–52. ISSN 00142972.
254. SELLERS, M. C. K., & SEEBAUER, E. G. Measurement method for carrier concentration in TiO_2 via the Mott-Schottky approach. *Thin Solid Films*. 2011. 519, 2103–2110. ISSN 0040-6090.

255. MA, S., SIMMONS, J. M., YUAN, D., LI, J. R., WENG, W., LIU, D. J., & ZHOU, H. C. A nanotubular metal–organic framework with permanent porosity: structure analysis and gas sorption studies. *Chemical Communications*. 2009. No. 27, 4049–4051. ISSN 1364-548X.
256. MELNICHENKO, Y. B. Neutron and X-Ray Porosimetry. *Small-Angle Scattering from Confined and Interfacial Fluids.* 2016. 173–204. ISBN 978-3-319-01104-2.
257. YLIVAARA, O. M. E., LANGNER, A., LIU, X., SCHNEIDER, D., JULIN, J., ARSTILA, K., SINTONEN, S., ALI, S., LIPSANEN, H., SAJAVAARA, T., HANNULA, S. P., & PUURUNEN, R. L. Mechanical and optical properties of as-grown and thermally annealed titanium dioxide from titanium tetrachloride and water by atomic layer deposition. *Thin Solid Films*. 2021. 732, 138758. ISSN 0040-6090.
258. NGUYEN-PHAN, T. D., & SHIN, E. W. Morphological effect of TiO_2 catalysts on photocatalytic degradation of methylene blue. *Journal of Industrial and Engineering Chemistry*. 2011. 17, (3), 397–400. ISSN 1226086X.
259. IIDA, Y., & OZAKI, S. Grain Growth and Phase Transformation of Titanium Oxide During Calcination. *Journal of the American Ceramic Society*. 1961. 44, (3), 120–127. ISSN 15512916.
260. LIANG, J., FENG, Y., LIANG, G., JI, Z., WANG, J., YAN, X., & JIN, Z. Effects of post-treatment on the photocatalytic activity of mesoporous TiO_2 thin films. *Journal of Materials Science Letters*. 2003. 22, (21), 1503–1506. ISSN 02618028.
261. YU, J., & ZHAO, X. Effect of substrates on the photocatalytic activity of nanometer TiO_2 thin films. *Materials Research Bulletin*. 2000. 35, (8), 1293–1301. ISSN 00255408.
262. ADUDA, B. O., RAVIRAJAN, P., CHOY, K. L., & NELSON, J. Effect of morphology on electron drift mobility in porous TiO_2. *International Journal of Photoenergy*. 2004. 6, (3), 141–147. ISSN 1110662X.
263. LIN, H., HUANG, C. P., LI, W., NI, C., SHAH, S. I., & TSENG, Y.-H. Size dependency of nanocrystalline TiO_2 on its optical property and photocatalytic reactivity exemplified by 2-chlorophenol. *Applied Catalysis B: Environmental*. 2006. 68, (1-2), 1-11. ISSN 0926-3373.
264. SENTHIL, T. . S., MUTHUKUMARASAMY, N., AGILAN, S., THAMBIDURAI, M., & BALASUNDARAPRABHU, R. Preparation and characterization of nanocrystalline TiO_2 thin films Prepared By Sol-Gel Spin Coating Method. *Mater. Sci. Eng. B*. 2010. 174, (10), 102–104. ISSN 09215107.
265. TAN, R.-J., TSENG, Y.-H., & KUO, C.-H. Crystal size control of TiO_2 using experimental strategies in sol–gel process. *Micro & Nano Letters*. 2010. 5, (6), 361. ISSN 17500443.
266. SURESH, C., BIJU, V., MUKUNDAN, P., & WARRIER, K. G. K. Anatase to rutile transformation in sol-gel titania by modification of precursor. *Polyhedron*. 1998. 17, (18), 3131–3135. ISSN 0277-5387.

267. PELAEZ, M., NOLAN, N. T., PILLAI, S. C., SEERY, M. K., FALARAS, P., KONTOS, A. G., DUNLOP, P. S. M., HAMILTON, J. W. J., BYRNE, J. A., O'SHEA, K., ENTEZARI, M. H., & DIONYSIOU, D. D. A review on the visible light active titanium dioxide photocatalysts for environmental applications. *Applied Catalysis B: Environmental*. 2012. 125, 331–349. ISSN 0926-3373.
268. NOLAN, N. T., SEERY, M. K., & PILLAI, S. C. Spectroscopic Investigation of the Anatase-to-Rutile Transformation of Sol-Gel-Synthesized TiO_2 Photocatalysts. *J. Phys. Chem. C.* 2009. 113, (36), 16151-16157. ISSN 1932-7455.
269. PERIYAT, P., PILLAI, S. C., MCCORMACK, D. E., COLREAVY, J., & HINDER, S. J. Improved High-Temperature Stability and Sun-Light-Driven Photocatalytic Activity of Sulfur-Doped Anatase TiO_2. *J. Phys. Chem. C.* 2008. 112, (20), 7644-7652. ISSN 1932-7455. .
270. SEERY, M. K., GEORGE, R., FLORIS, P., & PILLAI, S. C. Silver doped titanium dioxide nanomaterials for enhanced visible light photocatalysis. *Journal of Photochemistry and Photobiology A: Chemistry*. 2007. 189, (2–3), 258–263. ISSN 1010-6030.
271. LAFUENTE B, DOWNS R T, YANG H, S. N. Highlights in Mineralogical Crystallography. *The power of databases: the RRUFF project*. 2015. [Accessed 10 October 2020]. Available from: https://rruff.info/Anatase/R060277
272. HASSAN, A. T., HASSAN, E. S., & ABDULMUNEM, O. M. Effect of thermal annealing on the structural and optical properties of TiO_2 nanostructures. *Journal of the Mechanical Behavior of Materials*. 2021. 30, (1), 304–308. ISSN 21910243.
273. BAKRI, A. S., SAHDAN, M. Z., ADRIYANTO, F., RASHIP, N. A., SAID, N. D. M. M., ABDULLAH, S. A., & RAHIM, M. S. Effect of annealing temperature of titanium dioxide thin films on structural and electrical properties. *AIP Conference Proceedings*. 2017. 1788, 30030. ISSN 15517616.
274. MISZCZAK, S., & PIETRZYK, B. Anatase-rutile transformation of TiO_2 sol-gel coatings deposited on different substrates. *Ceramics International*. 2015. 41, (6), 7461–7465. ISSN 02728842.
275. TANG, H., PRASAD, K., SANJINÈS, R., SCHMID, P. E., & LÉVY, F. Electrical and optical properties of TiO_2 anatase thin films. *Journal of Applied Physics*. 1994. 75, (4), 2042–2047. ISSN 00218979.
276. SAHOO, N. K., THAKUR, S., & TOKAS, R. B. Achieving superior band gap, refractive index and morphology in composite oxide thin film systems violating the Moss rule. *Journal of Physics D: Applied Physics*. 2006. 39, (12), 2571–2579. ISSN 00223727.
277. MOSS, T. S. A Relationship between the Refractive Index and the Infra-Red Threshold of Sensitivity for Photoconductors. *Proceeding of the Physical Society: B.* 1950. 63, 167. ISSN 0370-1301.
278. FINKENRATH, H. The moss rule and the influence of doping on the optical dielectric constant of semiconductors-I. *Infrared Phys*. 1988. 28, (5), 327–332.

ISSN 1350-4495.
279. GOUMA, P. I., & MILLS, M. J. Anatase-to-Rutile Transformation in Titania Powders. *Journal of the American Ceramic Society*. 2001. 84, (3), 619–622. ISSN 1551-2916.
280. PENN, R. L., & BANFIELD, J. F. Formation of rutile nuclei at anatase {112} twin interfaces and the phase transformation mechanism in nanocrystalline titania. *American Mineralogist*. 1999. 84, (5–6), 871–876. ISSN 0003004X.
281. HYOUNG, G. L., & ZUO, J. M. Growth and Phase Transformation of Nanometer-Sized Titanium Oxide Powders Produced by the Precipitation Method. *Journal of the American Ceramic Society*. 2004. 87, (3), 473–479. ISSN 1551-2916.
282. ZEMAN, P., & TAKABAYASHI, S. Effect of total and oxygen partial pressures on structure of photocatalytic TiO_2 films sputtered on unheated substrate. *Surface and Coatings Technology*. 2002. 153, (1), 93–99. ISSN 0257-8972.
283. SAFEEN, K., MICHELI, V., BARTALI, R., GOTTARDI, G., & LAIDANI, N. Low temperature growth study of nano-crystalline TiO_2 thin films deposited by RF sputtering. *Journal of Physics D: Applied Physics*. 2015. 48, (29), 295201. ISSN 0022-3727.
284. JIA, J., YAMAMOTO, H., OKAJIMA, T., & SHIGESATO, Y. On the Crystal Structural Control of Sputtered TiO_2 Thin Films. *Nanoscale research letters*. 2016. 11, (1), 324. ISSN 1931-7573.
285. OKIMURA, K. Low temperature growth of rutile TiO_2 films in modified rf magnetron sputtering. *Surface and Coatings Technology*. 2001. 135, (2–3), 286–290. ISSN 0257-8972.
286. BURDETT, J. K., HUGHBANKS, T., MILLER, G. J., RICHARDSON, J. W., & SMITH, J. V. Structural-electronic relationships in inorganic solids: powder neutron diffraction studies of the rutile and anatase polymorphs of titanium dioxide at 15 and 295 K. *Journal of the American Chemical Society*. 1987. 109, (12), 3639–3646. ISSN 0002-7863.
287. BURANAWONG, A., WITIT-ANUN, N., & CHAIYAKUN, S. Total pressure and annealing temperature effects on structure and photo-induce hydrophilicity of reactive DC sputtered TiO_2 thin films. *Engineering Journal*. 2012. 16, (3), 79–89. ISSN 01258281.
288. BAROCH, P., MUSIL, J., VLCEK, J., NAM, K. H., & HAN, J. G. Reactive magnetron sputtering of TiO_x films. *Surface and Coatings Technology*. 2005. 193, (1-3 SPEC. ISS.), 107–111. ISSN 02578972.
289. Silicon - RRUFF Database: Raman, X-ray, Infrared, and Chemistry. . [Accessed 23 January 2022]. Available from: https://rruff.info/silicon/display=default/
290. Anatase R070582 - RRUFF Database: Raman, X-ray, Infrared, and Chemistry. . [Accessed 23 January 2022]. Available from: https://rruff.info/anatase/display=default/R070582
291. Rutile R050417 - RRUFF Database: Raman, X-ray, Infrared, and Chemistry. . [Accessed 23 January 2022]. Available from:

https://rruff.info/rutile/display=default/R050417
292. LANDMANN, M., RAULS, E., & SCHMIDT, W. G. The electronic structure and optical response of rutile, anatase and brookite TiO_2. *Journal of Physics Condensed Matter*. 2012. 24, (19), 195503. ISSN 09538984.
293. MALLIGA, P., PANDIARAJAN, J., PRITHIVIKUMARAN, N., & NEYVASAGAM, K. Influence of Film Thickness on Structural and Optical Properties of Sol-Gel Spin Coated TiO_2 Thin Film. *IOSR Journal of Applied Physics.* 2014. 6, (1), 22-28. ISSN 2278-4861.
294. SÖNMEZOLU, S., ARSLAN, A., SERIN, T., & SERIN, N. The effects of film thickness on the optical properties of TiO_2-SnO_2 compound thin films. *Physica Scripta*. 2011. 84, (6). ISSN 00318949.
295. ZERIBI, F., ATTAF, A., DERBALI, A., SAIDI, H., BENMEBROUK, L., AIDA, M. S., DAHNOUN, M., NOUADJI, R., & EZZAOUIA, H. Dependence of the Physical Properties of Titanium Dioxide (TiO_2) Thin Films Grown by Sol-Gel (Spin-Coating) Process on Thickness. *ECS Journal of Solid State Science and Technology*. 2022. 11, (2), 023003. ISSN 2162-8769.
296. IVANOVA, T., HARIZANOVA, A., KOUTZAROVA, T., & VERTRUYEN, B. Optical and structural characterization of TiO_2 films doped with silver nanoparticles obtained by sol-gel method. *Optical Materials*. 2013. 36, (2), 207–213. ISSN 09253467.
297. LI, L., LU, J., LI, R., SHEN, C., CHEN, Y., YANG, S., & GAO, X. The determination of the thickness and optical constants of the microcrystalline silicon thin film by using envelope method. *Optoelectronics and Advanced Materials, Rapid Communications*. 2009. 3, (6), 625–630. ISSN 20653824.
298. CHOUDHURY, B., & CHOUDHURY, A. Oxygen defect dependent variation of band gap, Urbach energy and luminescence property of anatase, anatase-rutile mixed phase and of rutile phases of TiO_2 nanoparticles. *Physica E: Low-Dimensional Systems and Nanostructures*. 2014. 56, 364–371. ISSN 13869477.
299. BIESINGER, M. C. X-Ray Photoelectron Spectroscopy (XPS) Reference Pages. Titanium. [Accessed 15 October 2021]. Available from: http://www.xpsfitting.com/2008/09/titanium.html
300. MOULDER, J. F., STICKLE, W. F., SOBOL, P. E., & BOMBEN, K. D. Handbook of X-ray Photoelectron Spectroscopy. *Surface And Interface Analysis*. ISSN 01422421.
301. MOULDER, F. J. Handbook of X-Ray Photoelectron Spectroscopy. *Physical Electronics*. 1995. 230–232. ISBN 096481241X.
302. KHAN, M. A., JUNG, H. T., & YANG, O. B. Synthesis and Characterization of Ultrahigh Crystalline TiO_2 Nanotubes. *Journal of Physical Chemistry B*. 2006. 110, (13), 6626–6630. ISSN 15206106.
303. YIN, W. J., WEN, B., ZHOU, C., SELLONI, A., & LIU, L. M. *Excess electrons in reduced rutile and anatase TiO2*. 2018. Elsevier B.V.
304. ATUCHIN, V. V., KESLER, V. G., PERVUKHINA, N. V., & ZHANG, Z. Ti 2p and O 1s core levels and chemical bonding in titanium-bearing oxides. *Journal of Electron Spectroscopy and Related Phenomena*. 2006. 152, (1–2),

18–24. ISSN 0368-2048.
305. BHARTI, B., KUMAR, S., LEE, H.-N., & KUMAR, R. Formation of oxygen vacancies and Ti^{3+} state in TiO_2 thin film and enhanced optical properties by air plasma treatment. *Scientific Reports*. 2016. 6, 32355. ISSN 2045-2322.
306. GUO, Q., ZHOU, C., MA, Z., & YANG, X. Fundamentals of TiO_2 Photocatalysis: Concepts, Mechanisms, and Challenges. *Advanced Materials*. 2019. 31, (50), 1–26. ISSN 15214095.
307. SCHNEIDER, J., MATSUOKA, M., TAKEUCHI, M., ZHANG, J., HORIUCHI, Y., ANPO, M., & BAHNEMANN, D. W. Understanding TiO_2 Photocatalysis: Mechanisms and Materials. *Chemical Reviews*. 2014. 114, (19), 9919–9986. ISSN 0009-2665.
308. ZHU, W. D., WANG, C. W., CHEN, J. B., LI, D. S., ZHOU, F., & ZHANG, H. L. Enhanced field emission from hydrogenated TiO_2 nanotube arrays. *Nanotechnology*. 2012. 23, (45). ISSN 09574484.
309. SIDARAVICIUTE, R., BUIVYDIENE, D., KRUGLY, E., VALATKA, E., & MARTUZEVICIUS, D. A composite microfibre-supported short-nanofibre photocatalyst for environmental pollutant decomposition. *Journal of Photochemistry and Photobiology A: Chemistry*. 2019. 368, 7–14. ISSN 1010-6030.
310. RATOVA, M., SAWTELL, D., & KELLY, P. J. Micro-Patterning of Magnetron Sputtered Titanium Dioxide Coatings and Their Efficiency for Photocatalytic Applications. *Coatings 2020, Vol. 10, Page 68*. 2020. 10, (1), 68. ISSN 20796412.
311. MARSCHALL, R. Semiconductor Composites: Strategies for Enhancing Charge Carrier Separation to Improve Photocatalytic Activity. *Advanced Functional Materials*. 2014. 24, (17), 2421–2440. ISSN 1616-3028.
312. GUZMÁN, D., ORDOÑEZ, S., SERAFINI, D., ROJAS, P., & BUSTOS, O. Effect of the milling energy on the production and thermal stability of amorphous $Mg_{50}Ni_{50}$. *Journal of Alloys and Compounds*. 2009. 471, (1–2), 435–441. ISSN 0925-8388.
313. LEE, S. Y., HUANG, E. W., WOO, W., YOON, C., CHAE, H., & YOON, S. G. Dynamic Strain Evolution around a Crack Tip under Steady- and Overloaded-Fatigue Conditions. *Metals 2015, Vol. 5, Pages 2109-2118*. 2015. 5, (4), 2109–2118. ISSN 20754701.
314. MURRAY, J. W., ALGODI, S. J., FAY, M. W., BROWN, P. D., & CLARE, A. T. Formation mechanism of electrical discharge TiC-Fe composite coatings. *Journal of Materials Processing Technology*. 2017. 243, 143–151. ISSN 0924-0136.
315. BETANCOURT-GALINDO, R., REYES-RODRIGUEZ, P. Y., PUENTE-URBINA, B. A., AVILA-ORTA, C. A., RODRÍGUEZ-FERNÁNDEZ, O. S., CADENAS-PLIEGO, G., LIRA-SALDIVAR, R. H., & GARCÍA-CERDA, L. A. Synthesis of copper nanoparticles by thermal decomposition and their antimicrobial properties. *Journal of Nanomaterials*. 2014. 2014. ISSN 16874110.
316. 430 Stainless Steel - Penn Stainless. . [Accessed 19 January 2022]. Available

from: https://www.pennstainless.com/resources/product-information/stainless-grades/300-series/304l-stainless-steel/
317. XPS Interpretation of Magnesium. . [Accessed 22 January 2022]. Available from: https://www.jp.xpssimplified.com/elements/magnesium.php
318. FEBVRIER, A. Le, JENSEN, J., & EKLUND, P. Wet-cleaning of MgO (001): Modification of surface chemistry and effects on thin film growth investigated by x-ray photoelectron spectroscopy and time-of-flight secondary ion mass spectroscopy. *Journal of Vacuum Science & Technology A: Vacuum, Surfaces, and Films*. 2017. 35, (2), 021407. ISSN 0734-2101.
319. WANG, Y., LÜ, Y., ZHAN, W., XIE, Z., KUANG, Q., & ZHENG, L. Synthesis of porous Cu_2O/CuO cages using Cu-based metal-organic frameworks as templates and their gas-sensing properties. *Journal of Materials Chemistry A*. 2015. 3, (24), 12796–12803. ISSN 20507496.
320. LU, Q. H., HUANG, R., WANG, L. S., WU, Z. G., LI, C., LUO, Q., ZUO, S. Y., LI, J., PENG, D. L., HAN, G. L., & YAN, P. X. Thermal annealing and magnetic anisotropy of NiFe thin films on n^+-Si for spintronic device applications. *Journal of Magnetism and Magnetic Materials*. 2015. 394, 253–259. ISSN 0304-8853.
321. CAREY, J. J., & MCKENNA, K. P. Screening Doping Strategies to Mitigate Electron Trapping at Anatase TiO_2 Surfaces. *Journal of Physical Chemistry C*. 2019. 123, (36), 22358–22367. ISSN 19327455.
322. JOHANSSON, P. G., KOPECKY, A., GALOPPINI, E., & MEYER, G. J. Distance dependent electron transfer at TiO_2 interfaces sensitized with phenylene ethynylene bridged RuII-isothiocyanate compounds. *Journal of the American Chemical Society*. 2013. 135, (22), 8331–8341. ISSN 00027863.
323. NAM, Y., LI, L., LEE, J. Y., & PREZHDO, O. V. Size and Shape Effects on Charge Recombination Dynamics of TiO_2 Nanoclusters. *Journal of Physical Chemistry C*. 2018. 122, (9), 5201–5208. ISSN 19327455.
324. BLOH, J. Z., DILLERT, R., & BAHNEMANN, D. W. Designing Optimal Metal-Doped Photocatalysts: Correlation between Photocatalytic Activity, Doping Ratio, and Particle Size. *The Journal of Physical Chemistry C*. 2012. 116, (48), 25558–25562. ISSN 1932-7447.
325. PRASAI, B., CAI, B., UNDERWOOD K. M., LEWIS, J. P., DRABOLD, D. A. Properties of amorphous and crystalline titanium dioxide from first principles. *Journal of Materials Science*. 2012. 47, (21), 7515–7521. ISSN 00222461.
326. HUANG, J., LIU, Y., LU, L., & LI, L. The photocatalytic properties of amorphous TiO_2 composite films deposited by magnetron sputtering. *Research on Chemical Intermediates*. 2012. 38, (2), 487–498. ISSN 0922-6168.
327. OHTANI, B., OGAWA, Y., & NISHIMOTO, S.-I. Photocatalytic Activity of Amorphous-Anatase Mixture of Titanium(IV) Oxide Particles Suspended in Aqueous Solutions. *J. Phys. Chem. B*. 1997. 101, (19), 3746-3752. ISSN 1520-5207.
328. MANZANARES, M., FÀBREGA, C., ORIOL OSSÓ, J., VEGA, L. F.,

ANDREU, T., & MORANTE, J. R. Engineering the TiO_2 outermost layers using magnesium for carbon dioxide photoreduction. *Applied Catalysis B: Environmental*. 2014. 150–151, 57–62. ISSN 09263373.

329. ZU, D., XU, Z., ZHANG, A., WANG, H., WEI, H., OU, G., HUANG, K., ZHANG, R., LI, L., HU, S., SUN, S., & WU, H. Room temperature Mg reduction of TiO_2: formation mechanism and application in photocatalysis. *Chemical Communications*. 2019. 55, (53), 7675–7678. ISSN 1364-548X.
330. TASBIHI, M., KOČÍ, K., TROPPOVÁ, I., EDELMANNOVÁ, M., RELI, M., ČAPEK, L., & SCHOMÄCKER, R. Photocatalytic reduction of carbon dioxide over Cu/TiO_2 photocatalysts. *Environmental Science and Pollution Research*. 2018. 25, (35), 34903–34911. ISSN 16147499.
331. BENSOUICI, F., BOUOUDINA, M., DAKHEL, A. A., TALA-IGHIL, R., TOUNANE, M., IRATNI, A., SOUIER, T., LIU, S., & CAI, W. Optical, structural and photocatalysis properties of Cu-doped TiO_2 thin films. *Applied Surface Science*. 2017. 395, 110–116. ISSN 01694332.
332. JUNG, M., SCOTT, J., NG, Y. H., JIANG, Y., & AMAL, R. CuO_x dispersion and reducibility on TiO_2 and its impact on photocatalytic hydrogen evolution. *International Journal of Hydrogen Energy*. 2014. 39, (24), 12499–12506. ISSN 0360-3199.
333. CHEN, W. T., CHAN, A., SUN-WATERHOUSE, D., MORIGA, T., IDRISS, H., & WATERHOUSE, G. I. N. Ni/TiO_2: A promising low-cost photocatalytic system for solar H_2 production from ethanol-water mixtures. *Journal of Catalysis*. 2015. 326, 43–53. ISSN 10902694.
334. WANG, Y., ZHAO, J., XIONG, X., LIU, S., & XU, Y. Role of Ni^{2+} ions in TiO_2 and Pt/TiO_2 photocatalysis for phenol degradation in aqueous suspensions. *Applied Catalysis B: Environmental*. 2019. 258, 117903. ISSN 0926-3373.
335. MICHAELSON, H. B. The work function of the elements and its periodicity. *Journal of Applied Physics*. 2008. 48, (11), 4729. ISSN 0021-8979.
336. HÖLZL, J., & SCHULTE, F. K. Work Function of Metals. *Solid Surface Physics*. 1979. 1–150. ISBN 978-3-540-35253-2.
337. KASHIWAYA, S., MORASCH, J., STREIBEL, V., TOUPANCE, T., JAEGERMANN, W., & KLEIN, A. The Work Function of TiO_2. *Surfaces*. 2018. 1, (1), 73–89. ISSN 2571-9637.
338. THOMPSON, C. V. Solid-State Dewetting of Thin Films. *Annual review of Materials Research.* 2012. 42, (1), 399–434. ISSN 1545-4118.
339. NSIMAMA, P. D., HERZ, A., WANG, D., & SCHAAF, P. Influence of the substrate on the morphological evolution of gold thin films during solid-state dewetting. *Applied Surface Science*. 2016. 388, 475–482. ISSN 0169-4332.
340. LEE, S. Y., KANG, D., JEONG, S., DO, H. T., & KIM, J. H. Photocatalytic Degradation of Rhodamine B Dye by TiO_2 and Gold Nanoparticles Supported on a Floating Porous Polydimethylsiloxane Sponge under Ultraviolet and Visible Light Irradiation. *ACS Omega*. 2020. 5, (8), 4233–4241. ISSN 24701343.
341. THE, V., LI, J., YAN, Y., SUN, G., YANG, J., WANG, Z., & YAN, X.

Preparative Separation of Isoquinoline Alkaloids from Phellodendri Cortex by pH-Zone-Refining Counter-Current Chromatography. *Química Nova*. 2021. 44, (3), 295–300. ISSN 0100-4042.
342. CHOURASIA, A. R. Core Level XPS Spectra of Elemental Silicon Using Zirconium Radiation. *Surface Science Spectra*. 2021. 5, (2), 115. ISSN 1055-5269.
343. JENSEN, D. S., KANYAL, S. S., MADAAN, N., VAIL, M. A., DADSON, A. E., ENGELHARD, M. H., & LINFORD, M. R. Silicon (100)/SiO_2 by XPS. *Surface Science Spectra*. 2013. 20, (1), 36. ISSN 1055-5269.
344. SHEN, L., MENG, F., & LIU, Z. Roles of the Fermi level of doped a-Si:H and band offsets at a-Si:H/c-Si interfaces in n-type HIT solar cells. *Solar Energy*. 2013. 97, 168–175. ISSN 0038092X.
345. PARASURAMAN, S. Lecture 7: Extrinsic semiconductors-Fermi level Contents. *NOC: Fundamentals of Electronic Materials and Devices.* 2016. 1-10. ISBN 978-0072456363.
346. NSM Archive - Band structure and carrier concentration of Silicon (Si). . [Accessed 16 January 2022]. Available from: http://www.matprop.ru/Si_bandstr
347. KAVALIUNAS, V., HATANAKA, Y., NEO, Y., LAUKAITIS, G., & MIMURA, H. Structural Design of TiO_2/Si Hybrid Photoelectrode and Pt-Free Counter Photoelectrodes for Charge Carrier Separation in Water-Splitting Reactions . *ECS Journal of Solid State Science and Technology*. 2021. 10, (10), 103015. ISSN 2162-8769.
348. CHEN, W., LU, Y., DONG, W., CHEN, Z., & SHEN, M. Plasmon mediated visible light photocurrent and photoelectrochemical hydrogen generation using Au nanoparticles/TiO_2 electrode. *Materials Research Bulletin*. 2014. 50, 31–35. ISSN 00255408.
349. TAN, F., LI, T., WANG, N., LAI, S. K., TSOI, C. C., YU, W., & ZHANG, X. Rough gold films as broadband absorbers for plasmonic enhancement of TiO_2 photocurrent over 400-800 nm. *Scientific Reports*. 2016. 6, (April), 1–10. ISSN 20452322.
350. LI, W., YAO, L., ZHANG, Z., GENG, H., LI, C. C., YU, Y., SHENG, P., & LI, S. Tiny Au nanoparticles mediation strategy for preparation of NIR $CuInS_2$ QDs based 1D TiO_2 hybrid photoelectrode with enhanced photocatalytic activity. *Materials Science in Semiconductor Processing*. 2019. 99, 106–113. ISSN 13698001.
351. BUBACZ, K., CHOINA, J., DOLAT, D., & MORAWSKI, A. W. Methylene blue and phenol photocatalytic degradation on nanoparticles of anatase TiO_2. *Polish Journal of Environmental Studies*. 2010. 19, (4), 685–691. ISSN 12301485.
352. HAQUE, M. M., & MUNEER, M. Photodegradation of norfloxacin in aqueous suspensions of titanium dioxide. *Journal of Hazardous Materials*. 2007. 145, (1–2), 51–57. ISSN 03043894.
353. ALKAIM, A. F., ALJEBOREE, A. M., ALRAZAQ, N. A., BAQIR, S. J., HUSSEIN, F. H., & LILO, A. J. Effect of pH on adsorption and photocatalytic

degradation efficiency of different catalysts on removal of methylene blue. *Asian Journal of Chemistry*. 2014. 26, (24), 8445–8448. ISSN 09707077.
354. LING, C. M., MOHAMED, A. R., & BHATIA, S. Performance of photocatalytic reactors using immobilized TiO_2 film for the degradation of phenol and methylene blue dye present in water stream. *Chemosphere*. 2004. 57, (7), 547–554. ISSN 00456535.
355. WANG, N., LI, J., ZHU, L., DONG, Y., & TANG, H. Highly photocatalytic activity of metallic hydroxide/titanium dioxide nanoparticles prepared via a modified wet precipitation process. *Journal of Photochemistry and Photobiology A: Chemistry*. 2008. 198, (2–3), 282–287. ISSN 10106030.
356. GUILLARD, C., LACHHEB, H., HOUAS, A., KSIBI, M., ELALOUI, E., & HERRMANN, J. M. Influence of chemical structure of dyes, of pH and of inorganic salts on their photocatalytic degradation by TiO_2 comparison of the efficiency of powder and supported TiO_2. *Journal of Photochemistry and Photobiology A: Chemistry*. 2003. 158, (1), 27–36. ISSN 10106030.
357. SENTHILKUMAAR, S., PORKODI, K., GOMATHI, R., GEETHA MAHESWARI, A., & MANONMANI, N. Sol-gel derived silver doped nanocrystalline titania catalysed photodegradation of methylene blue from aqueous solution. *Dyes and Pigments*. 2006. 69, (1–2), 22–30. ISSN 01437208.
358. POULIOS, I., AVRANAS, A., REKLITI, E., & ZOUBOULIS, A. Photocatalytic oxidation of Auramine O in the presence of semiconducting oxides. *Journal of Chemical Technology & Biotechnology*. 2000. 75, (3), 205–212. ISSN 0268-2575.

UDK 544.526.5+539.216.2](043.3)

SL 344. 2022-12-14, 19,25 leidyb. apsk. l. Tiražas 14 egz. Užsakymas 248.
Išleido Kauno technologijos universitetas, K. Donelaičio g. 73, 44249 Kaunas
Spausdino leidyklos „Technologija“ spaustuvė, Studentų g. 54, 51424 Kaunas